# Joint ERCOFTAC/EU-CTFF
# European Drag Reduction and Flow Control Meeting – EDRFCM 2022

## Tuesday 6th September

**Welcome** **10:40-10:50**

**Session 1.1** **10:50-12:30**

| | | | |
|---|---|---|---|
| Passive control | Pierre Ricco | NOTES ON THE SKIN-FRICTION COEFFICIENT OF BOUNDARY LAYERS AND CONFINED FLOWS | 1 |
| Passive control | Olaf van Campenhout | EXPERIMENTAL AND NUMERICAL INVESTIGATION INTO THE DRAG PERFORMANCE OF DIMPLED SURFACES IN A TURBULENT BOUNDARY LAYER | 2 |
| Passive control | Benedetto Mele | DRAG REDUCTION MODELING FOR ENGINEERING APPLICATIONS | 3 |
| Passive control | Saskia Pasch | MEASUREMENTS IN A TURBULENT CHANNEL FLOW BY MEANS OF AN LDV PROFILE SENSOR | 4 |
| Passive control | Mahmud Muhammad | EFFECT OF SLAT ATTACHMENT ON RUDDER LEADING EDGE OF A VERTICAL TAIL PLANE | 6 |

**Lunch** **12:30-14:00**

**Session 1.2** **14:00-16:00**

| | | | |
|---|---|---|---|
| Passive control | Federica Gattere | FLOW OVER RIBLETS: ANALYTICAL CORRECTION OF CORNER SINGULARITY | 7 |
| Passive control | Jeremy Wong | ASSESSING THE PROTRUSION-HEIGHT CONCEPT FOR PREDICTING THE DRAG-REDUCTION PERFORMANCE OF RIBLETS | 8 |
| Passive control | Jooha Kim | BIOMIMETIC FLOW CONTROL FOR A PARAGLIDER: FROM IDEA TO PRODUCT | 9 |
| Passive control | Zhihao Zhang | EXPERIMENTAL INVESTIGATION OF THE SESSILE DROPLET EVAPORATION PROCESS BASED ON DIFFERENT SURFACE ROUGHNESS AND WETTABILITY | 10 |
| Passive control | Fermin Mallor | CANCELLATION OF THE INVISCID CONTRIBUTION IN SKIN-FRICTION DECOMPOSITIONS | 11 |
| Passive control | Firoozeh Foroozan | SYNCHRONIZED MEASUREMENTS OF FLOW AND WALL FIELDS IN TURBULENT BOUNDARY LAYERS | 12 |

**Tea break** **16:00-16:30**

**Session 1.3** **16:30-18:30**

| | | | |
|---|---|---|---|
| EU-CTFF | Kwing-So Choi | PLASMA FLOW CONTROL OF THE TIP VORTICES OVER A VERY LOW ASPECT-RATIO WING | 13 |
| EU-CTFF | Francois Rogier | ELECTROHYDRODYNAMIC FORCE MODELLING AND APPLICATION TO FLOW CONTROL | 14 |
| EU-CTFF | Li He | TWO-SCALE COUPLING FOR WALL-BOUNDED TURBULENCE OVER ‘REGULAR ROUGHNESS’ | 15 |
| EU-CTFF | Arivazhagan Balasubramanian | PREDICTION OF WALL-BOUNDED TURBULENCE IN A VISCOELASTIC CHANNEL FLOW USING CONVOLUTIONAL NEURAL NETWORKS | 16 |
| EU-CTFF | Yaxing Wang | OPPOSITION CONTROL OF TURBULENT SPOTS | 17 |
| EU-CTFF | Amrit Kumar | SPREADING DYNAMICS OF A WATER DROP ON A MICRO-TEXTURED SURFACE | 18 |

**Reception** **18:30-20:00**

# Wednesday 7th September

**Session 2.1** **8:40-10:20**

| | | | |
|---|---|---|---|
| Wall forcing | Maurizio Quadrio | DRAG REDUCTION ON A TRANSONIC WING | 19 |
| Wall forcing | Emanuele Gallorini | COHERENT NEAR-WALL STRUCTURES AND DRAG REDUCTION BY SPANWISE FORCING | 20 |
| Wall forcing | Esther Mateling | INTERNAL FLOW STRUCTURE MODIFICATION GENERATED BY TRANSVERSAL SURFACE WAVES | 21 |
| Wall forcing | Amandine Capogna | NEAR-WALL MHD TURBULENCE CONTROL - EFFECT OF A HALBACH MAGNET CONFIGURATION | 22 |
| Wall forcing | Isabella Fumarola | SIMULTANEOUS MEASUREMENTS OF SURFACE AND FLUID VELOCITY IN A TURBULENT BOUNDARY LAYER WITH STANDING SPANWISE WAVES AT THE WALL | 23 |

**Coffee break** **10:20-10:50**

**Session 2.2** **10:50-12:30**

| | | | |
|---|---|---|---|
| Wall forcing | Dileep Chandran | TURBULENT DRAG REDUCTION BY SPANWISE WALL FORCING AT HIGH REYNOLDS NUMBERS | 24 |
| Wall forcing | Rahul Deshpande | TOWARDS ENERGY-EFFICIENT TURBULENT DRAG REDUCTION THROUGH ENHANCING THE INTER-SCALE COUPLING | 25 |
| Wall forcing | Alessandro Chiarini | TURBULENT DRAG REDUCTION USING SPANWISE FORCING IN COMPRESSIBLE REGIME | 26 |
| Wall forcing | Paolo Olivucci | MULTI-FIDELITY SURROGATE MODELLING OF THE NET POWER SAVINGS OF AN ACTUATED TURBULENT BOUNDARY-LAYER | 27 |
| Wall forcing | Mohammad Umair | REYNOLDS STRESSES TRANSPORT IN A TURBULENT CHANNEL FLOW CONTROLLED USING STREAMWISE TRAVELLING WAVES | 28 |

**Lunch** **12:30-14:00**

**Session 2.3** **14:00-16:00**

| | | | |
|---|---|---|---|
| Plasma control | Nicholas Benard | RING-TYPE DBD PLASMA ACTUATOR AT MILLIMETRIC SCALE | 29 |
| Plasma control | Kaisheng Peng | EXPERIMENTAL BASE FLOW MODIFICATION THROUGH PLASMA ACTUATION ON A SWEPT WING | 30 |
| Plasma control | Patricia Sujar-Garrido | PLASMA VORTEX GENERATORS USED FOR SEPARATION CONTROL AND DRAG REDUCTION ON A BLUFF BODY | 31 |
| Plasma control | Sergei Leonov | SHOCK WAVE REFLECTION CONTROL IN M=4 FLOW BY FILAMENTARY ELECTRICAL DISCHARGE | 32 |
| Plasma control | Giulia Zoppini | CONTROL OF STATIONARY CROSSFLOW INSTABILITIES THROUGH DESTRUCTIVE INTERFERENCE | 33 |
| Plasma control | Jacopo Serpieri | WALL-TURBULENCE CONDITIONING WITH STEADY CROSSFLOW-DIRECTED PLASMA JETS | 34 |

**Tea break** **16:00-16:30**

**Session 2.4** **16:30-18:30**

| | | | |
|---|---|---|---|
| Flow instabilities | Dongdong Xu | WALL COOLING AND HEATING EFFECTS ON THE EXCITATION OF GÅNORTLER VORTICES IN COMPRESSIBLE BOUNDARY LAYERS | 35 |
| Flow instabilities | Jordi Casacuberta | THE REVERSE LIFT-UP EFFECT IN CROSSFLOW INSTABILITIES OVER SURFACE IRREGULARITIES | 36 |
| Flow instabilities | Andras Szabo | STABILITY ANALYSIS OF MINIATURE VORTEX GENERATORS | 37 |
| Flow instabilities | Anna Spasova | DEVELOPMENT OF AN ALGORITHM FOR CREATING A DEVICE THAT FORMS THE SUBMERGED JET WITH REQUIRED INSTABILITY CHARACTERISTICS | 38 |
| Flow instabilities | Peter Nagy | THE DELAY OF NATURAL LAMINAR-TURBULENT TRANSITION USING ELASTIC COATING AND MINIATURE VORTEX GENERATORS | 39 |
| Flow instabilities | Gareev Linar | EXPERIMENTAL DETECTION OF NON-MODAL PERTURBATION GROWTH MECHANISM IN A LAMINAR JET | 40 |

# Thursday 8th September

**Session 3.1** **8:40-10:20**

| | | | |
|---|---|---|---|
| Blowing & suction | Iraj Mortazavi | MODAL ANALYSIS AND FLOW CONTROL ON A REDUCED SCALE SUV | 41 |
| Blowing & suction | Jonathan Morrison | SUPPRESSING THE PRESSURE DRAG OF A TURBULENT BLUFF BODY WAKE WITH PULSED JET FORCING | 42 |
| Blowing & suction | Hung Truong | AERODYNAMIC DRAG REDUCTION OF A TILT ROTOR AIRCRAFT USING ZERO-NET-MASS-FLUX DEVICES | 43 |
| Blowing & suction | Xiaodong Chen | DRAG REDUCTION PERFORMANCE OF SWEEPING JETS ON A SLANTED-BASED CYLINDER | 44 |
| Blowing & suction | Giulio Rota | ON-OFF PUMPING FOR DRAG REDUCTION IN A TURBULENT CHANNEL FLOW | 45 |

**Coffee break** **10:20-10:50**

**Session 3.2** **10:50-12:30**

| | | | |
|---|---|---|---|
| Blowing & suction | Davide Gatti | GLOBAL MOMENTUM BUDGET FOR TURBULENT FLOW CONTROL VIA MICROBLOWING | 46 |
| Blowing & suction | Babak Mohammadikalakoo | EFFECT OF THE REAR LINKING TUNNELS AND BLOWING ACTIVE FLOW CONTROL ON AERODYNAMIC PERFORMANCE OF BLUFF BODY | 47 |
| Blowing & suction | Mike Diessner | ON THE DEVELOPMENT OF A BAYESIAN OPTIMISATION FRAMEWORK FOR TURBULENT DRAG REDUCTION | 48 |
| Blowing & suction | Joseph O'Connor | FLOW PHYSICS OF A TURBULENT BOUNDARY LAYER ACTUATED VIA WALL-NORMAL BLOWING IN DIFFERENT CONFIGURATIONS | 49 |
| Blowing & suction | Annika Frede | NUMERICAL INVESTIGATION OF HOMOGENEOUS BLOWING AND SUCTION ON AN AIRFOIL IN COMPRESSIBLE FLOW | 50 |

**Lunch** **12:30-14:00**

**Session 3.3** **14:00-16:00**

| | | | |
|---|---|---|---|
| Liquid drag reduction | Keizo Watanabe | DRAG REDUCTION OF AQUEOUS SUSPENSIONS OF FINE SOLID MATTER IN PIPE FLOWS | 51 |
| Liquid drag reduction | Keizo Watanabe | HEAT TRANSFER IMPROVEMENT AND DRAG REDUCTION OF GRAPHENE OXIDE SUSPENSIONS | 52 |
| Liquid drag reduction | Ricardo Garcia-Mayoral | CAPTURING THE EFFECT OF SLIP/NO-SLIP SUPERHYDROPHOBIC TEXTURES IN TEXTURE-LESS SIMULATIONS | 53 |
| Liquid drag reduction | Michiel van Nesselrooij | DEVELOPMENT OF AN APPARATUS FOR FLAT PLATE DRAG MEASUREMENTS AND ITS APPLICATION FOR COMPLIANT COATINGS IN TURBULENT BOUNDARY LAYERS | 54 |
| Liquid drag reduction | Tao Liu | ON THE DETECTION AND CHARACTERISATION OF HIBERNATING TURBULENCE IN BOUNDARY-LAYER FLOWS | 55 |
| Liquid drag reduction | Dries vann Nimwegen | THE CHARACTERIZATION OF DRAG REDUCING AGENTS FOR APPLICATION IN LOW-ENTHALPY GEOTHERMAL WELLS AND DISTRICT HEATING SYSTEMS | 56 |

**Museum** **16:00-18:00**

**Banquet** **19:45**

# Friday 9th September

| | | | | |
|---|---|---|---|---|
| | **Session 4.1** | **9:00-10:20** | | |
| Machine learning | Laurent Cordier | | CONTROL OF UNSTEADY WAKE FLOWS BY MACHINE LEARNING | 57 |
| Machine learning | Fermin Mallor | | BAYESIAN OPTIMIZATION OF ACTIVE FLOW CONTROL IN THE TURBULENT BOUNDARY LAYER ON A NACA4412 PROFILE | 58 |
| Machine learning | Shaun Davey | | MEASURING THE UNSTEADY DRAG OF SUPERHYDROPHOBIC SURFACE TREATMENT USING NEURAL NETWORKS AND EXPERIMENTAL DISPLACEMENT TIME SERIES | 59 |
| Machine learning | Remy Hosseinkhan | | EXPLORATION STRATEGIES FOR CONTROL OF CHAOTIC DYNAMICAL SYSTEMS USING REINFORCEMENT LEARNING | 60 |
| | **Coffee break** | **10:20-10:50** | | |
| | **Session 4.2** | **10:50-12:30** | | |
| Machine learning | Chenwei Xia | | FLOW CONTROL FOR BLUFF BODY DRAG REDUCTION USING REINFORCEMENT LEARNING WITH PARTIAL MEASUREMENTS | 61 |
| Machine learning | Anna Guseva | | LARGE-SCALE OPPOSITION FLOW CONTROL OF THE LOGARITHMIC LAYER | 62 |
| Machine learning | Enrico Amico | | DEEP REINFORCEMENT LEARNING FOR BLUFF BODY WAKE CONTROL | 63 |
| Machine learning | Fabio Pino | | MACHINE LEARNING CONTROL OF 2D FALLING LIQUID FILM | 64 |
| Machine learning | Anand Sudhi | | DESIGN EXPLORATION OF LOW DRAG NLF AND HLFC WINGS | 65 |
| | **Session 4.3** | **14:00-15:40** | | |
| Porous surface | Alfredo Pinelli | | ON THE EFFECTS OF FILAMENTS INCLINATION ON CANOPY FLOWS | 66 |
| Porous surface | Essameldin Abdo | | TURBULENCE OVER ANISOTROPIC POROUS SUBSTRATES: A HOMOGENIZATION-BASED STUDY | 67 |
| Porous surface | F.H. Hartog | | TURBULENT BOUNDARY LAYERS OVER SURFACES WITH STREAMWISE-PREFERENTIAL PERMEABILITY | 68 |
| Porous surface | Mahiro Morimoto | | DISCUSSION ON THE POSSIBILITY OF TURBULENT DRAG REDUCTION BY A STREAMWISE PREFERENTIAL POROUS MEDIUM | 69 |
| Porous surface | Ludovico Fossa | | SUPERSONIC PRE-TRANSITIONAL STREAKS OVER POROUS SURFACES | 70 |
| | **Farewell** | **15:40-16:00** | | |
| | **Tea break** | **16:00-16:30** | | |

EDRFCM 2022 meeting room: Amphi Gaston-Planté (entrance 35, 1st floor), CNAM, 2 Rue Conté, 75018 Paris.

**Amphithéâtre**

| | | |
|---|---|---|
| Gaston Planté | (1) | GP |
| George Friedmann | (2) | GF |
| Aimé Laussedat | (3) | AL |
| Jean Fourastié | (T) | JF |
| Jean Prouvé | (V) | JP |
| Robert Faure | (Z) | RF |
| Jean Baptiste Say | (Y) | JBS |
| Paul Painlevé | (PP) | PP |
| Fabry Perot | (A) | FP |
| Abbé Grégoire | (C) | AG |

**Joint ERCOFTAC/EU-CTFF**
**European Drag Reduction and Flow Control Meeting – EDRFCM 2022**
**September $6^{\mathrm{th}}$–$9^{\mathrm{th}}$, 2022, Paris, France**

# NOTES ON THE SKIN-FRICTION COEFFICIENT OF BOUNDARY LAYERS AND CONFINED FLOWS

**Pierre Ricco**
Department of Mechanical Engineering, University of Sheffield, S1 3JD, United Kingdom
**Martin Skote**
School of Aerospace, Transport and Manufacturing, Cranfield University, MK43 0AL, United Kingdom

## INTRODUCTION

Turbulent wall-bounded flows are central in an immense range of technological and industrial fluid systems, e.g. over vehicles moving in air and water, through pipes and ducts used for oil and gas transport. In particular, free-stream turbulent boundary layers are important in aerodynamics applications. They present an additional difficulty with respect to confined flows because the streamwise direction is statistically inhomogeneous as the boundary-layer thickness grows downstream. A major objective is the accurate computation or measurement of their wall-shear stress.

A breakthrough in this area has been the discovery of the Fukagata-Iwamoto-Kasagi's identity (FIK) [2], which relates the wall-shear stress to an integral involving the Reynolds stresses in channel and pipe flows, with the addition of other integral terms in the case of free-stream boundary layers because of their streamwise inhomogeneity. Another important result has been the identity discovered by [5] (RD decomposition), for which the skin-friction coefficient is expressed as the sum of integral terms belonging to the mechanical energy equation. Both relations have been used widely to understand the impact of shear-layers dynamics on the wall-shear stress, in canonical and flow-control cases. The recent study by [1] is interesting because their identity expresses the skin-friction coefficient of free-stream boundary layers as the sum of the Blasius friction coefficient and an integrated contribution of the Reynolds stresses.

In this work, we present results on the FIK identity for free-stream boundary layers and channel flows and we interpret the skin-friction coefficient decomposition for boundary layers by [5] in terms of integral thicknesses. More results are presented in [6].

## FLOW SYSTEMS

We consider an incompressible free-stream boundary layer flowing past a flat plate in fully-developed conditions, scaled by using the free-stream velocity $U_\infty^*$ as the reference velocity and $\nu^*/U_\infty^*$ as the reference length scale, where $\nu^*$ is the kinematic viscosity of the fluid ($*$ indicates dimensional quantities). The Cartesian coordinates $x$, $y$, $z$ denote the streamwise, wall-normal, and spanwise directions, respectively. Averaging a quantity $q$ over $z$ along a distance $L_z$ and over $t$ for a time interval $T$ is defined as $\overline{q}(x,y) = L_z^{-1}T^{-1}\int_0^T\int_0^{L_z} q(x,y,z,t)\mathrm{d}z\mathrm{d}t$. Quantities are decomposed as $q(x,y,z,t) = \overline{q}(x,y) + q'(x,y,z,t)$ and $\{\overline{u},\overline{v},0\}$ is the mean flow. The data obtained by [7] via direct numerical simulations are used. We also study integral relations for channel flows by using the data computed by [3] via direct numerical simulations.

## RESULTS

We start by recalling the von Kármán momentum integral equation [4],

$$C_f = \frac{2\nu^*}{U_\infty^{*2}}\frac{\partial\overline{u}^*}{\partial y^*}\bigg|_{y^*=0} = 2\frac{\mathrm{d}\theta^*}{\mathrm{d}x^*}, \tag{1}$$

where

$$\theta = \int_0^\infty \overline{u}(1-\overline{u})\mathrm{d}y \tag{2}$$

is the momentum thickness.

We first prove that the identity discovered by [2], expressing the skin-friction coefficient of free-stream boundary layers as a function of integrated terms of the Reynolds-averaged streamwise momentum equation, simplifies to the von Kármán momentum integral equation relating the skin-friction coefficient and the momentum thickness. Analogously to [2], we integrate the Reynolds-averaged $x$-momentum equation to find

$$C_f = \underbrace{\frac{4}{h^2}\int_0^h (y-h)\overline{u'v'}\mathrm{d}y}_{\text{term 1}} + \underbrace{\frac{4}{h^2}\int_0^h \overline{u}\mathrm{d}y}_{\text{term 2}} - \frac{2}{h^2}\int_0^h (y-h)^2 I_x\mathrm{d}y, \tag{3}$$

where $h$ is located in the free stream and

$$I_x(x,y) = \frac{\partial\overline{u}\overline{u}}{\partial x} + \frac{\partial\overline{u}\,\overline{v}}{\partial y} - \frac{\partial^2\overline{u}}{\partial x^2}. \tag{4}$$

The terms on the right-hand side of (3) must not depend on $h$ because the skin-friction coefficient does not. The bound $h$ can therefore be taken asymptotically large. If the upper bound is finite, the weighted contributions of the terms of the streamwise momentum equation depend spuriously on the bound itself. In the limit $h \to \infty$, $C_f \to -2\int_0^\infty I_x\mathrm{d}y$, which then reduces to (1). The FIK identity therefore loses its power of revealing the contribution of the different terms of the $x$-momentum equation to the wall friction. The Reynolds stresses disappear from the identity. In the derivation of the FIK identity in channel or pipe flows, no ambiguity exists about the integration bounds, which are fixed by the walls and the centreline in the channel-flow case or the pipe axis in the pipe-flow case.

We show that the infinite number of identities obtained by successive integration all reduce to the von Kármán momentum equation for boundary layers. As shown by [8], an infinite number $n$ of successive integrations between 0 and $y$ can be performed before the final integration between 0 and $h$, i.e.

$$C_f = -\frac{2n}{h^n}\int_0^h (h-y)^{n-1}\overline{u'v'}\mathrm{d}y + \frac{2n(n-1)}{h^n}\int_0^h (h-y)^{n-2}\overline{u}\mathrm{d}y - \frac{2}{h^n}\int_0^h (h-y)^n I_x \mathrm{d}y. \tag{5}$$

The identities (5) are valid for $n \geq 2$. For $n = 2$, (5) is (3). For every $n$, the identities (5) simplify to (1) as $h \to \infty$. As the weighed influence of the terms in (5) depends on $n$, this dependence on $n$ is spurious because $n$ is not a physical parameter.

For channel flows,

$$\frac{C_{f,c}}{8(n+1)} = -\int_0^1 (1-y_c)^{n-1}\overline{u_c'v_c'}\mathrm{d}y_c + \frac{n-1}{R_b}\int_0^1 (1-y_c)^{n-2}\overline{u}_c\mathrm{d}y_c, \tag{6}$$

where $y_c = y^*/h_c^*$, $h_c^*$ is the half channel height, the velocity components are scaled by $2U_b^*$, where $U_b^*$ is the bulk velocity, $R_b = 2U_b^* h_c^*/\nu^*$ and $C_{f,c} = (8/R_b)\mathrm{d}\overline{u}_c/\mathrm{d}y_c|_{y_c=0}$. Only the original FIK identity ($n$=2) possesses a clear physical meaning because the term involving $\overline{u}_c$ in (6) reduces to the part of the skin-friction coefficient that pertains to a laminar channel flow by using the definition of bulk velocity, while, for $n$>2, the term containing $\overline{u}_c$ cannot be simplified and the laminar and turbulent contributions to the skin-friction coefficient cannot be distinguished. We write (6) as

$$C_{f,c} = -8(n+1)\int_0^\infty \overline{u_c'v_c'}e^{-ns}\mathrm{d}s + \frac{8(n^2-1)}{R_b}\int_0^\infty \overline{u}_c e^s e^{-ns}\mathrm{d}s, \tag{7}$$

where $s$=$-\ln(1-y_c)$. By using Watson's lemma, it is revealed that (7) collapses to the definition of skin-friction coefficient when $n \to \infty$, i.e. $C_{f,c} \to (8/R_b)\mathrm{d}\overline{u}_c/\mathrm{d}y_c|_{y_c=0}$ (refer to [6] for proof), further demonstrating that the dependence on $n$ is non-physical.

By a two-fold integration, we have found an identity, valid for channel and pipe flows, that links the skin-friction coefficient with the integrated Reynolds stresses and the centerline mean velocity. The identity is

$$C_{f,c} = \frac{16}{R_b}\overline{u}_c(y_c = 1) - 16\int_0^1 \overline{u_c'v_c'}\mathrm{d}y_c, \tag{8}$$

which is also valid for pipe flows, in which case $y_c = r^*/R^*$, $r^*$ is the radial coordinate, $R^*$ is the pipe radius, and $R_b = 2U_b^* R^*/\nu^*$ ($C_{f,c} = 16/R_b$ is found in the laminar case as $\overline{u_c'v_c'} = 0$ and $\overline{u}_c$=1 at the pipe axis). The identity for channel flows was also discovered independently by [1]. As the Reynolds number increases, it is progressively more difficult to measure the wall-shear stress via direct measurement of the wall-normal velocity gradient at the wall because the near-wall turbulent length scales become smaller and the viscous sublayer thinner. In the limit of large Reynolds number, it is instead easier to compute the skin-friction coefficient via (8) because the measurements of the bulk velocity and the integrated Reynolds stresses suffer progressively less from the large near-wall velocity gradients. These comments are also valid for the original identities by [2].

We also interpret the skin-friction coefficient decomposition for boundary layers by [5] in terms of integral thicknesses, by utilizing an energy thickness and an inertia thickness, the latter composed of two thicknesses related to the mean-flow wall-normal convection and the streamwise inhomogeneity. This decomposition has been useful to further interpret the skin-friction decomposition of [5] physically and for quantifying the role of the different momentum-equation terms on the friction drag. The result is

$$C_f = 2\frac{\mathrm{d}\theta}{\mathrm{d}x} = \frac{\mathrm{d}E}{\mathrm{d}x} + \frac{\mathrm{d}C}{\mathrm{d}x} + \frac{\mathrm{d}S}{\mathrm{d}x}, \tag{9}$$

where

$$E = \int_0^\infty \overline{u}\left(1-\overline{u}^2\right)\mathrm{d}y, \quad C = \int_0^\infty \overline{u}\left(1-\frac{1}{3}\overline{u}^2\right)\mathrm{d}y, \quad S = 2\int_0^\infty \overline{u}^2\left(\frac{2}{3}\overline{u}-1\right)\mathrm{d}y. \tag{10}$$

Similarly to [5], equation (9) is interpreted in the absolute frame of reference, i.e. where the wall is in motion. Equation (9) describes how the energy given by the wall motion to the fluid, measured by twice the change of $\theta$ with the streamwise direction, is divided into the change of $E$, representing the losses of mean kinetic energy due to the mean-flow viscous dissipation into heat and to the production of turbulence, and the change of $I$, representing the change in convective transport of the mean kinetic energy due to the mean velocity. The change of $I$ is expressed as the sum of the changes of the thicknesses $C$ and $S$, which represent the change in transport due to the wall-normal mean velocity and the streamwise mean velocity, respectively. The streamwise integral of (9) is useful to investigate what percentage of the different terms in the RD decomposition contribute to the total drag by calculating the difference in the corresponding integral thicknesses over the streamwise extent of interest.

## ACKNOWLEDGMENTS

PR has been partially supported by EPSRC (Grant No. EP/T01167X/1).

## REFERENCES

[1] A. Elnahhas and P.L. Johnson. On the enhancement of boundary layer skin friction by turbulence: an angular momentum approach. *J. Fluid Mech.*, 940, 2022.

[2] K. Fukagata, K. Iwamoto, and N. Kasagi. Contribution of Reynolds stress distribution to the skin friction in wall-bounded flows. *Phys. Fluids*, 14(11):73–76, 2002.

[3] S. Hoyas and J. Jiménez. Scaling of the velocity fluctuations in turbulent channels up to $\mathrm{Re}_\tau$=2003. *Phys. Fluids*, 18:011702, 2006.

[4] S.B. Pope. *Turbulent Flows.* Cambridge University Press, 2000.

[5] N. Renard and S. Deck. A theoretical decomposition of mean skin friction generation into physical phenomena across the boundary layer. *J. Fluid Mech.*, 790:339–367, 2016.

[6] P. Ricco and M. Skote. Integral relations for the skin-friction coefficient of canonical flows. *To appear in J. Fluid Mech.*, 2022.

[7] J.A. Sillero, J. Jiménez, and R.D. Moser. One-point statistics for turbulent wall-bounded flows at Reynolds numbers up to $\delta^+$=2000. *Phys. Fluids*, 25(10):105102, 2013.

[8] C. Wenzel, T. Gibis, and M. Kloker. About the influences of compressibility, heat transfer and pressure gradients in compressible turbulent boundary layers. *J. Fluid Mech.*, 930, 2022.

**Joint ERCOFTAC/EU-CTFF**
**European Drag Reduction and Flow Control Meeting – EDRFCM 2022**
**September 6th–9th, 2022, Paris, France**

# EXPERIMENTAL AND NUMERICAL INVESTIGATION INTO THE DRAG PERFORMANCE OF DIMPLED SURFACES IN A TURBULENT BOUNDARY LAYER

**O.W.G. van Campenhout**
Aerodynamics, Wind Energy, Flight Performance and Propulsion Department, Delft University of Technology,
2629 HS Delft, The Netherlands

## ABSTRACT

Although previous studies have reported a potential drag-reducing effect of dimpled surfaces in turbulent boundary layers, there is a lack of repeatability when experiments are replicated by other research groups. To contribute to the discussion, one of the most studied dimple geometries reported in the literature has been investigated. This dimple geometry, which is denoted model A, has a diameter of 20 mm and a depth of 500 µm. There is no general consensus in the literature on the drag-reduction performance of this particular dimple geometry. The present experimental and numerical study consists of two sets of wind tunnel experiments and implicit large-eddy simulations. The wind tunnel experiments and the implicit large-eddy simulations both depict a total drag increase of around 1-2% compared to the flat reference case. This finding agrees with a recent study by Spalart et al. [2019]. Furthermore, the present wind tunnel experiments have shed light on a plausible reason behind the discrepancy between the study by Spalart et al. [2019] and earlier results reported by van Nesselrooij et al. [2016]. An excerpt of the wind tunnel results from this study is depicted in Figure 1. Lastly, the results from the implicit large-eddy simulations depict a skin friction reduction over the dimpled surface. However, the detrimental impact of the pressure drag leads to an increase in the total drag. These novel results can possibly form the basis for a new consensus on the drag performance of this particular dimple geometry.

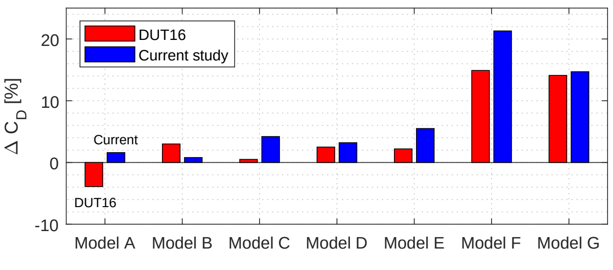

Figure 1: Drag relative to the flat reference case for seven different dimple geometries (denoted as models A to G). Comparison between the experiments from van Nesselrooij et al. [2016] (denoted as DUT16) and the current study at $Re_\tau \approx 1200$

## CORRESPONDING PAPER

O. W. G van Campenhout, M. van Nesselrooij, Y. Y. Lin, J. Casacuberta, B. W. van Oudheusden, and S. Hickel. Experimental and numerical investigation into the drag performance of dimpled surfaces in a turbulent boundary layer. *International Journal of Heat and Fluid Flow*, 2022. Manuscript in preparation.

## REFERENCES

P. R. Spalart, M. Shur, M. Strelets, A. Travin, K. B. Paschal, and S. P. Wilkinson. Experimental and numerical study of the turbulent boundary layer over shallow dimples. *International Journal of Heat and Fluid Flow*, 78:108438, 2019.

M. van Nesselrooij, L. L. M. Veldhuis, B. W. van Oudheusden, and F. F. J. Schrijer. Drag reduction by means of dimpled surfaces in turbulent boundary layers. *Experiments in Fluids*, 57(9):1–14, 2016.

**Joint ERCOFTAC/EU-CTFF**
**European Drag Reduction and Flow Control Meeting – EDRFCM 2022**
**September $6^{\text{th}}$–$9^{\text{th}}$, 2022, Paris, France**

# DRAG REDUCTION MODELING FOR ENGINEERING APPLICATIONS

**B. Mele & R. Tognaccini**
Industrial Engineering Department, University of Naples Fedrico II, P.zzle Tecchio 80, Italy

## INTRODUCTION

In the aviation sector, the reduction of pollutant emissions is clearly linked to the aerodynamic efficiency of aircraft, this led to an increasing interest in drag reduction that has become a keyword for the next generation aircraft and in general for lifting bodies. Riblets is one of the most interesting passive drag reduction technique that has a chance of application in the next generation aircraft. The drag reduction mechanism can be numerically detected only by Direct Numerical Simulations (DNS), still unfeasible for high Reynolds numbers and complex flows. There are different papers reporting DNS of flows on micro-grooved surfaces providing fundamental details on the drag reduction devices, but all limited to plate or channel flows far from engineering Reynolds numbers. The numerical simulation of riblets and other drag reduction devices at very high Reynolds numbers is difficult to perform due to riblet dimensions (micron in aeronautical applications). To overcome these difficulties, some models for riblets simulation have been developed in the last years, thanks to the data provided by DNS, experiments [1, 2] and theoretical analyses [4]. In all these models the drag reduction is modeled rather than effectively captured, however the analysis of some non-local effect of riblets on complex body shapes requires the adoption of these engineering models.

## ENGINEERING MODELS FOR RIBLETS SIMULATIONS

Both experiments and theory highlighted that the physical mechanism responsible of the drag reduction by riblets is local [1, 4], i.e. only depends on the local Reynolds number and it can be summarized in a modification of the constant $\Delta U^+$ in the log-law of the turbulent velocity profile. However some experiments investigating flow over flat plate under an adverse pressure gradient showed increased effectiveness of riblets[3]. Other experiments in airfoil flows reported an increasing efficiency of riblets while increasing the angle of attack implying an effect of pressure distribution on riblets performance. Log-law is not influenced by the pressure gradient, however, the boundary layer developing with the modified $\Delta U^+$ has a secondary influence on the outer inviscid flow and on the pressure distribution in particular, such as well known by Prandtl's boundary layer theory. $\Delta U^+$ can be introduced in different ways. Some models propose modifications to turbulence models, Mele and Tognaccini [7, 9] introduced the idea to model riblets as an ordered roughness in the transitional regime. They proposed a boundary condition for $\omega$ in the $k-\omega$ turbulence models written as a function of $l_g^+ = \sqrt{A_g^+}$, where $A_g^+$ is the riblet non dimensional cross section area. The boundary condition has been widely validated in flat plate and airfoil flows comparing numerical computation with available experiments [7, 9]. All these models are linked to turbulence modeling with all related limitations. More recently Mele and Tognaccini [6] proposed a slip boundary condition based on the physical mechanism described in [1, 4] where the drag reduction can be characterized in terms of the difference between the two so-called protrusion heights in the longitudinal and cross-flow directions. The two protrusion heights are defined as the distance between the tips of riblets and the average of the velocity profiles and are equivalent to the slip lengths.

Mele & Tognaccini derived a new law for protrusion height difference (i.e. slip length) as a function of riblet shapes valid also in the non linear region of drag reduction curve. This boundary condition based on the slip length can be applied to all drag reduction devices whose mechanism is related to a shift of the velocity profile. The slip boundary condition relates the components of the velocity tangent to the surface to the shear rate at the surface through the so called slip length $\lambda$: $u_w = \lambda \left(\frac{\partial u}{\partial y}\right)_w$. Increasing $\lambda$ the shift in the log-law $\Delta U^+$ increases. The relation for $Re_\lambda(l_g^+)$ proposed in [6] is here slightly modified with different coefficients and the introduction of a new term for a better characterization of riblet performance in the drag increase regime:

$$\begin{aligned} Re_\lambda = \frac{C_1}{\left[\left(l_g^+ - 10.5\right)^2 + C_2\right]} - \lambda_0 + \\ -C_3(l_g^+ - C_4)\frac{1}{2}\left[1 + sgn(l_g^+ - C_4)\right] \end{aligned} \tag{1}$$

where $C_1 = 1700$, $C_2 = 67.5$, $C_3 = 0.75$, $C_4 = 15$, $\lambda_0 = C_1/(10.5^2 + C_2)$, and $Re_\lambda$ the Reynolds number based on $\lambda$. The model has been widely validated in flat plate and airfoil flows adopting a RANS solver in [6] and a resolved LES solver in [10]. A similar equation linking $\lambda/s$ to $l_g^+$, where $s$ is the riblet spacing, is also proposed:

$$\begin{aligned} \frac{\lambda}{s} = \frac{C_1}{\left[\left(l_g^+ - 10.5\right)^2 + C_2\right]} - \lambda_0 + \\ -C_3(l_g^+ - C_4)\frac{1}{2}\left[1 + sgn(l_g^+ - C_4)\right] \end{aligned} \tag{2}$$

where $C_1 = 8$, $C_2 = 90$, $C_3 = 0.0023$ while $C_4$ and $\lambda_0$ are the same as equation (1). In figure 1 the results obtained applying the modified equations show the improvement in the characterization of riblet performance.

## EFFECT OF RIBLETS ON COMPLEX BODY SHAPES

The application of these models on complex configuration allows the analysis of interesting details on the effect of riblets. The boundary condition for $\omega$ has been applied in [8, 9] to a complete aircraft configuration in transonic condition, adopting two different flow solvers, showing the capability of the model to calculate the effectiveness of riblets and the aircraft zones where the riblets installation are more effective. Furthermore, a significant influence of the riblets on the location and strength of the shocks was noted for the first time. The ef-

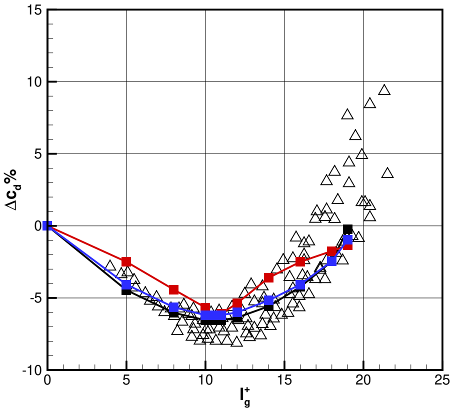

Figure 1: Computed drag reduction vs $l_g^+$. red: equation from [6], blue: equation (1), black: equation (2) △: experiment [1].

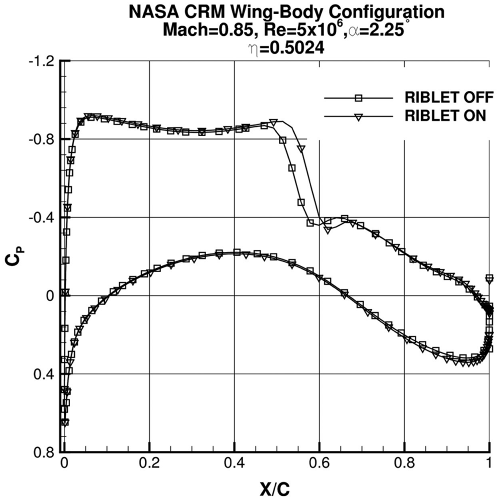

Figure 2: Effect of riblets on shock wave [9]

.

fect on the shock wave has been confirmed in [5] where a drag breakdown on a wing body configuration with and without riblets has been performed and by a recent DNS computation [11]. In [5] a significant effect of riblets on form drag has been also computed. In [6, 10] this effect has been analyzed in details adopting the slip length model previously described. The analyses provided a possible explanation to the increasing performance of riblets in pressure gradient flows. It has been shown that riblets reduce not only friction but also the form drag because they induce small but significant modifications of the pressure distribution which tends towards the inviscid one with an improved pressure recovery in the aft part of the airfoil. A quantitative analysis with the help of the classical matched asymptotic expansion technique reveals that riblets reduce the displacement thickness of the boundary layer, the reduced *thickening* of the equivalent body introduced by the boundary layer leads to form drag reduction (see fig. 3).

These results show that, even if these models cannot reproduce the flow field inside the grooves that presently can be captured only by DNS at low Reynolds numbers, they are able to compute the global performance and boundary layer quantities on complex shapes at high Reynolds numbers, providing also fine details on riblets effects.

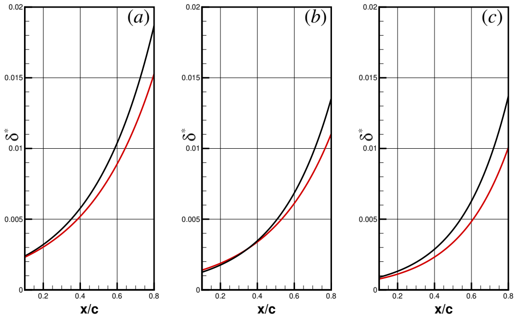

Figure 3: Effect of riblets on displacement thickness on airfoil suction side [10]. (*a*): NACA 0015, $Re_L = 180000$, $\alpha = 10°$; (*b*): NACA 0012, $Re_L = 300000$, $\alpha = 8°$; (c): EPPLER 387, $Re_L = 300000$, $\alpha = 7°$. —: riblets off, —: riblets on.

.

## REFERENCES

[1] D.W. Bechert, M. Bruse, W. Hage, J.G.T. van der Hoeven, and G. Hoppe. Experiments on drag-reducing surfaces and their optimization with an adjustable geometry. *J. FLuid Mech.*, 338:59–87, 1997.

[2] K. Choi. Near-wall structure of a turbulent boundary layer with riblets. *J. Fluid Mech.*, 208:417–458, 1989.

[3] J.R. Debisschop and F.T.M. Nieuwstadt. Turbulent boundary layer in an adverse pressure gradient: Effectiveness of riblets. *AIAA J.*, 34(5):932–937, 1996.

[4] P. Luchini, F. Manzo, and A. Pozzi. Resistance of grooved surface to parallel flow and cross-flow. *J. Fluid Mech.*, 228:87–109, 1991.

[5] B. Mele, L. Russo, and R. Tognaccini. Drag bookkeeping on an aircraft with riblets and NLF control. *Aerospace Science and Technology*, 98:105714, 2020.

[6] B. Mele and R. Tognaccini. Slip length based boundary condition for modeling drag reduction devices. *AIAA J.*, 56(9):3478–3490, 2018.

[7] B. Mele and R. Tognaccini. Numerical simulation of riblets on airfoils and wings. In *50th AIAA Aerospace Sciences Meeting*, AIAA 2012-0861, 2012.

[8] B. Mele, R. Tognaccini, and P. Catalano. Effect of riblets on a complex configuration in transonic conditions. In *EDRFCM 2015*, Cambridge (UK), 2015.

[9] B. Mele, R. Tognaccini, and P. Catalano. Performance assessment of a transonic wing-body configuration with riblets installed. *Journal of Aircraft*, 53(1):129–140, 2016.

[10] B. Mele, R. Tognaccini, P. Catalano, and D. de Rosa. Effect of body shape on riblets performance. *Phys. Rev. Fluids*, 5(12):124609, 2020.

[11] M. Quadrio, A. Chiarini, J. Banchetti, D. Gatti, A. Memmolo, and S. Pirozzoli. Drag reduction on a transonic airfoil. *J. Fluid Mech.*, 942, R2:68–104, 2022.

**Joint ERCOFTAC/EU-CTFF**
**European Drag Reduction and Flow Control Meeting – EDRFCM 2022**
**September $6^{\text{th}}$–$9^{\text{th}}$, 2022, Paris, France**

# MEASUREMENTS IN A TURBULENT CHANNEL FLOW BY MEANS OF AN LDV PROFILE SENSOR

**S. Pasch, D. Gatti, R. Leister, B. Frohnapfel, J. Kriegseis**
Institute of Fluids Mechanics (ISTM), Karlsruhe Institute of Technology (KIT), Germany

**R. Örlü**
Linné FLOW Centre, Dept. Engineering Mechanics, KTH Royal Institute of Technology, Stockholm, Sweden

## INTRODUCTION

Measurements of mean velocity profiles and fluctuations in turbulent flows are of great interest for the development and evaluation of flow control concepts. The mean flow velocity gradient in the wall-near region offers the possibility to directly estimate the wall shear stress and skin-friction coefficient, but its experimental determination is still a challenging task.

For particle image velocimetry (PIV), for instance, high velocity gradients require a large dynamic range and a trade-off has to be made between the spatial resolution and the size of the field of view [3]. While, for general laser Doppler velocimetry (LDV) measurements, the spatial resolution is limited to the size of the measurement volume in the order of magnitude of several hundred $\mu$m [10], a laser Doppler velocity profile sensor (LDV-PS) can spatially resolve a velocity profile within the measurement volume (MV) [1]. The LDV-PS measurement technique has been shown to be capable of measuring turbulent channel flow mean velocity profiles as well as fluctuations in the main flow direction [9]. In the present work, a newly developed commercial LDV-PS system is employed for flow measurements in a turbulent channel and the experimental procedure and measurement results will be discussed from an application perspective. The experiments build upon the experience gathered in measurements of a laminar Couette-like flow [5] and an experimental characterization study [7], which examined the interplay of the Fast Fourier Transforn (FFT) signal processing parameters, the scattering object size and the measurement uncertainty.

## MEASUREMENT TECHNIQUE AND SETUP

The LDV-PS measurement technique is based on two overlapping convergently-divergently oriented interference fringe systems with different wavelengths in the same plane as illustrated in Figure 1. Consequently, the fringe distances $d_i, i = 1, 2$ are a function of the $y'$ position within the MV. The position $y'$ of a particle passing through the MV can be determined by means of a calibration function from the quotient $q$ of the detected scattered light frequencies $f_i, i = 1, 2$ of both fringe systems according to

$$q(y) = \frac{f_2(y', u)}{f_1(y', u)} = \frac{u/d_2(y')}{u/d_1(y')} = \frac{d_1(y')}{d_2(y')}. \tag{1}$$

The particle velocity is calculated as $u = f_i d_i$. The frequencies $f_i$ of the scattered light signals are determined using FFT.

In previous experiments with the LDV-PS measurement system [5, 7], it was observed that the velocity uncertainty was generally small, while the position uncertainty strongly depends on the applied boundary conditions. For increasing flow velocities, the position standard deviation decreased for constant FFT parameters, i.e. sample frequency and sample number. However, when the sampling frequency was adjusted to the flow velocity, these effects could be avoided. These findings imply that the data processing routines are to be chosen accordingly. It is suggested to calculate flow statistics by averaging position values in $u$-range bins when velocity profiles are evaluated at very small flow velocities.

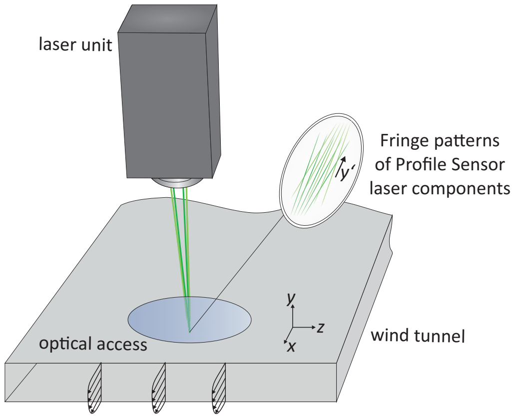

Figure 1: Experimental Setup; LDV-PS above wind tunnel.

A commercial *ILA R&D 1D2C* LDV-PS comprised of two Nd:YAG lasers ($\lambda = 532$ nm and $\lambda = 552$ nm) with a 5 MHz Bragg-shift was employed to measure the flow velocity $u$ in main flow direction and $y$ position above the lower channel wall by detecting Di-Ethyl-Hexyl-Sebacate tracer particles. The sensor was positioned above a glass window of 1 mm thickness in the channel and tilted by 20° around the $x$ axis as shown in Figure 1 to avoid reflection issues. The measured position values were accordingly corrected by means of trigonometric relations. The MV of 2000 $\mu$m length was traversed in 500 $\mu$m steps to acquire velocity profile data in the lower channel half. The FFT sample frequency was chosen to 100 MHz with a sample number of 2048. The channel length, width and height were 4000 mm, 300 mm and 25.2 mm and the measurements were conducted 100 mm upstream the outlet. The high aspect ratio enables comparison with skin friction coefficient data from pressure drop measurements in an identical tunnel.

## RESULTS AND DISCUSSION

In total, 624 000 burst events of particles passing through the MV were detected at 29 different traverse positions over the semi-channel height. The measured velocity and $y$-

position values are shown in Figure 2. Just above the wall at small flow velocities the $y$-position scattering of bursts is observed to increase, which has been found to be a characteristic phenomenon for measurements with constant FFT parameters [5, 7]. Correspondingly, the first data point of the mean velocity profile in Figure 3 is not determined correctly.

The wall position was determined by means of a linear extrapolation of the velocity profile near the wall based on averaged measured position values in 0.25 m/s-wide $u$ bins.

The centerline velocity $u_{cl}$ and corresponding channel half-hight position marked with the black asterisk in Figure 2 has been determined as the maximum of a quadratic fit function based on averaged measured velocity values in $y$-position bins in the central channel region.

The observed scattering of detected bursts is a superposition of turbulent fluctuations and measurement uncertainty. The latter has been found to decrease with increasing velocity and is therefore approximately constant at a certain velocity level [7]. Considering the burst distribution in the $y$ range between 2 000 $\mu$ and 12 000 $\mu$m, decreasing fluctuations are implied towards the middle of the channel. Consequently, the wider burst band closer to the wall implies the registration of the characteristic fluctuation profile which corresponds to the typical distribution in turbulent channel flows [8].

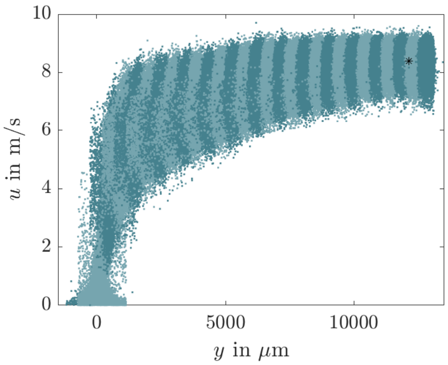

Figure 2: Velocity and position values of all detected bursts. Two different shades of blue indicate the individual measurements; the asterisk marks $u_{cl}$ and the channel semi-height.

To compare the measured velocity profile with direct numerical simulation (DNS) data allowing to evaluate the quality of the measurements, a transformation into viscous units is to be conducted. Figure 3 shows the mean velocity profile gained by statistical averaging of $y$ values in $u$ bins for smaller velocities and averaging of $u$ values in $y$ bins for larger velocities. The wall shear stress is estimated from the centerline velocity using the skin-friction correlation suggested by Dean [2], thus allowing a simple yet approximate transformation to viscous scales. Additionally, measurement data from stereo PIV measurements [3] and DNS data by Hoyas [4] is provided. In the wall-near region of the viscous sublayer, the LDV-PS measurements provide data points with a good spatial resolution. However, an advanced measurement processing routine needs to be developed for the velocity and position estimation in this region comprising high velocity gradients, as the deviation from the expected linear near-wall behaviour shows.

For further evaluation of the mean velocity profile, different approaches for the transformation to viscous scales will be evaluated and compared in the coming months. Firstly, as described by Hehner [3], fitting of the presented data with respect to a universal description of a turbulent velocity profile by Luchini [6] will be conducted. Alternatively, the wall shear stress can be determined directly from the wall-near velocity gradient. As shown before, the LDV-PS provides a good spatial resolution in the viscous sublayer so that this approach seems promising for more accurate further evaluations.

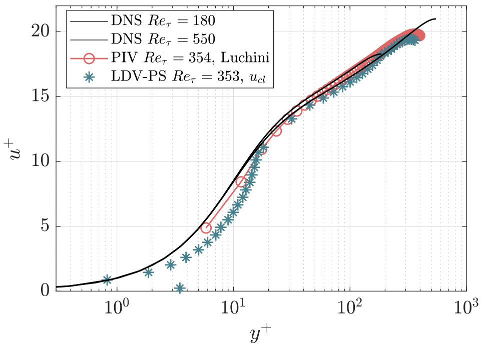

Figure 3: $u^+ - y^+$ profile of averaged LDV-PS data transformed to viscous scales using $u_{cl}$ and a correlation by Dean [2], PIV data [3] transformed to viscous scales with a fitting function by Luchini [6] and DNS data by Hoyas [4]

In continuation of the acquisition of measurement data presented here, advanced processing routines for the estimation of mean velocity profiles will be developed. Different methods for the conversion to viscous scales will be applied to enable an evaluation of the results. Finally, those evaluation approaches will be comparatively discussed.

## REFERENCES

[1] Jürgen Czarske, Lars Büttner, Thorsten Razik, and Harald Müller. *Measurement Science and Technology*, 13(12):1979, 2002.

[2] Roger Bruce Dean. *Journal of Fluids Engineering*, 100(2):215–223, 1978.

[3] Marc T Hehner, Lars H von Deyn, Jacopo Serpieri, Saskia Pasch, Timo Reinheimer, Davide Gatti, Bettina Frohnapfel, and Jochen Kriegseis. In *14th International Symposium on Particle Image Velocimetry*, 2021.

[4] Sergio Hoyas and Javier Jiménez. *Physics of Fluids*, 20(10):101511, 2008.

[5] Robin Leister, Saskia Pasch, and Jochen Kriegseis. *Experiments in Fluids*, page revised manuscript under review, 2022.

[6] Paolo Luchini. *European Journal of Mechanics-B/Fluids*, 71:15–34, 2018.

[7] Saskia Pasch, Robin Leister, Marius Egner, Lars Büttner, Jürgen Czarske, and Jochen Kriegseis. In *20th International Symposium on the Application of Laser and Imaging Techniques to Fluid Mechanics, Lisbon, Portugal*, 2022.

[8] Stephen B Pope. Cambridge university press, 2000.

[9] Katsuaki Shirai, T Pfister, L Büttner, J Czarske, H Müller, S Becker, H Lienhart, and F Durst. *Experiments in fluids*, 40(3):473–481, 2006.

[10] Cameron Tropea, Alexander L Yarin, and John F Foss. Springer, 2007.

**Joint ERCOFTAC/EU-CTFF**
**European Drag Reduction and Flow Control Meeting – EDRFCM 2022**
**September 6th–9th, 2022, Paris, France**

# EFFECT OF SLAT ATTACHMENT ON RUDDER LEADING EDGE OF A VERTICAL TAIL PLANE

**Mahmud Jamil Muhammad**
Department of Mechanical Engineering, University of Nottingham, NG7 2RD, United Kingdom

**Kwing-So Choi**
Department of Mechanical Engineering, University of Nottingham, NG7 2RD, United Kingdom

**Yaxing Wang**
Department of Mechanical Engineering, University of Nottingham, NG7 2RD, United Kingdom

## INTRODUCTION

The idea of flow stability and control started several decades ago. In1964, the challenges that arise in terms of interference, stability and control of a fighter jet aircraft were thoroughly investigated[1]. Several factors contributed to the instability and interference in both jet aircraft and commercial airplanes. For application in aerospace industry, it is necessary to employ a method that delay the separation and improve the turbulence transition. However, the study of flow control is regarded as a safety measure that saves life. The design identification of a control devices should as a rule of thumb be economical and less complex to handle. Several flow control methods were identified for application related to airplanes [2], [3], wind turbines [4], [5], and hydrokinetic turbines [6]. Usually, the control devices confirmed significant increase in both lift and drag for cruise and landing in the case of airplanes [7]. In the 21st century, the importance of flow separation and control has increased with numerical and experimental approaches as the suitable methods. It is difficult to predict and theoretically study this complex phenomenon as the flow tends to be more chaotic and fully developed. Optimization of the airfoil shape is also crucial in order to obtain the maximum value of the force coefficients[8].

As far we know, the study of vertical tail plane VTP with rudder leading edge slat has not been reported more commonly. The common reported studied is wing airfoil leading edge slat with extended flap. So far, there is no evidence of any study that extensively studied experimentally the vertical tail plane rudder-slat-attachment and compared it with numerical results.

The present study examined numerically the effect of slat on the performance of vertical tail plane using high-fidelity computational fluid dynamics CFD and wind tunnel experiment validation.

## GEOMETRY DESCRIPTION AND NUMERICAL SET-UP

The vertical tail plane is a tapered trapezoidal in shape with a span dimension of scale 0.4m, root chord 0.32m and tip chord of 0.1475m. The mean aerodynamic chord MAC was measured to be 0.2455m. The full 3D section of the VTP with the main airfoil, rudder and slat airfoil is shown in Figure 1. A structured mesh was adopted in this project with denser mesh located around the boundary layer region. A reasonable $Y+\approx1$ was ensured to satisfy the requirement of the viscous region of the boundary layer region. In this work, the $K$-$\omega$ SST and Large Eddy simulation LES models were chosen as they proved to be robust in external flow studies based on the condition that $Y+\approx1$. The slat was attached at one third of the spanwise from the tip side towards the root side and at 4mm gap from the rudder surface. The mesh volume is made up of 17.5 million hexahedral cells. The Reynolds number is based on the MAC of 0.2455m and freestream velocity of 10 m/s.

The primary goal of this study is to use Ansys Fluent as a numerical tool to analyze the air flow over the vertical tail plane and compare the result with wind tunnel result.

Figure 1: Geometrical Representation of Vertical stabilizer (main Airfoil), rudder and slat.

## FORCE COEFFICIENTS VALIDATION

The Reynolds Average Navier-Stokes RANS model $K\omega$-SST was employed to validate and compare the cases without slat (Baseline) and with slat attachment as shown in Figure 2. For the LES case, Figure 3 shows the side force coefficient for $\beta=20°$ with slat against dimensionless time $t^*=t(u/c)$ which is in good agreement with experimental data compared to the RANS result for $\beta=20°$.

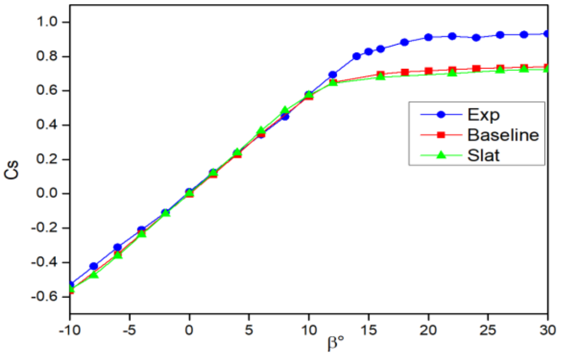

Figure 2: RANS K-w SST Validation and comparison of Baseline (without slat) and with slat case.

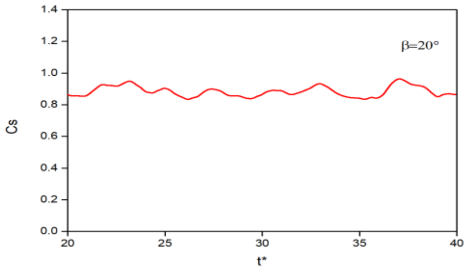

Figure 3: LES Side Force Coefficient against dimensionless time with slat for β=20°.

## EFFECT OF RUDDER LEADING EGDE SLAT

The findings of the numerical results highlight the significant effect of the rudder-slat attachment on the VTP structure. The present results investigate the effect of the rudder-slat attachment in terms of force coefficient performance and flow field parameters that confirm the development of the separation region and the effect of the slat control. Figure 4. Shows the LES result for rudder-slat TE vorticity at the wake region at side slip angle of 20° and deflection 0°. The 2D section shows a vorticity magnitude at 75% spanwise from the root side. The separation region without and with slat shows the effect of the slat. Figure 4(a) without slat indicated a large area of the separation region whereas the Figure 4 (b) with slat demonstrates a shift in the separation region due to the slat control.

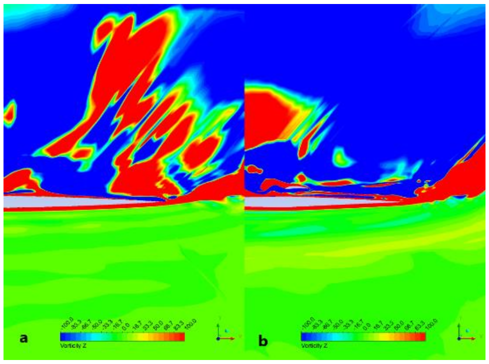

Figure 4: Instantaneous 2D vorticity for β=20° at η=0.75 spanwise (a) without slat (b) with slat.

Figure 5 and 6. Shows the λ-2 vortex structure without and with slat attachment for β=20° with iso-value of -5000. The 3D vortex structure is accompanied by a streamwise velocity. At higher angle of attack, the structures breakdowns into lesser structures at the rudder TE region. In addition, for both cases there exist a flow structure near the TE like the Kelvin-Helmholtz behavior. The flow phenomenon from both the pressure and suction side mixed-up at the rudder TE exit and flow downstream of the wake region. It is proved that the slat attachment changes the flow field physics by delaying the separation and collapse the large structures exhibited without slat.

## CONCLUSION

The goal of the current study is to determine the effect of the rudder- slat attachment using CFD. The 3D slat control shows a remarkable enhancement in terms of the fluid flow characteristics. It is also evident that the LE slat shifts the separation region due to the control performance demonstrated by the slat attachment. The RANS turbulence model failed to predict the stall angle compared to the experiment due to early loss of side force coefficient. Other turbulence models may be used to predict the experimental stall and post stall angle values. However, the LES case for β=20° prove to be in good agreement with the experimental data.

## AKNOWLEDGMENT

This project has received funding from Clean Sky 2 Joint Undertaking (JU) under grant agreement number 864290. Also, the funding from Petroleum Technology Development Fund PTDF is appreciated.

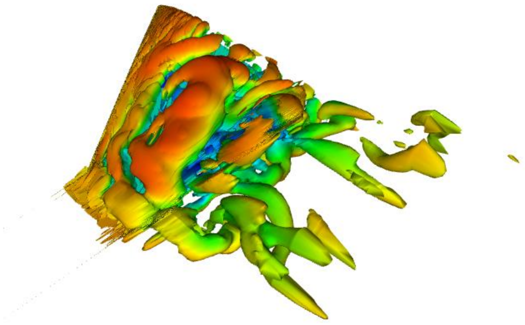

Figure 5: Iso-surface of λ-2 vortex structure without slat

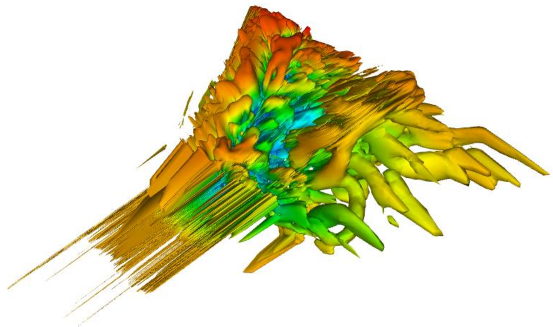

Figure 6: Iso-surface of λ-2 vortex structure with slat

## REFERENCES

[1] M. O. McKinney, R. E. Kuhn, and J. P. Reeder, “Aerodynamics and flying qualities of jet V/STOL airplanes,” *SAE Tech. Pap.*, 1964, doi: 10.4271/640789.

[2] E. Besnard, A. Schmitz, E. Boscher, N. Garcia, and T. Cebeci, “Two-dimensional aircraft high lift system design and optimization,” *36th AIAA Aerosp. Sci. Meet. Exhib.*, 1998, doi: 10.2514/6.1998-123.

[3] M. Singh, K. Dhanalakshmi, and J. Mathur, “Investigation of two dimensional flow past multi element airfoils for general transport aircraft,” *Int. J. Numer. Methods Heat Fluid Flow*, vol. 21, no. 8, pp. 1026–1049, 2011, doi: 10.1108/09615531111177778.

[4] S. Narsipur, B. W. Pomeroy, and M. S. Selig, “CFD analysis of multielement airfoils for wind turbines,” *30th AIAA Appl. Aerodyn. Conf. 2012*, no. June, pp. 474–491, 2012, doi: 10.2514/6.2012-2781.

[5] B. W. Pomeroy, G. A. Williamson, and M. S. Selig, “Experimental study of a multielement airfoil for large wind turbines,” *30th AIAA Appl. Aerodyn. Conf. 2012*, no. June, pp. 835–852, 2012, doi: 10.2514/6.2012-2892.

[6] Chica E, Aguilar J, and Rubio-Clemente A, “Analysis of a lift augmented hydrofoil for hydrokinetic turbines,” 2019, doi: 10.24084/repqj17.216.

[7] C. P. van Dam, “The re,” *Prog. Aerosp. Sci.*, vol. 38, no. 2, pp. 101–144, 2002.

[8] D. Anitha, G. K. Shamili, P. Ravi Kumar, and R. Sabari Vihar, “Air foil Shape Optimization Using Cfd and Parametrization Methods,” *Mater. Today Proc.*, vol. 5, no. 2, pp. 5364–5373, 2018, doi: 10.1016/j.matpr.2017.12.122.

**Joint ERCOFTAC/EU-CTFF**
**European Drag Reduction and Flow Control Meeting – EDRFCM 2022**
**April 11–14, 2022, Paris, France**

# TOWARDS RELIABLE AND COST-EFFECTIVE DNS OF TURBULENT FLOW OVER RIBLETS:
## ANALYTICAL CORRECTION OF CORNER SINGULARITY

**Federica Gattere, Alessandro Chiarini, Giorgio M. Cavallazzi, Andrea Rossi**,
Dipartimento di Scienze e Tecnologie Aerospaziali, Politecnico di Milano, 20156 Milano, Italy

**Davide Gatti**
Institute for Fluid Mechanics, Karlsruhe Institute of Technology, 76131 Karlsruhe, Germany

**Paolo Luchini**
Dipartimento di Ingegneria Industriale, Università di Salerno, 84084 Fisciano, Italy

**Maurizio Quadrio**
Dipartimento di Scienze e Tecnologie Aerospaziali, Politecnico di Milano, 20156 Milano, Italy

### BACKGROUND

Flow control for skin friction drag reduction aims at mitigating the negative effects of turbulence near the wall to cut energy consumption and boost cost-effectiveness and environmental efficiency. Drag reduction strategies can be classified into two categories, passive and active. Among the latter, riblets are the most promising and considered for application on commercial airplanes. Riblets are small two-dimensional surface protrusions aligned with the direction of the flow, that produce an anisotropic roughness: their particular shape blocks the near-wall spanwise flow more effectively than the streamwise one.

Studies by Luchini et al. [4] clarified their drag reducing mechanism, which produces a vertical shift of the velocity profile in the turbulent region of the boundary layer once plotted in the law-of-the-wall form. It was demonstrated that, when the spanwise period of the riblets is small (i.e. in the so-called viscous regime), the drag reduction (DR) rate depends on the protrusion height only. The protrusion height is the difference ($\Delta h$) between the longitudinal ($h_{\parallel}$) and the transverse ($h_{\perp}$) protrusion heights, which represent the virtual origin of the longitudinal and transverse velocity profile, each measurable from an arbitrary origin (e.g. the riblet tip). When $\Delta h$ is positive, the spanwise flow induced by the overlying turbulent streamwise vortices is hampered more than the longitudinal one, thus reducing turbulent activity and eventually drag.

Riblets have been extensively studied over the last 50 years, particularly by experimental works. A few geometries have been tested and V-grooves in which riblets have sharp triangular ridges have been found particularly effective, guaranteeing a maximum DR of $7-8\%$. More difficult is the corresponding numerical verification of the riblets performance, which requires an high-fidelity numerical approach such as Direct Numerical Simulation (DNS).

The geometric singularity at the tip that characterizes riblets for any cross-sectional shape is directly responsible for its drag reduction capabilities, but at the same time makes numerical simulations extremely challenging. In this contribution we will show how a brute-force approach where a large number of grid points in the spanwise direction are placed near the tip increases the computational cost at an extreme level, while still providing unacceptable performance. Hence, we introduce an analytical correction of the instantaneous solution near the corner, that combines solution accuracy and computational efficiency.

### METHODS

The local loss of accuracy of the numerical solution near the geometric singularity made by the riblets tip makes the measure of the friction drag reduction over surfaces with riblets a major challenge. Since properly resolving the tip by locally refining the grid is computationally prohibitive, we exploit the numerical method proposed by Luchini [2] for the analytical correction of the corner singularity. The method hinges upon the knowledge of the local behaviour of the solution close to the singularity, which is analytically determined and compensated for. Near the tip the velocity gradients become infinitely large, viscous effects are dominant over non-linear effects, and the local solution can be obtained from the analytically determined Stokes flow in polar coordinates (see figure 1). Let us consider two-dimensional riblets first. Actually the solution is provided by two distinct problems. Parallel to the riblets edge, the pressure is not affected and solving a Laplace problem provides the solution of the streamwise component of the velocity:

$$u = r^{\pi/(2\varphi_w)} \cos\left(\pi/(2\varphi_w)\theta\right).$$

In the plane of the cross-section of the riblets, a two-dimensional Stokes problem provides the local solution for the wall-normal and spanwise components of the velocity, and a

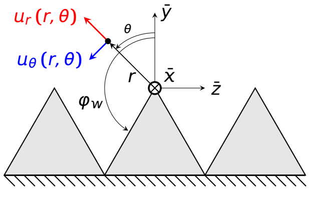

Figure 1: Local reference frame for a straight V-shape riblet.

Poisson problem provides the pressure:

$$u_r\,(r,\theta) = -r^{\gamma}\left[A\,(\gamma+1)\sin\left((\gamma+1)\,\theta\right) + B\,(\gamma-1)\sin\left((\gamma-1)\,\theta\right)\right]$$
$$u_\theta(r,\theta) = -(\gamma+1)r^{\gamma}\left[A\mathrm{cos}((\gamma+1)\theta) + B\mathrm{cos}((\gamma-1)\theta)\right]$$
$$\frac{1}{\nu}p\,(r,\theta) = -4\gamma B r^{\gamma-1}\sin\left((\gamma-1)\,\theta\right),$$

where $\gamma$ is the first mode of the spectrum of exact solutions and the constants $A$ and $B$ are provided enforcing the boundary conditions. The corner correction is enforced thanks to a tight integration into the DNS solver, which is based on an implicit immersed-boundary method. The correction is present close to the tip, and vanishes far from it. The DNS code was introduced by Luchini [3], and solves the incompressible Navier–Stokes equations in primitive variables. An implicit immersed-boundary method, implemented on staggered Cartesian grid, continuous with respect to boundary crossing and numerically stable at all distances from the boundary, describes the geometry of the non-planar wall.

We carry out a DNS at $Re_\tau = 200$ with a Constant Pressure Gradient strategy of a fully developed turbulent half-channel flow with the wall covered by 2D riblets with a triangular V-shaped cross-section with height to spacing ratio $h/s = \sqrt{3}/2$. The riblets spacing in viscous units is $s^+ = 16$, i.e. about the optimal value for reducing skin friction drag. The computational domain is $(L_x, L_y, L_z) = (7.5, 2.08, 1)$ with a computational grid with a number of points of $(N_x, N_y, N_z) = (240, 416, 186)$ in the streamwise, spanwise and wall-normal direction. Periodic boundary conditions are enforced in both the streamwise and spanwise directions, whereas an anti-symmetric boundary condition for the wall-normal velocity component is imposed at the centerline; no slip and no penetration boundary conditions are enforced at the wall.

## RESULTS

Figure 2 shows the significant enhancement of the reliability of the DNS results (in terms of value of the protrusion heights) when the corner correction is applied. The protrusion heights computed with/without the corner correction are compared to the analytical solution [4] for a laminar case. For the highest resolution with 16 grid points per riblets in spanwise direction, the error in computing of $\Delta h$ drops from 32.5 % to 1.7 % when the correction is applied. This error can be thought of as a relative error in computing drag reduction. The skin-friction drag of the channel covered by riblets is compared to the one of a reference smooth channel at the same Reynolds number to compute the drag reduction performance of riblets. The computed reduction of drag with the finer computational grid changes from 0.1 % without corner correction to 4.8 % with corner correction, which resembles the experimental results of Bechert et al.[1] who found a reduction of drag of 5 % for the same geometry.

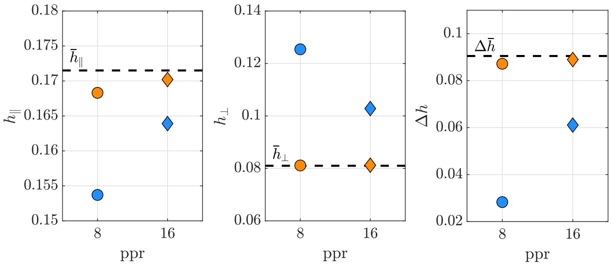

Figure 2: Protrusion heights of triangular riblets computed with (orange) and without (blue) corner correction. Dashed lines are the analytical values taken from [4]. The horizontal axis represents the number of grid points per single riblets (ppr) in the spanwise direction.

After assessing the validity of the corner correction for straight riblets, its extension to three-dimensional riblets is considered. If the sharp edge of the riblets is not straight the decoupling of the local solution in the Laplace and 2D Stokes problems fails in a global reference frame. Decoupling is still obtained in a reference frame aligned with the local cross-section, but the components of the velocity vector become intermixed, and an implicit discretization becomes impossible. Even an explicit treatment would be difficult if the mesh is staggered. Thus, in this preliminary attempt we neglect the mixed terms in the correction, limiting it to the diagonal components of the correction matrix, under the assumption that the local misalignment of three-dimensional riblets is small.

At the Meeting, we will present preliminary results obtained with our DNS code for the case of sinusoidal riblets, a particular class of 3D configurations where the riblet tip varies its spanwise position along the streamwise direction following a sinusoidal law, and the spanwise spacing between the riblets remains constant (see figure 3). A few attempts have been made in the past to characterize this geometry, with scattered results. We consider sinusoidal riblets with a wavelength $\lambda_x^+ = 1500$ and a maximum angle between the streamwise direction and the riblets crest $\beta_{max} = 2°$. Sinusoidal riblets have been found to outperform straight riblets, bumping up DR from 4.8% to 6.4%. Although the result is still preliminary, and the full corner correction needs to be implemented, given our methodological approach, we are inclined to believe that such geometry can in fact perform better than straight riblets, albeit moderately so as long as the cross-sectional shape of the riblets remains unchanged along the streamwise direction.

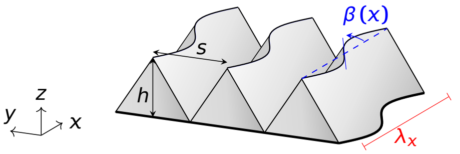

Figure 3: Sinusoidal riblets with geometric characteristics highlighted: $h$ is height, $s$ the spacing, $\beta(x)$ is the angle between the crests and the streamwise direction and $\lambda_x$ is the wavelength. Straight riblets have $\beta(x) = 0$.

## REFERENCES

[1] D.W. Bechert, M. Bruse, W. Hage, J.G.T. Van Der Hoeven, and G. Hoppe. Experiments on drag-reducing surfaces and their optimization with an adjustable geometry. *Journal of Fluid Mechanics*, 338:59–87, 1997.

[2] P. Luchini. A deferred correction multigrid algorithm based on a new smoother for the Navier–Stokes equations. *Journal of Computational Physics*, 92:349–368, 1991.

[3] P. Luchini. Immersed-boundary simulation of turbulent flow past a sinusoidally undulated river bottom. *European Journal of Mechanics - B/Fluids*, 55:340–347, 2016.

[4] P. Luchini, F. Manzo, and A. Pozzi. Resistance of a grooved surface to parallel flow and cross-flow. *Journal of Fluid Mechanics*, 228:87–109, 1991.

**Joint ERCOFTAC/EU-CTFF**
**European Drag Reduction and Flow Control Meeting – EDRFCM 2022**
**September 6th–9th, 2022, Paris, France**

# ASSESSING THE PROTRUSION-HEIGHT CONCEPT FOR PREDICTING THE DRAG-REDUCTION PERFORMANCE OF RIBLETS

**Jeremy Wong**
Department of Mechanical Engineering, University of Melbourne, Victoria 3010, Australia

**Ricardo García-Mayoral**
Department of Engineering, University of Cambridge, Cambridge CB2 1PZ, UK

**Nicholas Hutchins**
Department of Mechanical Engineering, University of Melbourne, Victoria 3010, Australia

**Daniel Chung**
Department of Mechanical Engineering, University of Melbourne, Victoria 3010, Australia

## INTRODUCTION

Large transport systems with slender bodies, e.g. aircraft [12], primarily expend energy to overcome skin-friction drag. A promising approach to reducing the skin-friction drag is through the use of riblets. Riblets are intentionally roughened surfaces in the form of streamwise-uniform micro-grooves that have been shown to reduce drag below that of a smooth surface without energy input [1, 5]. The optimal geometry of riblets typically have sharp tips [11, 1] and the optimal size of riblets on a passenger aircraft are on the order of 50–100 microns [12]. Because of these small features, the widespread use of riblets today is hampered by the complexity in manufacturing, maintenance and wear [2, 3]. Currently, it remains difficult to assess whether the performance of imperfectly manufactured or worn riblet surfaces remains acceptable and ultimately, cost-effective across their life span. To address the sensitivity of the performance due to imperfections, an accurate routine predictive tool is needed. Such a tool was advanced by Luchini [11, 10] using the concept of protrusion heights, however its application [1, 5] has not been scrutinised in detail owing to the lack of systematic high-fidelity data.

## PROTRUSION HEIGHTS AND DRAG REDUCTION

We can quantify the drag reduction $DR$ as the fractional change in skin-friction coefficient $C_f$ relative to a baseline smooth wall (subscript 0) via $DR \equiv 1 - C_f/C_{f0}$ at matched friction Reynolds number $\delta^+ \equiv Re_\tau$, where $\delta$ is the thickness of the wall-bounded turbulence and the superscript $+$ refers to viscous scaling using the friction velocity $u_\tau$ and kinematic viscosity $\nu$. However, it is preferable to quantify the drag using the $Re_\tau$-independent roughness function $\Delta U^+ = U^+_{\delta 0} - U^+_\delta$, where $U^+_\delta$ is the mean velocity at the edge of the wall-bounded turbulence. Since $C_f \equiv 2/U^{+2}_\delta$,

$$DR = 1 - (1 - \Delta U^+/U^+_{\delta 0})^{-2} \sim -2\Delta U^+/U^+_{\delta 0}, \qquad (1)$$

for small changes, or, equivalently, $DR \sim -(2C_{f0})^{1/2}\Delta U^+$.

For small riblets, $DR$ increases linearly with size [11, 10]:

$$-\Delta U^+ = \mu_0(\ell^+_x - \ell^+_y) = \mu_0(\ell_x/\ell_g - \ell_y/\ell_g)\ell^+_g. \qquad (2)$$

Here the riblet size is characterized by the square root of the riblet groove cross-sectional area $\ell_g$ [6] labeled in figure 1, and $\ell_x$ and $\ell_y$ are the protrusion heights meant to locate the virtual origins perceived by streamwise and spanwise motions, respectively. Both $\ell_x/\ell_g$ and $\ell_y/\ell_g$ can be routinely obtained from Stokes flow calculations for a given riblet shape [11, 1, 5], and in this way they encapsulate the effect of riblet shape. Luchini [10] proposed that $-\Delta U^+ = \ell^+_x - \ell^+_y$, i.e. $\mu_0 = 1$, but the values $\mu_0 = 0.785$ [1] and $\mu_0 = 0.66$ [9, 6] have also been used, consistent with the scatter among the present riblet shapes in figure 1($a$) up to $\ell^+_g = 8$. Maximum drag reduction is shown by García-Mayoral & Jiménez [5] to occur at $\ell^+_{g,\mathrm{opt}} \approx 10.7$ independent of riblet shape, also consistent with the present data in figure 1($a$). However, we observe a 50% discrepancy in maximum drag-reduction predictions due to a typical departure from linearity at the optimum. Evaluating (1) and (2) at this optimum then yields $DR_{\max} = (2C_{f0})^{1/2} 0.83\mu_0(\ell_x/\ell_g - \ell_y/\ell_g)\ell^+_{g,\mathrm{opt}}$, the empirical constant 0.83 introduced to characterise this non-linearity at the optimum [5]. However, the flow physics behind 0.83 and the scatter of $\mu_0$ have not been thoroughly addressed.

We first step back from (2) to demonstrate that the effect on drag of riblets can indeed be reduced to the virtual origins of the mean ($z^+ = -\ell^+_U$) and turbulent flow ($z^+ = -\ell^+_T$), where $z^+$ is the wall-normal coordinate measured from the riblet crest or smooth wall, but the flow above the crest ($z^+ > 0$) is otherwise similar to that above a smooth wall [10, 8]. If so, the relationship between $\Delta U^+$ and $\ell^+_U$ and $\ell^+_T$ then follows from the stress balance $\mathrm{d}U^+/\mathrm{d}z^+ = 1 + \overline{u'w'}^+$, which constrains the riblet and smooth-wall mean gradients ($\mathrm{d}U^+/\mathrm{d}z^+$) to collapse above the crest when the Reynolds stress profiles ($\overline{u'w'}^+$) are matched by the use of a wall-normal shift $\ell^+_T$ (contrast figures 2$a$ and 2$b$). With unity viscous-scaled gradient near the wall, the mean-velocity difference in the vicinity above the crest is now $U^+_0 - U^+ = \ell^+_T - \ell^+_U$, a uniform difference that propagates into the overlying flow since the gradient is matched at every $z^+ + \ell^+_T$ above the crest [10]:

$$-\Delta U^+ = \ell^+_U - \ell^+_T, \qquad (3)$$

which we observe to be valid for the present riblets up to the optimum, $\ell^+_g \lesssim 10.7$ (figures 1$b$ and 2$d$). Luchini [10] further proposed that the virtual origins of mean and turbulence are identical the protrusion heights of streamwise and spanwise motions, i.e. $\ell^+_U = \ell^+_x$ and $\ell^+_T = \ell^+_y$, recovering

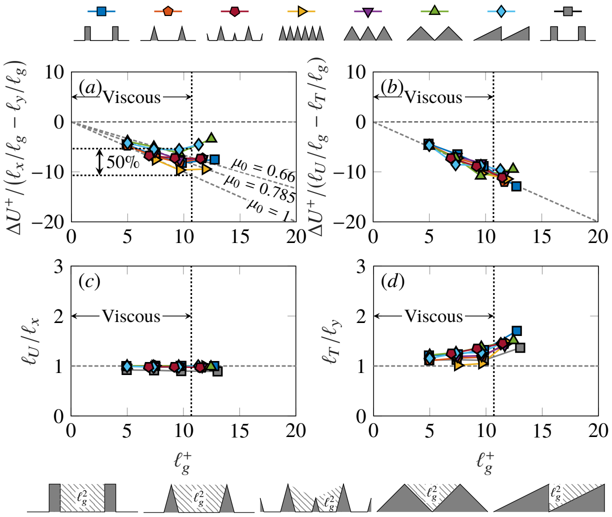

Figure 1: ($a$) Roughness function $\Delta U^+$ scaled by protrusion-height difference $\ell_x/\ell_g - \ell_y/\ell_g$ shows discrepancies near the optimum ($\ell_g^+ \approx 10.7$), consistent with the scatter in quoted $\mu_0$ in (2): $\mu_0 = 0.66$ [9], $\mu_0 = 0.785$ [1] and $\mu_0 = 1$ [10] up to $\ell_g^+ \approx 8$. A 50% discrepancy in drag predictions is observed at the optimum ($\ell_g^+ \approx 10.7$). ($b$) The discrepancies are alleviated when $\Delta U^+$ is scaled by the difference in mean and turbulence origin $\ell_U/\ell_g - \ell_T/\ell_g$ and this verifies (3). ($c$, $d$) Comparing the mean- and turbulent-flow virtual origins ($\ell_U$, $\ell_T$) with streamwise and spanwise protrusion heights ($\ell_x$, $\ell_y$) shows that $\ell_U \approx \ell_x$ but $\ell_T > \ell_y$, the latter responsible for the discrepancy in drag predictions at the optimum. Coloured markers denote minimal-span DNS data, some of which are taken from [4], while grey markers denote DNS data from [7].

(2), such that $\mu_0 = 1$. Although the mean origin $\ell_U^+ = \ell_x^+$ is validated by the present data (figure 1$c$), the turbulence origin $\ell_T^+ = \ell_y^+$ is invalid for the riblet sizes near the optimum $5 < \ell_g^+ < 10.7$ (figure 1$d$). The turbulence origins $\ell_T^+$ are generally deeper than $\ell_y^+$ ($\ell_T/\ell_y > 1$) but do seem to asymptote to $\ell_y^+$ as $\ell_g^+ \to 0$. Hence, towards this vanishingly small $\ell_g^+$, the protrusion height-scaled drag $\Delta U^+/(\ell_x/\ell_g - \ell_y/\ell_g)$ tends to $\mu_0 = 1$ for all riblets in figure 1($a$), as proposed by Luchini [10]. Towards the optimal size, however, we observe a riblet-shape-dependent deviation of $\ell_T^+$ from $\ell_y^+$ in figure 1($d$), with lesser deviation for riblets with sharper and narrower tips (e.g. ᐱᐱᐱᐱᐱ). This deviation results in the aforementioned typical departure from linearity which explains the 50% discrepancy in drag predictions. In summary, an accurate riblet drag model now relies on the accurate prediction of $\ell_T^+$ for each shape and size up to the optimum $\ell_g^+ \lesssim 10.7$.

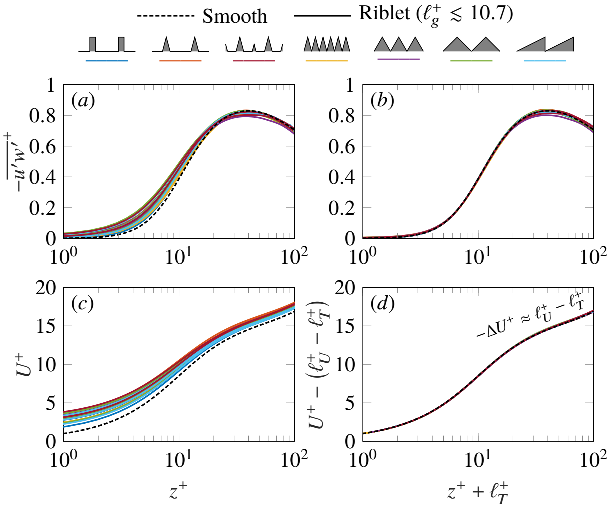

Figure 2: ($a$, $b$) Viscous-scaled Reynolds stress profiles for all small riblets ($\ell_g^+ \lesssim 10.7$), plotted against ($a$) the wall-normal coordinate measured from the riblet crest or smooth wall $z^+$ and ($b$) the wall-normal coordinate measured from the turbulence origin $z^+ + \ell_T^+$, collapse in the latter demonstrating smooth wall-like behaviour. ($c$, $d$) Mean-velocity profiles for all small riblets up to the optimum ($\ell_g^+ \lesssim 10.7$) as a function of ($c$) $z^+$ and ($d$) $z^+ + \ell_T^+$. The velocity profiles in ($d$) are shifted downwards by $\ell_U^+ - \ell_T^+$, showing collapse with the smooth-wall profile ($\ell_U^+ = \ell_T^+ = 0$), hence $-\Delta U^+ = \ell_U^+ - \ell_T^+$ for all small riblets up to the optimum ($\ell_g^+ \lesssim 10.7$).

## ACKNOWLEDGEMENTS

This material is based upon work supported by the Air Force Office of Scientific Research under award number FA2386-21-1-4018 (program manager: Ryan Carr, AOARD). We also thank Doug Smith (EOARD). This research was partially supported by the Australian Government through the Australian Research Council's Discovery Projects funding scheme (project DP170102595). This work was supported by computational resources provided by the Australian Government through the National Computational Infrastructure (NCI) under the National Computational Merit Allocation Scheme (NCMAS), by the Pawsey Supercomputing Centre with funding from the Australian Government and the Government of Western Australia and by the Sustaining and strengthening merit-based access to NCI LIEF Grant (LE190100021) facilitated by The University of Melbourne.

## REFERENCES

[1] D. W. Bechert, M. Bruse, W. Hage, J. G. T. Van Der Hoeven, and G. Hoppe. *J. Fluid Mech.*, 338:59–87, 1997.

[2] D. M. Bushnell. *Proc. Inst. Mech. Eng. G J. Aerosp. Eng.*, 217:1–18, 2003.

[3] K. S. Choi. *Adv. Mat. Res.*, 745:27–40, 2013.

[4] S. Endrikat, D. Modesti, N. Hutchins M. MacDonald, R. García-Mayoral, and D. Chung. *Flow Turb. Comb.*, 107:1–29, 2021.

[5] R. García-Mayoral and J. Jiménez. *Phil. Trans. R. Soc. A*, 369:1412–1427, 2011.

[6] R. García-Mayoral and J. Jiménez. *J. Fluid Mech.*, 678:317–347, 2011.

[7] R. García-Mayoral and J. Jiménez. *Phys. Fluids*, 24:105101, 2012.

[8] J. Ibrahim, G. Gómez-de-Segura, D. Chung, and R. García-Mayoral. *J. Fluid Mech.*, 915:A56, 2021.

[9] J. Jiménez. *Phys. Fluids*, 6:944–953, 1994.

[10] P. Luchini. In *Comput. Methods Appl. Sci. '96*, pages 466–470. 1996.

[11] P. Luchini, F. Manzo, and A. Pozzi. *J. Fluid Mech.*, 228:87–109, 1991.

[12] P. R. Viswanath. *Prog. Aerosp. Sci.*, 38:571–600, 08 2002.

**Joint ERCOFTAC/EU-CTFF**
**European Drag Reduction and Flow Control Meeting – EDRFCM 2022**
**September 6th–9th, 2022, Paris, France**

# BIOMIMETIC FLOW CONTROL FOR A PARAGLIDER: FROM IDEA TO PRODUCT

**Jeonghan Shin**
Department of Mechanical Engineering, Ulsan National Institute of Science and Technology,
44919 Ulsan, South Korea

**Jooha Kim**
Department of Mechanical Engineering, Ulsan National Institute of Science and Technology,
44919 Ulsan, South Korea

**Jungmok Park**
Gin Gliders, 17036 Gyeonggi-do, South Korea

**Ginseok Song**
Gin Gliders, 17036 Gyeonggi-do, South Korea

## INTRODUCTION

Paragliding is a sport in which a pilot flies through the air in a harness suspended below a fabric wing. The goal of paragliding is to fly a predetermined course faster or cover a greater distance in a given amount of time. Therefore, improving the aerodynamic performance of the paraglider is directly related to achieving better results in competition and ensuring the safety of the pilot.

Streamlining the shape of the wing and the harness has been a successful strategy for improving the aerodynamic performance of the paraglider. As a result of the streamlining, most pilots now sit in cocoon-shaped harnesses during flight, and the paraglider wing, called the canopy, has an airfoil-shaped cross-section. In addition, to reduce drag on the paraglider further, the number of lines connecting the canopy to the harness has been reduced continuously. Thus most paraglider designs now appear to be converging into a similar shape.

This study aims to take the design of paraglider to the next level through biomimetic flow controls. Since paragliders fly without input of any fuel or energy source, this study focuses on developing passive flow control methods that apply the morphological characteristics of living things to a paraglider.

## CONTROL METHODS APPLIED TO A PARAGLIDER

Paragliders can fly long distances (up to many hundreds of kilometers) while generating lift from the canopy through repeated ascending and descending flights. Therefore, it is important to control the flow around the canopy to enhance or maintain lift over a wide range of angles of attack. In this study, to achieve this purpose, (i) the tubercles of humpback whales [3] and (ii) the ridges of leatherback turtles [1] are separately applied to the leading edge and suction surface of the canopy, respectively. The sizes of the control devices (e.g., tubercle width and ridge height) are determined within the range that is practically applicable to the canopy when they are manufactured.

## LAB-SCALE EXPERIMENTS AND REAL FLIGHT TESTS

Since the canopy is a three-dimensional tapered ram-air wing curved in the spanwise direction, it has different flow characteristics than a two-dimensional airfoil or a conventional tapered wing [2]. Therefore, before applying the control devices to the canopy, flow visualization experiments are conducted in a wind tunnel to examine the flow features of the canopy.

Control devices are placed to provide efficient flow control based on the flow separation characteristics of the baseline canopy. To find the shape of tubercle and ridge that maximizes aerodynamic performance, parametric studies are conducted through wind tunnel experiments.

The control device with an optimized shape is installed on an actual paraglider (Boomerang 11 of Gin Gliders), and then a real flight test is conducted. In the real flight test, two paragliders without and with biomimetic flow control fly side-by-side at the same time to compare the lift-to-drag ratio or glide ratio.

## RESULTS

The control devices developed in this study have been shown to substantially improve the aerodynamic performance and stability of the paraglider. A new paraglider with tubercles (Fig. 1) has been recently released on the market after being certified. The detailed results of this study will be discussed in the presentation.

## REFERENCES

[1] K. Bang, J. Kim, S.-I. Lee, and H. Choi. Hydrodynamic role of longitudinal dorsal ridges in a leatherback turtle swimming. *Scientific Reports*, 6(1):1–10, 2016.

Figure 1: New paraglider with leading-edge tubercles.

[2] S. Chae, J. Shin, Y. Shin, S. Hwang, J. Park, G. Song, and J. Kim. Aerodynamic effects of canopy inflation in paragliding. *Journal of Mechanical Science and Technology*, 36(4):1835–1846, 2022.

[3] H. Kim, J. Kim, and H. Choi. Flow structure modifications by leading-edge tubercles on a 3D wing. *Bioinspiration & Biomimetics*, 13(6):066011, 2018.

**Joint ERCOFTAC/EU-CTFF**
**European Drag Reduction and Flow Control Meeting – EDRFCM 2022**
**September 6th–9th, 2022, Paris, France**

# EXPERIMENTAL INVESTIGATION OF THE SESSILE DROPLET EVAPORATION PROCESS BASED ON DIFFERENT SURFACE ROUGHNESS AND WETTABILITY

**Zhihao Zhang**
Fluids & Thermal Engineering Research Group, University of Nottingham, NG7 2RD, Nottingham, UK

**Yuying Yan**
Fluids & Thermal Engineering Research Group, University of Nottingham, NG7 2RD, Nottingham, UK

## ABSTRACT

Droplet evaporation is one of the most common physical processes in nature, and the studies on the sessile droplet evaporation have become increasingly active since Maxwell first deduced the equations of droplet evaporation in 1877 [1]. Nowadays, the process of droplet evaporation is used widely, such as electronic cooling, inkjet printing, biological and medical diagnostics, precision machining, etc. [2]. Therefore, exploring the factors which could affect the droplet evaporation dynamics has become crucial. For a sessile droplet, the surface wettability could significantly affect the evaporation dynamics [3]. Among the many factors influencing surface wettability, surface roughness is one of the most common factors [4] and attracted researchers to study this issue. Furuta et al. [5] based on the experimental studies found that the evaporation mode transition radius is related to the average roughness distance and height. Chen et al. [6] revealed that the critical Cassie-Wenzel transition base size for the sessile droplet have a strong relationship with the surface roughness. Bussonnière et al. [4] also pointed that the Cassie–Baxter state of the droplet could be prolonged with the increase of roughness on the hydrophobic micro/nano-structures surface. Madhu et al. [7] proposed to convert dynamic roughness changes into heterogeneities and combined it into the model which could predict the process of droplet evaporation. But among them the link between roughness and droplet evaporation processes has not been fully revealed.

In the present study, an experimental investigation of sessile pure water droplets evaporating on copper surfaces with different roughness and wettability is carried out. The effect of roughness as a factor on the evaporation rate is considered. It is demonstrated that the changes in surface roughness not only affect the wetting state of the sessile droplet but also influence the heat and mass transfer processes at the liquid-vapour interface. In this study, the results trying to highlight the interplay between the surface roughness and the universality of the evaporation dynamics for the sessile droplet. Using both experimental and theoretical approaches to reveal the relationship between the surface roughness and sessile droplet evaporation process. Fig. 1 shows the experimental details. The droplet of deionized water was placed on the copper surface. The Drop Shape Analyzer and IR Camera were used to observe the geometric parameters and temperature changes of the sessile droplet, correspondingly. Fig. 2 shows the preliminary results. On the copper surface with a certain level of roughness, the sessile droplet mainly goes through the CCR (Constant Contact Radius) mode during evaporation when the initial wetting phase is not considered. Then, the sessile droplet will go through the SS (Stick-Slip) mode at the last stage of evaporation. Therefore, it is confirmed that the roughness does affect the droplet evaporation mode and further affect the evaporation dynamics.

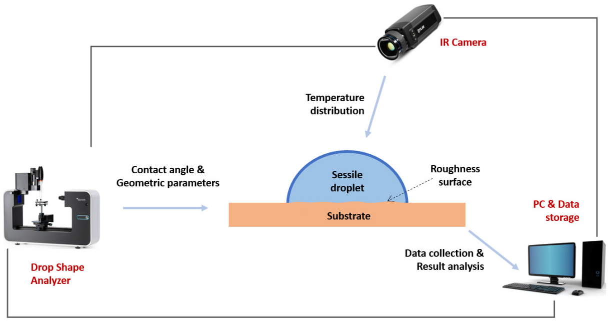

Figure 1: The schematic diagram of the experimental apparatus for sessile droplet evaporation study.

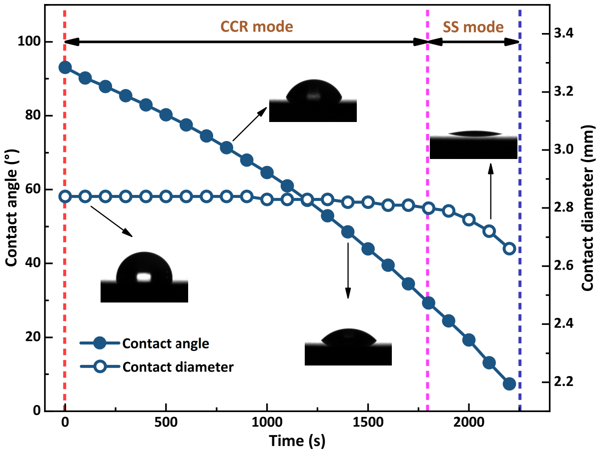

Figure 2: The schematic diagram of the change of droplet contact angle and diameter with time.

## REFERENCES

[1] James Clerk Maxwell. *The Scientific Papers of James Clerk Maxwell...*, volume 2. University Press, 1890.

[2] Duyang Zang, Sujata Tarafdar, Yuri Yu Tarasevich, Moutushi Dutta Choudhury, and Tapati Dutta. Evaporation of a droplet: From physics to applications. *Physics Reports*, 804:1–56, 2019.

[3] D Brutin and V Starov. Recent advances in droplet wetting and evaporation. *Chemical Society Reviews*, 47(2):558–585, 2018.

[4] Adrien Bussonnière, Masoud B Bigdeli, Di-Yen Chueh, Qingxia Liu, Peilin Chen, and Peichun Amy Tsai. Universal wetting transition of an evaporating water droplet on hydrophobic micro-and nano-structures. *Soft matter*, 13(5):978–984, 2017.

[5] Tsutomu Furuta, Toshihiro Isobe, Munetoshi Sakai, Sachiko Matsushita, and Akira Nakajima. Wetting mode transition of nanoliter scale water droplets during evaporation on superhydrophobic surfaces with random roughness structure. *Applied surface science*, 258(7):2378–2383, 2012.

[6] Xuemei Chen, Ruiyuan Ma, Jintao Li, Chonglei Hao, Wei Guo, Bing Lam Luk, Shuai Cheng Li, Shuhuai Yao, and Zuankai Wang. Evaporation of droplets on superhydrophobic surfaces: Surface roughness and small droplet size effects. *Physical review letters*, 109(11):116101, 2012.

[7] Madhu Ranjan Gunjan and Rishi Raj. Dynamic roughness ratio-based framework for modeling mixed mode of droplet evaporation. *Langmuir*, 33(28):7191–7201, 2017.

**Joint ERCOFTAC/EU-CTFF**
**European Drag Reduction and Flow Control Meeting – EDRFCM 2022**
**September 6th–9th, 2022, Paris, France**

# CANCELLATION OF THE INVISCID CONTRIBUTION IN SKIN-FRICTION DECOMPOSITIONS

**M. Atzori**
Department of Particulate Flow Modelling, Johannes Kepler University, 4040 Linz, Austria

**F. Mallor**
SimEx/FLOW, Engineering Mechanics, KTH Royal Institute of Technology, 10044 Stockholm, Sweden

**A. Stroh & D. Gatti**
Institute of Fluid Mechanics (ISTM), Karlsruhe Institute of Technology, 76131 Karlsruhe, Germany

**K. Fukagata**
Department of Mechanical Engineering, Keio University, 223-8522 Yokohama, Japan

**R. Vinuesa & P. Schlatter**
SimEx/FLOW, Engineering Mechanics, KTH Royal Institute of Technology, 10044 Stockholm, Sweden

## INTRODUCTION

Identities such as the so-called FIK [2] and RD [3] decompositions have been proposed to study different contributions to skin friction. In the case of non-homogeneous flows, both decompositions give rise to a high number of terms, posing difficulties in the interpretation of results. This fact is particularly evident in the case of turbulent boundary layers (TBLs) subjected to strong adverse pressure gradients (APGs), where contributions can have absolute values as high as many times the total skin friction [1]. We used the concept of dynamic pressure to reorganize terms of the FIK and RD identities. The new formulations are applied to two cases with control on the suction side of an airfoil, showing that they allow a more straightforward identification of the main phenomena responsible for friction and for control effects.

## DATA-SET AND NUMERICAL METHODS

We consider data obtained with highly-resolved large-eddy simulations (LESs) of the flow around a NACA4412 airfoil at angle of attack 5° and Reynolds number $Re_c = 400,000$ ($Re_c = U_\infty c/\nu$, where $U_\infty$ is the velocity of the incoming flow, $c$ is the chord length, and $\nu$ is the kinematic viscosity). Two different control strategies are examined: uniform blowing and body-force damping. Uniform blowing is implemented as a boundary condition imposing a value of $0.1\% U_\infty$ to the wall-normal velocity component. Body-force damping, which is an idealized model for the effects of opposition control, is implemented in a way similar to Stroh *et al.* [4], in the region below $y^+ = 25$. Note that $y^+ = y/l^*$ denotes the distance from the wall normalized with the local wall-shear stress for the uncontrolled case, where $l^* = \nu/u_\tau$, $u_\tau = \sqrt{\tau_w/\rho}$, $\tau_w = \rho\nu(\mathrm{d}U/\mathrm{d}y)_{y=0}$, and $U$ and $\rho$ are the mean wall-tangential velocity component and the density of the flow, respetively. For both control strategies, the control region on the airfoil is between $x/c = 0.24$ and $x/c = 0.86$. The reference case and that with uniform blowing are part of the data-sets already described by Vinuesa *et al.* [5] and Atzori *et al.* [1], respectively. The case with body-force damping is considered here for the first time but it is analogous to a case at $Re_c = 200,000$ with the same control in Ref. [1]. The skin-friction coefficients for the three cases, denoted by $c_f = 2\tau_w/(\rho U_e^2)$, are shown in Fig. 1 ($U_e$ is the edge velocity). Note that the body force is calibrated to have effects similar to those of uniform blowing on $c_f$.

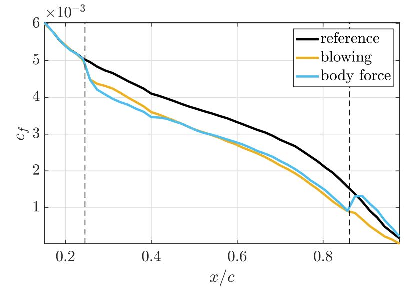

Figure 1: Local skin-friction coefficient for the suction side of the airfoil in the three study cases. The dashed vertical lines denote the control region.

## SKIN-FRICTION DECOMPOSITION

In APG TBLs, the four most relevant terms of the FIK decomposition written in the standard form are those related to turbulent fluctuations ($c_f^T = -4\int_0^1 (1-\eta)\overline{uv}\,\mathrm{d}\eta$), streamwise derivative of the wall-tangential mean velocity ($c_f^{D1} = -2\int_0^1 (1-\eta)\frac{\partial U^2}{\partial x}\,\mathrm{d}\eta$), mean wall-normal convection ($c_f^{D3} = -2\int_0^1 (1-\eta)\frac{\partial UV}{\partial x}\,\mathrm{d}\eta$), and pressure gradient ($c_f^P = -2\int_0^1 (1-\eta)\frac{\partial P}{\partial x}\,\mathrm{d}\eta$). In these expressions, the integration variable is the wall distance normalized with the boudary-layer thickness, $\eta = y/\delta_{99}$. Rewriting $c_f^{D1}$ and $c_f^{D3}$ using the continuity equation, we can introduce the following three terms:

$$\begin{aligned} c_f^{DP} &= -2\int_0^1 (1-\eta)^2 \left(U\frac{\partial U}{\partial x} + \frac{\partial P}{\partial x}\right)\mathrm{d}\eta\,, \\ c_f^{D\Omega} &= +2\int_0^1 (1-\eta)^2 V\Omega_z\,\mathrm{d}\eta\,, \\ c_f^{DVV} &= -2\int_0^1 (1-\eta)^2 \left(V\frac{\partial V}{\partial x}\right)\mathrm{d}\eta\,, \end{aligned} \tag{1}$$

where $\Omega_z$ is the streamwise vorticity. The term $c_f^{DP}$ vanishes in region of irrotational flow, where the $\frac{1}{2}\rho U^2 + P = P_0$ (the total pressure $P_0$ is constant). The reason for defining $c_f^{DP}$ is thus to factor out the contribution due to the streamwise development of the inviscid flow above the boundary layer. The new term $c_f^{DVV}$ is typically negligible.

A similar reorganization of terms is also possible for the RD decomposition. In particular, the two terms related to energy convection and work caused by the pressure gradient, $c_f^{GC} = \frac{2}{U_e^3}\int_0^{\delta_{99}}(U - U_e)\left(U\frac{\partial U}{\partial x} + V\frac{\partial U}{\partial y}\right)\mathrm{d}y$ and $c_f^{GP} = \frac{2}{U_e^3}\int_0^{\delta_{99}}(U - U_e)\left(\frac{1}{\rho}\frac{\partial P}{\partial x}\right)\mathrm{d}y$, respectively, can be written as:

$$\begin{aligned} c_f^{GDP} &= \frac{2}{U_e^3}\int_0^{\delta_{99}}(U - U_e)\left(U\frac{\partial U}{\partial x} + \frac{1}{\rho}\frac{\partial P}{\partial x}\right)\mathrm{d}y\,, \\ c_f^{G\Omega} &= \frac{2}{U_e^3}\int_0^{\delta_{99}}(U - U_e)\,(-V\Omega_z)\,\mathrm{d}y\,, \\ c_f^{GVV} &= \frac{2}{U_e^3}\int_0^{\delta_{99}}(U - U_e)\left(V\frac{\partial V}{\partial x}\right)\mathrm{d}y\,. \end{aligned} \tag{2}$$

Of these terms, $c_f^{GVV}$ can usually be neglected. Note that the other RD contribution relevant in TBL is the term $c_f^{Pr} = \frac{2}{U_e^3}\int_0^{\delta_{99}} -\overline{uv}\frac{\partial U}{\partial y}\mathrm{d}y$, associated with production of turbulent kinetic energy.

## RESULTS AND DISCUSSION

The most relevant terms of the FIK and RD decompositions are reported in Fig. 2 for the streamwise region $0.4 < x/c < 0.8$. In the reference case and at $x/c = 0.8$, for example, $c_f^T + c_f^{D1} + c_f^{D3} + c_f^P \simeq 95\% c_f$, showing that it is possible to focus on these contributions ($c_f^{D1} + c_f^{D3} + c_f^P = c_f^{DP} + c_f^{DP} + c_f^{DVV}$ by definition). Due to the APG, $c_f^T$ has relative high values in these cases, and it becomes progressively higher moving downstream even though $c_f$ decreases, reaching $c_f^T \approx 2c_f$ at $x/c = 0.8$ in the reference case. The three original contributions $c_f^{D1}$, $c_f^{D3}$, and $c_f^P$, however, have all even higher values, *e.g.* $c_f^{D1} \approx 14c_f$ and $c_f^P \approx -6c_f$ at the same streamwise location. Because of the these very high values and the fact that both $c_f^{D3}$ and $c_f^P$ are negative, it is difficult to clearly isolate the most relevant APG and control effects on the skin friction. Furthermore, the fact that all terms related to streamwise inhomogeneity in the standard formulation are higher than $c_f^T$ gives the contour-intuitive result that turbulent fluctuations play only a minor role in generating friction. On the other hand, the new contribution $c_f^{DP}$ captures the balance between streamwise convection and pressure-gradient so that, *e.g.* at $x/c = 0.8$, $c_f^{DP} \approx c_f$ and $c_f^{D\Omega} \approx -2c_f$, while $c_f^{DVV}$ is negligible. The decreases of $c_f$ due to the stronger APG is then immediately attributed to mean convection.

Control effects are also easier to recognize. Body-force damping modifies the total $c_f$ acting on the turbulent fluctuations contribution, $c_f^T$, which is reduced by an amount approximately equal to $30\% c_f$ of the reference case at $x/c = 0.8$. Contributions $c_f^{D1}$ however, is also reduced by $70\% c_f$, while both $c_f^{D3}$ and $c_f^P$ are increased by $45\% c_f$ and $29\% c_f$, respectively. On the other hand, this control changes $c_f^{DP}$ only by $-6\% c_f$ and $c_f^{D\Omega}$ by $+10\% c_f$.

Similar observations also hold for the RD decomposition. Partially because the term related to mean convection, $c_f^{GC}$, already includes both wall-normal- and wall-tangential-convection contributions in the traditional formulation of this decomposition, the cancellation of the inviscid term seems to have a lower impact on the overall results. Nevertheless, $c^{GDP}$ and $c^{G\Omega}$ have lower values than $c^{GC}$, and $c^{GP}$, and their modules becomes higher than the total $c_f$ only where the APG is particularly intense.

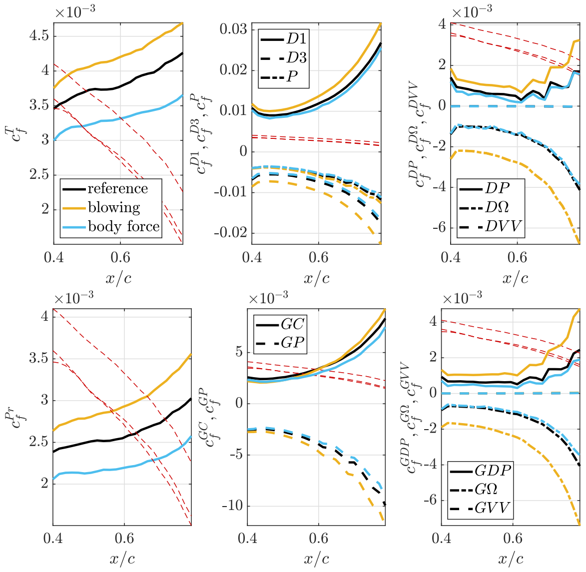

Figure 2: Selected FIK and RD contributions (top and bottom row, respetively) The dashed red lines denoted the total $c_f$ for the three cases, which are the same values as in Fig. 1 (the lower lines are the controlled cases).

## CONCLUSIONS

We proposed an alternative formulation of the FIK and RD decompositions to examine adverse-pressure-gradient and control effects using highly-resolved large-eddy simulations of the flow around a NACA4412 airfoil. In this new formulation, the terms related to streamwise convection and pressure gradient are considered together to cancel out contributions due to the development of the inviscid flow outside the turbulent boundary layer. The new decompositions allow to better describe the role of turbulent fluctuations in the generation of friction, and summarize pressure-gradient and control effects. The higher sensitivity of the newly introduced dynamic-pressure contributions will also be used to examine different pressure-gradient conditions.

## REFERENCES

[1] M. Atzori, R. Vinuesa, A. Stroh, D. Gatti, B. Frohnapfel, and P. Schlatter. Uniform blowing and suction applied to non-uniform adverse-pressure-gradient wing boundary layers. *Phys. Rev. Fluids*, 6:113904, 2021.

[2] K. Fukagata, K. Iwamoto, and Kasagi. N. Contribution of Reynolds stress distribution to the skin friction in wall-bounded flows. *Phys. Fluids*, 14:L73–L76, 2002.

[3] N. Renard and S. Deck. A theoretical decomposition of mean skin friction generation into physical phenomena across the boundary layer. *J. Fluid Mech.*, 790:339–367, 2016.

[4] A. Stroh, Y. Hasegawa, P. Schlatter, and B. Frohnapfel. Global effect of local skin friction drag reduction in spatially developing turbulent boundary layer. *J. Fluid Mech.*, 805:303–321, 2016.

[5] R. Vinuesa, P.S. Negi, M. Atzori, A. Hanifi, D.S. Henningson, and P. Schlatter. Turbulent boundary layers around wing sections up to $Re_c = 1{,}000{,}000$. *Int. J. Heat Fluid Flow*, 72:86–99, 2018.

**Joint ERCOFTAC/EU-CTFF**
**European Drag Reduction and Flow Control Meeting – EDRFCM 2022**
**September $6^{\mathrm{th}}$–$9^{\mathrm{th}}$, 2022, Paris, France**

# SYNCHRONIZED MEASUREMENTS OF FLOW AND WALL FIELDS IN TURBULENT BOUNDARY LAYERS

**F. Foroozan, A. Güemess, R. Castellanos, M. Raiola, A. Ianiro and S. Discetti**
Aerospace Engineering Research Group, Universidad Carlos III de Madrid (UC3M), 28911 Leganés, Spain

## INTRODUCTION

Turbulent Boundary Layers (TBLs) have been the focus of research in aerodynamics for decades, mainly due to their significant contribution to wall friction drag in a large variety of industrial and aeronautical applications. The importance of wall-attached coherent structures populating TBLs, which are responsible for carrying approximately 60% of the tangential-Reynolds stress in wall turbulence, has aroused a great interest to propose non-intrusive methods to estimate them from the wall, and they have been shown to possess a dynamical coherence over time [1]. For instance, linear stochastic estimation has been used to provide velocity-field estimations from wall measurements in turbulent channels [2]. The results reveal that instantaneous information on the wall governs the success of the estimation in the vicinity of the wall. Furthermore, understanding these coherent structures and the driving mechanisms behind them has become of utmost importance to propose successful control methodologies, which is receiving significant attention from the turbulence research community in recent years [3].

The literature offers several studies of TBLs, containing synchronized measurements between velocity probes located at different wall-normal distances[4], or between velocity and wall probes [5]. Although the one-dimensional measurements in these studies have substantially improved the knowledge of turbulence, there is a lack of experimental investigations where non-intrusive synchronized measurements of flow and wall fields are acquired. More recently, the advent of powerful deep-learning techniques has been exploited for the same purpose [6]. However, these studies have been carried out with numerical databases, so experimental studies are necessary to demonstrate the applicability of these methods in engineering applications. This work therefore, presents synchronized wall and flow field measurements in a turbulent boundary layer.

## METHODOLOGY AND RESULTS

The experiments are carried out in the water tunnel facility of the Aerospace Engineering research group at UC3M. The water tunnel has a test section of 2.5m length and a square $0.5 \times 0.5m^2$ cross-plane with full optical access. The water tunnel speed ranges from 0.1 to 2 m/s, showing a free-stream turbulence intensity below 1%. For the present experiments, the free-stream velocity, $U_\infty$, is estimated to be approximately $0.6m/s$ from TBL characterization performed using wall normal planar particle image velocimetry (PIV). A zero-pressure-gradient TBL is developed over a vertically-mounted flat plate installed in the test section, spanning its entire length and induced by a zigzag tripping wire. A schematic of the experimental setup is shown in figure 1.

For the heat transfer measurements, a heated-thin-foil sensor has been designed, manufactured, and mounted on the flat plate nearly where $\delta_{99} \approx 31mm$. At the measurement location, the TBL is characterized by a friction-based Reynolds number of 900. The schematic of this sensor is shown in figure 2. This sensor is covered by a thin constantan foil of $28\mu m$ thickness, which is heated by direct current distributed uniformly across the foil using embedded indium wires on both sides. The wall temperature is assumed to be constant through the foil thickness and the heat transfer on the back side of the foil is considered as negligible. The foil thickness is verified since the Biot number $Bi = h\delta/k_{foil}$ is much smaller than unity and the modified Fourier number $Fo = k_{foil}/(\rho c \pi f \delta^2)$ is much greater than one, i.e. the characteristic period of the observed phenomenon is much greater than the characteristic time of heat diffusion through the foil.

The Infrared (IR) snapshots are acquired from the backside of the sensor through a custom-designed flush-mounted periscope. This periscope contains two mirrors at each end, located at an angle of 45°, through which we are able to observe and record the temperature fluctuations on the wall using an IR camera. The image resolution is $1.1pixel/mm$, and the frame rate of the IR camera is 200 Hz. The instantaneous distribution of the convective heat transfer coefficient ($h$) is estimated from the energy balance model through the foil:

$$h = \frac{\dot{q}_{in} - \dot{q}_{cd} - \dot{q}_{rd} - B}{T_W - T_0}, \tag{1}$$

where $\dot{q}_{in}, \dot{q}_{cd}$, and $\dot{q}_{rd}$ are indications of the input, conduction, and radiation heat fluxes respectively. $B$ is referred to the unsteady term and $T_W$ and $T_0$ are wall and bulk temperature. Data are presented in terms of Nusselt number $Nu = hl/k$ where the characteristic length is the TBL thickness, and $k$ is the thermal conductivity of water. In order to properly capture the convective heat-transfer coefficient fluctuations, the measurement accuracy of the small temperature fluctuations involved in the problem needs to be improved beyond the limit of the IR camera. The optimal POD-based filter developed by [7] is used to remove random noise fluctuations.

On the other hand, the flow velocity field is measured using a Tomographic PIV system. The synchronized TomoPIV system contains three vertically-mounted high-speed cameras, mounted with an angular offset of 45°. The 3D snapshots span $y^+ \approx 100 - 200$ (located in the logarithmic region of TBL) with the resolution of $27pixel/mm$. The wall unit is estimated through the characterization of the TBL where $u_\tau = 0.028m/s$. A combination of optical lenses has been used in order to obtain a laser sheet thickness of almost 3mm. A dataset of 2000 images is captured with a frequency of 10 Hz and pre-processed to remove the background due to the strong reflections using the eigenbackground removal procedure. Velocity fields are evaluated using a custom-made PIV software developed at the University of Naples Federico II with final interrogation windows of $48 \times 48 \times$ voxels with 75% overlap.

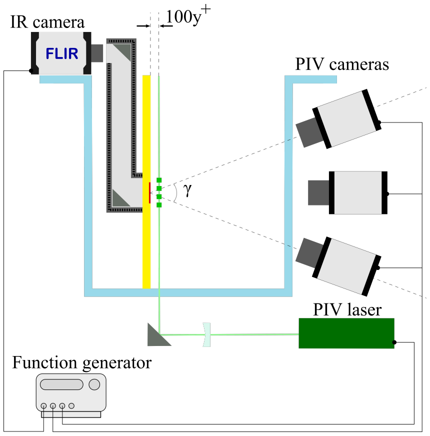

Figure 1: The experimental setup showed in lateral view. The flat plate is indicated in yellow, the TomoPIV and IR measurement planes in green and red, respectively.

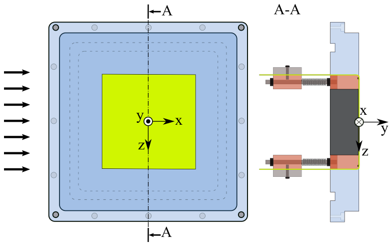

Figure 2: The schematic of the designed heated-thin-foil sensor with a lateral cross section view. The origin of the coordinate system is located at the middle of the foil.

Finally, the IR and PIV camera shutters and the emission of a double-pulse laser are synchronized using a function generator to acquire the two fields simultaneously.

Preliminary results are presented in figure 3 where correlation map for the velocity fields at $y^+ \approx 100$ and a Nusselt probe located at the wall is shown. A dimensionality analysis using Proper Orthogonal Decomposition (POD) is also performed to show the correlated dominant modes of the two fields (figure 4).

## CONCLUSIONS

This work presents an innovative experimental setup for acquiring synchronized measurements of wall and flow fields in a TBL. Synchronized wall-parallel velocity fields and convective heat transfer fields at the wall are acquired and analysed. The time-resolved heat transfer measurements resulted to capture instantaneous temperature fluctuations at the wall that depicts the footprint of the flow structures. The correlation between the streamwise velocity component at $y^+ \approx 100$ and a Nusselt fluctuation probe at the wall (figure 3) shows a region of high correlation downstream of the probe. In the spanwise direction the correlation decays monotonously. This result is compatible with the result of the two-point correlations and so supports the correctness of the experiments. We foresee to exploit synchronized measurements to identify the flow structures showing highest correlation with the convective heat flux distribution.

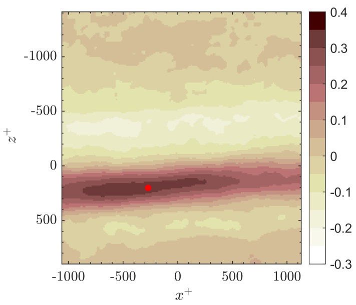

Figure 3: Correlation map between velocity field and Nusselt probe at the wall.

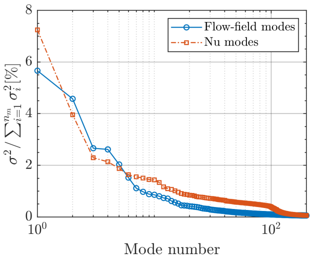

Figure 4: Relative weight of the POD modes for both Nusselt number distribution and flow field.

## REFERENCES

[1] Lozano-Durán, A & Jiménez, J (2014) "Time-resolved evolution of coherent structures in turbulent channels: characterization of eddies and cascades". J. Fluid Mech., **759**, 432—471.

[2] Encinar, M P & Jiménez, J (2019) "Logarithmic-layer turbulence: A view from the wall", Phys. Rev. Fluids, **4**, 114603.

[3] Jiménez, J (2018) "Coherent structures in wall-bounded turbulence", J. Fluid Mech., **842**, P1.

[4] Mathis, R & Hutchins, N & Marusic, I (2009) "Large-scale amplitude modulation of the small-scale structures in turbulent boundary layers", J. Fluid Mech., **628**, 311–337.

[5] Hutchins, N & Monty, J & Ganapathisubramani, B & NG, H & Marusic, I (2011) "Logarithmic-layer turbulence: A view from the wall", J. Fluid Mech., **673**, 255–285.

[6] Güemes, A & Discetti, S & Ianiro, A & Sirmacek, B & Azizpour, H & Vinuesa, R (2021) "Logarithmic-layer turbulence: A view from the wall", Phys. Fluids, **33**.

[7] Raiola, M & Greco, C & Contino, M & Discetti, S & Ianiro, A (2017) "Towards enabling time-resolved measurements of turbulent convective heat transfer maps with IR thermography and a heated thin foil", J. Heat and Mass Transfer", **108**, 199-209.

## ACKNOWLEDGEMENT

This work has been supported by the COTURB project, funded by the European Research Council (ERC), under grant $ERC - 2014.AdG - 669505$.

**Joint ERCOFTAC/EU-CTFF**
**European Drag Reduction and Flow Control Meeting – EDRFCM 2022**
**September 6$^{\text{th}}$–9$^{\text{th}}$, 2022, Paris, France**

# PLASMA FLOW CONTROL OF THE TIP VORTICES OVER A VERY LOW ASPECT-RATIO WING

**Lei Dong, Kwing-So Choi and Yaxing Wang**
Faculty of Engineering, University of Nottingham, NG7 2RD Nottingham, UK

## INTRODUCTION

The aerodynamics of a low aspect ratio (AR) wing is fundamentally different from a two-dimensional (2D) aerofoil. It has been demonstrated that low AR wings are dominated by a leading-edge vortex (LEV) with a pair of tip vortices (TVs) [1, 2]. Here, the formation of the TVs is attributed to the pressure difference between the pressure and suction sides of the wing. In other words, the flow near the wing tip is pulled outboard and moves towards the suction side of the wing, forming the streamwise vortices known as the TVs. The existence of the TVs influences the behaviour of the leading-edge flow [3, 4], promoting the formation of the recirculation area near the leading edge of the wing. Besides, the interaction of these vortices influences the flow field over the wing body, creating a three-dimensional (3D), complex wake region [5]. The existence of the TVs over a low AR wing leads to a significantly different lift curve as compared to that of the 2D aerofoil. It is also shown that the maximum lift angle of the wing is further increased with a reduction in the AR [5, 6]. For low AR wings, the total lift on the wing is a combination of the spanwise circulation of the LEV through the Kutta-Joukowski theorem and the pressure force of the TVs (i.e., the vortex lift). The development of the LEV, however, is influenced by the TVs through velocity induction due to the Biot-Savart law [4, 7]. The interaction between the LEV and the TVs was studied by Dong *et al.* [4] who demonstrated that the reattachment of the leading-edge flow and the subsequent formation of the LEV were strongly influenced by the TVs.

Previously, we have studied the interaction between the TVs and the LEV over a stationary and pitching very low AR = 0.277 plate wing, where the influence of the TVs on the development of the LEV was demonstrated [4]. Building on the understanding of the vortex interactions gained from these studies, a flow control study of a very low AR wing was carried out using the blowing and suction DBD plasma actuators. By controlling the TVs using the plasma jet at the wing tip, we were able to influence the aerodynamic forces of the wing. The influence of the plasma actuators on the TVs was analysed.

## RESULTS AND DISCUSSIONS

The results for lift and drag coefficients with blowing and suction plasma actuators are compared with those of the baseline (plasma off) as shown in Fig. 1a. This clearly shows that the aerodynamic forces are modified by the plasma actuators, where $C_L$ is significantly increased by the blowing plasma actuator, but is reduced by the suction plasma actuator between $\alpha = 4°$ and $\alpha = 20°$. Compared to the lift coefficient, the change of the drag coefficient is relatively small with the plasma actuator, which is less than 10% for all cases. The percentage changes in $C_L$ and $C_D$ due to the plasma actuators are shown in Fig. 1b, where the plasma data are indicated by $C_{Lp}$ and $C_{Dp}$, while the baseline data are given by $C_{L0}$ and $C_{D0}$, respectively. The most effective control is

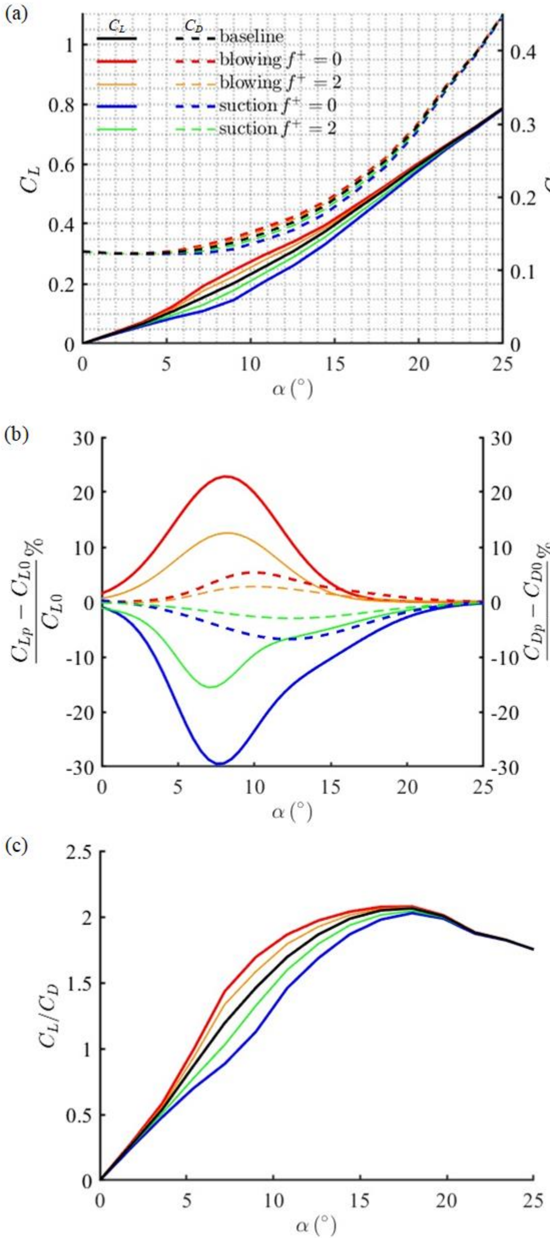

Figure 1: Effect of the plasma actuators on the aerodynamic forces on a very low AR wing: (a) $C_L$ and $C_D$, (b) the increment or decrement of $C_L$ and $C_D$, (c) lift-to-drag ratio.

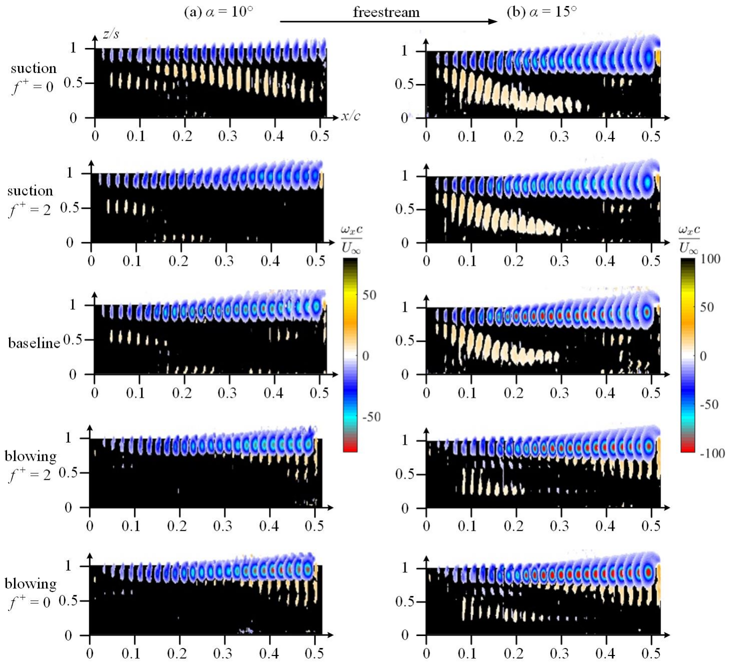

Figure 2: Side view of the time-averaged, normalised streamwise vorticity ($\omega_x c/U_\infty$) under the influence of the plasma actuators at $\alpha = 10°$ and $15°$ compared with that of the baseline case.

found at $f^+ = 0$ (steady mode) for both types of plasma actuators. Here, the maximum reduction in $C_{L0}$ can reach 30% by the suction plasma, while the blowing plasma actuator produces an enhancement of $C_{L0}$ by 23%. With a pulsed mode of plasma actuation, the control effect is reduced, where only 16% reduction and 13% enhancement in the lift coefficient are achieved by the suction and blowing plasma at $f^+ = 2$, respectively. This is due to that the plasma momentum coefficient of the steady mode of actuation is about twice that of the pulsed mode of plasma actuation which is operating at 50% of the duty cycle. It is also observed that the most effective control of the plasma on the $C_L$ occurs at around $\alpha = 8°$ for all cases. With a further increase in the AoA, the influence of the plasma actuators gradually vanishes. Fig. 1c shows the lift-to-drag ratio of the very low AR wing, which takes the maximum value of $C_L/C_D = 2$ at $\alpha = 18°$. The changes in $C_L/C_D$ as shown in Fig. 1c indicate that the aerodynamic efficiency of the wing can be manipulated by controlling the TV using the plasma actuator.

The effect of the plasma actuators on the time-averaged, normalised streamwise vorticity ($\omega_x c/U_\infty$) is shown in Fig. 2, where $\omega_x$ is the streamwise vorticity, $c$ is the chord length of the wing and $U_\infty$is the free-stream velocity. This figure consists of the slices of separate PIV measurements in the $y$-$z$ planes. Here, the separated flow at the wing tip wraps around from the pressure side to the suction side of the wing, forming a conical-shaped TV stretching along the wing chord. The size and strength of the TV increase downstream with an increase in the AoA. However, there is no sign of the TV breakdown in this figure at least for $0 < x/c < 0.52$ at $\alpha \leq 15°$. A weak, positive vorticity distribution near the leading edge ($x/c < 0.2$) is resulted from the interaction of the TV with the LEV [4, 8]. Applying the plasma actuators, the streamwise vorticity within the TV core becomes weaker with the suction control and stronger with the blowing control. The diameter of the TV remains unchanged by the plasma control, except for suction plasma control ($f^+ = 0$) at $\alpha = 10°$ where a reduction of the TV diameter is clearly seen.

## REFERENCES

[1] A. E. Winkelman and J. B. Barlow. Flowfield model for a rectangular planform wing beyond stall. *AIAA J.*, 18(8):1006–1008, 1980.

[2] P. Freymuth. Three-dimensional vortex systems of finite wings. *J. Aircr.*, 25(10):971–972, 1988.

[3] A. C. DeVoria and K. Mohseni. On the mechanism of high-incidence lift generation for steadily translating low-aspect-ratio wings. *J. Fluid Mech.*, 813:110–126, 2017.

[4] L. Dong, K-S. Choi, and X. R. Mao. Interplay of the leading-edge vortex and the tip vortex of a low-aspect-ratio thin wing. *Exp. Fluids*, 61(9):1–15, 2020.

[5] K. Taira and T. Colonius. Three-dimensional flows around low-aspect-ratio flat-plate wings at low reynolds numbers. *J. Fluid Mech.*, 623:187–207, 2009.

[6] G. E. Torres and T. J. Mueller. Low aspect ratio aerodynamics at low reynolds numbers. *AIAA J.*, 42(5):865–873, 2004.

[7] R. R. Harbig, J. Sheridan, and M. C. Thompson. Reynolds number and aspect ratio effects on the leading-edge vortex for rotating insect wing planforms. *J. Fluid Mech.*, 717:166–192, 2013.

[8] T. O. Yilmaz and D. Rockwell. Flow structure on finite-span wings due to pitch-up motion. *J. Fluid Mech.*, 691:518–545, 2012.

**Joint ERCOFTAC/EU-CTFF**
**European Drag Reduction and Flow Control Meeting – EDRFCM 2022**
**September 6$^{\text{th}}$–9$^{\text{th}}$, 2022, Paris, France**

# ELECTROHYDRODYNAMIC FORCE MODELLING AND APPLICATION TO FLOW CONTROL

**F. Rogier, G. Dufour**
ONERA-Centre de Toulouse-FRANCE

**K. Kourtzanidis**
ONERA-Centre de Toulouse-FRANCE and CERTH -
and Centre for Research and Technology-Hellas, Thessaloniki, GREECE

## INTRODUCTION

This presentation report on the work accomplished during the CTFF project by ONERA. Control of the friction force can be obtained by the use of Surface Dielectric Barrier Discharge (SDBD) located at judicious positions of the airfoil. The understanding of the discharge is crucial if one want to maximise the effects of the actuators. It is a well known fact that the ElectroHydroDynamic body force $\vec{F_{EHD}}$ is responsible of the plasma effect (the so called ionic wind), indeed it has been demonstrated by simulation [1] and modelling

which describe the physics of the discharge from scratch.

This talk aims to show the ability of these models to describe finely phenomena observed in experiment by numerical simulation. It is well known that plasma is a multiscale medium which render simulations very expensive. The high computational cost is related to the various scale of the plasma discharge such that Debye length, ionisation, electron and heavy transport spatial lengths and also time scales that change from pico-seconds to milli-seconds. A full simulation of a DBD requires a refined and largemesh along with a tremendous number of timesteps for realistic applications. So, an effort on the development of efficient numerical methods and their application on parallel HPC machines has been realized. This presentation will discuss, numerical modelling, algorithms and present numerical simulation of SDBDs and their effect on the flow. Thanks to CTFF project, a collaboration with Nothingham University has been achieved and fruitful results have been obtained. We refer to publications which complete the results describing the work achieved.

## THE PLASMA MODELLING

The in house code COPAIER, [3] solve the cold plasma equations (under the drift-diffusion approximation) and provides the EHD force profiles that can be introduced as input in various CFD solvers (CEDRE, OPENFOAM,..).
The plasma model use a fluid description for each species of the plasma mixture : electrons, ions, neutrals etc. :

$$\frac{\partial n_\alpha}{\partial t} + \boldsymbol{\nabla} \cdot n_\alpha \boldsymbol{U}_\alpha = S_\alpha \tag{1}$$

$$\boldsymbol{U}_\alpha = q_\alpha \mu_\alpha \boldsymbol{E} - D_\alpha \frac{\nabla n_\alpha}{n_\alpha} \tag{2}$$

where $\boldsymbol{E}$ is the electric field,

$$\boldsymbol{\nabla} \cdot (\varepsilon \boldsymbol{E}) = \sum_i n_i q_i, \tag{3}$$

$D_\alpha, \mu_\alpha$ the transport of coefficient and $S_\alpha$ the production/cancellation term describing the chemical process. The transport, kinetic coefficient depend of the local electronic temperature where $\varepsilon$ is the material permittivity, $q_\alpha$ is the charge of the $\alpha$-th species. Finally the EHD force is given by :

$$\boldsymbol{F_{EHD}} = \sum_i n_i q_i \boldsymbol{E} \tag{4}$$

As the ionization rate is low (about $10^{-4} - 10^{-6}$, the plasma is supposed to be not influenced by the flow. So the induced flow is solved separately from the plasma, and the induced flow solve the incompressible Navier-Stokes equations with $\boldsymbol{F_{EHD}}$ as RHS.

$$\frac{\partial \boldsymbol{u}}{\partial t} = -(\boldsymbol{u} \cdot \boldsymbol{\nabla})\boldsymbol{u} + \nu \boldsymbol{\nabla}^2 \boldsymbol{u} + \boldsymbol{F_{EHD}} \tag{5}$$

.

## NUMERICAL SCHEMES AND CODE

COPAIER is a 2D/2Daxi, code fully parallelized and working on massively parallel machines.
Structured as well as unstructured meshes are used to mesh the computational domain. Second-order finite volume explicit schemes solve the drift-diffusion **??** and **??**. The use of explicit schemes allow to capture all the scale of the plasma, even if the cost of each simulation is very high. Sub-cycling allow to solve separately electron from heavy particles ad allow to gain significant speed up without lost of precision. We use a 4-species fluid model to describe the plasma mixture, which has been proved a sufficient (although quite simplified) approximation for a $N_2/O_2$ mixture under atmospheric conditions.

## SIMULATIONS AND RESULTS

COPAIER has been used to perform DBD simulations. Illustration of these simulations and corresponding development of the solver are given here and they have been published in [5], [4] and [2]. Figure 2 shows the simulation results for a typical $SDBD$ configuration 1. The voltage is $20KV$, exposed electrode thickness is set to 70 and the dielectric thickness is $3mm$. The AC frequency used in the simulations is increased compared to the typical experimental results (100 kHz instead of 1 kHz) in order to reduce the CPU time and obtain qualitative results. Fig. 3, shows the conduction current during the 3rd period of the AC actuation. A single streamer during the positive phase and four microdischarges of reduced current during the negative phase are clearly visible, in good agreement with experimental findings. Figure 2 shows the total

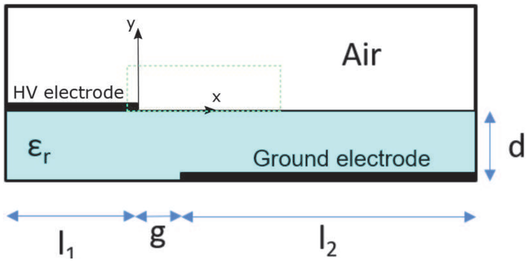

Figure 1: The AC-DBD actuators

EHD force averaged on one AC period. The EHD force occupies a volume of approx. 4–5 mm in x-direction (Fx ) and 1.5–2 mm in y-direction (Fy ).

## CITATIONS

*

References

[1] J. P. Boeuf and L. C. Pitchford. Electrohydrodynamic force and aerodynamic flow acceleration in surface dielectric barrier discharge. *Journal of Applied Physics*, 97(10), 2005.

[2] Huw Borradaile, Konstantinos Kourtzanidis, Francois Rogier, Kwing-So Choi, and Xuerui Mao. Flow reversal in millimetric annular dbd plasma actuator. *Journal of Physics D: Applied Physics*, 54(34):345202, 2021.

[3] G Dufour and F Rogier. Numerical modeling of dielectric barrier discharge based plasma actuators for flow control: the copaier/cedre example. *Aerospace Lab*, (10), 2015.

[4] K Kourtzanidis, G Dufour, and F Rogier. The electrohydrodynamic force distribution in surface AC dielectric barrier discharge actuators: do streamers dictate the ionic wind profiles? *Journal of Physics D: Applied Physics*, 54(26):26LT01, apr 2021.

[5] Konstantinos Kourtzanidis, Guillaume Dufour, and François Rogier. Self-consistent modeling of a surface ac dielectric barrier discharge actuator: in-depth analysis of positive and negative phases. *Journal of Physics D: Applied Physics*, 54(4):045203, 2020.

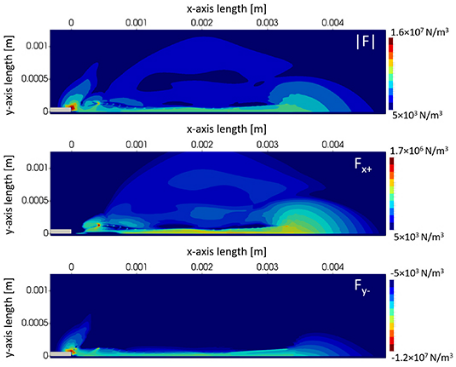

Figure 2: Isovalues of the EHD force modules , X-component and -y component, extracted from [4]

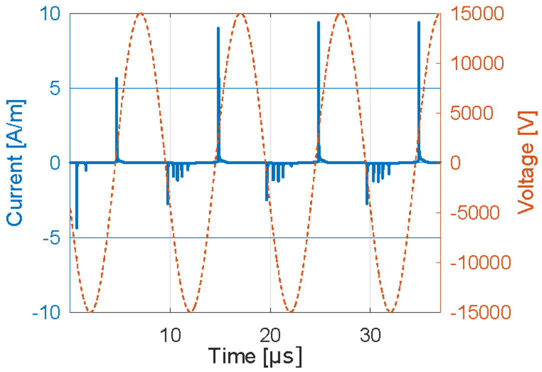

Figure 3: Current in 3rd period vs Time

**Joint ERCOFTAC/EU-CTFF**
**European Drag Reduction and Flow Control Meeting – EDRFCM 2022**
**September 6th –9th, 2022, Paris, France**

# TWO-SCALE COUPLING FOR WALL-BOUNDED TURBULENCE OVER 'REGULAR ROUGHNESS'

**L. He**

Department of Engineering Science, University of Oxford, OX2 0ES, Oxford, UK

## BACKGROUD & MOTIVATION

Fluid flow and convective heat transfer for micro-structured surfaces are of relevance to applications. Comprehensive understanding of how roughness affects aerothermal behaviour of wall bounded turbulence is still lacking, particularly for relatively large roughness scales. The motivation in resolving, rather than modelling, surface micro-structures is further heightened by the development of additive manufacturing (AM). AM-made components tend to exhibit surface finishes which deviate significantly from stochastic roughness, pointing the need for new predictive tools. The major challenges of such development arise from the huge scale disparities, in space (micro elements vs. main flow path), and in time (fluid vs solid). Given the complexity, it is of interest to develop a scale-resolving turbulent flow (LES) and solid domain coupled (conjugate heat transfer) method for a micro-structured surface (e.g. Fig.1)

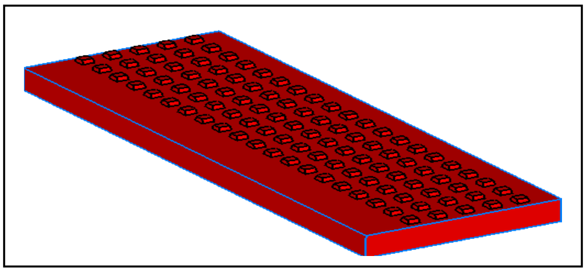

*Figure 1: Solid domain with micro-structured top wall*

## SPACE AND TIME TWO-SCALE SOLUTIONS

Firstly, the spatial scale disparity may be addressed by harnessing the scale-dependent solvability: high local resolution required for the micro-flow field around each micro-structure, but a much smoother variation on a macro-scale (in time averaged in particular) from one micro-structure to another. The consideration leads to a two-scale framework coupling a local fine-mesh solution for a small sub-set micro-elements with a global coarse-mesh solution, by upscaling the space-time averaged equations driven by source terms propagated by Block-spectral mapping, He, 2018 [1]. Examples of a full solution with refined meshes for the entire near-wall regions of all micro-structures (Fig.2a) can be compared with the two-scale solution with only a sub set of near wall blocks refined (Fig.2b). The validity of the two-scale method is also underpinned for a systematic examination of canonical channel flows, indicating a significant potential gain in the mesh count - Reynolds number scaling from $O(Re^2)$ for the wall-resolved LES to $O(Re^1)$ for the present two-scale method, Chen and He, 2022 [2].

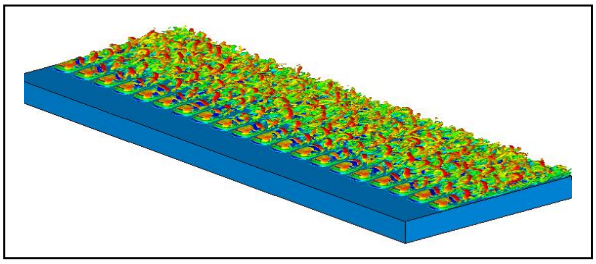

(a) Full Solution (fine-mesh for 100 micro-structures)

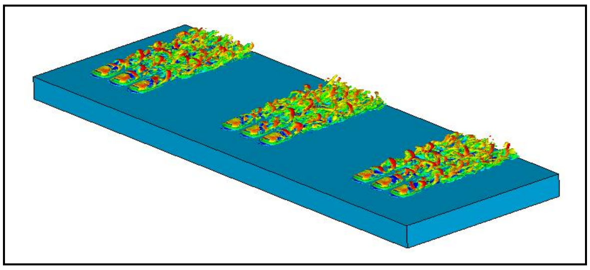

(b) Two-scale (fine-mesh for 45 micro-structures)

*Figure 2: Instantaneous near-wall flows (Q criterion)*

The two-scale method has been recently extended to a solid domain conduction solution (Fig.3).

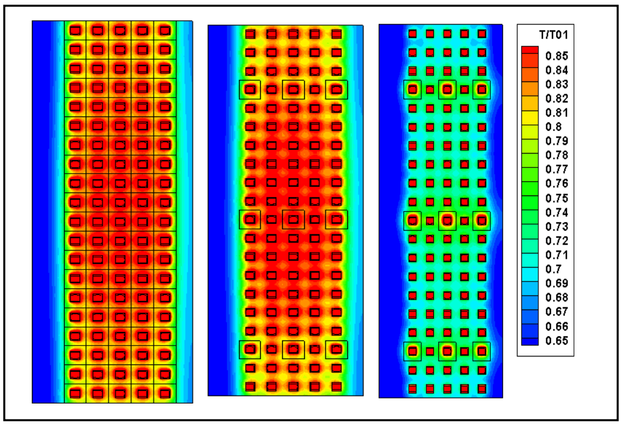

(a) Full solution, (b) Two-scale, (c) One-scale (no coupling)

*Figure 3: Surface temperatures (solid conduction solutions)*

Secondly, the temporal scale disparity manifests most acutely in the fluid-solid interface treatment for a coupled conjugate heat transfer (CHT) solution. The overall approach pursued in the present work is to decompose a full unsteady variable into the time-mean and unsteady fluctuation parts, and to treat these two parts differently according to their distinctive characteristics and scales respectively. The time-mean part can be easily treated in the same way as for a steady CHT. The unsteady part is solved in frequency domain, as firstly demonstrated for a solid-domain harmonic solution periodic unsteadiness by He and Oldfield, 2011 [3]. By retaining a large enough number of frequency harmonics for each mesh cell, their corresponding spatial modes should be captured in LES solution of the near wall flow field. A moving average based interface treatment for the two temporal scales provides these desired attributes as recent tested for LES based CHT for a smooth surface, He 2019 [4].

Sample results of time-mean surface temperatures by the present coupled LES-CHT method are shown in Fig.4. For all three cases, the local refinement in the near wall region is made by embedding each coarse-mesh cell with 5x5x5 fine-mesh cells (i.e. a coarse-fine mesh density ratio ~O($10^2$) ). In the direct solution (Fig.4a), the mesh refinement is made in near wall fluid and solid domain for all 100 micro-structures. In the two-scale solution (Fig.4b), the global coarse mesh solution is coupled with the fluid domain locally embedded with fine mesh blocks for 45 micro-structures, and the solid domain locally embedded around 9 micro-structures. The one-scale solution (Fig.4c) uses the same coarse and fine meshes, but the two-domains are simply solved without the coupling through the source terms. We can see that the coarse-mesh solution is clearly poorly resolved in comparison with the full solution with the near wall refinement. The two-scale solution on the other hand agrees well with the full direct solution. Therefore the present method offers good accuracy, as well as significant potential computational cost benefit.

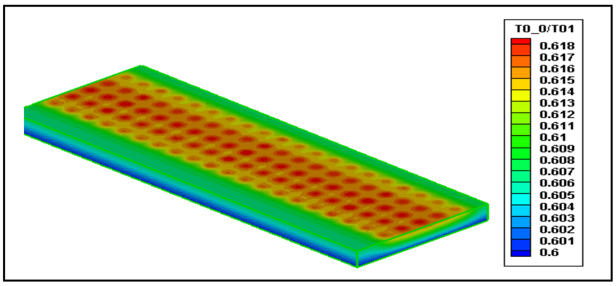

(a) Direct Solution (fine-mesh for all micro-structures)

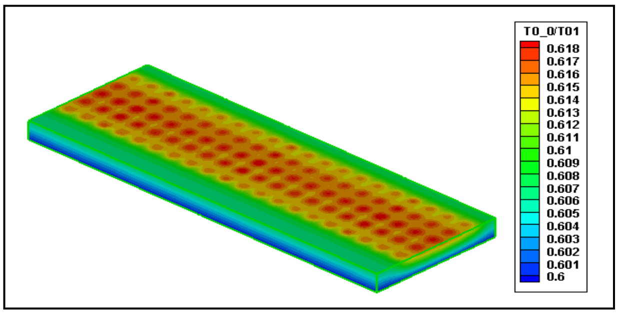

(b) Two-scale Solution
(fine-mesh blocks for 45 micro-structures in fluid domain)
(fine-mesh blocks for 9 micro-structures in solid domain)

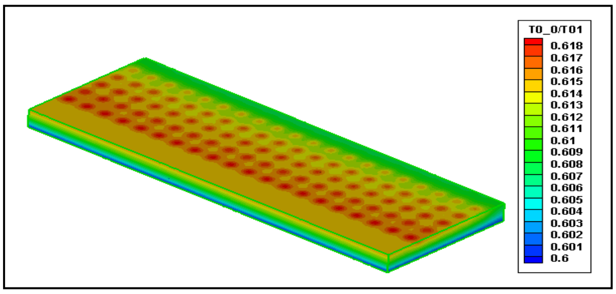

(c) One-scale Solution (base coarse-mesh)

*Figure 4: Solid temperatures (conjugate heat transfer solutions).*

## REFERENCES

[1] L. He. Multiscale block spectral solution for unsteady flows. International Journal for Numerical Methods in Fluids, Vol.86, Issue 10, pp655–678, Nov, 2017.

[2] C. Chen, and L. He. On locally embedded two-scale solution for wall-bounded turbulent flows. Journal of Fluid Mechanics, Vol.933, A47, 2022.

[3] L. He, and M.L.G. Oldfield. Unsteady conjugate heat transfer modelling. Journal of Turbomachinery, Vo1.133, No.3, 2011.

[4] L. He,. Closely coupled fluid-solid interface method with moving-average for LES based conjugate heat transfer solution. International Journal of Heat and Fluid Flow, Vol.79, 108440, 2019.

**Joint ERCOFTAC/EU-CTFF**
**European Drag Reduction and Flow Control Meeting – EDRFCM 2022**
**September 6–9, 2022, Paris, France**

# PREDICTION OF WALL-BOUNDED TURBULENCE IN A VISCOELASTIC CHANNEL FLOW USING CONVOLUTIONAL NEURAL NETWORKS

**Arivazhagan Geetha Balasubramanian**
Engineering Mechanics, KTH Royal Institute of Technology, SE-100 44 Stockholm, Sweden

**Ricardo Vinuesa**
Engineering Mechanics, KTH Royal Institute of Technology, SE-100 44 Stockholm, Sweden

**Outi Tammisola**
Engineering Mechanics, KTH Royal Institute of Technology, SE-100 44 Stockholm, Sweden

## INTRODUCTION

Turbulent flow of purely viscoelastic fluids has gained attention in the drag-reduction and flow control communities, since a tiny amount of polymer (parts per million) has proven efficient in reducing friction drag in pipe flows [9]. Drag reduction by polymers (elasticity) is related to their ability to modify coherent structures in wall-bounded turbulence [1],[2]. Elasticity influences the turbulent cycle in two ways: by attenuating near-wall vortices, but at the same time increasing the streamwise kinetic energy of the near-wall streaks. The effect of polymers are considered to be local and triggered by energetic structures and are as intermittent as the near-wall vortices [3]. The numerical studies by [7] indicated that the viscoelastic flow is dominated by long streaks disrupted by rapid and localised perturbations whereas the Newtonian flow, on the other hand, displays short streaks and a more chaotic dynamics. When it comes to practical flows of interest, numerical simulations becomes challenging due to the associated computational cost in capturing the multiple physical mechanisms that drive the flow. On the other hand, experimental investigations of drag reduction in viscoelastic flows are limited by the near-wall measurements and the capability of the experimental techniques to accurately quantify the flow, without disturbing it. A complete description of viscoelastic turbulence would require characterization of both velocity and polymeric stresses. However, the polymer deformation cannot be accessed directly from the experiments.

Recently, neural network models have shown excellent results in predicting the instantaneous state of the flow using quantities measured at the wall [4]. Hence, in the objective of the present study, the idea of non-intrusive sensing has been applied to viscoelastic channel flow to predict the velocity fluctuations and polymeric stress components near the wall using the quantities measured at the wall. To this aim, the convolutional neural network (CNN) models trained on direct-numerical-simulation (DNS) data are employed to predict the two-dimensional velocity fluctuation and polymeric stress fluctuation fields at different wall-normal distances in a viscoelastic channel flow. The present work would highlight the capability of a data-driven approach to model turbulence in complex fluid flows. In addition to this, the developed non-intrusive sensing models will also find useful applications in experimental settings and in closed-loop control of wall-bounded turbulence in viscoelastic flows.

## DATASET

The dataset for training and evaluation of the network model is obtained through a direct-numerical-simulation of turbulent channel flow of viscoelastic fluid at a Reynolds number based on the bulk velocity, i.e. $Re = U_b h/\nu = 2800$ (where the bulk velocity $U_b$ corresponds to the average value of the mean velocity in the whole domain, $h$ is the channel height and $\nu (= \mu_0/\rho)$ denotes the kinematic viscosity of the fluid, with $\rho$ and $\mu_0$ being the density and total viscosity of the fluid). The bulk Reynolds number corresponds to a friction Reynolds number $Re_\tau = 180$ (where $Re_\tau$ is defined in terms of the channel half-width and friction velocity $u_\tau$) for a Newtonian fluid. In this study, the turbulent channel flow simulations are performed at a Weissenberg number $Wi = 8$, (where $Wi$ quantifies the elastic forces to viscous forces). A complete description of the numerical simulation can be found in [5].

A database consisting of instantaneous fields of wall-shear-stress components, wall-pressure, two-dimensional velocity-fluctuation and polymeric-stress-fluctuation fields at various wall-normal locations, $y^+ = 15, 30$ and 50 (where the superscript '+' denotes scaling in terms of friction velocity $u_\tau$ and the viscous length $\ell^* = \nu/u_\tau$) is obtained. The corresponding wall-parallel fields are sampled with a constant sampling period of $\Delta t_s^+ \approx 1$. A total of 17,058 samples is obtained for training the network model, which is split into training and validation set with a ratio of 4 to 1. The networks are evaluated with the samples in the test dataset which consists of 3,400 samples.

## NEURAL-NETWORK MODEL

We utilize a specific type of neural network, the convolutional neural network in this work because of its success in computer vision [8]. The CNN consists of convolutional layers that are defined in terms of kernels (or filters) which convolves with the inputs and produces a transformed output. The learnable parameters are contained in the kernels and the transformed output is called the feature map which contains certain features extracted from the input image. Multiple feature maps are stacked and followed by an activation function to obtain a non-linear transformation. The activated feature maps are sequentially fed into the successive convolutional layers as input, which helps in combining extracted features to predict larger and more complex features with a deeper CNN.

In this work, a fully convolutional neural network (FCN) similar to the one proposed by [4] is used and a deeper FCN is

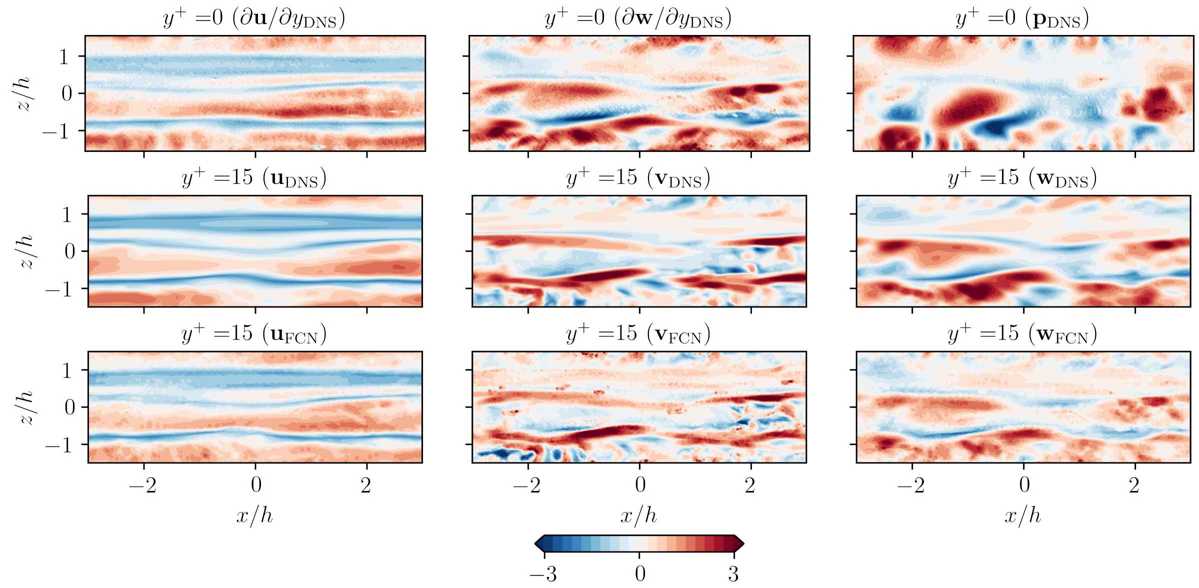

Figure 1: (Top row) Wall inputs to the FCN model: (left column) streamwise shear, (middle column) spanwise shear and (right column) wall-pressure. (Middle row) reference DNS and (bottom row) FCN predictions of (left column) streamwise, (middle column) wall-normal and (right column) spanwise velocity fluctuations at $y^+ = 15$. The fields are scaled with the corresponding RMS values.

also investigated. The inputs to the FCN are normalized with the mean and standard deviation computed on the training samples. The velocity-fluctuation fields are scaled with the ratio of corresponding root-mean-squared (RMS) values and the streamwise RMS value as performed in [4]. In the case of prediction of polymeric-stress fluctuation fields, the data is scaled with RMS values as performed for inputs. The FCN is trained using the Adam [6] stochastic algorithm to minimize the loss function for the FCN network:

$$\mathcal{L}(\mathbf{u}_{\mathrm{FCN}}; \mathbf{u}_{\mathrm{DNS}}) = \frac{\sum_{i=1}^{N_x} \sum_{j=1}^{N_z} |\mathbf{u}_{\mathrm{FCN}}(i,j) - \mathbf{u}_{\mathrm{DNS}}(i,j)|^2}{N_x N_z}, \tag{1}$$

which is the mean-squared error (MSE) between the instantaneous DNS field ($\mathbf{u}_{\mathrm{DNS}}$) and the predictions ($\mathbf{u}_{\mathrm{FCN}}$). The predictions are evaluated from the statistical point of view, namely considering the error in RMS quantities of velocity fluctuations:

$$E_{\mathrm{RMS}}(u) = \frac{|u_{\mathrm{RMS,FCN}} - u_{\mathrm{RMS,DNS}}|}{u_{\mathrm{RMS,DNS}}}, \tag{2}$$

and the correlation coefficient between the predicted and the DNS fields:

$$R_{\mathrm{FCN;DNS}}(u) = \frac{\langle u_{\mathrm{FCN}} u_{\mathrm{DNS}} \rangle_{x,z,t}}{u_{\mathrm{RMS,FCN}} u_{\mathrm{RMS,DNS}}}, \tag{3}$$

with $\langle \cdot \rangle$ corresponding to the average in space or time, depending on the subscript.

A sample instantaneous prediction of velocity fluctuation field in a viscoelastic turbulent channel flow at $y^+ = 15$ is provided in figure 1.

## REFERENCES

[1] Yves Dubief, Vincent E Terrapon, and Julio Soria. On the mechanism of elasto-inertial turbulence. *Phys. Fluids*, 25(11):110817, 2013.

[2] Yves Dubief, Vincent E Terrapon, Christopher M White, Eric SG Shaqfeh, Parviz Moin, and Sanjiva K Lele. New answers on the interaction between polymers and vortices in turbulent flows. *Flow Turbul. Combust*, 74(4):311–329, 2005.

[3] Yves Dubief, Christopher M White, Vincent E Terrapon, Eric SG Shaqfeh, Parviz Moin, and Sanjiva K Lele. On the coherent drag-reducing and turbulence-enhancing behaviour of polymers in wall flows. *J. Fluid Mech.*, 514:271–280, 2004.

[4] Luca Guastoni, Alejandro Güemes, Andrea Ianiro, Stefano Discetti, Philipp Schlatter, Hossein Azizpour, and Ricardo Vinuesa. Convolutional-network models to predict wall-bounded turbulence from wall quantities. *J. Fluid Mech.*, 928, 2021.

[5] Daulet Izbassarov, Marco E Rosti, Luca Brandt, and Outi Tammisola. Effect of finite weissenberg number on turbulent channel flows of an elastoviscoplastic fluid. *J. Fluid Mech.*, 927, 2021.

[6] D. P. Kingma and J Ba. Adam: A method for stochastic optimization. In *3rd Int. Conf. on Learning Representations, ICLR 2015, San Diego, CA, USA, May 7-9, 2015*, 2015.

[7] S Le Clainche, Daulet Izbassarov, M Rosti, Luca Brandt, and Outi Tammisola. Coherent structures in the turbulent channel flow of an elastoviscoplastic fluid. *J. Fluid Mech.*, 888, 2020.

[8] Yann LeCun, Léon Bottou, Yoshua Bengio, and Patrick Haffner. Gradient-based learning applied to document recognition. *Proc. IEEE*, 86(11):2278–2324, 1998.

[9] PS Virk. Drag reduction in rough pipes. *J. Fluid Mech.*, 45(2):225–246, 1971.

Joint ERCOFTAC/EU-CTFF
European Drag Reduction and Flow Control Meeting – EDRFCM 2022
Sept. 6th–9th, 2022, Paris, France

# OPPOSITION CONTROL OF TURBULENT SPOTS

**Y. X. Wang, K.-S. Choi**
Faculty of Engineering, University of Nottingham, NG7 2RD, Nottingham, UK

**M. Gaster, C. Atkin**
School of Engineering, City, University of London, EC1V 0HB, London, UK

**Y. Kachanov, V. Borodulin**
Institute of Theoretical and Applied Mechanics, Novosibirsk, Russia

## INTRODUCTION

In a low turbulence environment, such as in the aircraft flight conditions, the transition mechanism and the onset of turbulence in a wall boundary layer comprises three main stages: receptivity; linear stability and non-linear development and breakdown. The boundary layer flow development under a weak broadband 3-D random excitation is regarded to be resembled to that of a naturally grown turbulent boundary layer. Recent theory and wind tunnel experiments found that when a wall boundary layer transition was caused by convective instabilities, the flow could be deterministic in the transitional region or in the early fully developed turbulence region. In other words, the instantaneous flow structures in the boundary layer can be reproduced from the same initial conditions. This *deterministic turbulence* concept was used to study the development of turbulent spots and their control [1, 2].

## METHODOLOGY

Wind tunnel experiments were carried out in a low turbulence wind tunnel to study the boundary layer flow characteristics under repeated broadband random excitations from a point source. The evolutions of boundary layer flow fields, covering the laminar, transitional and turbulent stages, were measured by a hot-wire anemometer. The measured velocity revealed well organized large-scale vortex structures. Experimental data indicated that these large turbulent spot look-like events in the later transitional region are deterministic and reproducible in the space-time positions.

Then opposition control of artificially initiated turbulent spots in a laminar boundary layer was carried out with the aim to delay transition to turbulence by modifying the turbulent structure within the turbulent spots. The timing and duration of control, which was carried out using wall-normal jets from a spanwise slot, were pre-determined based on the baseline measurements of the transitional boundary layer. The results indicated that the high-speed region of the turbulent spots was cancelled by opposition control, which was replaced by a carpet of low-speed fluid. The application of the variable-interval time-averaging (VITA) technique on the velocity fluctuation signals demonstrated a reduction in both the burst duration and intensity within the turbulent spots, but the burst frequency was increased.

## EXPERIMENTAL SET-UP

The experiments were carried out in the Gaster low turbulence wind tunnel at City, University of London. The test model is a flat plate, see Fig. 1. The wind tunnel speed was set at 18 m/s. The undisturbed baseline flow was laminar and set to be with a zero pressure gradient.

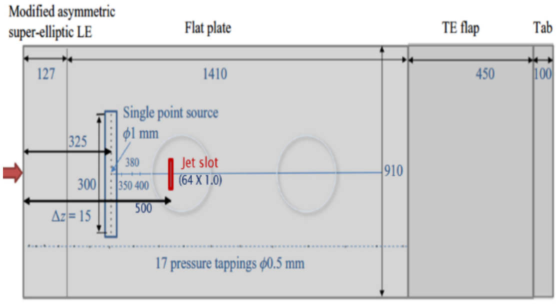

Figure 1: Schematic of the flat test plate with a miniature speaker as the single point source to generate turbulent spots, and the spanwise air-jet slot used for opposition control of the turbulent spots

A point excitation source of a miniature speaker was positioned at the central span at 325 mm from the leading edge, and half-embedded inside the back of the flat plate. A broadband noise was applied to the point source to generate turbulent spots. Opposition control of the turbulent spots was carried out by issuing a wall-normal jet from a spanwise slot, 64-mm long and 1.0 mm wide, see figure 1. Here, the spanwise length of the control slot was chosen to match the maximum spanwise size of the turbulent spots at the control location (x = 500 mm). The air jet was driven by an audio speaker with a balanced-mode radiator. The control timing and duration were pre-determined based on the baseline measurements of the turbulent spots.

## RESULTS AND DISCUSSIONS

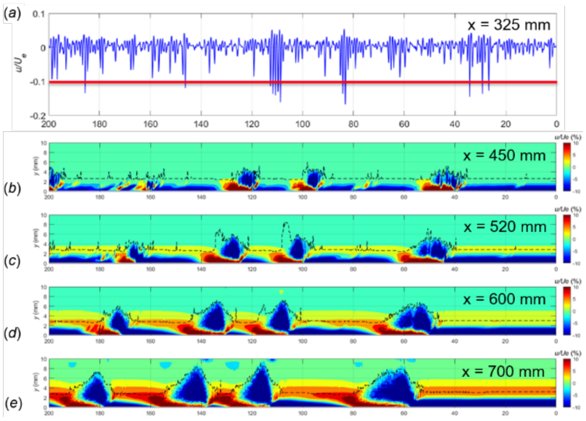

Figure 2: The velocity time series from a hot-wire probe immediately above the disturbance source (x = 325 mm) at y = 0.5 mm, z = 0 mm (a); the downstream development of the ensemble-averaged streamwise fluctuating velocity at (b) x = 450 mm, (c) x = 520 mm, (d) x = 600 mm and (e) x = 700 mm, where the dotted lines indicate the boundary layer thickness.

The downstream developments of the ensemble streamwise fluctuation velocity under a random excitation from a point source are shown in Fig. 2 in the velocity contours. The measurements were taken on the central line and covered a streamwise distance from 350mm to 700mm from the leading edge. The turbulent spots were clearly revealed in the velocity contour. These large-amplitude events consisted of the large positive fluctuation velocity in the near-wall region and the accompanying large negative fluctuation velocity away from the wall and extended to the edge of the boundary layer. The number of these events and the extension in the wall-normal distance were increased with the increasing of the downstream distance. There was an excellent repeatability in the velocity measurements due to the "deterministic turbulence" technique in a low-turbulence wind tunnel.

Figure 3 (a) and (b) show the ensemble-averaged fluctuating streamwise velocities in the center plane of the boundary layer at x = 520 mm (20 mm downstream of the control slot) without and with opposition control, respectively, where the dotted lines indicate the boundary layer thickness. They clearly demonstrate that the high-speed region of the turbulent spots near the wall surface was cancelled by the wall-normal jet during control. Figure 3 (c) and (d) are the velocity contours at x = 600 mm without and with opposition control, respectively, showing the lasting effect of opposition control of the turbulent spots 100 mm downstream of the control slot. The reduction of the high-speed region of the turbulent spots is still evident but the effectiveness of opposition control of turbulent spots seems to be reduced at this downstream location.

The perspective views of turbulent spots without and with opposition control are given in Fig. 4, where the iso-surfaces of ensemble averaged streamwise velocity fluctuations at 15% (orange) and -15% (blue) are shown. These figures confirm the results given in Fig. 3 demonstrating that the high-speed region near the trailing edge (upstream end) of the turbulent spots, as shown in orange in the figure, was destroyed by opposition control using wall-normal jets. However, the wing-shaped, low-speed region near the leading edge (downstream end) of the turbulent spots, as shown in blue, is still visible after opposition control

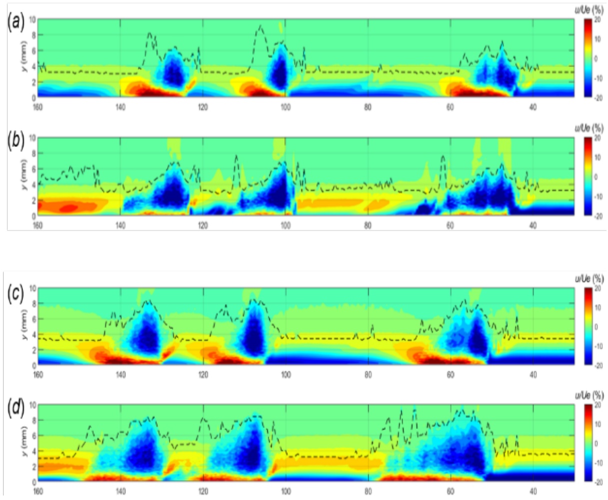

Figure 3: Effect of opposition control on the turbulent spots at x = 520 mm (a) Ensemble-averaged fluctuating velocity contour without control and (b) with control. At x = 600 mm, (c) Ensemble-averaged fluctuating velocity contour without control and (d) with control

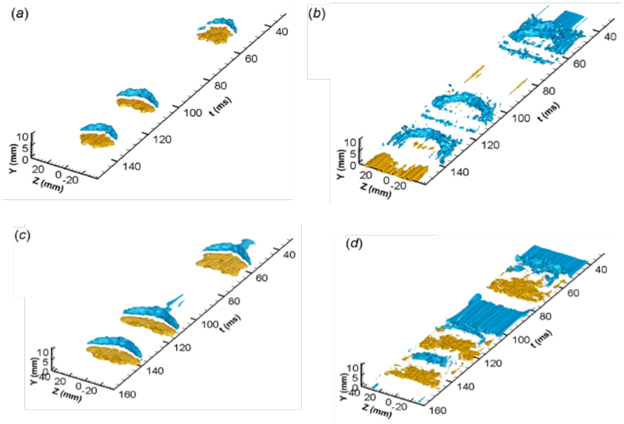

Figure 4: Perspective views of turbulent spots without (a) and with control (b) at x = 520 mm; without (c) and with control (d) at x = 600 mm, which are depicted by iso-surfaces of ensemble-averaged streamwise velocity fluctuations at 15% (orange) and −15% (blue) of the freestream velocity.

## REFERENCES

[1] Y.X. Wang, K.-S. Choi, M. Gaster, C. Atkin, V.I. Borodulin, and Y.S. Kachanov. Early development of artificially initiated turbulent spots. J. Fluid Mech. 916, A1, 2021.

[2] Y.X. Wang, K.-S. Choi, M. Gaster, C. Atkin, V.I. Borodulin, and Y.S. Kachanov. Opposition control of turbulent spots. J. Fluid Mech. 943, A3, 2022.

**Joint ERCOFTAC/EU-CTFF**
**European Drag Reduction and Flow Control Meeting – EDRFCM 2022**
**September 6$^{\text{th}}$–9$^{\text{th}}$, 2022, Paris, France**

# SPREADING DYNAMICS OF A WATER DROP ON A MICRO-TEXTURED SURFACE

**A. Kumar**
Faculty of Engineering (M3), University of Nottingham, NG72RD Nottingham, United Kingdom

**D. K. Mandal**
Department of Mechanical Engineering, IIT (ISM) Dhanbad, 826004 Dhanbad, India

**K-S. Choi**
Faculty of Engineering (M3), University of Nottingham, NG72RD Nottingham, United Kingdom

## INTRODUCTION

The problem of drop impact on solid dry substrates is important in many industrial applications, including aerospace (wing design) and coating [1], [4]. Textured solid surfaces are used to investigate the influence of surface roughness geometry on drop-surface interaction and can be used to reduce drag [6]. A liquid drop impacting a solid substrate has a maximum spreading diameter ($D_{max}$), which is a direct measure of the maximum solid-liquid contact. It is a significant parameter in interfacial fluid flow and heat transfer applications, such as icing and anti-icing of aircraft wings. $D_{max}$ is often normalized with the pre-impact diameter of the drop ($D_0$) to give the maximum spreading factor (i.e., $\beta_{max} = \mathrm{D}_{max}/D_0$). Generally, $\beta_{max}$ depends on the liquid properties, surface features, and impact parameters. Often these are grouped into dimensionless parameters such as Weber number (We=$\rho U_0{}^2 \mathrm{D}_0/\sigma$), Reynolds number (Re= $\rho U_0 D_0/\mu$), and Ohnesorge number (Oh= $We^{(1/2)}/Re$).

Recent studies found that the maximum spreading diameter on rough surfaces depends on the Weber number and the contact angle at the maximum spreading [6]. The substrate roughness is known to influence the wettability and the contact angles of the drops resting on a substrate. In the present study, we focus on understanding the role of surface micro-texturing on the maximum spreading of the drop during impact.

## EXPERIMENTAL DETAILS

The experimental setup consisted of a high-speed camera (Fastec IL5) fitted with a telecentric lens to record the impact process as an image sequence at 3000 frames per second (fps). The water drops were generated using a hypodermic needle-syringe arrangement. The outer diameter of the needle was 0.8 mm, and the diameter of the water drop ($D_0$) produced was 2.50 ± 0.1 mm. Two different solid surfaces were used as a target: a plane and a micro-textured aluminium surface. The micro-textures on the aluminium surface were created through micro-milling. Square pillars of a cross-section of 100 µm × 100 µm and a height of 30 µm were created. The distance between two consecutive pillars was 185 µm (see Figure 1).

The images of the drop impact recorded by the high-speed camera were processed in the image processing toolbox of MATLAB to obtain the instantaneous spreading diameter of the drop ($D$) with time. The properties of water at 25 °C are: density ($\rho$) = 980 $kg/m^3$, dynamic viscosity ($\mu$) = 0.89 × $10^{-3}$ PaS, and surface tension ($\sigma$) = 0.072 N/m. The details of the experimental parameter are given in Table 1.

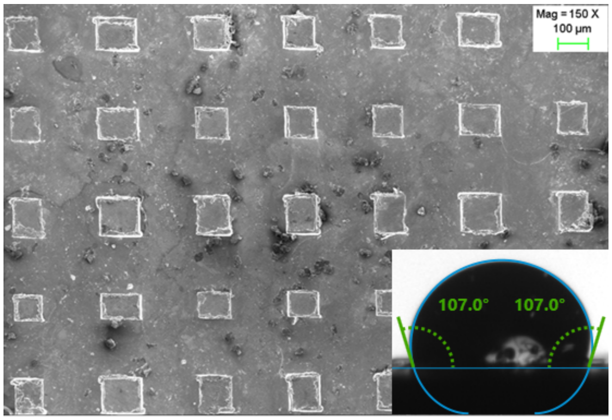

Figure 1: FESEM of the micro-textured aluminium surface and the static contact angle of the water drop (107°) obtained on it (botom-rignt corner).

| $U_0$ (m/s) | 1.04 | 1.42 | 1.73 | 2.0 |
|---|---|---|---|---|
| $We$ | 38 | 70 | 104 | 139 |
| $Re$ | 2920 | 3987 | 4865 | 5614 |
| $Oh$ | 0.0021 | 0.0021 | 0.0021 | 0.0021 |

Table 1: Details of the experimental parameters

## RESULTS AND DISCUSSION

The measurement of static contact angles ($\theta_S$) on the plane and micro-textured aluminium surfaces revealed that the plane aluminium surface was hydrophilic and the micro-textured surface was hydrophobic. For the plane surface, $\theta_S$ was observed to be 68 ± 2°, while it was found to be 107± 2°for the micro-textured surface (see Figure 1).

The spreading morphology of the water drop on the plane and textured surface for We= 70 and 139 is shown in Figure 2. Some differences can be observed in the spreading lamella on the textured surface such as rim perturbations (t= 3.67 and 4.67) and splashing (We= 139; t= 2.67 and 3.67). These observation on the textured surface (and not in the plane surface) indicate penetration of the liquid within the micro-texture pores during impact. Seo et al. [5] reported the onset of the failure in retaining the air pockets between the micro-pillars for turbulent water flow over superhydrophobic surfaces.

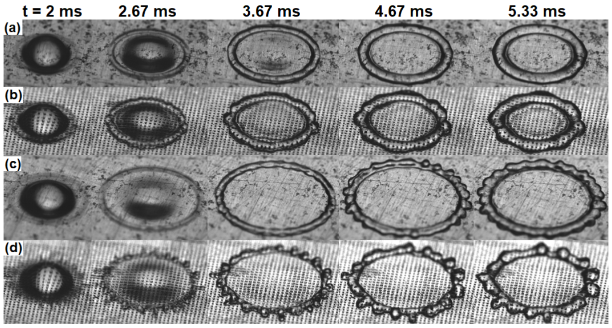

Figure 2: The image sequence for the spreading of the water drop on the plane (a: We= 70 and c: We= 139) and micro-textured surface (b: We= 70 and d: We= 139).

The variation of $\beta_{max}$ with We for a water drop impacting on a plane aluminium surface is compared to that with a micro-textured surface in Figure 3. $\beta_{max}$ is observed to increase with We (or impact velocity) due to the rise in the inertial energy. $\beta_{max}$ for the micro-textured surface is found lower than that for the plane surface at all We. The reason is the penetration of the liquid in the micro-pores and the increased roughness due to the micro-pillars, which cause pinning and deceleration of the lower layers of the advancing liquid. Similar observations were reported for drop impact on a hydrophobic micro-grooved surface [2]. The deceleration of the liquid causes higher viscous resistance in the spreading lamella, resulting in additional losses in the inertial energy of the drop. The difference in $\beta_{max}$ between the two surfaces is more prominent at higher We, possibly because the spreading lamella is thinner at higher We, which is more prone to pinning due to the micro-pillars.

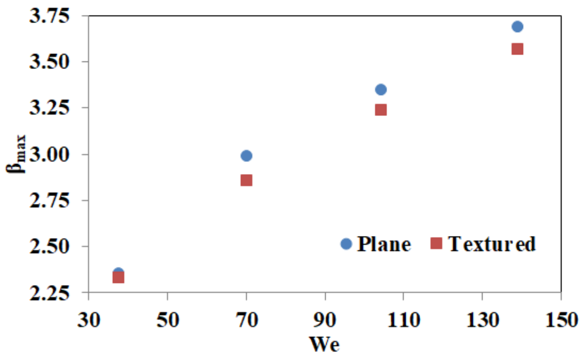

Figure 3: Variation of $\beta_{max}$ with We for a water drop impacting on a plane and micro-textured aluminium surface.

Figure 4 shows the comparison of the time taken by the drop to reach the maximum spreading ($T_{max}$) with We for a water drop impacting the plane and the micro-textured surface. It is observed that $T_{max}$ for the micro-textured surface is significantly lower than that for the plane surface for all We.

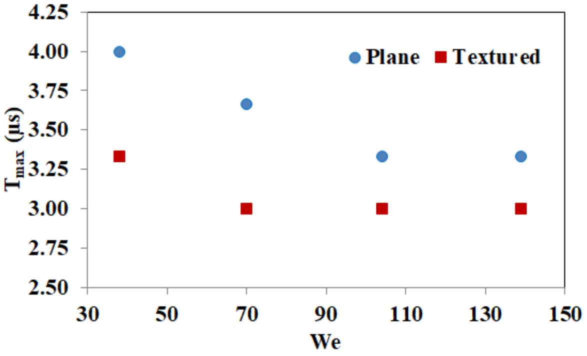

Figure 4: Variation of $T_{max}$ with We for a water drop impacting on a plane and micro-textured aluminium surface.

The heat transfer ($q_s$) between the solid and the drop is influenced by the maximum spreading diameter of the drop [3]

$$q_s = \frac{\pi}{3}\frac{D_{max}^2}{U_0} k \Delta T Re^{0.5} Pr^{0.4} \qquad (1)$$

where k is thermal conductivity of the liquid, $\Delta T$ is temperature difference between the solid and the drop, and Pr is Prandtl number. Hence, the heat transfer from the solid to the drop would be lower in the case of a micro-textured surface than a plane surface.

## CONCLUSIONS AND FUTURE RECOMMENDATIONS

The study compares the impact and spreading dynamics of a water drop on a plane (hydrophilic) and a micro-textured (hydrophobic) aluminium surface. $\beta_{max}$ for the water drop was found to be lower for the micro-textured surface than the plane surface at all We. The reason is the penetration of the drop in the micro-pores during impact which results higher surface roughness and increased viscous losses in the drop due to the deceleration of the lower lamella by the micro-pillars. The difference in $\beta_{max}$ was found to increase with We as the effect of the micro-roughness is more prominent when the lamella is thinner. This decrease in the maximum spreading would result in lower heat transfer between the solid and the drop. The time taken by the drop to reach $D_{max}$ is also lower for the micro-textured surface at all We as compared to the plane surface. These results can be useful in modelling of drop-surface interaction and the related heat transfer for aircraft surfaces.

In the future, the impact of water drop on heated micro-textured hydrophobic surfaces can be studied to elucidate the surface temperature and the heat transfer on the impact dynamics. Also, the hydrophobicity of the micro-textured surface can be increased by adding a hydrophobic thin film coating on it for further drop impact studies.

## REFERENCES

[1] S. G Cober and G. A. Isaac. *J Appl Meteorol Climatol*, 51(2):265–284, 2012.

[2] R Kannan and D Sivakumar. *Colloids Surf. A Physicochem. Eng. Asp.*, 317(1-3):694–704, 2008.

[3] A. Kumar and D. K. Mandal. *Heat Mass Transf.*, 56(2):445–457, 2020.

[4] M. Quero, D. Hammond, R. Purvis, and F. Smith. In *44th AIAA Aerospace Sciences Meeting Exhibit*, page 466, 2006.

[5] J. Seo, R García-Mayoral, and A. Mani. *J. Fluid Mech.*, 835:45–85, 2018.

[6] V. Vaikuntanathan and D. Sivakumar. *Langmuir*, 32(10):2399–2409, 2016.

**Joint ERCOFTAC/EU-CTFF**
**European Drag Reduction and Flow Control Meeting – EDRFCM 2022**
**September 6$^{\text{th}}$–9$^{\text{th}}$, 2022, Paris, France**

# DRAG REDUCTION ON A TRANSONIC WING

**Maurizio Quadrio**
Dip. Scienze e Tecnologie Aerospaziali, Politecnico di Milano, 20156 Milano, Italy

**Alessandro Chiarini**
Dip. Scienze e Tecnologie Aerospaziali, Politecnico di Milano, 20156 Milano, Italy

**Davide Gatti**
Institute for Fluid Mechanics, Karlsruhe Institute of Technology, 76131 Karlsruhe, Germany

**Jacopo Banchetti**
Dip. Scienze e Tecnologie Aerospaziali, Politecnico di Milano, 20156 Milano, Italy

**Antonio Memmolo**
High Performance Computing Department, CINECA, 40033 Bologna, Italy

**Sergio Pirozzoli**
Dipartimento di Ingegneria Meccanica e Aerospaziale, Roma La Sapienza Univ, 00184 Roma, Italy

## ABSTRACT

Skin-friction drag reduction is applied to a transonic wing to modify its aerodynamic performance. A Direct Numerical Simulations with up to 1.8 billions cells of the compressible flow around a wing slab is presented, at $Re_\infty = 3 \times 10^5$ and $M_\infty = 0.7$. Control is applied only on a limited portion of the suction side of the wing via streamwise-travelling waves of spanwise forcing. Besides locally reducing friction, control modifies the shock wave, significantly increasing the global efficiency of the wing. The increased efficiency implies that the airplane can fly at a lower angle of attack and, therefore, with a lower drag. Estrapolating the benefits at the airplane level yields 9% reduction for the drag coefficient of the aircraft, with negligible energy cost from the active control.

## BACKGROUND

Most of the research on skin-friction drag reduction has taken place in plane wall flows, where drag is entirely made by viscous friction. In more complex flows, where additional contributions to drag are present (pressure drag, parasitic drag, separation, lift-induced drag and wave drag), reducing the total drag is the goal. At EDRFCM 2017 we proposed [4] that localized friction reduction (specifically obtained via spanwise forcing) might bring in substantial advantages in aeronautical configurations; and at EDRFCM 2019 [3] we described how skin-friction drag reduction enables additional pressure drag reduction for a non-planar wall flow in the incompressible regime [2]. The idea is now being explored [1].

In this work we present the first direct numerical simulation (DNS) of the compressible turbulent flow over a wing slab in the transonic regime with flow control. We explore to what extent a localised control for skin-friction reduction alters the aerodynamic performances of the wing; the results will be extrapolated to the entire airplane. The active control technique chosen for the study is the streamwise-traveling waves of spanwise forcing [6], which offers the double advantage of producing large (hence easily measurable) effects and large net savings. However, the general conclusions are valid for any skin-friction reduction technology.

## METHODS

We consider by DNS the transonic flow around a wing slab made by a supercritical airfoil. The Reynolds and Mach numbers of the flow are $Re_\infty = U_\infty c/\nu_\infty = 3 \times 10^5$ and $M_\infty = U_\infty / a_\infty = 0.7$, where $c$ is the airfoil chord and $U_\infty$, $\nu_\infty$ and $a_\infty$ are the free-stream velocity, kinematic viscosity and sound speed. The angle of attack is $\alpha = 4^\circ$, which corresponds to the maximum aerodynamic efficiency of the profile. The DNS code [5] solves the compressible Navier–Stokes equations for a calorically perfect gas. The incoming flow is laminar, and transition to turbulence is enforced on both sides of the airfoil via a volume force located at $x = 0.1c$.

On a portion of the suction side of the wing, streamwise-travelling waves of spanwise velocity are applied. The spanwise velocity component $w_w$ at the wall is:

$$w_w(x,t) = f(x) A \sin\left(\kappa_x x - \omega t\right)$$

where $A$ is the maximum forcing amplitude and $\kappa_x, \omega$ are the spatial and temporal frequencies of the wave. A smoothing function $f(x)$ is used to raise the spanwise velocity at the initial position $x_s$ and then return it to zero at $x_e$. Two control cases, C1 and C2, are considered. Both are of moderate intensity, with forcing applied locally on the mid portion of the suction side; however, slight changes in $A, x_s, x_e$ render control C2 more effective (higher intensity and wider extension).

DNS are carried out with/without control on two meshes: the baseline grid has 536 million cells, and a finer grid with 1.8 billions cells is used for validation. The finest grid has $N_x, N_y, N_z = 6144, 768, 384$ cells.

## RESULTS

An overview of the instantaneous fields is given in figure 1, where vortical structures for the no-control case are visualised via isosurfaces of the imaginary part of the complex conjugate eigenvalue pair of the velocity gradient tensor $\Im(\lambda_{ci})$. The three sonic lines at $M = 1$ are shown for the no-control (red), C1 (blue) and C2 (green) cases. The flow becomes supersonic at the nose and remains laminar up to the tripping. The supersonic region extends up to $x \approx 0.5c$, where the flow undergoes abrupt recompression due to the shock wave. The control moves the shock wave downstream and enlarges the supersonic region, and increases the shock wave intensity. Consistently, the maximum Mach number increases from $M = 1.087$ (no-control) to $M = 1.093$ (C1) and $M = 1.116$ (C2), while its position remain almost unchanged. All these changes are consistent with a decreased friction in the actuated region.

Figure 2 plots the mean friction and pressure coefficients. Since on the pressure side there is no actuation, the curves are virtually unchanged. In the controlled cases, after $x_s$ the forcing effectively reduces friction in the actuated region. A short spatial transient is required [7] for drag reduction to develop. In both cases, $c_f$ becomes negative after the shock wave. Unlike $c_f$, control modifies $c_p$ even outside the actuated region. Two distinct control effects are observed: (i) the compression associated with the shock wave is moved downstream and (ii) the expansion at the leading edge is stronger, leading to a plateau with lower $c_p$. The recirculating region in the controlled cases decreases the adverse pressure gradient in the area close to the shock; see the milder slope of $c_p$ in correspondence of the pressure recovery before the shock-induced compression. Thus the shock wave moves downstream and enlarges the supersonic bubble, resulting in an increase of the velocity within the bubble and, therefore, into more intense expansion in the fore part of the airfoil. Both effects are more evident in C2, that is stronger and designed to produce an evident recirculation after the shock wave. Overall, the control effect on $c_p$ can be assimilated to that of an increase of the free-stream Mach number, but only for the suction side.

The control-induced changes in the distributions of friction and pressure positively affect both lift and drag. The combined changes of friction and pressure result into a reduction of the total drag for both cases, quantified by 4.5% for C1 and by a marginal 0.8% for C2. However, the crucial control effect is the increase of the lift coefficient, by 1.5% for C1 and 11.3% for C2. The wing efficiency, therefore, is significantly enhanced in both cases, by 6.8% for C1 and 13.5% for C2. Increased wing efficiency implies that the required lift can be obtained at a lower angle of attack $\alpha$ and, therefore, at the cost of a lower drag. By running a further DNS at the smaller angle of attack required to achieve the same lift, a total drag reduction of almost 15% is obtained.

At the Meeting we will show how these figures can be scaled up to the airplane level: the outcome is that the energy cost of the active control, once deployed only on a fraction of the surface, becomes negligible. Its effects, though, remain finite, and we estimate a 9% for the entire airplane in cruise flight.

Although demonstrated for spanwise forcing only, the idea behind the present results is general and valid for any type of control, including passive strategies, e.g. riblets. Moreover, the study is just a first attempt and should not be taken as indicative of the maximum achievable gain: design and placement of skin-friction control devices over a complex body for drag reduction is a new optimization problem that might yield interesting outcomes. Considering skin-friction drag reduction as a tool and not only as a goal in flows where friction drag is not the key target for optimisation will open new avenues to a widespread use of flow control.

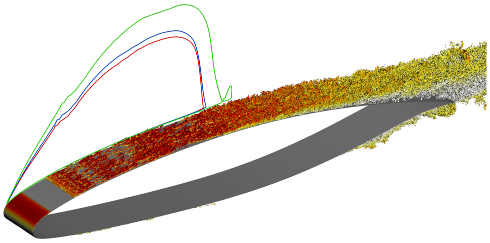

Figure 1: Isosurfaces of the swirling strength $\Im(\lambda_{ci}) = 100$ in the no-control case, coloured with the kinetic energy $k$ with a white-to-red colormap in the range $0 \leq k \leq 1$. Lines are the sonic line $M = 1$ for reference (red), C1 (blue) and C2 (green)

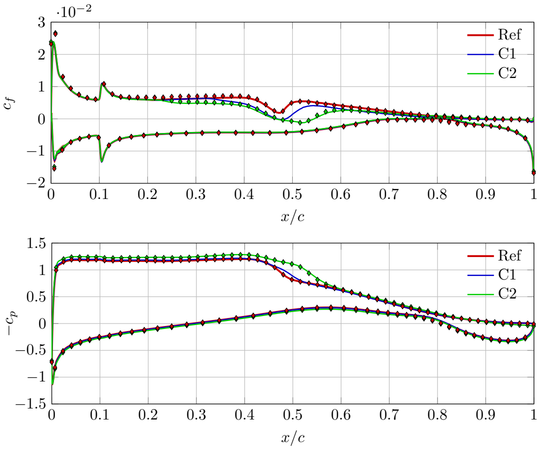

Figure 2: Friction coefficient $c_f$ (top) and pressure coefficient $c_p$ (bottom). Reference and C2 results obtained on the finer grid are shown with symbols. Tripping is at $x/c = 0.1$. Forcing starts at $x/c = 0.3$ for C1 and $x/c = 0.2$ for C2, and ends at $x/c = 0.78$ for both.

## REFERENCES

[1] M. Albers and W. Schröder. Lower drag and higher lift for turbulent airfoil flow by moving surfaces. *International Journal of Heat and Fluid Flow*, 88:108770, April 2021.

[2] J. Banchetti, P. Luchini, and M. Quadrio. Turbulent drag reduction over curved walls. *J. Fluid Mech.*, 896:1–23, August 2020.

[3] J. Banchetti and M. Quadrio. Turbulent drag reduction for a wall with a bump. In *17th EDRFCM, Bad Reichenhall*, 2019.

[4] A. Gadda, J. Banchetti, G. Romanelli, and M. Quadrio. Drag reduction of a whole-aircraft configuration via spanwise forcing. In *16th EDRFCM, Monteporziocatone*, 2017.

[5] A. Memmolo, M. Bernardini, and S. Pirozzoli. Scrutiny of buffet mechanisms in transonic flow. *Int. J. Numer. Methods Heat Fluid Flow*, 28(5):1031–1046, January 2018.

[6] M. Quadrio, P. Ricco, and C. Viotti. Streamwise-traveling waves of spanwise wall velocity for turbulent drag reduction. *J. Fluid Mech.*, 627:161–178, 2009.

[7] M. Skote. Temporal and spatial transients in turbulent boundary layer flow over an oscillating wall. *Int. J. Heat Fluid Flow*, 38:1–12, 2012.

**Joint ERCOFTAC/EU-CTFF**
**European Drag Reduction and Flow Control Meeting – EDRFCM 2022**
**September 6$^{\text{th}}$–9$^{\text{th}}$, 2022, Paris, France**

# COHERENT NEAR-WALL STRUCTURES AND DRAG REDUCTION BY SPANWISE FORCING

**E. Gallorini & M. Quadrio**
Department of Aerospace Sciences and Technologies, Politecnico di Milano, via La Masa 34, 20156 Milano, Italy

**D. Gatti**
Institute of Fluid Mechanics, Karlsruhe Institute of Technology, 76131 Karlsruhe, Germany

The aim of the present work is to study the effect of streamwise-traveling waves of spanwise wall velocity (StTW) on the quasi-streamwise vortices (QSV) populating the near-wall region of a turbulent channel. This study estends the analysis of [4], where the particular case of spatially uniform wall oscillation (OW) is considered and studied by conditional-averaging of DNS data.

The travelling waves are enforced as a spanwise wall velocity of the form:

$$w_w\left(x,t\right) = A\sin\left(\omega t - \kappa_x x\right) \tag{1}$$

being $w_w\left(x,t\right)$ the spanwise velocity, which periodically varies according to the phase $\phi = \omega t - \kappa_x x$, function of both the time $t$ and the streamwise coordinate $x$. The control parameters are the maximum wall velocity $A$, the wavenumber $\kappa_x$ and the angular frequency $\omega$. These, in turn, determine the wavelength $\lambda_x = 2\pi/\kappa_x$, the period $T = 2\pi/\omega$ and the phase speed $c = \omega/\kappa_x$ of the wall velocity wave. The law 1 contains the two limiting cases of the stationary wave when $\omega = 0$ and the spanwise oscillating wall (OW) when $\kappa_x = 0$.

The application of StTW results in the formation of a periodic and streamwise-varying crossflow called generalised Stokes layer (GSL). The GSL interacts with quasi-stramwise vortices and longitudinal low-speed streaks which are essential in the near-wall turbulence regeneration cycle. Altering this cycle through a perturbation of the structures is generally recognised as the foundation of the drag-reducing effect of the GSL. However, the details of the interaction between the wall forcing and the near-wall turbulent structures remain partially unclear.

Similarly incomplete is the research of a predictive correlation, based on physical or empirical arguments, to estimate the drag reduction as a function of the control parameters.

The goal of this work is therefore twofold: we first extend the conditional analysis of [4] to the general case of StTW and we developed a new predictive correlation to arrive at a satisfactory drag-reduction prediction based upon GSL quantities alone.

The data are provided by five incompressible Direct Numerical Simulations (DNS) of a fully developed turbulent channel flow: one DNS provides the reference case, whereas for each control technique two configurations are simulated, one with good performance and the other that performs weakly (smaller drag reduction for OW and drag increase for StTW).

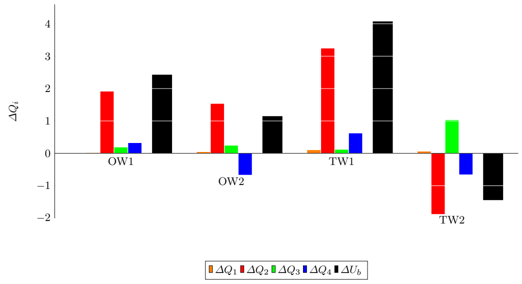

Figure 1: Changes $\Delta Q_i$ of the quadrant contributions to $U_b$, from Eq.3. The sum of the four $\Delta Q_i$ equals the total change $\Delta U_b$ (shown with a black bar) from the uncontrolled case.

The variation of bulk velocity $\Delta U_b = U_b - U_{b,Ref}$ is used to quantify the friction drag changes induced by the control, where $U_{b,Ref} = 15.90$ is the bulk velocity of the reference case. The variation of bulk velocity can be rearranged in the case of Constant Pressure Gradient (CPG) as derived in [2]:

$$U_b = \frac{Re_\tau}{3} - \int_0^{Re_\tau} \left(1 - \frac{y}{Re_\tau}\right)\left(-\overline{u'v'}\right) dy^+. \tag{2}$$

where the overbar is the temporal mean, and the prime indicates a fluctuating turbulent quantity according to the Reynolds decomposition.

This equation can be written as:

$$U_b = \frac{Re_\tau}{3} + \sum_{i=1}^{4} Q_i, \tag{3}$$

where $Q_i$ is the event contribution of quadrant $i$ to the weighted integral of the Reynolds shear stresses (see Ref. [3]). The laminar term remains unchanged between controlled and uncontrolled flows, so the change of bulk velocity is the sum of the changes of quadrant contributions to the shear stress: $\Delta U_b = \sum_{i=1}^{4} \Delta Q_i$.

The results of the quadrant analysis for the considered cases are presented in Fig.1. OW results are in agreement with the previous results of [4] and it can be observed as the variation of Q2 events is the dominant mechanism for the travelling waves too, bearing a suppression of Q2 events in TW1 case, whereas in the drag-increasing TW2 case they are significantly enhanced. TW2 presents other peculiarities: similarly to OW2, control performances are decreased by a negative $\Delta Q_4$, but this is compensated by the large $\Delta Q_3 > 0$.

The extraction procedure for the QSV is based on the swirling strength criterion, introduced by Zhou et al. [5], and the conditional average process follows the steps of [4].

The conditionally-averaged flow fields for cases OW1, OW2 and TW1 (not shown for brevity) qualitatively confirm the picture of [4], with $Q_2$ and $Q_4$ contributions possessing an evident phase dependency and drag reduction mostly related to

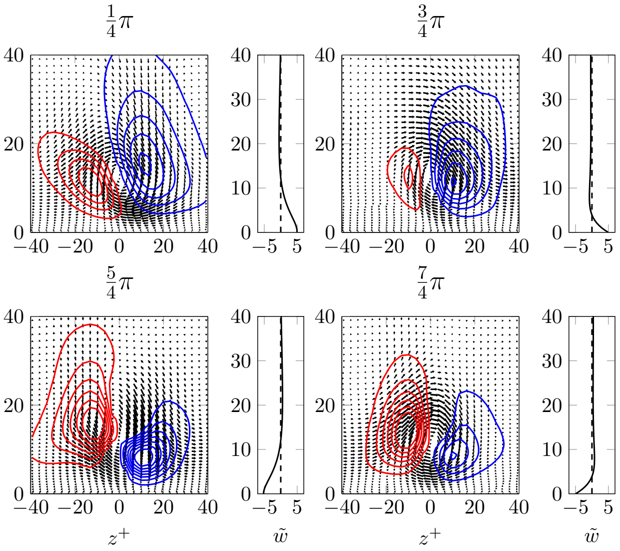

Figure 2: Four phases of the conditionally-averaged flow field (TW2) with QSV extracted at $y_c^+ = 11.3$. The additional right panels plot the phase-averaged mean velocity profile.

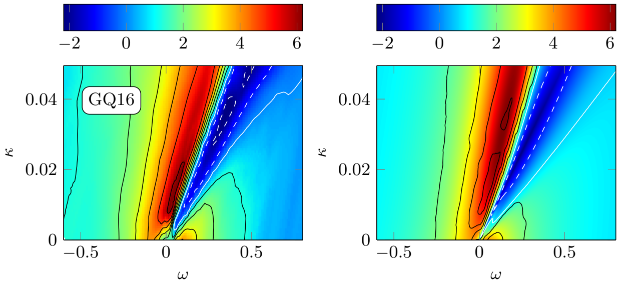

Figure 3: Left: drag-reduction map from the database of [1] at $Re_\tau = 200$. Right: drag changes predicted by Eq.6.

a reduction of $Q_2$. The drag-increasing TW2 case displayed in Fig. 2, however, behaves differently, showing a considerable variation in $Q_2$ values along the cycle, varying from the minimum at $\phi = 3/4\pi$ to larger values, with a significant maximum at $5/4\pi$. Changes of Q4 events are of lesser evidence, as expected from Fig. 1, but generally sweeps do appear as more intense in controlled cases than in the uncontrolled one.

A peculiar feature of the TW cases, visible in figures in Fig. 2, is the phase-related vertical shift of $Q_2$ and $Q_4$ conditional fields around the vortex center: the center of the $Q_2$- and $Q_4$-structures appears to move vertically during the forcing cycle. The angle $\beta$ formed by the straight line connecting the maxima of the $Q_2$ and $Q_4$ fields at the center of the QSV has been found to be in agreement with the angle $\alpha$ formed by the direction of the second eigenvector of the phase-averaged strain-rate tensor $\langle S \rangle_{ij}$ evaluated at $y^+ = 12$. The structure of $\langle S \rangle_{ij}$ is indeed modified between OW and StTW by the introduction of a $x$ dependance on the phase $\phi$. We observe as both $\alpha$ and $\beta$ are larger in modulus for the TW2 case, supporting the idea that large wall-normal excursion of the Reynolds shear stress structures relate to drag increase.

Existing strategies for drag reduction prediction are mostly restricted to OW: they can be extended to the TW cases leading to satisfactory results. The drag reduction predicion formula proposed in [4]:

$$\Delta U_b = a \frac{\partial \widetilde{w}}{\partial y}\bigg|^{rms}_{y^+=10} - b \frac{\partial \widetilde{w}}{\partial y}\bigg|^{rms}_{y^+=15}. \tag{4}$$

has been extend to include the effects of the travelling waves. In particular, we we augmented the original formulation to include the rms value of the $\alpha$ angle evaluated at $y^+ = 12$, $\alpha^{rms}_{y^+=12}$, and the parameter $S'$:

$$S'(\omega, \kappa_x) = \int_0^\ell a_m(\omega, \kappa_x, y) dy. \tag{5}$$

being $S'$ the maximum over the forcing cycle of the GSL acceleration integrated over its penetration depth $l$. This expression for $S'$ reflects the speed difference of turbulent structures and the travelling wave and the ensuing forcing timescale $2\pi/\omega_{eq}$, while $\alpha^{rms}_{y^+=12}$ is used to take into account for the drag increase effect of StTW. The prediction formula 4 is modified as:

$$\Delta U = S' \left( a\tau_z|^{rms}_{y^+=10} + b\tau_z|^{rms}_{y^+=15} \right) - c\alpha^{rms}_{y^+=12}. \tag{6}$$

where $a, b, c$ are empirical coefficients determined with a least square fit to the dataset available from Ref. [1]. Despite being obtained through simple observations, the prediction produces a strikingly similar map compared to the numerical results, and it performs significantly better than the alternative predictive formulas. This result confirms that (this type of) drag reduction is mostly a linear phenomenon, albeit non-linear effects need to be included for a quantitatively accurate prediction. The empirical coefficients appearing in the formula reflect our current inability to relate the properties of the GSL with the vertical dynamics/bouncing of the QSV, which could be the direction for further work.

## REFERENCES

[1] D. Gatti and M. Quadrio. Reynolds-number dependence of turbulent skin-friction drag reduction induced by spanwise forcing. *Journal of Fluid Mechanics*, 802:553–58, 2016.

[2] I. Marusic, D. D. Joseph, and K. Mahesh. Laminar and turbulent comparisons for channel flow and flow control. *Journal of Fluid Mechanics*, 570:467–477, 2007.

[3] J. M. Wallace, H. Eckelmann, and R. S. Brodkey. The wall region in turbulent shear flow. *Journal of Fluid Mechanics*, 54(1):39â–48, 1972.

[4] A. Yakeno, Y. Hasegawa, and N. Kasagi. Modification of quasi-streamwise vortical structure in a drag-reduced turbulent channel flow with spanwise wall oscillation. *Physics of Fluids*, 26:085109, 2014.

[5] J. Zhou, R. J. Adrian, S. Balachandar, and Kendall T. M. Mechanisms for generating coherent packets of hairpin vortices in channel flow. *Journal of Fluid Mechanics*, 387:353–396, 1999.

**Joint ERCOFTAC/EU-CTFF**
**European Drag Reduction and Flow Control Meeting – EDRFCM 2022**
**September 6th–9th, 2022, Paris, France**

# INTERNAL FLOW STRUCTURE MODIFICATION GENERATED BY TRANSVERSAL SURFACE WAVES

**E. Mäteling[1], M. Albers[1], W. Schröder[1,2]**
[1] Institute of Aerodynamics, RWTH Aachen University, Wüllnerstraße 5a, 52062 Aachen, Germany
[2] JARA Center for Simulation and Data Science, RWTH Aachen University, Seffenter Weg 23, 52074 Aachen, Germany

## INTRODUCTION

To meet the modern challenges of sustainability and conservation of resources, the interest in methods for drag reduction has increased substantially lately. A recent review by Ricco et al. [4] provides an extensive overview of the latest achievements, however, the physical causes leading to drag reduction are still not fully understood. In the present study, a turbulent boundary layer (TBL) flow is subjected to a spanwise traveling transversal surface wave and the fluid dynamical processes that are responsible for the resulting drag reduction of approximately 26.5% are analyzed. The approach involves an inner-outer interaction analysis based on an enhanced method to extract common scales across different variates, the 2D Noise-Assisted Multivariate Empirical Mode Decomposition (NA-MEMD) [3], and a study of the effects of the secondary flow field superimposed by the actuation.

## COMPUTATIONAL SETUP

Actuated flat plate TBL flow is simulated by direct numerical simulations. A schematic of the computational setup is depicted in figure 1. The domain size is $L_x \times L_y \times L_z = 603\,\theta \times 101\,\theta \times 15.8\,\theta$, where $\theta$ is the momentum thickness at $x_0$. The Mach number is $M = 0.2$ and the friction Reynolds number is $Re_\tau \approx 1,500$ in the test section, i.e., the region where wall is actuated. The wave motion is introduced through a space and time dependent function

$$y^+|_{\text{wall}}(z^+, t^+) = A^+ \cos\left(\frac{2\pi}{\lambda^+} z^+ + \frac{2\pi}{T^+} t^+\right). \qquad (1)$$

Within the actuated region the actuation parameters approximately correspond to inner-scaled values, i.e., scaled by the kinematic viscosity $\nu$ and the friction velocity $u_\tau(x)$ of the non-actuated reference case, of the amplitude $A^+ \approx 100$, the wavelength $\lambda^+ \approx 3000$, and the period $T^+ \approx 50$. The setup is similar to the one introduced in [1], however, a significantly higher Reynolds number is used in this study.

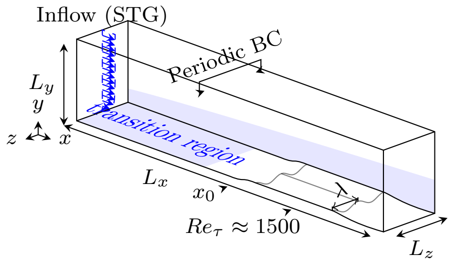

Figure 1: Physical domain of the actuated TBL flow.

## RESULTS

A 2D NA-MEMD is applied to wall-parallel planes within the test section, which simultaneously decomposes the streamwise and the wall-normal velocity fluctuations at the inner layer ($y^+_{NW} = 1$) and the outer layer ($y^+_{OL} = 156$) into physically relevant modes. The obtained large-scale components are used to investigate the inner-outer interaction with respect to the superposition (index $S$), the bursting activity, i.e., sweeps (index $sw$) and ejections (index $ej$), and the amplitude modulation (index $AM$). Details of the decomposition method and the interaction analysis are described in [3].

Table 1: Time-averaged maximum correlation coefficients of the inner-outer interaction at $\{y^+_{NW} = 1, y^+_{OL} = 156\}$.

| | $\bar{R}_{S,max}$ | $\bar{R}_{sw,max}$ | $\bar{R}_{ej,max}$ | $\bar{R}_{AM,max}$ |
|---|---|---|---|---|
| REF | 0.61 | 0.60 | 0.36 | 0.65 |
| ACT | 0.51 | 0.51 | 0.52 | 0.64 |

The correlation coefficients of the respective phenomena are time-averaged and listed in table 1 for the non-actuated reference (REF) and the actuated case (ACT). It is obvious that, on average, the actuation reduces the inner-outer coherence of superposition and sweeping motion ($R_S, R_{sw}$) but increases the correlation of ejections ($R_{ej}$). Thus, the top-down communication appears to be attenuated while the bottom-up communication is enhanced. To further investigate the root cause of this modification, the joint probability density distribution (jPDF) of the near-wall large-scale velocity fluctuations is shown in figure 2.

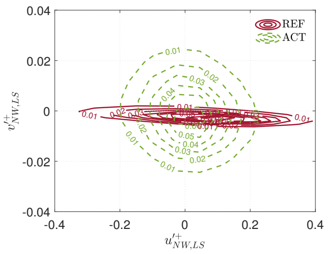

Figure 2: jPDF of near-wall, large-scale velocity fluctuations $u'^+_{NW,LS}, v'^+_{NW,LS}$ at $y^+_{NW} = 1$.

It clearly reveals that the actuation yields an increased probability of near-wall large-scale sweeps and ejections induced by a massive increase of near-wall wall-normal velocity fluctuations - negative and positive - that overcompensate for the reduced absolute streamwise fluctuations. Since the probability and the strength of near-wall ejections is substantially increased compared to the reference flow, it is more likely that they reach the outer layer, which explains the increased correlation $R_{ej}$. The decreased correlation of sweeping motion can be explained by the following observation. The near-wall sweeps do not originate from the outer layer. Since the jPDF is nearly symmetric, the sweeps are mostly "artificially" introduced by the actuation similarly to the ejections and they are confined to the near-wall region, which was confirmed by an interaction analysis between $y^+ = 1$ and $y^+ = 5, 15$ and the respective jPDFs (not shown). Thus, they transport only low high-momentum fluid from layers very close to the wall and thus, have a less severe effect on the wall-shear stress level.

This still poses the question why the top-down communication is less efficient in the actuated flow. Therefore, a closer look is taken at the severely reduced streamwise fluctuations near the wall, which can be associated with less intense streaks. This indicates a modification of the related vortical structures, especially the quasi-streamwise vortices (QSV). In figure 3, the transition area between the flat TBL and the developing surface wave actuation, which is fully deployed at $x^+ \approx 4,500$, is shown. The depicted QSV are visualized by the squared streamwise swirling strength with an isosurface level of 0.01 and the multicolored plane displays the streamwise velocity fluctuations $u'^+$ at $y^+ = 15$. With increasing influence of the actuation, QSV are eliminated, which was already noted in previous studies [4].

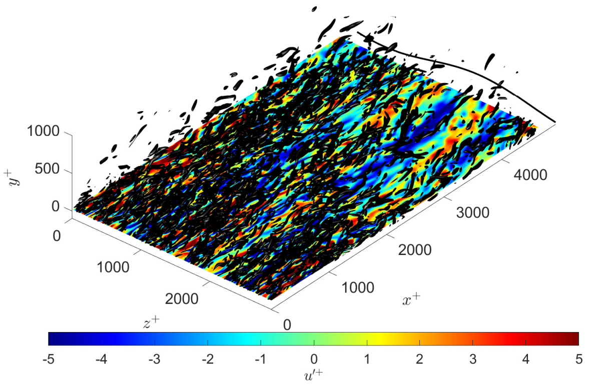

Figure 3: QSV (black isosurfaces) and streamwise velocity fluctuations $u'^+$ (colored) at $y^+ = 15$ in the transition region. Wall is flattened for simplicity.

By tracking the centroid's position of the QSV, it is revealed that the vortex break-up happens predominantly in the lower buffer layer, i.e., the region where the mean shear imposed by the actuation is most intense. The reduced number of near-wall vortices attenuates the wall-normal momentum exchange and is accompanied by less intense and widened streaks, which, in turn, yields a reduced wall-shear stress.

Figures 4 and 5 give further insight into the mechanisms involved in the vortex disintegration. The velocity gradients of the secondary flow field acting on the QSV during break-up are used to generate the displayed jPDFs. Note that the gradients are normalized by the maximum gradient at the wall-normal position of the vortex' centroid to consider the $y$-dependent gradient changes. The jPDFs are complemented by sketches of a QSV in the $y-z$ plane and its deformation when the gradient combinations act on it. The investigation shows that gradient combinations that deform the vortex into an elliptical shape are the driving forces for vortex break-up.

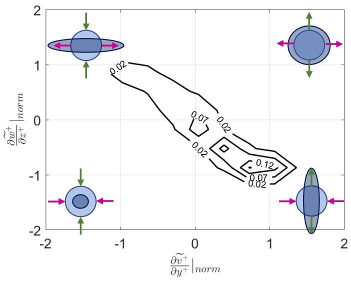

Figure 4: jPDF of superimposed velocity gradients $d\tilde{v}^+/dy^+, d\tilde{w}^+/dz^+$ related to QSV break-up.

Vortices with an elliptical cross-section are usually unstable and disintegrate [2]. Since only specific combinations of the secondary velocity gradients can provoke such effects and since these combinations occur jointly only in limited phases, only a portion of the QSV is affected and regeneration might happen in the remaining phases.

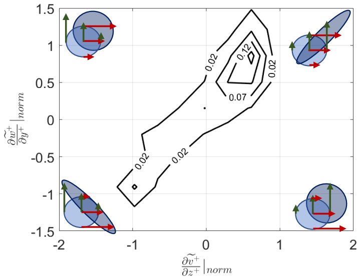

Figure 5: jPDF of superimposed velocity gradients $d\tilde{v}^+/dz^+, d\tilde{w}^+/dy^+$ related to QSV break-up.

Every process that we observe with respect to the QSV must also happen to the involved upwards and downwards traveling fluid portions, i.e., also to the large-scale bursts. That means that a lot of sweeps get distorted by the mean shear as well, which dissolves their localized highly energetic nature into a broader, less intense pool of downwards oriented fluid. In addition, the liaison with the massively increased number and strength of near-wall ejections drains a lot of energy from the sweeps. It is interesting to note that $R_S \approx R_{sw} \approx R_{ej} \approx 0.51$ for the actuated flow, which indicates that the less energetic near-wall area allows top-down and bottom-up communication to pass through similarly.

## REFERENCES

[1] M. Albers, P. S. Meysonnat, D. Fernex, R. Semaan, B. R. Noack, and W. Schröder. Drag reduction and energy saving by spanwise traveling transversal surface waves for flat plate flow. *Flow Turb. Combust.*, 105:125–157, 2020.

[2] K. V. Koshel, E. A. Ryzhov, and X. J. Carton. Vortex interactions subjected to deformation flows: A review. *Fluids*, 4(1):14, 2019.

[3] E. Mäteling and W. Schröder. Analysis of spatiotemporal inner-outer large-scale interactions in turbulent channel flow by multivariate empirical mode decomposition. *Phys. Rev. Fluids*, 7(3):034603, 2022.

[4] P. Ricco, M. Skote, and M. A. Leschziner. A review of turbulent skin-friction drag reduction by near-wall transverse forcing. *Prog. Aerosp. Sci.*, 123:100713, 2021.

**Joint ERCOFTAC/EU-CTFF**
**European Drag Reduction and Flow Control Meeting – EDRFCM 2022**
**September 6th–9th, 2022, Paris, France**

# NEAR-WALL MHD TURBULENCE CONTROL - EFFECT OF A HALBACH MAGNET CONFIGURATION

**A. CAPOGNA**
EPM group SIMaP Laboratory, Université Grenoble Alpes, 38402 Saint Martin d'Hères, France

**O. DOCHE**
EPM group SIMaP Laboratory, Université Grenoble Alpes, 38402 Saint Martin d'Hères, France

**L. DAVOUST**
EPM group SIMaP Laboratory, Université Grenoble Alpes, 38402 Saint Martin d'Hères, France

## INTRODUCTION

The shaping or processing of molten or liquid metals for energy or metallurgical applications requires the control of flows, which are more often turbulent than laminar, given the large length scale and the high throuput of the industrial processes involved. For this purpose, the use of magnetohydrodynamic forces is interesting as a non-contact actuation technique to control turbulent flow in a channel. However, the application of a uniform magnetic field is difficult to achieve in practice, as it requires the use of a large-scale electromagnet consuming a significant amount of electrical power. The feasibility of the passive control of a turbulent channel flow by means of permanent magnets placed at the upper and lower walls is studied here. However, one of the main problems associated with the use of magnets is the limited penetration depth of the generated magnetic field within the flow.

A detailed analysis of Reynolds stress transport [2] has shown that the application of a uniform magnetic field in the transverse, wall-parallel direction is more effective than a longitudinal field (*i.e.* in the direction of flow) in reducing turbulent activity and the viscous drag. It has also been shown that a flow can reach a quasi-relaminarised state only if the transverse magnetic field affects the entire logarithmic layer [1]. These results led us to perform Direct Numerical Simulations of permanent magnet arrays arranged at the walls of a turbulent channel flow. In particular, we have shown that a regular spanwise distribution (figure 1(a)) of permanent magnets located on the upper and lower wall is an effective way to reduce the turbulent activity. This configuration mainly generates magnetic field components perpendicular and transverse to the wall, $B_y$ and $B_z$ respectively.

The aim of this study is to compare the classical spanwise configuration with a more complex configuration called Halbach.

## GENERATION OF THE MAGNETIC FIELD

A fully developed turbulent channel flow submitted to a non-uniform magnetic field produced by a Halbach configuration [3] embedded into the wall is analyzed through Direct Numerical Simulation (DNS) for a low turbulent Reynolds number (4200). The Halbach magnet configuration corresponds to a specific arrangement of the magnets which enables magnetization enhancement on the inner (flow) side of the channel wall at the expense of the outer side. This is achieved by the successive 90° angular rotation of the magnetic dipolar moments delivered by a series of permanent magnets (figure 1(b)). The latter are stripes elongated in the streamwise ($x$) direction, so that only wall-normal ($B_y$) and transverse ($B_z$) magnetic field components are generated respectively above magnets disposed with vertical and horizontal magnetizations.

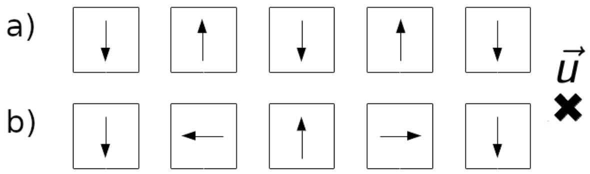

Figure 1: Disposition of the magnetization of the permanent magnets in a) the spanwise and b) the Halbach configurations. $\vec{u}$ gives the direction of the flow.

We can first compare the two configurations by taking the same magnets, with the same magnetization, and see which configuration is the most efficient in reducing turbulent activity.

To compare the magnetic intensity in these two configurations, the mean magnetic field deposited in the turbulent inner layer is defined as $B_{mean} = \frac{1}{0.3hL_xL_z}\int_0^{0.3h}\int_0^{L_x}\int_0^{L_z}\sqrt{B_y^2}dxdydz$, corresponding to a magnetic intensity of $N_\tau^{eq} = \frac{\sigma B_{mean}^2 \nu}{\rho u_\tau^2}$ where $\sigma$, $\nu$ and $\rho$ stand respectively for the electric conductivity, the viscosity and the density of the fluid, and $u_\tau$ is defined as the shear (or friction) velocity.

As shown in figure 2, the profiles of the magnetic field modulus deposited in the inner layer of turbulence are pratically identical, even if the magnetic field of the Halbach configuration is slightly more spread outside the inner layer.

## EFFECT OF THE CONFIGURATIONS ON THE TURBULENCE DAMPING

Since the wall shear stress and the mean velocity exhibit different behaviours depending on whether the magnetic moment is vertical ($B_y$) or horizontal ($B_z$), the problem is investigated making use of a spatial averaging based on the transverse periodicity of the magnetic pattern. We show (figure 3 and 4) that the Halbach configuration is more efficient to relaminarize the turbulent flow than the spanwise configuration even if an slightly lower magnetic intensity is deposited in the turbulent

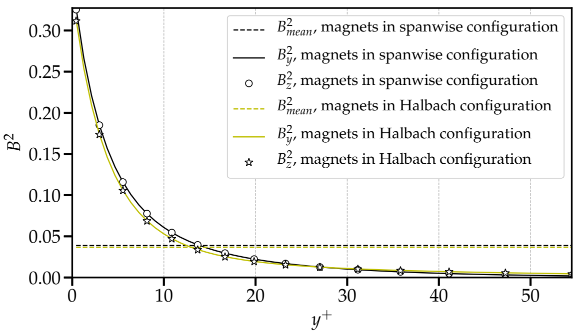

Figure 2: Profile of the magnetic field deposited in the channel flow for the spanwise and the Halbach configurations with the same magnet magnetization.

inner layer in the Halbach configuration. This is also showed by the maximum value of the *rms* fluctuations of the longitudinal velocity (figure 3), with a decrease of the fluctuations of 26.5% of the unmanipulated case in the spanwise configuration and a decrease of 37% of the unmanipulated case in the Halbach configuration.

As such, the magnetic modulus profile is not sufficient to explain the better efficiency of the Halbach configuration and other parameters must be taken into account.

The mean wall shear stress scaled by its value in the unmanipulated flow, on the other hand, seems to follow the magnetic modulus at the wall quite well, since it goes from $\partial u/\partial y|_{y=0} = 1.41$ in the spanwise configuration to $\partial u/\partial y|_{y=0} = 1.36$ in the Halbach configuration, which corresponds to a 3% decrease.

Here, the wall friction as well as the inlet pressure, imposed in the channel to compensate for losses, do not allow us to measure the effect of the magnetic configurations on turbulence reduction, as it is usually done in turbulence control. Indeed, the wall shear stress is higher in the spanwise or Halbach configurations than in the unmanipulated case, whereas the turbulent activity is reduced. However, the turbulent drag related to the turbulent activity decreases with it. Thus, the total wall sher stress measured at the wall is not only composed of the turbulent drag, and another shear stress comes into competition here. This shear stress is directly linked to the configuration of magnets used. Indeed, above the permanent magnets, inducing $B_y$, the mean spanwise vorticity is increased. This is due in particular to the current loops in the flow, which close above the permanent magnets and near the insulating wall. It results in a high value of the near-wall Lorentz (MHD) force, which increases significantly the near wall streamwise velocity and consequently the wall shear-stress.

## REFERENCES

[1] A. Capogna, O. Doche, S. Tardu, J. Schillings, and L. Davoust. Effect of a localized MHD body force on near–wall turbulence. *Magnetohydrodynamics*, 58.1–2(8):125–132, 2022.

[2] O. Doche, S. Tardu, J. Schillings, and A. Capogna. Transportation and coherent structures in MHD turbulent channel flow subject to uniform streamwise and spanwise magnetic fields. *Physical Review Fluids*, 6(9):094605, 2022.

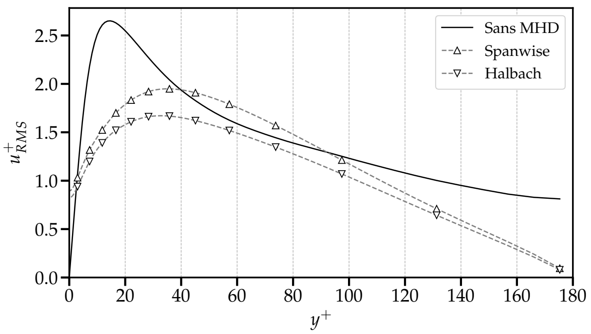

Figure 3: *rms* fluctuations of the streamwise velocity in the channel for the spanwise and the Halbach configurations

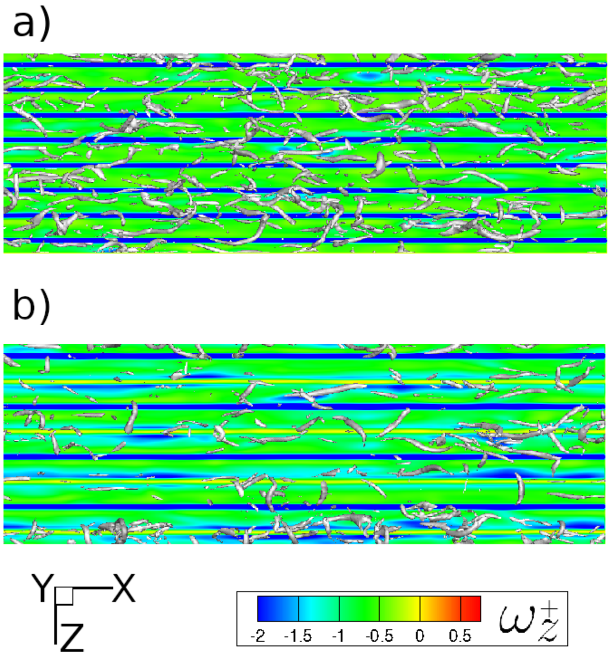

Figure 4: Instantaneous coherent structures detection ($\lambda_2 = 0.01$) in a turbulent flow submitted to (a) a spanwise and (b) a Halbach wall magnet configuration.

[3] K. Halbach. Design of permanent multipole magnets with oriented rare earth cobalt material. *Nuclear Instruments and Methods*, 169(1):1–10, February 1980.

**Joint ERCOFTAC/EU-CTFF**
**European Drag Reduction and Flow Control Meeting – EDRFCM 2022**
**April 11–14, 2022, Paris, France**

# SIMULTANEOUS MEASUREMENTS OF SURFACE AND FLUID VELOCITY IN A TURBULENT BOUNDARY LAYER WITH STANDING SPANWISE WAVES AT THE WALL

**I. Fumarola, Z. Soltani, M. Santer, J. Morrison**
Department of Aeronautics
Imperial College
London SW7 2AZ

## INTRODUCTION

Simulations and experiments have demonstrated that skin friction drag reduction greater than 40% can be achieved by moving wall with different types of motion, such as oscillating walls or spanwise waves travelling in the streamwise direction. Nevertheless, many open questions remain on how surface waves interact with the turbulent boundary layer. To this end, systematic experimental research is necessary to investigate the effectiveness and the mechanism of the active control at high Reynolds number.

In this work, a novel active surface for flow control is presented. The surface is able to generate spanwise standing waves at different amplitudes and frequencies allowing a wide range of wave parameters. In addition, the work focuses on the development of simultaneous measurements of the flow field and of the surface deformation by combining Particle Image Velocimetry (PIV) with Digital Image Correlation (DIC). The methodology proposed here provides a valid tool to experimentally investigate the fluid structure interaction between spanwise waves and turbulent boundary layer.

## THE MODEL

The model, figure 1, comprises a flat plate, with a modified super-elliptic leading edge, resting on the floor of the wind tunnel with a 1.2 m of active surface starting 2.4 m downstream of the leading edge. The active surface consists of a silicone skin two sets of carbon fibre rods that are driven in opposite directions by an electric motor through a Scotch-Yoke mechanism (see figure 2). The silicone skin deforms so that it generates an in-plane triangular wave. The model is design to be quite versatile in terms of wave parameters. The frequency can be easily changed through the motor controller, the amplitude can be chosen between a minimum of 10 mm and a maximum of 35 mm. The wavelength is the only parameter that is imposed by the distance between the rods, which is 40 mm. Nevertheless, the wavelength can be increased by attaching the skin to alternate rods. Experiments have been carried out at amplitude of 10 mm and wavelength 40 mm and at amplitude at 35 mm and wavelength at 120 mm, respectively at $U_\infty = 10$ m/s and $U_\infty = 6$ m/s corresponding to $Re_\tau = 2060$ and $Re_\tau = 1440$.

## METHODOLOGY AND RESULTS

PIV and DIC are both based on the correlation of image pairs. PIV captures the motion of the seeding particles in a narrow area illuminated by a laser sheet, while DIC the motion of random dots painted on the surface illuminated by a diffuse light that generates a speckle pattern.

The implementation of PIV and DIC together for wind tunnel experiments is a relatively new approach for fluid-structure interaction problems. Figure 3 shows the setup of the current experiment which adopts a three-colour scheme to avoid any interferer between images: the seeding particles are illuminated by green light from the laser; the speckle pattern emits orange light from the fluorescent paint illuminated by blue LED light. To make the methodology effective, a green bandpass filter is mounted on the PIV camera and orange long-pass filters on the DIC cameras. The biggest advantage of this experimental methodology is that the two measurement techniques are synchronised but do not interfere: this becomes important if the surface and the flow field are expected to have different velocities.

Figure 3 shows the speckle illuminated by the blue LED and green laser, which can be compared to figure 4 showing the raw image of the DIC cameras with on top the synchronised instantaneous PIV flow field during the surface motion. An example of instantaneous displacement field from the DIC raw image at the instant of maximum displacement for the 10 mm case is shown in figure 5. Further results describe the flow response to a range of surface wave parameters.

## CONCLUSION

A new active surface able to create standing waves of spanwise amplitude to reduce skin friction drag of turbulent boundary layer has been presented. The model has been tested for the first time in the wind tunnel acquiring simultaneous PIV and DIC measurements. This approach of combining the two experimental techniques provides a powerful tool for unveiling some of the unknowns concerning the interaction between a surface wave and the turbulent boundary layer. In this work, results of time-resolved PIV synchronised with DIC will be presented for a range of actuated parameters. In addition, the measurements will be accompanied by hot-wire and oil film interferometry to measure the turbulent boundary layer and of the skin friction. Future implementation will be to integrate a kagome lattice between the carbon rods and the silicone skin to produce spatially well-defined sinusoidal waves.

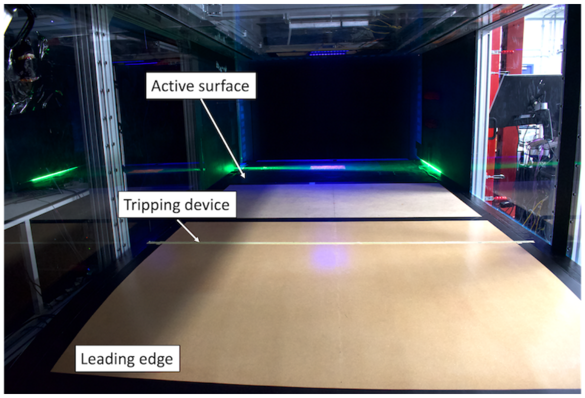

Figure 1: The model in the T2 wind tunnel.

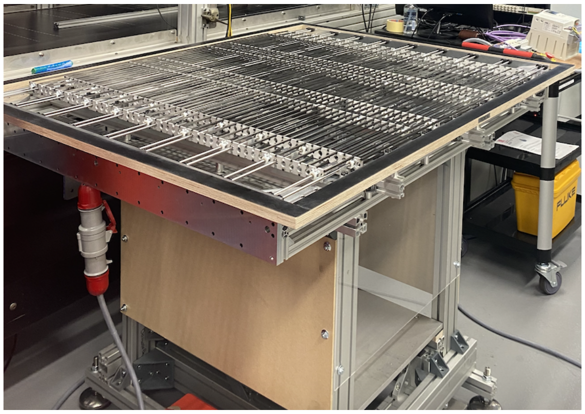

Figure 2: The active surface without the silicone skin.

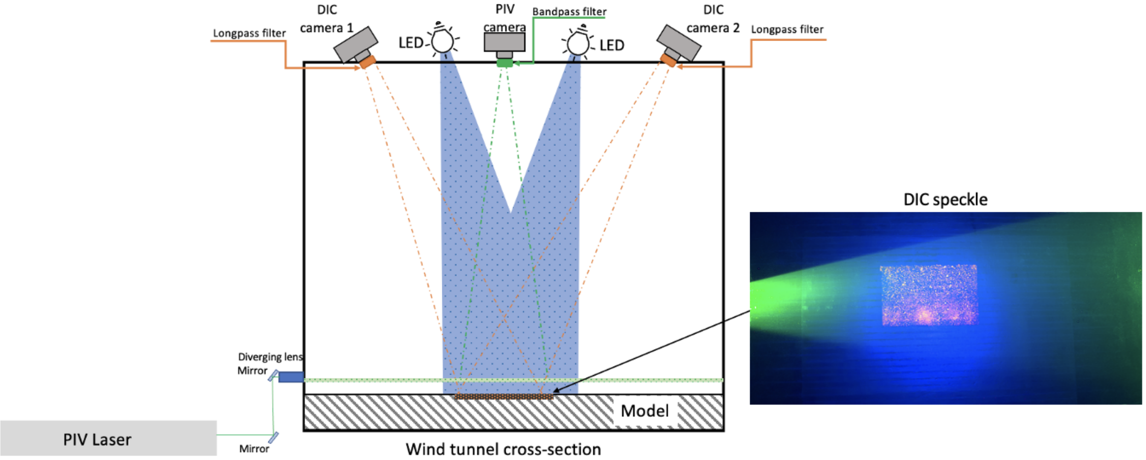

Figure 3: Schematic of the experiment from a cross-section view of the wind tunnel. On the roof the DIC and PIV cameras with filters and the LED blue light. On the side the PIV laser and the optics. The dash lines indicate the field of views of the cameras. On the floor of the tunnel the model with the top surface painted in fluorescent orange.

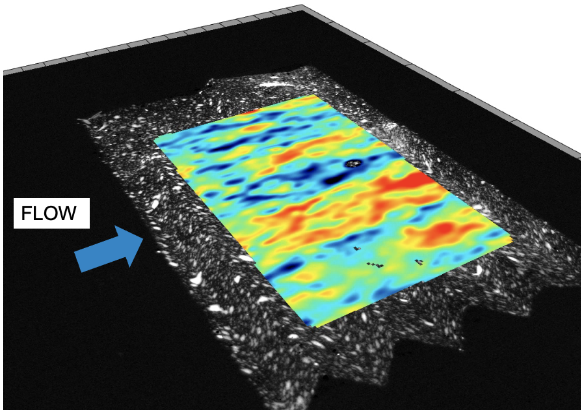

Figure 4: Example of istantaneous DIC and PIV at the maximum deformation of the silicone skin.

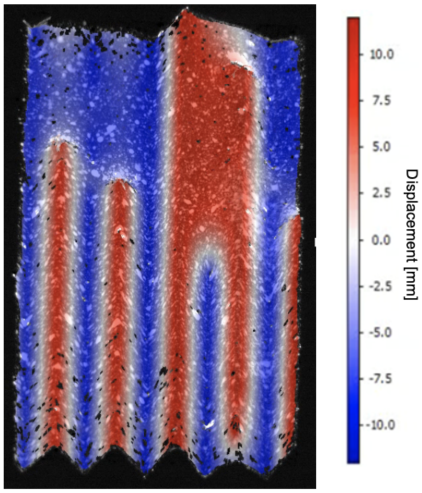

Figure 5: Example of DIC photos (background) with processed displacement on top. Flow is left to right

**Joint ERCOFTAC/EU-CTFF**
**European Drag Reduction and Flow Control Meeting – EDRFCM 2022**
**September 6th–9th, 2022, Paris, France**

# TURBULENT DRAG REDUCTION BY SPANWISE WALL FORCING AT HIGH REYNOLDS NUMBERS

**D. Chandran[1], A. Zampiron[2], A. Rouhi[3], M. K. Fu[4], D. Wine[5],**
**A. J. Smits[6], I. Marusic[1]**
[1]Department of Mechanical Engineering, University of Melbourne, Victoria 3010, Australia
[2] School of Engineering, University of Aberdeen, Aberdeen, UK
[3]Department of Engineering, School of Science and Technology, Nottingham Trent University, Nottingham, UK
[4]Graduate Aerospace Laboratories (GALCIT), Caltech, Pasadena, CA, USA
[5]Intellectual Ventures, Bellevue, WA, USA
[6]Department of Mechanical and Aerospace Engineering,Princeton University, Princeton, NJ, USA

In the present study, we report the measurements of skin-friction drag reduction in high-Reynolds-number turbulent boundary layers. A custom-built surface actuation test bed (SATB) [3] actuates the boundary layer by generating streamwise travelling surface waves of spanwise velocity [2, 6], and the actuation scheme is tested at friction Reynolds numbers ranging from 4500 to 15000. We use a variety of experimental techniques including hot-wire anemometry, drag balance and stereo-PIV (particle image velocimetry) to (i) measure the changes to the skin-friction drag due to the wall-actuation and (ii) examine how the wall-actuation affects the turbulence statistics and the scale-specific turbulence, both near the wall and in the logarithmic region of the turbulent boundary layer.

In the experiments, the wall-actuation is implemented by replacing a 2.4 m × 0.7 m section of the wind tunnel surface with the SATB. As shown by the schematic in figure 1, SATB comprises a series of 50 mm-wide slats that oscillate in the spanwise direction in a synchronous manner to produce an upstream travelling wave of spanwise velocity, $w_s$. The actuation is given by,

$$w_s(x,t) = A\sin\left(\kappa_x x - \frac{2\pi}{T_{osc}}t\right), \tag{1}$$

where, $A$ and $T_{osc}$ are the amplitude and time period of spanwise oscillation, respectively, and $\kappa_x = 2\pi/\lambda$ is the streamwise wavenumber of the travelling wave. Streamwise, wall-normal and spanwise coordinates are denoted by $x$, $y$, and $z$, respectively, and $t$ is time. The design of SATB and the parametric space of actuation, $[A,\, T_{osc},\, \kappa_x]$, have been carefully considered to selectively target the flow structures that make a significant contribution to the wall shear stress ($\tau_w$) at high Reynolds numbers.

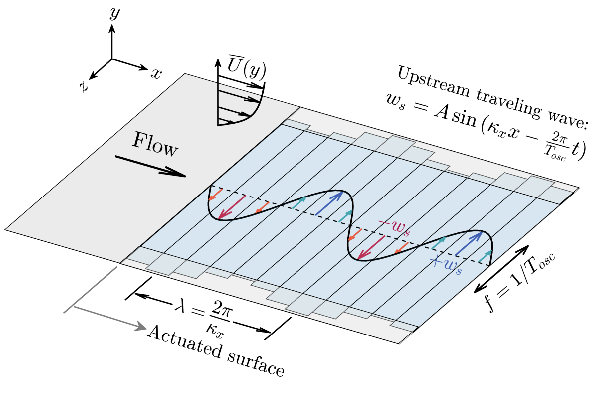

Figure 1: Schematic of the wall-actuation scheme. A 2$\lambda$-section ($\lambda$ = 0.3 m) of the 8-$\lambda$ long SATB is shown which actuates a boundary layer flow. The boundary layer has a mean streamwise velocity profile $\overline{U}(y)$.

Reynolds number is the important non-dimensional parameter that describes the range of length and time scales of turbulent motions present in the current flow. Specifically, friction Reynolds number is defined as $Re_\tau = \delta\, u_{\tau 0}/\nu$, and indicates the separation of length scales in the flow that ranges from $\mathcal{O}(\nu/u_{\tau 0})$ (viscous length scale) to $\mathcal{O}(\delta)$. Here, $\nu$ is the kinematic viscosity of the fluid, $u_{\tau 0}$ is the friction velocity of a non-actuated flow and $\delta$ is the boundary layer thickness. Consequently, at high $Re_\tau$, a broader range of turbulent scales contribute to the skin-friction drag. Figure 2 shows the pre-multiplied wall shear stress spectra ($f^+\phi^+_{\tau\tau}$) for $Re_\tau$ ranging from $10^3$ to $10^6$ [3]. The spectra show the contribution to the intensity of $\tau_w$ by turbulent motions of different time scales ($T^+ = Tu^2_{\tau 0}/\nu$). Based on the work of Mathis et al. [4], a spectral-cut-off of $T^+ = 350$ is used to decompose the spectra into the $Re_\tau-$invariant contribution from the small, viscous-scaled motions ($T^+ < 350$, grey-shaded region) and the $Re_\tau-$dependent contribution from the large, inertial, outer region structures ($T^+ > 350$, blue-shaded regions). The contribution of large-scale motions to $\tau_w$ increases with $Re_\tau$, nominally as $\ln(Re_\tau)$, from about 8% at $Re_\tau = 10^3$

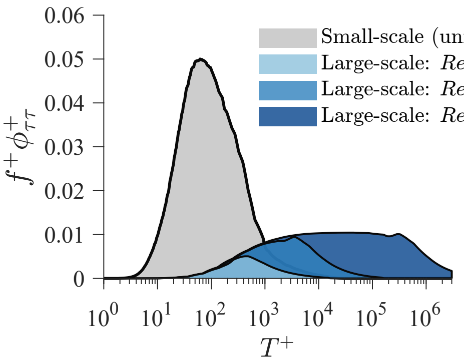

Figure 2: The contributions of viscous small-eddies (grey) and inertial large-eddies (blue) to the pre-multiplied spectra of the wall stress $\tau_w$ computed using predictive models [3] at $Re_\tau = 10^3$, $10^4$ and $10^6$.

to about 35% at $Re_\tau = 10^6$. Based on this, in our previous work [3], we presented two distinct pathways to achieve turbulent drag reduction for high-Reynolds-number flows - (i) the 'small-eddy actuation' that targeted the high-frequency ($T^+ < 350$) viscous-scaled events (grey-shaded region in figure 2) and (ii) the 'large-eddy actuation' that targeted the low-frequency ($T^+ > 350$) inertial-scale motions (blue-shaded regions in figure 2) and required significantly lower input power. Here, to make the terminologies more precise, the 'small-eddy actuation' and the 'large-eddy actuation' are renamed as 'viscous-eddy actuation' (VEA) and 'inertial-eddy actuation' (IEA), respectively.

In the present study, based on the combined operational envelope of the wind tunnel and the SATB, we investigate the actuation scheme for $4500 \lesssim Re_\tau \lesssim 15000$, and across the parameter space: $81 < T^+_{osc} < 1975$, $1.5 < A^+ < 16.3$ and $0.00046 < \kappa^+_x < 0.0018$, thereby enabling us to study both VEA and IEA pathways. Here, $T^+_{osc} = T_{osc}\, u^2_{\tau 0}/\nu$, $A^+ = A/u_{\tau 0}$ and $\kappa^+_x = \kappa_x\, \nu/u_{\tau 0}$. At $Re_\tau = 4500$, a peak $DR \approx 24\%$ is achieved with VEA at $T^+_{osc} \approx 100$ and for $A^+ \approx 13$ (figure 3). The time scale of this actuation corresponds to the time scale of the near-wall streaks that contribute to the peak in figure 2. However, by also factoring in the power input for the actuation which is calculated using the generalised Stokes layer theory [5], the above VEA is observed to incur negative net power savings ($NPS$) of $-40\%$ (i.e., a net power cost). In the VEA regime, the net power cost is found to increase further up to almost $NPS = -85\%$ as $T^+_{osc}$ is reduced below roughly 100. Instead, while the time period of actuation is increased beyond $T^+_{osc} = 350$ to target the IEA pathway, positive net power savings of $NPS = +7\%$ is achieved with a moderate $DR = 9\%$. A similar trend is observed at a higher $Re_\tau = 9700$, where IEA consistently results in positive net power savings in the range $4\% \leq NPS \leq 9\%$, which corresponded to $17\% \geq DR \geq 7\%$. It is important to note that the positive $NPS$ are achieved here with modest amplitudes, $7.8 \geq A^+ \geq 1.5$. At even higher $Re_\tau$, the energy-efficiency offered by the IEA pathway improves further [3].

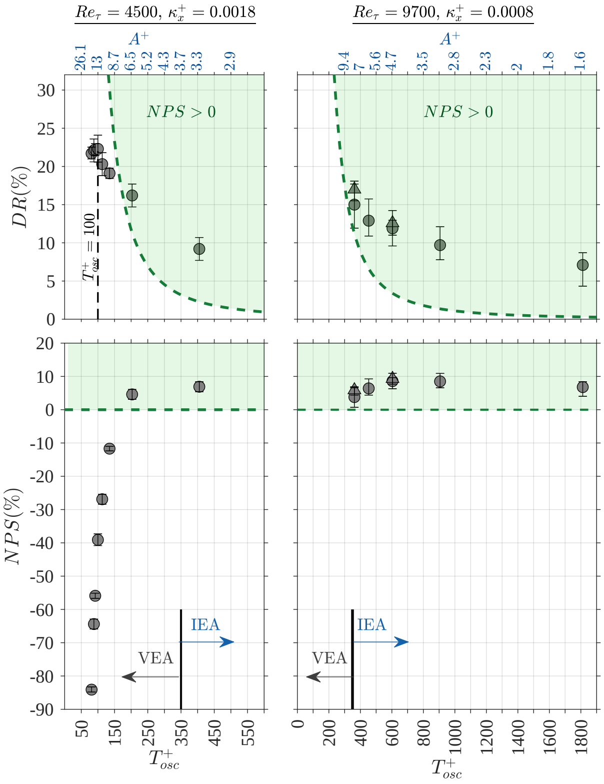

Figure 3: Drag reduction ($DR$) and net power savings ($NPS$) as function of $T^+_{osc}$ and $A^+$ for $Re_\tau = 4500$ and 9700. The circles and triangles represent the hot-wire data and drag balance data, respectively. The dashed green curves correspond to $NPS = 0$. The error bars indicate one standard deviation uncertainty ranges.

In addition to the drag measurements, we will present the results obtained from the three-component, stereo-PIV measurements. In the PIV measurements, we focus on the effect of actuation on the turbulence statistics and scale-specific energy distribution (spectrogram) at wall-heights up to the end of the logarithmic region. The observed attenuation of the turbulent stresses and the attenuation in the spectrogram across a broad range of scales, due to the actuation, suggest a complex inter-scale interaction between the viscous-scaled and the inertial-scaled motions. For example, although IEA directly targets the large-scales, it is also observed to attenuate the wall stress fluctuations associated with the small, viscous-scaled eddies. At higher Reynolds numbers, when the large-scale and very-large-scale motions emerge and contribute meaningfully to the drag composition of the flow, this inter-scale coupling is expected to be significant. Further to exploiting its significantly lower input power requirements, leveraging this coupling would make IEA a potential candidate for energy-efficient drag reduction at high Reynolds numbers [3].

A detailed analysis of the inter-scale coupling between the viscous-scaled and the inertial-scaled eddies for this actuation strategy will be presented by Deshpande et al. [1] in an accompanying talk.

## REFERENCES

[1] R. Deshpande, D. Chandran, A. J. Smits, and I. Marusic. Towards energy-efficient drag reduction through enhancing the inter-scale coupling. In *EDRFCM-2022, Paris, France*, 2022.

[2] D. Gatti and M. Quadrio. Reynolds-number dependence of turbulent skin-friction drag reduction induced by spanwise forcing. 802:553–582, 2016.

[3] I. Marusic, D. Chandran, A. Rouhi, M. K. Fu, D. Wine, B. Holloway, D. Chung, and A. J. Smits. An energy-efficient pathway to turbulent drag reduction. *Nat. Commun.*, 12(1):1–8, 2021.

[4] R. Mathis, I. Marusic, S. I. Chernyshenko, and N. Hutchins. Estimating wall-shear-stress fluctuations given an outer region input. *J. Fluid Mech.*, 715:163, 2013.

[5] M. Quadrio and P. Ricco. The laminar generalized Stokes layer and turbulent drag reduction. 667:135–157, 2011.

[6] Pierre Ricco, Martin Skote, and Michael A Leschziner. A review of turbulent skin-friction drag reduction by near-wall transverse forcing. *Progress in Aerospace Sciences*, 123:100713, 2021.

**Joint ERCOFTAC/EU-CTFF**
**European Drag Reduction and Flow Control Meeting – EDRFCM 2022**
**September 6th–9th, 2022, Paris, France**

# TOWARDS ENERGY-EFFICIENT TURBULENT DRAG REDUCTION THROUGH ENHANCING THE INTER-SCALE COUPLING

**Rahul Deshpande**[1], **Dileep Chandran**[1], **Alexander J. Smits**[2], **Ivan Marusic**[1]

[1]Dept. of Mechanical Engg., University of Melbourne, Parkville, VIC 3010, Australia
[2]Dept. of Mechanical and Aerospace Engg., Princeton University, Princeton, NJ 08544, USA

Prediction and control of skin friction drag has long been a primary motivation behind the scientific investigation of turbulent wall-bounded flows, which began over a century ago. Despite such concerted efforts from the community, achieving even moderate levels of drag reduction for commercial vehicles such as airplanes and ships has remained a challenge. Some of the primary reasons behind the poor efficacy of drag reduction schemes are associated with the complex flow physics through which the turbulent flow generates drag. This includes (but is not limited to): (i) contribution from a broadband range of turbulent scales or 'eddies', the span of which increases with the friction Reynolds number ($Re_{\tau_o} = \delta U_{\tau_o}/\nu$) of the wall-bounded flow, and (ii) changes in the percentage contribution from these eddies with $Re_{\tau_o}$ [5]. Figures 1(b,c) gives an evidence of the former, by depicting the premultiplied energy spectra ($f\phi_{\tau^+\tau^+}$) of the wall shear stress fluctuations ($\tau_w$) over a broadband range of non-dimensional time scales $T^+$ ($= 1/f^+ = U_{\tau_o}^2/(f\nu)$), for zero-pressure gradient (ZPG) turbulent boundary layers (TBL) at two different $Re_{\tau_o}$. Here, $f$ is the frequency of turbulent scales, $\delta$ is the boundary layer thickness, $\nu$ is the kinematic viscosity and $U_{\tau_o}$ is the skin-friction velocity of the unactuated flow, with the latter two used to normalize the flow in viscous units (indicated by superscript '+'). At low $Re_{\tau_o}$ ($\lesssim \mathcal{O}(10^3)$), eddies corresponding to small time scales ($T^+ < 350$; henceforth referred as small eddies), which are associated predominantly with the viscous-scaled near-wall turbulence cycle, are the dominant contributors to the drag [5]. This scenario, however, changes with the increase in $Re_{\tau_o}$, which leads to a logarithmic increase in contribution from the inertia-dominated large eddies ($T^+ > 350$; [4]). This makes both the viscous and inertial-eddy contributions statistically significant when considering the net skin-friction drag generated over a ship or an airplane ($Re_{\tau_o} \gtrsim \mathcal{O}(10^5)$). Thus, the success of a flow control scheme for the transportation industry depends on its ability to attenuate $\tau_w$-fluctuations across such a broad range of scales. Further to that, the control mechanism should be able to deliver net power savings, i.e. the power spent in actuating/controlling the flow should be less than that saved by reducing the drag.

One flow control mechanism that promises net power savings for high $Re_{\tau_o}$ wall-bounded flows is through the spanwise oscillation of the wall elements [3], wherein the oscillating wall elements are synchronized in a manner to produce an upstream traveling wave with respect to the mean flow direction. Figure 1(a) presents a schematic of the control strategy employed by Marusic et al. [3], where the instantaneous spanwise velocity ($w_s$) imposed on the wall can be defined as: $w_s(x,t) = A \sin(\kappa_x x - 2\pi f_{osc} t)$. Here, $f_{osc}$ and $A$ are respectively the frequency and amplitude of the spanwise oscillation and $\kappa_x = 2\pi/\lambda$ is the streamwise wavenumber of the traveling wave generated by the synchronized oscillation of the wall elements. In the present study, we denote $u$, $v$ and $w$ as the velocity fluctuations along the streamwise ($x$), wall-normal ($y$) and spanwise ($z$) directions, respectively, while $t$ denotes time. This control mechanism has been investigated extensively in the past [6] predominantly for its ability to achieve drag reduction (DR) through actuation of the viscous-scaled small eddies, which we will refer to here as the viscous-eddy actuation strategy (VEA; figures 1(b,d)). However, oscillating the wall elements at such small time periods incurs a significantly large power requirement (i.e. no net power savings), thereby making it unsuitable for implementation at high $Re_{\tau_o}$. Based on the premise that the large-scale inertial contributions to the turbulent skin-friction increases with $Re_{\tau_o}$ [4], Marusic et al. [3] recently discovered that spanwise wall-actuation targeting these large-scales can also yield DR in case of a high $Re_{\tau_o}$ flow (figures 1(c,e)). More importantly, the power requirement to actuate at the corresponding large $T^+$ is significantly smaller, which makes this 'inertial-eddy actuation strategy' (IEA) energy efficient (i.e. net power savings are feasible). Interested readers can attend the accompanying talk of Chandran et al.[1] for a comprehensive description of the novel experimental set-up and measurements reported in [3]. It is to be noted here that the VEA and IEA strategies defined here were originally referred to as the 'small-eddy' and 'large-eddy' actuation strategies, respectively by Marusic et al.[3]. However, we believe that this new terminology is more precise in terms of description of the eddies being targeted by the actuation.

Interestingly, Marusic et al. [3] also noted that the turbulent DRs achieved from both the VEA and IEA strategies are associated with energy attenuation across a broadband range of scales (figures 1(b,c)). This scale range overlaps with the energy containing hierarchy in a high-$Re_{\tau_o}$ TBL, spanning from the viscous-scaled small eddies to the inertial large eddies. This observation suggests that the spanwise wall-actuation, although enforced at a specific frequency $f_{osc}$, 'activates' a mechanism that facilitates enhanced coupling between the inertial and viscous-scaled eddies in the flow, thereby making this broadband attenuation possible. The percentage attenuation of energy, however, can be noted to be varying from scale to scale for each strategy (figures 1(d,e)). Interestingly, in case of IEA, a significant portion of the DR is in fact associated with the attenuation of the viscous-scales ($\sim$ 40% at $T^+ \sim 100$) as compared to that for the inertial eddies ($\sim$ 20% at $T^+ \sim 600$). One can thus infer that the enhanced inter-scale coupling is key to the success of the IEA strategy, since it facilitates a substantial attenuation of major drag contributing viscous-scales despite the flow being actuated at the large scales (at much less power).

This presentation discusses the mechanism that enhances

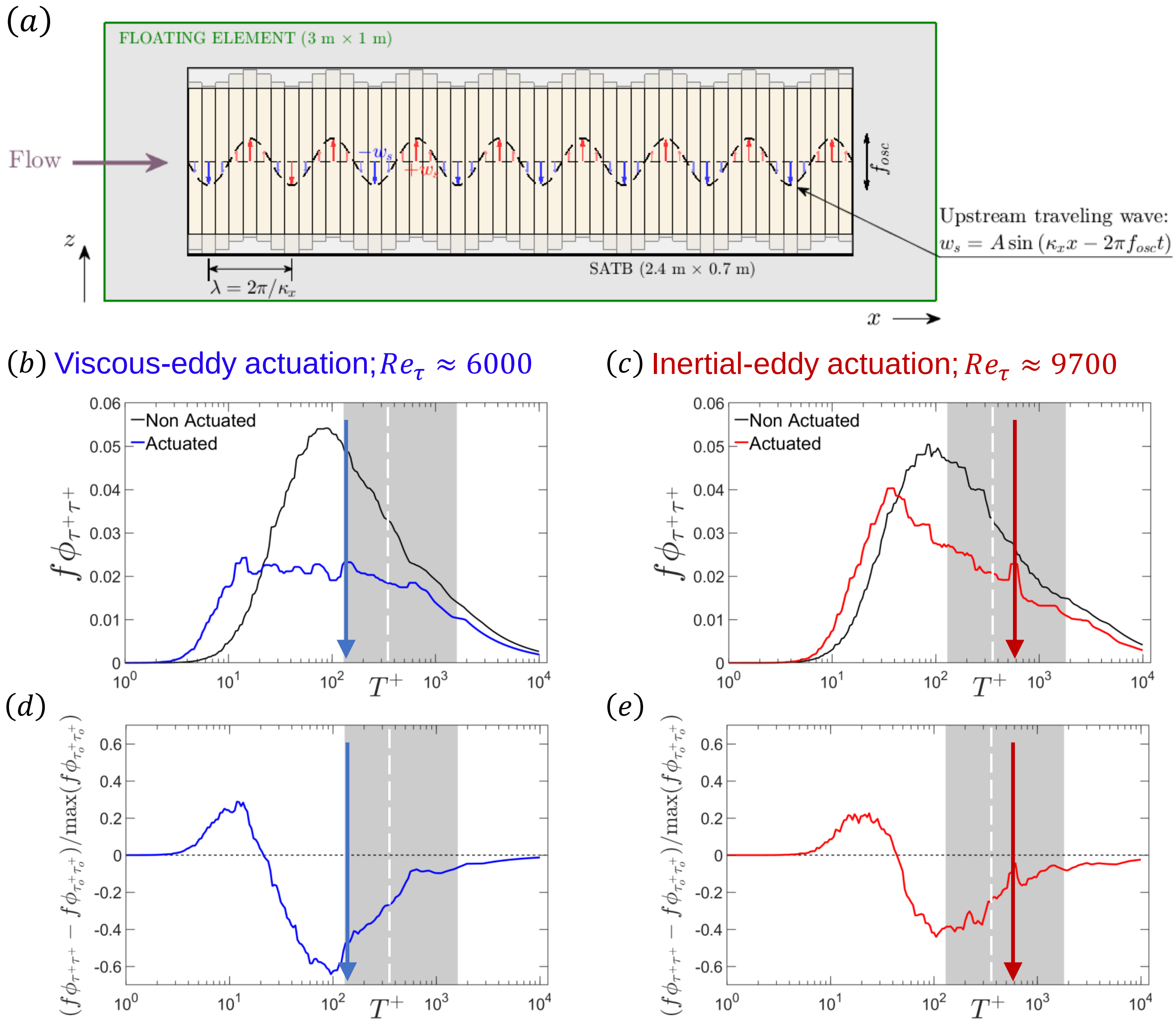

Figure 1: (a) Schematic of the spanwise wall-actuation scheme employed by Marusic et al. [3]. (b,c) Premultiplied spectra of the $\tau_w$ with (in color) and without (in black) wall-actuation, as reported in [3]. The spectra has been normalized by the skin-friction velocity of the corresponding non-actuated case, $U_{\tau_o}$. (d,e) shows the difference between the two curves in (b,c) respectively, normalized by the spectra from the unactuated case. (b,d) corresponds to VEA with parameters: $T^+_{osc} \approx 140$, $A^+ \approx 12$, $k^+_x \approx 0.0014$ for a ZPG TBL at $Re_{\tau_o} \approx 6\,000$, while (c,e) corresponds to IEA with parameters: $T^+_{osc} \approx 604$, $A^+ \approx 4.6$, $k^+_x \approx 0.0008$ for a ZPG TBL at $Re_{\tau_o} \approx 9\,700$. Grey background in (b-e) represents the hierarchy of energy-containing scales between the inner (viscous) and outer (inertial) spectral peak at the respective $Re_{\tau_o}$. Dashed white line indicates nominal demarcation between viscous and inertial-eddy time-scales, $T^+_c = 350$ while the arrow indicates the wall-oscillation time scale, $T^+_{osc}$.

this inter-scale coupling for both the VEA and IEA spanwise wall actuation strategies. The investigation follows the framework laid out in the literature by McKeon and co-workers[2], who studied the changes in the inter-scale coupling for a ZPG TBL perturbed by spatially impulsive dynamic wall roughness. This effort forms the first step towards a broader and more ambitious goal of leveraging the inter-scale interactions to optimize the energy-efficient turbulent DR, via the newly discovered IEA strategy.

## REFERENCES

[1] D. Chandran, A. Zampiron, A. Rouhi, M. K. Fu, D. Wine, A. J. Smits, and I. Marusic. *EDRFCM-2022*, Paris, FRA.

[2] I. Jacobi, D. Chung, S. Duvvuri, and B. J. McKeon. *J. Fluid Mech.*, 914:A7, 2021.

[3] I. Marusic, D. Chandran, A. Rouhi, M. K. Fu, D. Wine, B. Holloway, D. Chung, and A. J. Smits. *Nat. Comm.*, 12:1–8, 2021.

[4] R. Mathis, I. Marusic, S. I. Chernyshenko, and N. Hutchins. *J. Fluid Mech.*, 715:163–180, 2013.

[5] R. Örlü and P. Schlatter. *Phys. Fluids*, 23:021704, 2011.

[6] P. Ricco, M. Skote, and M. A. Leschziner. *Prog. Aero. Sciences*, 123:100713, 2021.

**Joint ERCOFTAC/EU-CTFF**
**European Drag Reduction and Flow Control Meeting – EDRFCM 2022**
**September $6^{\text{th}}$–$9^{\text{th}}$, 2022, Paris, France**

# TURBULENT DRAG REDUCTION USING SPANWISE FORCING IN COMPRESSIBLE REGIME

**F. Gattere, A. Chiarini, M. Zanolini**
Dip. Scienze e Tecnologie Aerospaziali, Politecnico di Milano, 20156 Milano, Italy

**D. Gatti**
Institute for Fluid Mechanics, Karlsruhe Institute of Technology, 76131 Karlsruhe, Germany

**M. Bernardini**
Dip. di Ingegneria Meccanica e Aerospaziale, Roma La Sapienza Univ, 00184 Roma, Italy

**M. Quadrio**
Dip. Scienze e Tecnologie Aerospaziali, Politecnico di Milano, 20156 Milano, Italy

## ABSTRACT

This work addresses the natural extension of streamwise travelling waves of spanwise velocity to the compressible subsonic and supersonic regime. Three values of the bulk Mach number $M_b = 0.3, 0.8$ and 1.5 are investigated with a set of 252 direct numerical simulations (DNS) at friction Reynolds number of $Re_\tau = 200$ and $Re_\tau = 400$. The maximum drag reduction is found to increase with the Mach number. For a supersonic flow the maximum drag reduction occurs at larger frequencies and larger wavenumbers compared to the incompressible data. In the limit of oscillating wall, however, the opposite trend is observed, with the peak moving towards lower frequencies as the Mach number increases, confirming the results of other authors.

## BACKGROUND

Drag reduction strategies can be classified into two categories, namely passive and active. The former usually needs a deformation of the surface of the wall without the need for energy supply. Among passive technologies, riblets are the closest to be implemented in practical applications. Laboratory tests showed that they can reduce drag up to 8%, but they have the main drawback of needing continuous maintenance. Among active strategies, the ones concerning the motion of the walls are the most promising. This work focuses on the technique of the streamwise travelling waves of spanwise velocity [5] defined by the spanwise velocity forcing at the wall $w_w(x,t) = A\sin(\kappa_x x - \omega t)$, where $A$ is the amplitude, $\kappa_x$ is the wavenumber and $\omega$ is the frequency, which define the wavelength $\lambda_x = 2\pi/\kappa_x$ and the period of the oscillation $T = 2\pi/\omega$. The spanwise oscillating wall [3] and the stationary wave [6] can be considered as two limit cases of these travelling waves when $\kappa_x = 0$ and $\omega = 0$, respectively. The numerical experiments of [5] in an incompressible turbulent channel flow at $Re_\tau = 200$ showed a maximum drag reduction of 48% in correspondence of a net power saving of 17% for $A^+ = 12$; the + superscript indicates wall units.

To estimate the real potential of skin friction drag reduction via spanwise wall oscillation in real applications it is of paramount importance to take into account the effects of compressibility. Recently, [7] carried out a DNS study of a compressible channel flow subjected to spanwise oscillating walls ($\kappa_x = 0$) at Mach number $M_b = 0.3, 0.8$ and 1.5, $Re_\tau = 200$, $A^+ = 12$ and $T^+ = 25 - 300$. The drag reduction rate was found to increase with the Mach number and the optimum period to shift toward higher values with respect to incompressible data. The higher Mach simulations, however, led to an anomalous monotonic increase of DR with frequency, which required further investigations for different Reynolds numbers and domain sizes. This particular behaviour was found to depend on low Reynolds effect and relaminarization problems, which can be produced by a too small domain for a given value of $Re_\tau$, or to an excessive value of $Re_\tau$ for a given domain.

The present work is the first comprehensive extension of the streamwise travelling waves drag reduction technique to the compressible regime for both $\kappa_x \neq 0$ and $\omega \neq 0$. [4] already performed a direct numerical simulation of streamwise travelling waves on the surface of an airfoil in transonic regime, investigating the effect of the actuation on the aerodynamic forces. However, a parametric study to assess the dependence of the Mach number on the drag reduction performances still lacks. In this work we aim to fully characterise the dependence of both the drag reduction rate and the power budgets on the Mach number varying the parameters of the travelling wave applied to the wall of a fully developed turbulent channel flow.

## METHODS

A database of direct numerical simulations is computed for this analysis using STREAmS (Supersonic TuRbulEnt Accelerated Navier–Stokes Solver), a high-fidelity solver for large-scale simulations of compressible turbulent wall-bounded flows developed by [1]. Three sets of simulations at different values of the bulk Mach number $M_b = 0.3, 0.8$ and 1.5 are performed to assess the effects of the compressibility on the behaviour of a fully developed turbulent channel flow subjected to streamwise travelling waves of spanwise oscillation. For all cases the Prandtl number is set to $Pr = 0.72$. For each value of the imposed bulk Mach number, two sets of direct numerical simulations are performed, with initial friction Reynolds numbers $Re_\tau = u_\tau h/\nu$ set at $Re_\tau = 200$ and $Re_\tau = 400$; here $u_\tau$ is the friction velocity, $h$ is the channel semi-height and $\nu$ is the kinematic viscosity. For each one of the six sets of simulations described above, a single uncontrolled and 42 controlled simulations have been performed. The wave amplitude

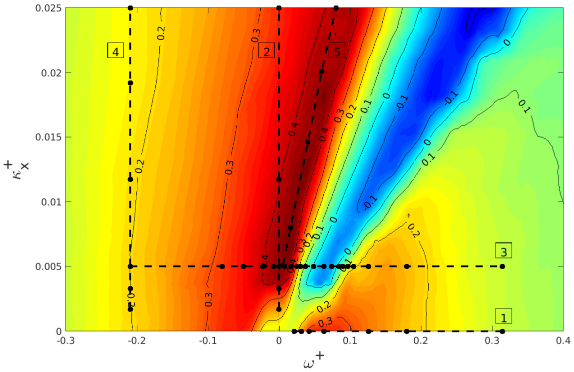

Figure 1: Control map of the drag reduction rate DR (adapted from [5]). The dashed lines are the investigated regions and the black dots correspond to the actual simulations.

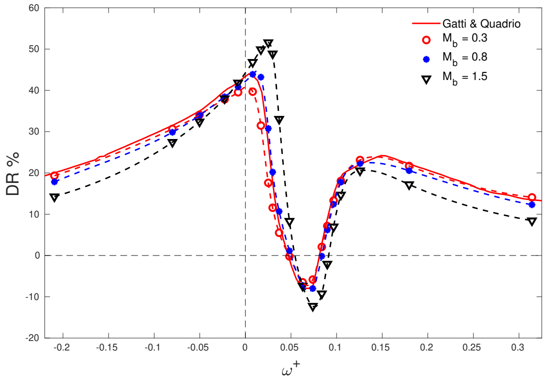

Figure 2: Percentage of DR versus frequency $\omega^+$ for the streamwise-travelling waves at $A^+ = 12$ and $\kappa_x^+ = 0.005$ (line 3) for $Re_\tau = 400$. The red solid line represents the incompressible reference data [2].

is fixed at $A^+ = A/u_\tau = 12$, while different combinations of the $(\omega, \kappa_x)$ values are selected. Figure 1 reports the DR map for the incompressible regime, where the control parameters of each simulations (black dots) are chosen. The dashed line 1 refers to the oscillating wall case with $\kappa_x = 0$, while the dashed line 2 to the steady wave with $\omega = 0$. Line 3 considers a constant wavelength and sets $\kappa_x^+ = 0.005$. Line 4 investigates the area of low drag reduction and fixes the oscillating frequency at $\omega^+ = -0.21$. Finally, line 5 analyses the optimum ridge for drag reduction. The size of the computational domain is $(L_x, L_y, L_z) = (6\pi h, 2h, 2\pi h)$ in the streamwise, wall-normal and spanwise directions. For the $Re_\tau = 400$ cases the number of mesh points in the three directions is $N_x = 768$, $N_y = 258$, $N_z = 528$ for the subsonic regime and $N_x = 1024$, $Ny = 258$, $Nz = 512$ for the supersonic regime. For $Re_\tau = 200$, instead, half the number of points is used in each direction. In wall units this corresponds to a mesh spacing of $\Delta x^+ = 9.8$, $\Delta y^+ = 0.51 - 6.35$, $\Delta z^+ = 4.8$ and $\Delta x^+ = 7.4$, $\Delta y^+ = 0.50 - 6.19$, $\Delta z^+ = 4.9$.

## RESULTS

As an example figure 2 shows of the effect of the $M_b$ numbers along line 3 in figure 1 for $Re_\tau = 400$ and investigates the effect of compressibility in regions of the $(\kappa_x, \omega)$ map where both drag reduction (DR) and drag increase (DI) may occur.

The DR trend for low compressible regime is in good agreement with [2], with a non-negligible mismatch only for $\omega^+ \approx 0$. Compressibility shows two main positive effects on the drag reduction performance of the travelling waves. First, the DR increases between slightly small negative value of $\omega$ and $\omega^+ \approx 0.05$, whereas decreases elsewhere. This is a promising result since it outlines an improvement in the drag reduction for increasing $M_b$ precisely in the region of interest of the control map, i.e. near the peak, while the performance worsens in the regions of minor interest. Second, the global peak shifts at larger $\omega^+$, whereas the second positive peak shifts at smaller $\omega^+$, shrinking the DI zone and consequently, widening the values of frequency for which the control is effective. However, the DI peak also shows increasing negative values with increasing $M_b$ and it shifts towards larger $\omega^+$. Overall, for the low and moderate Mach number, the drag reduction peak occurs for an oscillation frequency of $\omega^+ = 0.008$ and reads $DR_{max} = 40\%$ and $DR_{max} = 44\%$ for $M_b = 0.3$ and $M_b = 0.8$ respectively. For the supersonic regime, instead, the peak occurs at higher frequency, i.e. $\omega^+ = 0.025$ and for $M_b = 1.5$ reaches the large value of $DR_{max} = 52\%$.

In the case of active control, information about the drag reduction is not sufficient to fully assess the efficiency of a technique, being also the energy expenditure to control the flow a parameter to be considered. Therefore, the balance between the cost, i.e. the energy injected to the system to move the walls, and the benefits, i.e. the reduction of the skin friction drag, has to be examined. Generally the cost to control the flow $|P_{in}|$ decreases with increasing values of the Mach number, thus compressibility shows a positive effect also on the energy expenditure and this effect is larger for increasing values of the control frequency.

## REFERENCES

[1] M. Bernardini, D. Modesti, F. Salvadore, and S. Pirozzoli. STREAmS: A high-fidelity accelerated solver for direct numerical simulation of compressible turbulent flows. *Comput. Phys. Commun.*, 263:107906, 2021.

[2] D. Gatti and M. Quadrio. Reynolds-number dependence of turbulent skin-friction drag reduction induced by spanwise forcing. *J. Fluid Mech.*, 802:553–58, 2016.

[3] W.J. Jung, N. Mangiavacchi, and R. Akhavan. Suppression of turbulence in wall-bounded flows by high-frequency spanwise oscillations. *Phys. Fluids A*, 4 (8):1605–1607, 1992.

[4] M. Quadrio, A. Chiarini, J. Banchetti, D. Gatti, A. Memmolo, and S. Pirozzoli. Drag reduction on a transonic airfoil. *J. Fluid Mech.*, 942, 2022.

[5] M. Quadrio, P. Ricco, and C. Viotti. Streamwise-traveling waves of spanwise wall velocity for turbulent drag reduction. *J. Fluid Mech.*, 627:161–178, 2009.

[6] M. Quadrio, C. Viotti, and P. Luchini. Skin-friction drag reduction via steady streamwise oscillations of spanwise velocity. In J.M.L.M. Palma and Silva Lopes A., editors, *Advances in Turbulence XI*, Advances in Turbulence XI, pages 659–661. Springer, Berlin, 2007.

[7] J. Yao and F. Hussain. Supersonic turbulent boundary layer drag control using spanwise wall oscillation. *J. Fluid Mech.*, 880:388–429, December 2019.

**Joint ERCOFTAC/EU-CTFF**
**European Drag Reduction and Flow Control Meeting – EDRFCM 2022**
**September 6$^{\text{th}}$–9$^{\text{th}}$, 2022, Paris, France**

# MULTI-FIDELITY SURROGATE MODELLING OF THE NET POWER SAVINGS OF AN ACTUATED TURBULENT BOUNDARY-LAYER

**Paolo Olivucci, Richard Semaan**
Institut für Strömungsmechanik, Technische Universität Braunschweig, Germany

**Marian Albers, Wolfgang Schröder**
Aerodynamisches Institut, RWTH Achen, Germany

## INTRODUCTION

Active wall-motion control for frictional drag reduction in turbulent boundary layer include a range of techniques including spanwise wall oscillations, travelling waves of spanwise velocity, travelling wall-normal deflection and others [8, 5, 7, 9]. Although its effectiveness and adaptability have been established through numerous numerical and experimental studies, most of active wall-based control has, at present, a low level of technological readiness. The net saved energy yield represents a crucial hurdle on the way to practical implementation of active boundary-layer control owing to the power that has to be supplied externally to sustain the wall motion. One promising wall-control actuation technique [5, 10, 1] is the spanwise-travelling surface wave that is defined as a periodic, wall-normal displacement of the wall surface of amplitude $A$ and wavelength $\lambda$ that travels in the spanwise direction with period $T$.

The net power saving (NPS) is obtained by discounting the input power necessary to displace the wall from the power saved through the skin-friction reduction, according to the expression:

$$\mathrm{NPS}(\lambda^+, T^+, A^+) = \mathrm{DR}(\lambda^+, T^+, A^+) - \mathrm{IP}(\lambda^+, T^+, A^+), \tag{1}$$

where DR is the drag reduction rate, IP is the ratio of the power supplied to the wall deformations to the power dissipated by the uncontrolled boundary layer and the superscript '+' indicates scaling in reference inner units.

Such surface waves were found capable of significant drag reductions [1]; positive NPS values of up to about 10% were also found for a range of parameter values different than that in which the highest DR occurs. However, the NPS response topology, the existence of a ridgeline, their sensitivity to the control parameters, and its physical interpretation, were left as open questions. In this work, we address these points with the aid of a data-driven surrogate model of the NPS response to the actuation parameters.

## SURROGATE MODELLING OF NPS

The surrogate model is trained on two qualitatively different data sets. The first, denoted by $\mathcal{D}_{\mathrm{hf}}$, consists of 80 high-fidelity large-eddy simulation data for both DR and IP, for a range of actuation settings [1, 4]. The second set comprises solely input power data for 2400 additional parameter combinations, supplied from low-fidelity two-dimensional simulations of the transverse wall motion, and is denoted by $\mathcal{D}_{\mathrm{lf}}$. Building a regression model from such data presents a twofold challenge: first, the high-resolution data are sparse, suffer from statistical noise and are unevenly distributed across the parameter space; the second set is more abundant, but the information has a lesser degree of reliability and must be combined carefully with the high-fidelity data to yield a predictive advantage.

The surrogate model is constructed using a Gaussian Process (GP) framework [11, 3], which is flexible and provides a model of the uncertainty associated with the predictions:

$$\mathrm{NPS}(\lambda^+, T^+, A^+) \sim \mathcal{GP}_{\mathrm{DR}}(\mathrm{DR}|\mathcal{D}_{\mathrm{hf}}) - \mathcal{GP}_{\mathrm{IP}}(\mathrm{IP}|\mathcal{D}_{\mathrm{lf}}, \mathcal{D}_{\mathrm{hf}}) \tag{2}$$

where $\mathcal{GP}_{\mathrm{DR}}$ is a GP fitted on high-fidelity DR data; $\mathcal{GP}_{\mathrm{IP}}$ is a linear auto-regressive multi-fidelity GP model [6, 2], which is selected as it outperforms other multi-fidelity approaches on the present data. The use of model (2) also potentially enables multi-fidelity Bayesian optimization, alongside with the possibility of recursive modelling using other regression algorithms.

The predictive accuracy of the trained model is assessed via five-fold cross-validation using various metrics, including for the uncertainty model. Good predictive performance is attested by a correlation coefficient greater than 96%, a normalised root-mean-square error lower than 7%, and a mean test log-likelihood of $-8$, which are superior to those achieved using a single-fidelity model.

Exploiting the model prediction, we infer the response topology and examine its dependence to the three actuation parameters. The region of higher NPS values is located at high wavelengths but lower amplitudes and longer periods than the optimal DR. In the high-NPS region, the sensitivity to a change in the parameters is weaker than elsewhere and thus extra care was taken in assessing the model quality in the face of noisy and scarce data. Preliminary results (Fig. 1) reveal the existence of a broad, unique peak, reaching a maximum of NPS = 10.4% around $(T^+, A^+) = (86, 72)$ on the data domain boundary at $\lambda^+ = 3000$. The existence of a ridgeline extending beyond the domain boundaries along the positive $\lambda$ direction is also speculated. Potential for extrapolation beyond the high-fidelity parameter range and physical scaling will also be discussed.

## REFERENCES

[1] M. Albers, P. S. Meysonnat, D. Fernex, R. Semaan, B. R. Noack, and W. Schröder. Drag reduction and energy saving by spanwise traveling transversal surface waves for flat plate flow. *Flow Turbul. Combust.*, 105(1):125–157, 2020.

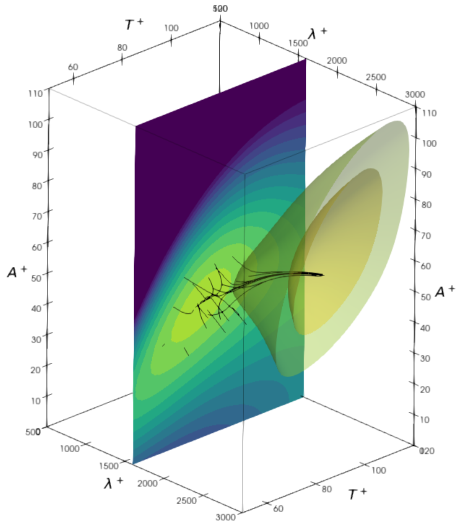

Figure 1: Visualization of the Net Saving Power surrogate model. The two iso-surfaces correspond to the values 6.5% and 8.5%.

[2] L. Brevault, M. Balesdent, and A. Hebbal. Overview of gaussian process based multi-fidelity techniques with variable relationship between fidelities, application to aerospace systems. *Aerosp Sci Technol*, 107:106339, 2020.

[3] D. Duvenaud. *Automatic model construction with Gaussian processes*. PhD thesis, University of Cambridge, 2014.

[4] D. Fernex, R. Semaan, M. Albers, P. S. Meysonnat, W. Schröder, and B. R. Noack. Actuation response model from sparse data for wall turbulence drag reduction. *Phys Rev Fluids*, 5(7):073901, 2020.

[5] M. Itoh, S. Tamano, K. Yokota, and S. Taniguchi. Drag reduction in a turbulent boundary layer on a flexible sheet undergoing a spanwise traveling wave motion. *J Turbul*, 7:N27, 2006.

[6] M. Kennedy and A. O'Hagan. Predicting the output from a complex computer code when fast approximations are available. *Biometrika*, 87(1):1–13, 2000.

[7] S. Klumpp, M. Meinke, and W. Schröder. Drag reduction by spanwise transversal surface waves. *J Turbul*, 11:N22, 2010.

[8] M. Quadrio. Drag reduction in turbulent boundary layers by in-plane wall motion. *Philos Trans R Soc Math Phys Eng Sci*, 369(1940):1428–1442, 2011.

[9] P. Ricco, M. Skote, and M. A. Leschziner. A review of turbulent skin-friction drag reduction by near-wall transverse forcing. *Prog Aerosp Sci*, 123:100713, 2021.

[10] N. Tomiyama and K. Fukagata. Direct numerical simulation of drag reduction in a turbulent channel flow using spanwise traveling wave-like wall deformation. *Physics of Fluids*, 25(10):105115, 2013.

[11] C.K.I. Williams and C.E. Rasmussen. *Gaussian Processes for Machine Learning*. MIT Press, 2006.

**Joint ERCOFTAC/EU-CTFF**
**European Drag Reduction and Flow Control Meeting – EDRFCM 2022**
**September 6$^{\text{th}}$–9$^{\text{th}}$, 2022, Paris, France**

# REYNOLDS STRESSES TRANSPORT IN A TURBULENT CHANNEL FLOW CONTROLLED USING STREAMWISE TRAVELLING WAVES

**M. Umair & S. Tardu**
LEGI, CNRS, Grenoble-INP, Université Grenoble-Alpes, 38400 Saint-Martin d'Hères, France

**O. Doche**
SIMAP-EPM, CNRS, Grenoble-INP, Université Grenoble-Alpes, 38400 Saint-Martin d'Hères, France

## INTRODUCTION

A plethora of investigations, numerical [4, 1, 5] as well as experimental [3, 6], have shown that transverse wall oscillations in the form of streamwise travelling waves (STW) perform far better in reducing skin-friction compared to simple homogeneous wall oscillations (HWO). Recent work of Marusic et al. [3] has shown that a net positive power savings can be attained at very large Reynolds number.

While the focus of most of the previous investigations has been to find a scaling parameter that dictates DR margin, to this date, limited progress is made to reveal the physical insights in the flows controlled by STW.

The objective of the present work is, therefore, to gain further insight into the physical mechanism behind STW control by analyzing and identifying the important interactions occurring within the budgets of Reynolds stresses.

## METHOD

Direct numerical simulations of the incompressible turbulent channel flow were performed at Reynolds number Re=$hU_c/\nu$=4200 (Re$_\tau$=$hu_\tau/\nu$=180), where $h$, $U_c$, $\nu$, and $u_\tau$ are the channel half-width, centerline velocity of Poiseuille flow, kinematic viscosity, and friction velocity, respectively. The flow is subjected to spanwise wall oscillations in the form of STW, given as:

$$W(x, y = 0, z, t) = A\ sin(\kappa x - \omega t), \tag{1}$$

where $A$, $\kappa$, $\omega$ is the amplitude, wave number, angular frequency of the travelling wave, respectively, and $W$ is the instantaneous spanwise velocity. Here, $x$, $y$, $z$ represent the streamwise, wall-normal, spanwise direction, and $t$ is time. The values of $\omega$ and $\kappa$ were kept fixed at 0.16 and 1.66 (outer units), respectively, while $A$ was varied from 0.15 to 1.25 (outer units), resulting in the drag reduction margins ranging from 26% to 58%. To compare the travelling wave effects with the simple homogeneous wall oscillations case (HWO), we opted for HWO optimal configuration with $A = 12$ and $T = 100$ (in wall units based on the $u_\tau$ of the uncontrolled flow).

All the computations were performed using our in-house developed code MULTIFAST which employs explicit optimized schemes for spatial discretization and Runge-Kutta third order method for time integration. The computational box is of size $L_x \times L_y \times L_z = 6\pi h \times 2h \times 3\pi h$, and is covered by $N_x \times N_y \times N_z = 401 \times 129 \times 335$ nodes, distributed uniformly in the streamwise and spanwise directions, and clustered in the wall-normal direction. The corresponding grid resolution is $\Delta x$, $\Delta y$, $\Delta z$ = 8.5, 0.5-5.5, 5 (wall-units), respectively. All the simulations were performed at time-step $dt \leq 10^{-3}$. The statistics of uncontrolled flow were obtained using a total of 50 snapshots covering a time window of 37000 wall-units, separated by 770 wall-units, while statistics of the controlled flow field were derived by using the classical triple decomposition of Hussain and Reynolds [2]. At least 20 initial cycles were discarded pertaining to the initial transient period, and the data was collected for at least 40 cycles corresponding to a time window of 12000 wall-units. The details are given in Umair et al. [6].

## RESULTS

STW forcing results in a substantial decline in the Reynolds stresses components, especially close to the wall. However, a strikingly different response was observed for the mean spanwise component ($\overline{ww}$) shown in Fig. 1(a). When scaled with the friction velocity of the controlled flow, the profiles of $\overline{ww}$ exhibits a second peak near the edge of the viscous sublayer at $y \approx 8$. This is found to be related to the appearance of the two extra production terms related to the streamwise and spanwise gradient of the phase-averaged spanwise velocity, that emerge in the transport equation of $\overline{ww}$. These extra production terms account for the interaction of the phase averaged Reynolds stresses and the gradients of the periodic fluctuations due to forcing. The total production $\overline{P_{ww}}$ (shown in Fig. 1(b)) increases in the low buffer layer, and its maxima is located at the same location where the second peak is observed in $\overline{ww}$. In canonical turbulent flows, the level of the mean spanwise Reynolds stress component $\overline{ww}$ is maintained solely by the inter-component transfer term $\overline{\Pi_{ww}}$, which extracts energy from the streamwise component $\overline{uu}$ and transfer it to $\overline{ww}$. It is observed in Fig. 1(c) that the increase in $\overline{P_{ww}}$ is accompanied by a strong decrease in the $\overline{\Pi_{ww}}$, which is entirely annihilated within the low buffer layer and viscous sublayer for STW of large imposed amplitudes $A \geq 0.5$. Thus, interestingly enough, the communication between $\overline{uu}$ and $\overline{ww}$ is cut off at $y < 8$, and as a consequence $\overline{ww}$ evolves somewhat freely, with a local equilibrium between the production and dissipation, in a rough sense.

The streaky structures in the buffer layer were also strongly modified, especially at large amplitudes. The most spectacular modification occurs in $\partial w/\partial x$ shear layers (shown in Fig. 2), that become strongly inclined in the spanwise direction and alternates between positive and negative values quite coherently. The intensity in these shear layers are related to the major streamwise vorticity production in the low buffer layer, in both the controlled and uncontrolled flows. However, no

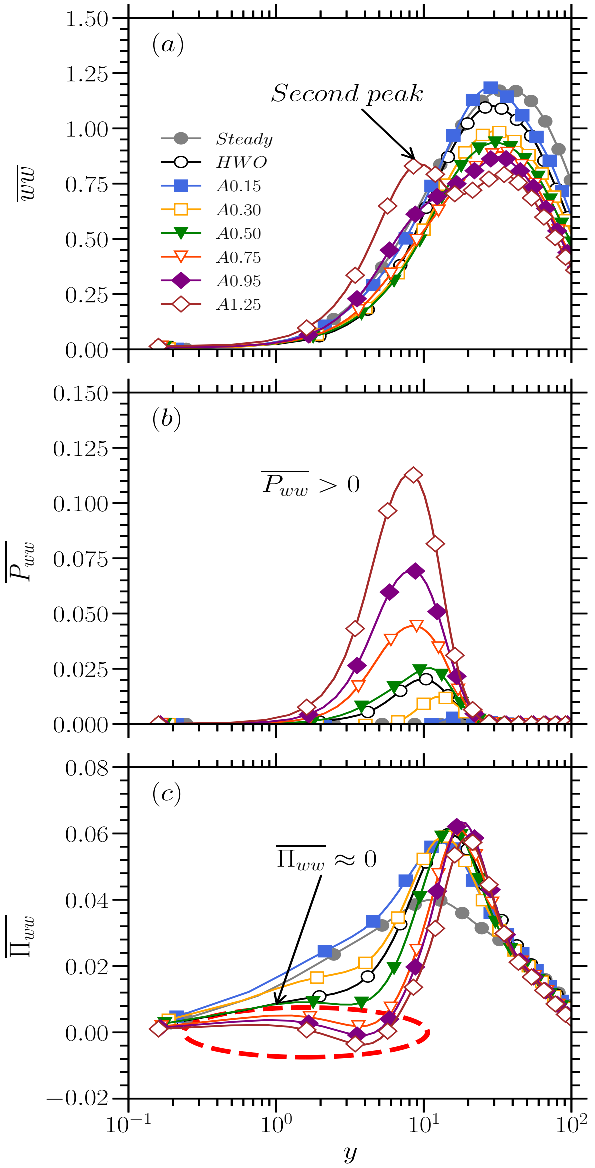

Figure 1: (a) Mean spanwise Reynolds stress component ($\overline{ww}$), its (b) production ($\overline{P_{ww}}$), and (c) inter-component transfer ($\overline{\Pi_{ww}}$) term. All the quantities were scaled by the friction velocity of the controlled flow.

topological signature of these shear layers were observed in the active eddies' regeneration process. Thus, these shear layers do not roll up in the low buffer layer. For $A > 0.75$, the quasi-streamwise vortices (shown in Fig. 3) are organized as packets of several vortices typical of transitional turbulent spots.

At the meeting, we will show more interesting features in the Reynolds stresses transport that are directly related to the streamwise travelling waves.

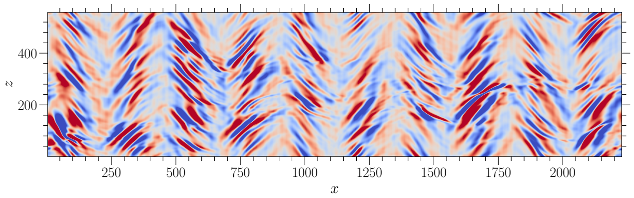

Figure 2: $\partial w/\partial x$ shear layers at $y = 10$ for $A1.25$ case. Blue color: negative values, Red color: positive values. The contours are in the range $-0.1$ to $+0.1$. All the quantities were scaled by the friction velocity of the controlled flow.

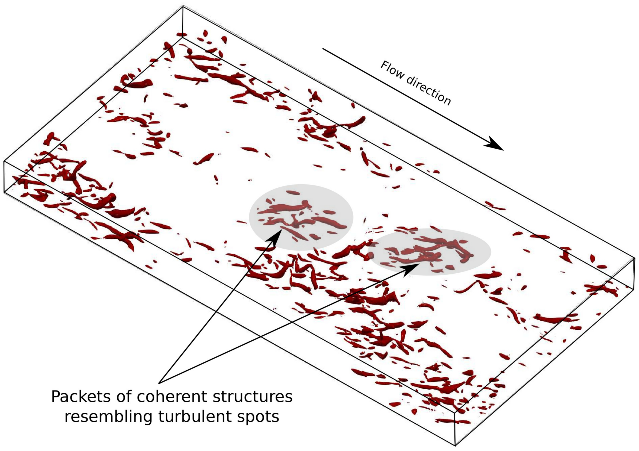

Figure 3: Coherent structures ($\lambda_2 = -0.03$) for A=1.25 case.

## ACKNOWLEDGEMENTS

The simulations of the controlled cases were performed using the GRICAD infrastructure (https://gricad.univ-grenoble-alpes.fr), which is supported by Grenoble research communities, Région Auvergne-Rhône-Alpes (GRANT CPER07_13 CIRA) and the Agence Nationale de la Recherche (Equip@Meso project Reference No. ANR-10-EQPX-29-01 of the programme Investissements d'Avenir).

## REFERENCES

[1] Davide Gatti and Maurizio Quadrio. Reynolds-number dependence of turbulent skin-friction drag reduction induced by spanwise forcing. *J. Fluid Mech.*, 802:553–582, 2016.

[2] A. K.M.F. Hussain and W. C. Reynolds. The mechanics of an organized wave in turbulent shear flow. *J. Fluid Mech.*, 41:241–258, 1970.

[3] Ivan Marusic, Dileep Chandaran, Amirreza Rouhi, Matt K. Fu, David Wine, Brian Holloway, Daniel Chung, and Alexander J. Smits. An energy-efficient pathway to turbulent drag reduction. *Nature Communications*, 12(5805), 2021.

[4] Maurizio Quadrio, Pierre Ricco, and Claudio Viotti. Streamwise-travelling waves of spanwise wall velocity for turbulent drag reduction. *J. Fluid Mech.*, 627:161–178, 2009.

[5] Emile Touber and Michael A. Leschziner. Near-wall streak modification by spanwise oscillatory wall motion and drag-reduction mechanisms. *J. Fluid Mech.*, 693:150–200, 2012.

[6] Mohammad Umair, Sedat Tardu, and Olivier Doche. Reynolds stresses transport in a turbulent channel flow subjected to streamwise traveling waves. *Phys. Rev. Fluids*, 7:054601, 2022.

Joint ERCOFTAC/EU-CTFF
European Drag Reduction and Flow Control Meeting – EDRFCM 2022
September 6th–9th, 2022, Paris, France

# RING-TYPE DBD PLASMA ACTUATOR AT MILLIMETRIC SCALE

**T. Fridlender[1], S. Yadala[1,2], N. Benard[1], and E. Moreau[1]**

[1]Institut PPRIME (CNRS UPR3346, Université de Poitiers, ISAE-ENSMA), Bd Marie and Pierre Curie, BP 30279, 86962 Futuroscope, Poitiers, France

[2]Department of Energy and Process Engineering, Norwegian University of Science and Technology, Trondheim, Norway

## INTRODUCTION

The discipline of flow control has garnered considerable attention from both researchers and engineers alike, as a mean to improve the efficiency of many fluid-mechanic systems. Many flow configurations see their dynamics predominantly governed by hydrodynamic instability mechanisms whose natural amplification of instability waves can be controlled with very low amplitude forcing. Delaying laminar-to-turbulent transition is an example of flow control that exploits the high sensitivity of stationary instabilities to localized perturbation [1, 2]. Sub-critical modes of three-dimensional boundary layers can be amplified and can lead to a delay of the flow transition to turbulence.

Among the proposed solutions attempted to reproduce the influence of periodic perturbations, plasma actuators have been viewed as cost-effective and convenient candidates [3]. In Choi and Kim [4], ring-type DBD plasma actuators are used to successfully re-organized the boundary layer according to the forced stationary instability. This actuator presents a singular behavior as it can produce wall-normal or suction jet depending on the inner diameter of the ring [5, 6, 7].

The objective of this study is to detail the flow physics of ring-type DBD by a close inspection of the flow field using experimental optical measurements as well as high-definition electrical measurements dedicated to a complete description of the efficiency of the system.

## RESULTS

The ring-type DBD plasma actuator is composed of a circular grounded electrode beneath a dielectric plate with a thickness (d) of 2 mm (PCB) and an air-exposed electrode with inner radius (r) ranging from 10.5 down to 1 mm. For all test cases, the AC voltage waveform was sinusoidal with amplitude $V_{ac}$ ranging from 1 to 21 $kV_{amp}$ and carrier frequency fixed at $f_{ac}$ = 1kHz.

The time evolution of voltage and current for a radius of 3 and 10.5 mm is reproduced in Figure 1. The current time evolution shows a typical DBD plasma regime with a streamer regime (a corona zone in contact with the active electrode and an extension from this spot towards the dielectric) followed by a glow regime (cathodic half cycle with a plume shape extension, enlarging from a spot on the electrode to the dielectric). For r/d=5.25, the ionized channels observed in the streamer regime are not as elongated as in a linear DBD because of the reduced electric field in the central region. Intense ionization channels occur during the glow regime in addition to the usual Trichel pulses. At low r/d ratio, the current time evolution clearly exhibits a strong reduction of the number of current positive and negative peaks. As a direct result, the electrical power consumption is greatly affected (Fig. 3). At E = 20 $kV_{amp}$, the power consumption is about 220 W/m for r = 10.5 mm and this quantity is reduced by 80% for a ring radius of 1.5.

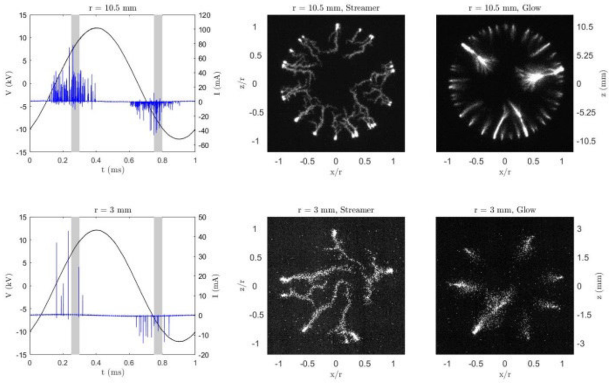

Fig. 1 Voltage and current signals measured by 500 MHz, 12 bit digital oscilloscope and top-view of the plasma by ICCD imaging. The exposure time corresponds to the grey shaded area in voltage/current plots.

The time-averaged flow field measured by PIV is presented in Figure 3. For the larger r/d ratio the flow field corresponds to a wall-normal jet whose central velocity does not exceed 1.8 m/s. The momentum transfer promoted by the discharge in this geometry was then directed towards the center of the geometry. This produces wall jets continuously distributed along the air-exposed electrode edge that collide in the central region of the design to finally form a wall-normal jet with a diameter roughly equal to 2r. By reducing the radius of the design, the flow topology totally differs. In such a configuration, a negative v velocity component and reversed u velocity component are measured. The surrounding flow is now attracted toward the wall and the ring-type actuator acts as a suction device with low fluid flow velocity (0.06 m/s).

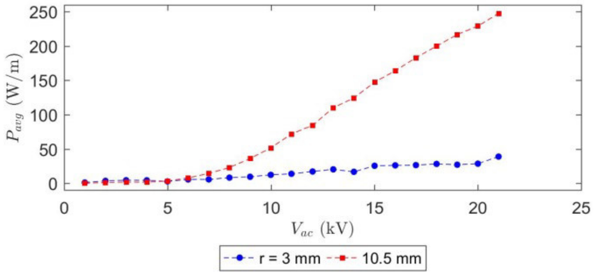

Fig. 2 Time-averaged electrical power consumption of the ring-type DBD for r=3 mm (r/d=1.5) and r=10.5 mm (r/d=5.25).

Similar measurements have been conducted for radius from 10.5 down to 1 mm. Velocity profiles at y/r=1 are shown in Figure 4. By reducing the radius, the central jet flow velocity progressively lowers and a wall-normal jet is reported even for r/d ratio of 2.25. As it was observed from results shown in Figure 3, the flow reversal is observed at r = 3 mm but also at r = 1 mm. However, at r = 1 mm (r/d = 0.5), the velocity magnitude of the fluid attracted toward the wall is only about a few cm/s.

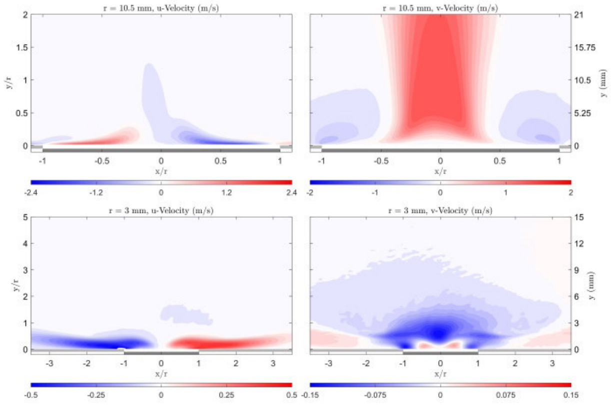

Fig. 3 Time-averaged spatial distribution of the fluid flow velocity components u and v (E=12 kV, $f_{ac}$=1000Hz).

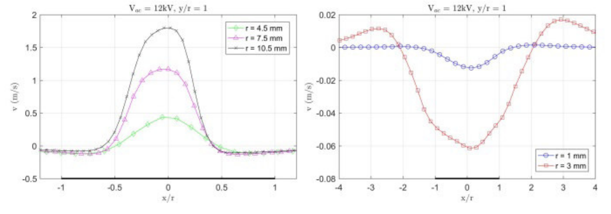

Fig. 4 Velocity profiles of the fluid flow velocity at one radius from the wall.

Fluctuations of the flow are also analyzed thanks to measurements with a time-resolved PIV system running at 20 kHz. The fluid flow velocity is extracted at different locations and power spectra density is computed (Fig. 5, top plots). As in linear DBD plasma actuators, the flow produced by the ring-type DBD periodically oscillates at the electrical frequency of the applied signal command. This is verified regardless of the ring's radius but the location of the maximal fluctuation amplitude filtered around 1 kHz differs. When a wall-normal jet is produced, the fluctuations are concentrated in the jet region at a few mm from the dielectric wall while they are limited to the wall surface above the ring for low r/d.

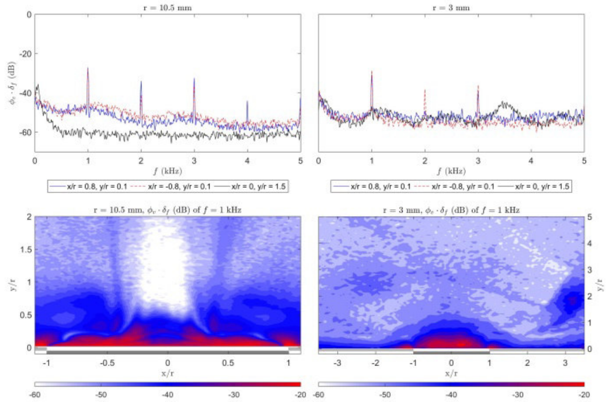

Fig. 5 Power density spectra at specific locations (top plots) and spatial distribution of the fluid flow with frequency content filtered (bandpass) at 1 kHz.

## CONCLUSION

The present experiments illustrate how the flow produced by a ring-type plasma actuator can be modified when a downsizing procedure is applied to the design. Reducing the diameter of the ring modifies the plasma morphology and the local electric field. As a result, ring-type DBD can produce a reversed flow when the ratio r/d reaches a certain limit (r/D=1.5 here).

## ACKNOWLEDGEMENT

This work was supported by the French government program "Investissements d'Avenir" (LABEX INTERACTIFS, ANR-11-LABX-0017-01).

## REFERENCES

[1] Reibert, M.S., Saric, W.S., Carrillo R.B., Jr., & Chapman, K. (1996). Experiments in nonlinear saturation of stationary crossflow vortices in a swept-wing boundary layer. AIAA Paper 96-0184

[2] Saric, W.S., Carrillo R.B., Jr., & Reibert, M.S. (1998). Leading-edge roughness as a transition control mechanism. AIAA Paper 1998-781

[3] Moralev, I., Sherbakovaa, V., Selivonina, I., Bityurin, V., and Ustinov, M. (2018). Effect of the discharge constriction in DBD plasma actuator on the laminar boundary layer. *Int. J. of Heat and Mass Trans.*, 116.

[4] Choi, KS., Kim, JH. (2018). Plasma virtual roughness elements for cross-flow instability control. *Exp Fluids* **59,** 159.

[5] Shuele, C.Y. (2011). Control of stationary cross-flow modes in a Mach 3.5 boundary layer using patterned passive and active roughness. PhD dissertation ND University

[6] Borradaile, H., Kourtzanidis, K., Rogier, F., Choi, K.S. and Mao, X. (2021). Flow reversal in millimetric annular DBD plasma actuator, *J. Phys. D: Appl. Phys.*, 54.

[7] Humble, R.A., Craig, S.A., Vadyak, J., McClure, P.D., Hofferth, J.W., and Saric, W.S. (2013). Spatiotemporal structure of a millimetric annular dielectric barrier discharge plasma actuator, Phys. Fluids, 25.

**Joint ERCOFTAC/EU-CTFF**
**European Drag Reduction and Flow Control Meeting – EDRFCM 2022**
**September 6th–9th, 2022, Paris, France**

# EXPERIMENTAL BASE FLOW MODIFICATION THROUGH PLASMA ACTUATION ON A SWEPT WING

**K. Peng, J.P.W. Arkesteijn, F. Avallone and M.Kotsonis**
AWEP Department, Delft University of Technology, 2629HS Delft, The Netherlands

## INTRODUCTION

The swept wings used on modern aircraft result in three-dimensional boundary layers, which are subject to the so-called crossflow (CF), ultimately responsible for the laminar-turbulent transition process [1]. In recent years, the Dielectric Discharge Barrier (DBD) plasma actuator (PA) has been proposed to delay the transition (thus reducing the skin friction) by controlling the CF component and, by extension, CF instabilities. A few studies have investigated the PA effects on the CF and CF instabilities based on several strategies including the Base Flow Modification (BFM). To achieve BFM, a typical configuration is to orient a spanwise-invariant PA to directly force against the CF component, as shown in figure 1. Compared with other forcing strategies, BFM appears to be more feasible and robust in realistic applications, due to the simplicity of actuator fabrication and its independence to the wavelength, phase and amplitude of the incoming instabilities. However, while the effectiveness of BFM to delay transition was recently demonstrated by Yadala et al. [3], the direct effect of an operating PA on the CF component as well as the CF instabilities has yet to be observed or detailed experimentally. In this work, a BFM-tailored PA is experimentally investigated on a scaled swept wing model. The achieved CF reduction is traced under various PA operating conditions. Moreover, the streamwise growth of stationary CF instabilities is investigated with respect to the PA *off* and PA *on* condition.

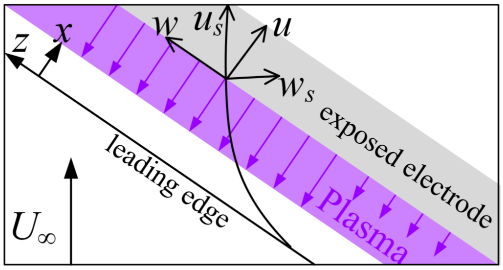

Figure 1: Schematic of the PA forcing mechanism based on the BFM strategy.

## METHODOLOGY

The experiment is conducted in the anechoic vertical tunnel (A-tunnel) at Delft University of Technology, featuring sufficiently low turbulence intensity $T_u < 0.1\%$. The scaled swept wing model $K-M3J$ used in this experiment is purposely designed to replicate the initial pressure coefficient of the reference model $66018M3J$. The complete design and performance of $K-M3J$ can be found in [2]. Two reference systems are utilised, namely the windtunnel-based $XYZ$ and the unswept wing-based $xyz$, with corresponding velocity vectors $[U, V, W]$ and $[u, v, w]$ respectively. To be noted that the $xyz$ coordinate is body-fitted to the surface of the the wing. As such all velocity field results presented here are spatially transformed. An additional streamline-based reference system is introduced where $x_s$ is tangential to the inviscid streamline with $z_s$ normal to the inviscid streamline. The corresponding velocity vector is denoted as $[u_s, v_s, w_s]$, as shown in figure 1. The PA electrodes feature a width of $5\,mm$ and are fabricated using automatic deposition of silver conductive paint. The grounded electrode is placed upstream of the exposed electrode (similar to that used in [3]). Specifically, the electrodes' interface is located at $x/c_x = 0.073$. Two PIV arrangements are used for the measurement, namely stereo-PIV for the base flow modification and planar-PIV for the CF instabilities. Two LaVision Imager cameras (sCMOS, 2560 × 2160 pixels) are aligned from each side of the test section in a suitable aperture angle, acquiring at the frequency of $13\,Hz$. A schematic of the experimental set up is displayed in figure 2.

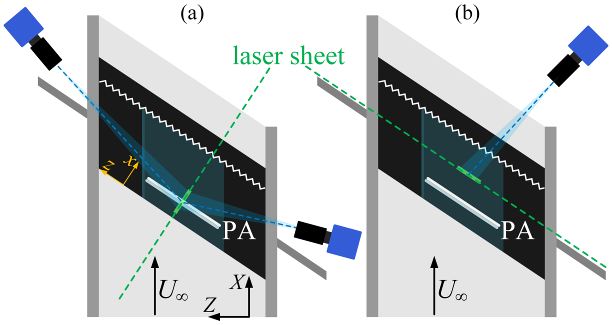

Figure 2: (a) Schematic of stereo-PIV setup and the $K-M3J$ assembled with the test section. The flow comes from the bottom; (b) Schematic of planar-PIV setup.

## RESULTS

The stereo-PIV measurement is performed in the $xy$ plane where the wing curvature cannot be ignored. As mentioned earlier, body-fitted coordinate transformation is performed for extracting the velocity vector $[u,\ v,\ w]$ to facilitate the comparison of results. The processed velocity $u$ and $w$ are later used to calculate the streamline velocity $u_s$ and the corresponding CF velocity $w_s$, following the transformation as below.

$$\begin{pmatrix} u_s \\ w_s \end{pmatrix} = \begin{pmatrix} cos\ \phi_s & sin\ \phi_s \\ cos\ \phi_s & -sin\ \phi_s \end{pmatrix} \begin{pmatrix} u \\ w \end{pmatrix} \tag{1}$$

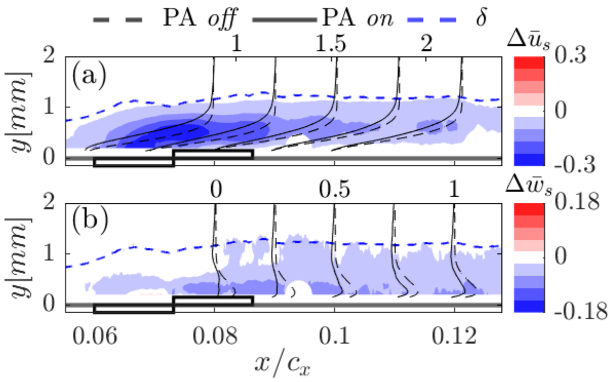

Figure 3: Mean velocity reduction $\Delta\bar{u}_s$ and $\Delta\bar{w}_s$ for $U_\infty = 18\,m/s$ where the PA operates at $V_{p-p} = 15\,kV$, $f = 5\,kHz$. The flow direction is to the right and the blue dashed line indicates the boundary layer thickness $\delta$.

where $\phi_s$ is the local angle between the inviscid external streamline and $x$ axis, defined as $\phi_s = tan^{-1}(w_\infty/u_\infty)$ where $u_\infty$ and $w_\infty$ are the freestream velocities in $x$ and $z$ respectively. Figure 3 illustrates the time-averaged flow field subtraction between the PA *on* and PA *off* condition. Evidently, both $u_s$ and $w_s$ are significantly reduced by the PA forcing, where the PA effect is mainly limited inside the boundary layer. In addition, the flow above the grounded electrode is found decelerated which corresponds to the effect of the localised body force. On the other hand, the $u_s$ profile becomes less full under the PA action, indicating a locally reduced skin friction in the PA vicinity due to the reduced $du_s/d_y$.

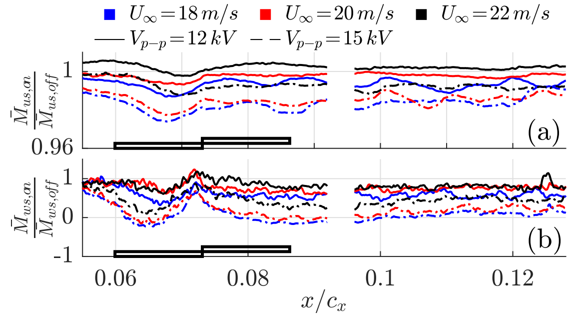

Figure 4: The momentum integral alteration of (a) $\bar{M}_{us}$ and (b) $\bar{M}_{ws}$ where the PA operates at various conditions.

The PA influence on the base flow is further quantified by calculating the non-dimensional momentum integral $\bar{M}$ at each location $x/c_x$ following equation 2.

$$\bar{M}_{us} = \frac{1}{\delta}\int_0^\delta |\rho\bar{u}_s|\bar{u}_s dy \quad \& \quad \bar{M}_{ws} = \frac{1}{\delta}\int_0^\delta |\rho\bar{w}_s|\bar{w}_s dy \quad (2)$$

where $\rho$ is the incompressible flow density. The momentum ratio $\frac{\bar{M}_{us,on}}{\bar{M}_{us,off}}$ and $\frac{\bar{M}_{ws,on}}{\bar{M}_{ws,off}}$ is calculated as a measure of the boundary layer momentum change due to the PA forcing. As shown in figure 4, the outcomes demonstrate a general momentum loss along the directions of both $u_s$ and $w_s$ in the boundary layer. The reduction effect of the PA highly depends on the operating condition whereupon higher $V_{p-p}$ and lower $U_\infty$ enhance the PA authority for base flow modification. Compared with the $w_s$, the PA effects on the $u_s$ appear to be minimal as the maximum reduction of $\frac{\bar{M}_{us,on}}{\bar{M}_{us,off}}$ is only around 2%. It can be concluded that the BFM strategy modifies the base flow mainly by modifying the much weaker $w_s$ component instead of $u_s$.

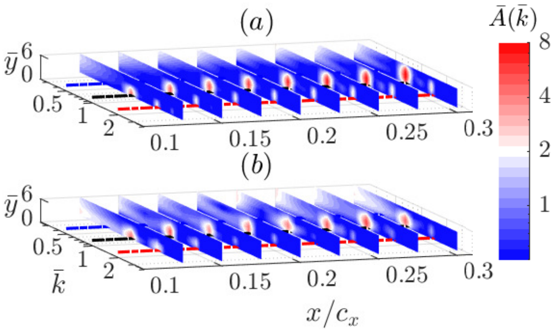

Figure 5: Non-dimensional FFT amplitude $\bar{A}$ for the stationary CF instabilities. (a) PA-*off* (b) PA-*on*. The slices are plotted from $x/c_x = 0.125$ to 0.3 with a step of 0.025. The wavenumber $\bar{k}$ of 0.5, 1 and 2 correspond to the wavelength $\lambda$ of 16, 8 and $4\,mm$, respectively.

Critical stationary CF instabilities (wavelength $\lambda = 8\,mm$) are enhanced by Discrete Roughness Elements (DRE) positioned at $x/c_x = 0.02$. The PA effect on the stationary CF instabilities is investigated by tracing the spanwise Fast Fourier Transform (FFT) of the mean flow fluctuation $\bar{w}'$. Figure 5 illustrates the spectral amplitudes of stationary modes featuring various wavenumber $\bar{k}$ from $x/c_x = 0.125$ to 0.3. The wavenumber $\bar{k} = 1$ corresponds to the critical stationary mode and hereafter refers to the fundamental mode. Generally, disturbances of $\bar{k} < 1$ are found mildly amplified, which might be attributed to slight deviations from absolute spanwise-invariance of the PA forcing due to fabrication and/or placement misalignment. In contrast, the important fundamental mode and super-harmonics are evidently weakened by the PA due to the reduced CF.

## CONCLUSION

This paper experimentally investigates PA effects on the base flow and stationary CF instabilities in the context of Base Flow Modification. The results demonstrate that the BFM-based PA can reduce both the streamline velocity $u_s$ and CF velocity $w_s$ while being more effective for the $w_s$. The PA effect on the stationary CF instabilities is investigated by a spanwise FFT spectrum. Stationary CF instabilities of $\bar{k} < 1$ are mildly amplified while the fundamental mode and super-harmonics are significantly reduced by the PA forcing.

## REFERENCES

[1] Hans Bippes. Basic experiments on transition in three-dimensional boundary layers dominated by crossflow instability. *Progress in aerospace sciences*, 35(4):363–412, 1999.

[2] Kaisheng Peng and Marios Kotsonis. Cross-flow instabilities under plasma actuation: Design, commissioning and preliminary results of a new experimental facility. In *AIAA Scitech 2021 Forum*, page 1194, 2021.

[3] Srikar Yadala, Marc T Hehner, Jacopo Serpieri, Nicolas Benard, Philipp C Dörr, Markus J Kloker, and Marios Kotsonis. Experimental control of swept-wing transition through base-flow modification by plasma actuators. *Journal of Fluid Mechanics*, 844, 2018.

**Joint ERCOFTAC/EU-CTFF**
**European Drag Reduction and Flow Control Meeting – EDRFCM 2022**
**September 6$^{th}$–9$^{th}$, 2022, Paris, France**

# PLASMA VORTEX GENERATORS USED FOR SEPARATION CONTROL AND DRAG REDUCTION ON A BLUFF BODY

**P. Sujar-Garrido**
Department of Engineering Mechanics, KTH Royal Institute of Technology, 10044 Stockholm, Sweden

**R. Örlü**
Department of Engineering Mechanics, KTH Royal Institute of Technology, 10044 Stockholm, Sweden

## INTRODUCTION

Plasma actuators have become a quite effective technique during the last two decades. This is mainly due to their peculiarity to transform electrical power into mechanical power without the need for moving/mechanical parts nor do they require large spaces. Dielectric-Barrier-Discharge (DBD) plasma actuators have predominantly been used as momentum injectors in the near-wall region of aerodynamic surfaces [1] and as vortex generators [2]. For the latter, an array of DBD plasma actuators are oriented in the streamwise direction, thereby producing an electric wind perpendicular to the flow direction, known as plasma vortex generators (DBD-VGs). This technique used the actuators as a mixing tool instead of the classical injection of momentum.

The suppression of separated flow regions around road vehicles is key to reduce their aerodynamic drag and optimize their power consumption. When considering a zero degree yaw angle, the front drag of heavy-duty vehicle accounts for about 20% of the total energy loss and the trailer base drag is around 30%. The front drag contribution comes from the flow separation from the truck surface while passing the A-pillars (front corners) of the tractor. The aerodynamic design of these corners has improved during the last decades considering zero yaw angle (i.e., for headwind). However, the side winds can have a significant detrimental effect on the drag.

The present investigation is part of the PROMETHEUS (Plasma drag ReductiOn METHodology for effective Energy USage) project, as an extension of the FRANCE (Flow Research on Active and Novel Control Efficiency) project. Previous results of a scaled truck [6] showed that a reduction of the total drag of up to 20 % could be achieved for a yaw angle of 9°. These results can be improved operating the DBD VGs in an unsteady actuation mode. A pulsed actuation with an optimal duty-cycle would reduce the power consumption while keeping the effectiveness [5]. The effect of the excitation amplitude and duty-cycle parameters on the evolution of the starting vortex has been studied in quiescent air [4], concluding that the burst mode created greater mixing than continuous operation. Nonetheless, there is still a lack of studies exploring these advantages in complex flow-control configurations such as the 3D flow around an A-pillar.

## BLUFF BODY SETUP

The main objective of the present investigation is to study a flow configuration close to an A-pillar that is still generic enough and can be simulated and compared with other existing cases as in [3]. Besides of studying the wake generated by a standard 3D bluff body. Thus, the chosen geometry is a modified bluff body (Figure 1) with a square-back and round corners on the leading edges. The main characteristic of our geometry is its flexibility to study separation on different front and back designs and with yaw effects to demonstrate the potential of unsteady plasma VGs. The body also includes pressure taps distributed along the model surface and is, in a first step, implemented with tufts.

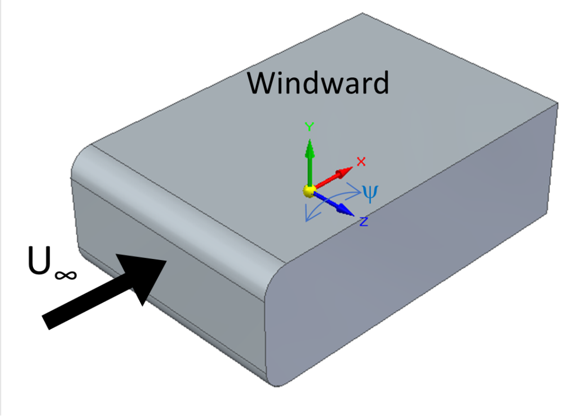

Figure 1: A 3D sketch of the model indicating the wind direction and windward side.

## BASELINE FLOW

In a first stage, flow tuft visualizations were chosen as a quick and simple manner to asses the flow behavior at different velocities $U_\infty (m/s)$ and different yaw angles $\psi(°)$ on the leeward side. Although the body is three-dimensional, the spanwise dimension was chosen to have at least 1/3 of two-dimensional flow after the A-pillars' separation. This is corroborated by the tuft visualizations. Several inlet velocities up to 20 m/s were operated for two yaw angles: 0° and 10°. At the maximum velocity (20 m/s) and $\psi = 0°$, the reattachment of the separation bubble is at the middle of the length of the leeward side, while the reattachment increase by around 50% at 10°.

For a more quantitative result, pressure measurements are acquired on each side of the BB (i.e., front, back, windward and leeward). A Scanivalve MPS4264 digital pressure scanner was used to compute the pressure coefficient. The scanner is able to simultaneously sample 64 pressure ports with a stated accuracy of 0.20% of its full scale range of ±1 kPa (corresponding to a measurement error of ±2 Pa). Here, time-averaged pressure distributions are evaluated with 25 pressure taps on the surfaces of each side (windward or leeward). The front and back sides are equipped with 15 pressure taps symmetrically distributed. For the time-averaged results, the acquisition runs for 2 min at 10 Hz.

Figure 2 indicates the overlapping, on both windward and leeward sides, of the $C_p$ distribution for the symmetric case ($\psi = 0°$). The $C_p$ distribution increases with the yaw angle in the windward side, while in the side of the separation bubble the effects are not evenly coupled with the yaw angle. In fact, the separation behaves very similar for angles ranging between 0° and 5° and in another way in the range of 7° to 10°. It seems that a threshold exits between 5° and 7°. This is being investigated further with planar PIV measurements. Moreover, hot-wire anemometry (HWA) is used to acquire and analyze the incoming flow conditions as well as the characteristics of the wake.

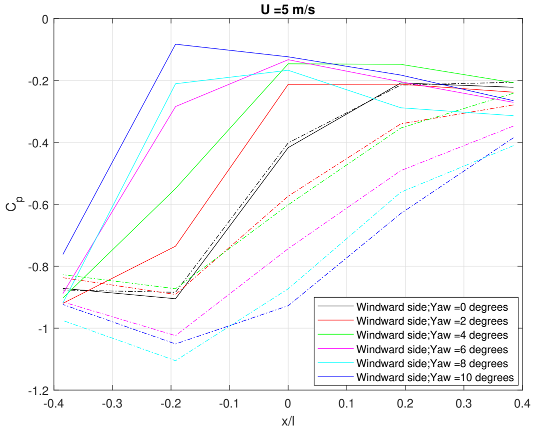

Figure 2: Example of $C_p$ evolution on the windward (solid lines) and leeward (dashed lines) sides at different yaw angles for an incoming velocity of 5 $m/s$.

## DBD VORTEX GENERATORS

The actuator used is the same as in Ref. [6]. Their results showed a reduction of the total drag of up to 20% for a yaw angle of 9° using a “steady” vortex generator. In the current case, the applied voltage has a sinusoidal waveform modulated by a low-frequency function (Figure 3). This modulation means that the applied voltage is switched on and off at a frequency equal to 5 Hz and a duty-cycle of 25 %. This “burst signal” is relevant since it has been demonstrated to be effective for flow control configurations with lower power consumption [5].

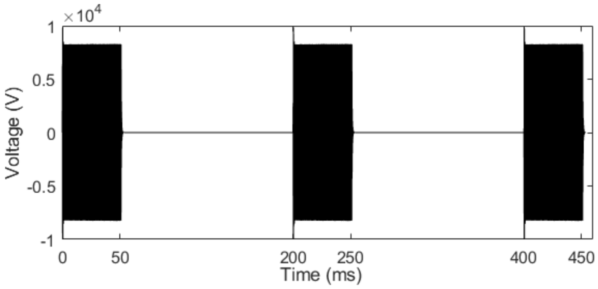

Figure 3: Example of a full envelope of the high voltage signal applied to the DBD actuator.

## CONCLUSIONS & WORK IN PROGRESS

A modified 3D bluff body with front-round corners is studied using pressure measurements. Currently, single hot-wire measurements are conducted with and without control to analyze the influence of the discharge on the wake dynamics. Two point-correlation measurements can be added in the near future.

Regarding the actuator, planar PIV measurements are performed to give details of the effects of the unsteady actuation for separation control and provide more information about the effect of the train of vortex on the A-pillars. To complement these results, a 3D LDV system from TSI is being used to get the spectral characteristics on the wake.

## REFERENCES

[1] T. C. Corke, C. L. Enloe, and S. P. Wilkinson. Dielectric Barrier Discharge Plasma Actuators for Flow Control. *Annu. Rev. Fluid Mech.*, 42:505–529, 2010.

[2] T. N. Jukes and K. S. Choi. On the formation of streamwise vortices by plasma vortex generators. *J. Fluid Mech.*, 733:370–393, 2013.

[3] G. Minelli, M. Tokarev, J. Zhang, T. Liu, V. Chernoray, B. Basara, and S. Krajnovic. Active aerodynamic control of a separated flow using streamwise synthetic jets. *Flow Turbulence and Combustion*, 103(4), 2019.

[4] B. K. Mishra and P. K. Panigrahi. Formation and characterization of the vortices generated by a dbd plasma actuator in burst mode. *Physics of Fluids*, 29(2), 2017.

[5] P. Sujar-Garrido, N. Benard, E. Moreau, and J. P. Bonnet. Dielectric barrier discharge plasma actuator to control turbulent flow downstream of a backward-facing step. *Exp. Fluids*, 56:70, 2015.

[6] J. A. Vernet, R. Örlü, D. Söderblom, P. Elofsson, and P. H. Alfredsson. Plasma streamwise vortex generators for flow separation control on trucks: A proof-of-concept experiment. *Flow Turbulence and Combustion*, 100:1101–1109, 2018.

**Joint ERCOFTAC/EU-CTFF**
**European Drag Reduction and Flow Control Meeting – EDRFCM 2022**
**September 6th–9th, 2022, Paris, France**

# SHOCK WAVE REFLECTION CONTROL IN M=4 FLOW BY FILAMENTARY ELECTRICAL DISCHARGE

**P. Andrews, P. Lax and S. Leonov**
AME Department, University of Notre Dame, 46556, USA

## INTRODUCTION

This work focuses on the experimental study of near-surface filamentary plasma interactions with an impinging shock wave (SW) aiming for active control of duct-driven shock-dominated flows in supersonic airflow. The results are relevant to flow manipulation in compression inlets, scramjet isolators, and supersonic ducts [1-2]. Tests were performed at the supersonic blowdown wind tunnel SBR-50 of the University of Notre Dame. Previous studies were conducted at Mach 2 and used a filamentary plasma to demonstrate pressure redistribution due to presence of longitudinal subsonic zones induced by each plasma filament [3]. This past work provided experimental characterization of a single plasma filament interacting with an incoming shock wave. Mach 2 study demonstrated cross-flow surface pressure redistribution in vicinity of the plasma area and the impinging SW. In accordance with the model of interaction and the data acquired for a multi-filamentary patterned plasma array, a semi-cone shape of the plasma-induced SW was predicted with a zone of augmented pressure within that cone and a significantly lower pressure outside of it. This predicted effect was demonstrated experimentally by analysis of cross-flow pressure distribution for single and triple plasma filament configurations as well as through acetone Mie scattering visualization. Compared to a single discharge, which creates a semi-conical SW, the actuation of three plasma filaments is characterized by an induction of an almost planar SW originating from the location of the discharge electrodes as shown in Figure 1. The interference of individual semi-conical SWs resulting in a new plane SW setup is considered to be equivalent to shifting of the entire shock train upstream.

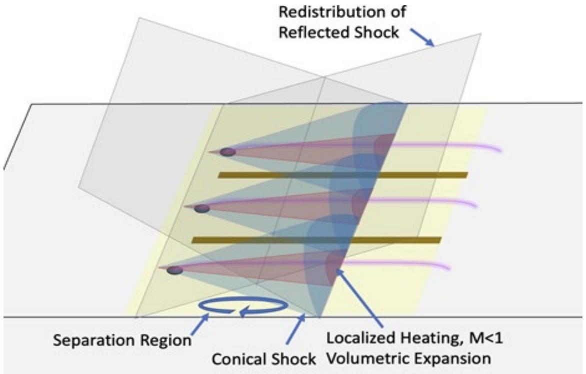

Figure 1. Illustration of SW-BL-plasma interaction pattern.

## TEST SETUP

Tests were performed at the SBR-50 supersonic blowdown test rig at the University of Notre Dame. The facility test section has an initial cross section of $Z \times Y = 76.2 \times 76.2$ mm and length of $X = 715$ mm, with a $1^\circ$ expansion of the top and bottom walls to compensate for the boundary layer growth. The facility operated at M = 4 with stagnation pressures in the range of $P0 = 1 - 4$ bar, stagnation temperature $T0 = 297$ K and steady-state run time $t = 0.5$-1 s depending on stagnation conditions. The upper wall of the test section was arranged with a $10^\circ$ wedge with a height of 6.6mm to generate a planar shock impinging in the plasma region on the bottom wall, see Figure 1.

The plasma was generated using a quasi-DC electric discharge from three high voltage electrodes embedded in ceramic insert spaced 19mm apart from each other and from the side walls and located 149mm downstream of the nozzle exit. Two grounding rails of width 2.6mm were placed 19.05mm apart from each other and 28.5mm from the side walls in order to elongate the plasma filaments. For this test series, the basic instrumentation includes pressure measurements, schlieren imaging, high speed plasma imaging, and electrical measurements.

## RESULTS of MEASUREMENTS and OBSERVATIONS

The basic effect of plasma actuation on the shock train generated by the ramp and on the flow-field structure is seen in schlieren images in two key regions: (1) compression wedge shock impact on the plasma array and (2) the reflection of this shock back to the upper wall.

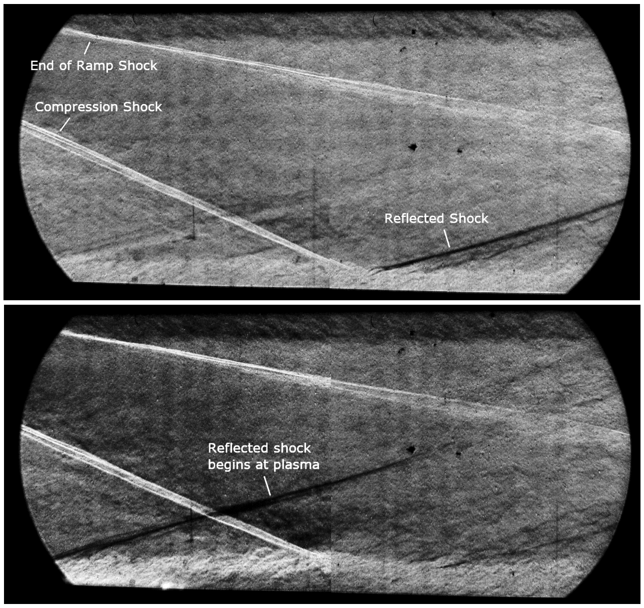

Figure 2. Schlieren images at $P0 = 2.6$bar, $T0 = 297$ K showing (a) no plasma actuation, (b) three plasma filaments on.

Figure 2 presents schlieren images collected at 1kHz with a 100ns effective exposure time. Images compare the plasma off flow and three plasma filaments configuration. Prior to plasma activation, the flow field is dominated by a strong shock from the leading edge of the compression wedge and the end shock from the ramp back wedge. The first reflection of the leading edge oblique shock from the bottom wall is seen near the center of Fig. 2a. After extended plasma forms on the bottom wall, the reflection of the shock impinging on the plasma array is largely mitigated. A new shock forms upstream at the location of the high voltage electrodes as demonstrated in Fig. 6b. This causes an upstream movement of the entire shock train as proven in further detail in previous experiments [3].

The effect of plasma on shock structure configuration is well reflected in pressure data taken from the two rows of pressure taps arranged perpendicular to the flow as well as static pressure ports along the top wall. By looking at key pressure ports along the top wall where the reflected shock is impinging, pressure data can corroborate the movement of the shock train displayed in schlieren images. As the reflected shock impacting the top wall moves upstream due to plasma actuation, the pressure at x = 252 mm on the top wall dramatically increases indicating this sensor now locates behind the new shock front. Likewise, examining the two perpendicular rows of sensors in the plasma region reveals a movement of existing shocks upstream and can also reveal cross-sectional structure for the single filament case.

When plasma is actuated on, rapid near-adiabatic heating creates a localized subsonic region which causes an upstream movement of the existing shock so that a new shock is generated starting at the plasma electrodes location. Thus, pressure taps in both rows are now behind the new shock and exhibit increased pressure. Preliminary data demonstrates that in the case of single plasma filament test, pressure increases primarily along the centerline, in the region local to the single filament whereas with three filaments the pressure rises more uniformly across the entire row. Pressure distribution profiles from row 2 are shown graphed across three plasma pulses in time are included in Figure 3. This data provides clear evidence of the semi-conical pressure redistribution caused by an increase in pressure local to just the central single filament.

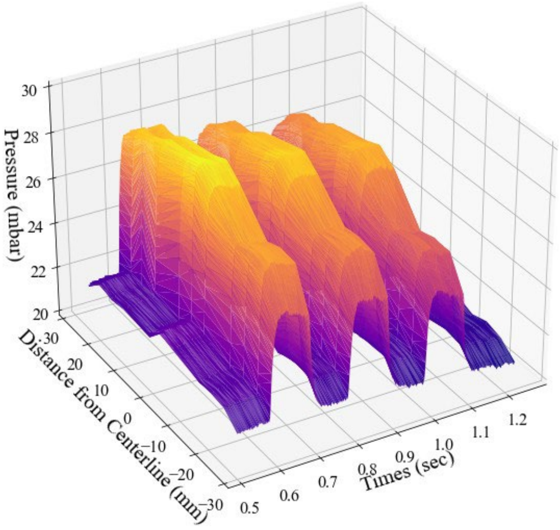

Figure 3. Time series of row 2 pressure distribution during three plasma pulses at $M$=4, $P_0$ = 2.6bar.

## SUMMARY

In this work, there was experimentally demonstrated that the longitudinal filamentary plasma generated in front of the impinging SW significantly modifies the pattern of SWBL interaction. This appears in a mitigation effect of the reflected SW and the redistribution of the wall pressure in flow-wise and cross-flow directions. Presence of a reversal X-gradient of the wall pressure was detected, resulting in a modification of a shape and parameters of the separation zone associated with the SWBLI. This was demonstrated at a single and three plasma filaments arrangement at as low as <1kW of the electrical power deposition.

The authors would like to thank the US Air Force Office of Scientific Research (PM Dr. Gregg Abate) for funding this work, grant # FA9550-21-1-0006.

## References

[1] Wagner, J. L., Yuceil, K. B., Valdivia, A., Clemens, N. T., and Dolling, D. S., “Experimental investigation of unstart in an inlet/isolator model in Mach 5 flow,” AIAA Journal, Vol. 47, No. 6, 2009, pp. 1528, 1542.

[2] K. Matsuo, Y. M., and Kim, H., “Shock train and pseudoshock phenomena in internal gas flows,” Prog. Aerosp. Sci., Vol. 35, 1999, pp. 33–100.

[3] Elliott, S., Hasegawa, M., Sakaue, H., and Leonov, S., “Shock-dominated flow control by plasma array: Pressure analysis including pressure-sensitive paint visualization,” Experimental Thermal and Fluid Science, Vol. 131, 2022, p. 110522

**Joint ERCOFTAC/EU-CTFF**
**European Drag Reduction and Flow Control Meeting – EDRFCM 2022**
**September $6^{th}$–$9^{th}$, 2022, Paris, France**

# CONTROL OF STATIONARY CROSSFLOW INSTABILITIES THROUGH DESTRUCTIVE INTERFERENCE

**G.Zoppini***
Section of Aerodynamics, Delft University of Technology, Delft, The Netherlands, 2629HS

**T. Michelis**
Section of Aerodynamics, Delft University of Technology, Delft, The Netherlands, 2629HS

**D. Ragni**
Section of Aerodynamics, Delft University of Technology, Delft, The Netherlands, 2629HS

**M.Kotsonis**
Section of Aerodynamics, Delft University of Technology, Delft, The Netherlands, 2629HS

## INTRODUCTION

In low freestream turbulence environments, laminar to turbulent transition of swept wings boundary layers (BL) subject to favourable pressure gradient, is dominated by stationary crossflow instabilities (CFI, [1, 5, 6]). To generate CFI focussed on a monochromatic mode, many experimental and numerical works apply arrays of discrete roughness elements (DRE) periodically distributed along the wing span [3, 5]. This enhances the spanwise uniformity of the BL, such that its development is dominated by a monochromatic CFI with wavelength corresponding to the DRE inter-spacing. In most research applications, the forced wavelength coincides with the naturally most unstable CFI mode (i.e. $\lambda_1$).

The main purpose of the presented experimental investigation is to map the effect of multiple DRE arrays in controlling CFI artificially introduced by a reference forcing array. Specifically, up to 4 successive arrays with fixed amplitude and wavelength are applied on the wing surface. The first array initiates the most unstable CFI mode, while the following arrays are optimally arranged to superpose velocity disturbance systems that are destructively interacting, damping of the preexisting CFI.

## METHODOLOGY

The presented measurements are performed on a constant-chord (c=1273 mm) swept wing model in a low-speed low-turbulence wind tunnel at the TU Delft [6]. Data acquisition is performed at a fixed Reynolds number ($Re_{c_X}=2.17\times10^6$) and angle of attack ($\alpha$=-3.36) for a forcing configuration composed by 4 DRE arrays. A reference system integral to the wind tunnel floor (X,Y,Z), and one integral to the swept wing (x,y,z) are used throughout this work.

The applied DRE arrays force the most unstable CFI mode (i.e. $\lambda_1$=8mm for the current set-up [6]), with a fixed element height of k=0.2mm. The multiple arrays configuration is designed accounting for the existing angle between the DRE near-wake flow structures and the freestream flow (i.e. $\simeq 6^\circ$, following preliminary tomographic investigations conducted by the authors). Specifically, the first forcing array (*reference* array, $A_1$) is located at $x_{DRE}/c=0.125$, while the following *control* array ($A_2$) is applied with a chordwise spacing of x/c=0.02. The spanwise shift between $A_1$ and $A_2$, accounts for the tilt of the developing flow structures and for an additional spanwise phase shift of $\lambda_1/2$. As such, the high (low) speed regions induced by $A_2$ superimpose to the already existing low (high) speed regions induced by $A_1$. The following control arrays ($A_3$, $A_4$) are applied at successive intervals of x/c=0.02, with spanwise shift only accounting for the flow structures tilt.

The global flow field characteristics are measured with infrared (IR) thermograpy, allowing for the identification of the BL laminar-to-turbulent transition location [5, 6]. Additionally, 2D particle tracking velocimetry (PTV) locally acquires the time-averaged BL velocity fields in the spanwise-wall normal direction, i.e. z and y respectively. The BL development in the zy plane is described by the spanwise time-averaged velocity component, $\overline{w}$. Its root mean square is representative for the disturbance shape function, that can be integrated along the y-direction to estimate the CFI amplitude ($A(\overline{w})$, [2]). The BL spectral content is investigated through a spatial spanwise Fast Fourier Transform applied to $\overline{w}$ (i.e. $FFT_z(\overline{w})$).

## RESULTS

The acquired IR and PTV data show that, if suitably designed, the multiple DRE forcing configuration successfully controls the CFI introduced by the applied reference array.

The IR images corresponding to the sole reference array (i.e. $A_1$) and to the multiple arrays forcing ($A_{1-4}$), are reported in figure 1(a, b). The differential thermography image (DIT, [4]), obtained by subtracting the IR images corresponding to the $A_1$ and $A_{1-4}$ cases, is presented in figure 1(c). In the latter, the bright portion of the flow extending between X/c=0.4-0.55, indicates that the addition of multiple control arrays successfully delays the BL transition location. Specifically, the transition front chordwise location in the multiple DRE forcing case, is shifted almost 8% of chord more downstream with respect to the sole $A_1$ forcing.

The local BL flow field acquired by PTV is reported in figure 2, and shows that the developing CFI are significantly reduced in geometrical size and intensity in case $A_{1-4}$. This is in agreement with the observed transition delay, and is further confirmed by the estimation of $A(\overline{w})$. Specifically, figure 3(a),

---

*Presenting author, email address: G.Zoppini@tudelft.nl

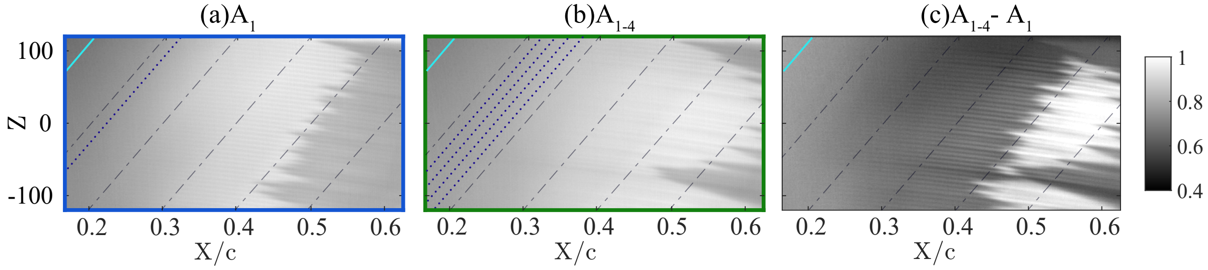

Figure 1: IR images for (a) $A_1$ and (b) $A_{1-4}$ forcing. Flow comes from the left, wing leading edge (light blue line), DRE location (dotted blue lines). (c) DIT image computed subtracting $A_1$ case to $A_{1-4}$.

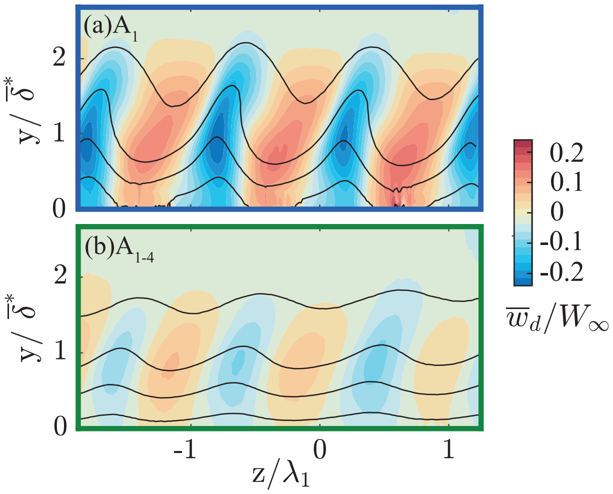

Figure 2: PTV $\overline{w}$ contours at x/c=0.3 for (a) $A_1$ and (b) $A_{1-4}$ forcing. BL displacement thickness at x/c=0.25 ($\overline{\delta}^*$).

shows that the CFI amplitude in the multiple array forcing case is reduced to almost 50% of the $A(\overline{w})$ pertaining to the $A_1$ forcing. Furthermore, the $A(\overline{w})$ reduction appears to be mostly driven by the superposition of the velocity disturbances induced by arrays $A_1$ and $A_2$. Nonetheless, the cumulative contribution of control arrays $A_3$ and $A_4$ further dampens the developing CFI. The spanwise spatial FFT spectra extracted at a fixed xy location (figure 3(b)), confirm that the BL forced by $A_1$ is dominated by the $\lambda_1$ mode, accompanied by the development of higher harmonic modes. Interestingly, the addition of successive control arrays leaves the dominant flow periodicity unaltered, as indicated by the dominant spectral peak. This suggests that the control mechanism leading to the damping of the CFI introduced by $A_1$, is based on the linear superposition and interaction of the velocity disturbance systems introduced by each of the applied control arrays. Nonetheless, in agreement with the observed transition delay and amplitude reduction, the spectral peak amplitude associated to both $\lambda_1$ and its higher harmonics is reduced in case $A_{1-4}$.

## CONCLUSIONS

The presented experimental investigation shows that a monochromatic stationary CFI can be controlled through the destructive interference of the velocity disturbances induced by purposely designed DRE arrays. The performed IR and PTV measurements, indicate that the multiple DRE configuration successfully dampens the CFI introduced by the reference array, delaying the BL transition to turbulence. The conducted spatial FFT confirms that the BL forced by multiple arrays is still dominated by the forced $\lambda_1$ mode. Therefore, the CFI control is achieved thanks to the linear superposition of the velocity disturbances introduced by the applied arrays.

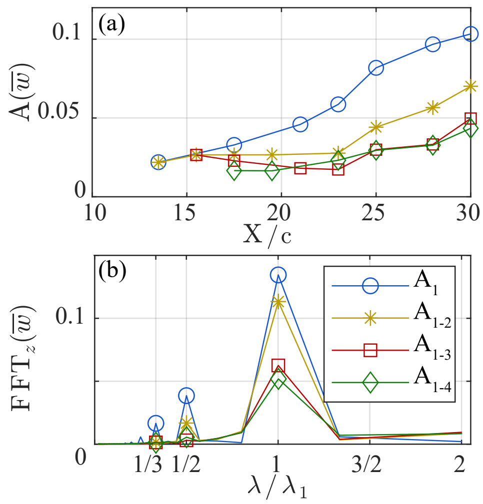

Figure 3: (a) $A(\overline{w})$ evolution and (b) FFT spectra extracted at x/c=0.3 for $y/\overline{\delta}^*$=1 for single and multiple array forcing.

## REFERENCES

[1] H. Bippes. Basic experiments on transition in three-dimensional boundary layers dominated by crossflow instability. *Progress in Aerospace Sciences*, (35):363–412, 1999.

[2] R.S. Downs and E.B. White. Free-stream turbulence and the development of cross-flow disturbances. *Journal of Fluid Mechanics*, 735:347–380, 2013.

[3] R.H. Radeztsky, M.S. Reibert, and W.S. Saric. Effect of isolated micron-sized roughness on transition in swept-wing flows. *AIAA Journal*, 37(11):1370–1377, 1999.

[4] M. Raffel, C.B. Merz, T. Schwermer, and K. Richter. Differential infrared thermography for boundary layer transition detection on pitching rotor blade models. *Experiments in Fluids*, 56(2), 2015.

[5] W.S. Saric, H.L. Reed, and E.B. White. Stability and transition of three dimensional boundary layers. *Annual Review of Fluid Mechanics*, 35(1):413–440, 2003.

[6] J. Serpieri and M. Kotsonis. Three-dimensional organisation of primary and secondary crossflow instability. *Journal of Fluid Mechanics*, 799:200–245, 2016.

**Joint ERCOFTAC/EU-CTFF**
**European Drag Reduction and Flow Control Meeting – EDRFCM 2022**
**September 6th–9th, 2022, Paris, France**

# WALL-TURBULENCE CONDITIONING WITH STEADY CROSSFLOW-DIRECTED PLASMA JETS

**J. Serpieri, Marc T. Hehner & Jochen Kriegseis**
Institute of Fluid Mechanics, Karlsruhe Institute of Technology, 76131, Karlsruhe, Germany

## INTRODUCTION

The viscous drag exerted by turbulent wall-bounded flows can be reduced by a Stokes layer of flow right at the wall [5]. Many numerical studies have been carried out in the last years [e.g. 8, 4], whereas experimental efforts are rather limited [e.g. 1, 3]. This because of the difficulty to physically induce the desired forcing. Recently, dielectric-barrier-discharge (DBD) plasma actuators (PA) have been considered as plausible flow actuators as they can induce a mainly-wall-directed jet near the wall [e.g. 2]. Moreover, their technological embodiment is much simplified when compared to mechanical or piezo-electric devices [6]. Nevertheless, it is not straightforward to operate large PAs and this can limit the flow diagnostics and the related analyses and conclusions to reduced flow portions which risks to capture only a part of underlying flow mechanisms. In this study, two large PAs were built and installed in a ducted-flow facility. The extent of the performed actuation is such to assess the effect on the operated flow and its evolution.

## EXPERIMENTAL SETUP

The ducted-flow facility has permanently-assembled side-walls that are in near-perfect alignment, with exchangeable top and bottom plates. The full length of the test section is 3950 mm, consisting of 950 mm of flow development area and 3000 mm of the actual measurement area. A schematic of the facility can be seen in figure 1. A total of 21 pressure-taps pairs is located on each side of the channel sidewall. The taps span the full test section length at 200 mm apart in the streamwise direction, with the first tap located 100 mm after the test section inlet. These pressure taps are connected in series to a high-precision pressure transducer (MKS Baratron 698A) with an accuracy of ±0.05% of its full scale (100 Torr). The measurements were performed at friction Reynolds numbers ($Re_\tau$) ranging between $250 \leq Re_\tau \leq 405$.

The DBD PAs in this study used Polyethylene terephthalate (PET) sheets as the dielectric layer. The electrodes were made with copper tape and the isolation of the encapsulated electrodes was guaranteed by multiple layers of Kapton tape. To ensure there is no undesired plasma formation between the electrodes and the wind-tunnel itself and to avoid influencing the static-pressure measurements, a distance of 20 mm from the tunnel side-walls was left clear of electrodes. This results in PAs of 290 mm in width and 730 mm in length. The PAs generated a mono-directional forcing similarly to the numerical setup of [7] with the crossflow-directed jets spaced at a distance of 15.12 mm. This value leads to 378 viscous units for the test case at $Re_\tau = 315$ and was found by [7] to lead to the highest value of drag reduction. A schematic of the induced effects they generated is shown in figure 2 whereas figure 3 shows a picture of one of the actuators being operated. The PAs were mounted in two configurations. One (parallel configuration) featured them one mounted on the upper and one on the lower wall of the tunnel, at the same streamwise station, and blowing in opposite crossflow directions. The other (series configuration), instead, considered both of them mounted on the upper wall, one after the other in the streamwise direction and both blowing along the same crossflow direction.

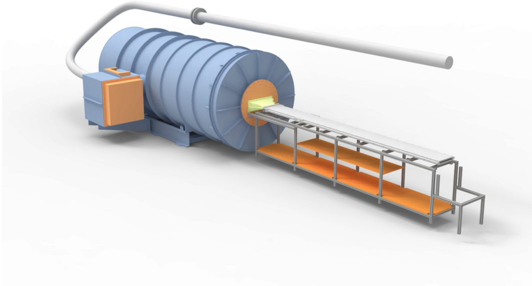

Figure 1: Schematics of the ducted-flow facility at the ISTM.

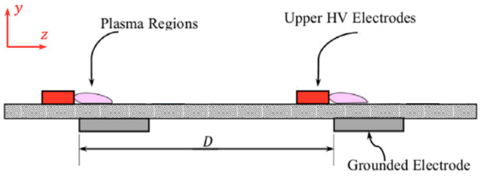

Figure 2: Schematics of the DBD plasma actuators' induced jets.

The power supply used in this experiment is an HP 6269B which is capable of up to 40 V and 50 A. This was used to power two, one per PA, high-voltage transformers: Minipuls 6 by GBS Elektronik GmbH. An Agilent Technology DSOX2004A oscilloscope was used to generate the input signals and to measure the voltage and the charge on the PAs by means of two HV probes and of two 104 K capacitors. These signals allow to assess the power consumed by the actuators. Finally, a peak-to-peak voltage ($V_{pp}$) of 7-10 kV was supplied to the PAs at the AC frequency of 4 kHz.

## RESULTS & DISCUSSION

First, some tests were done to investigate whether the actuators would directly impact the measured static pressure. The actuators were tested in the tunnel but without incoming flow and showed just mildly lower values of static pressure compared to the ambient. Also the two electrodes of the actuators closer to the tunnel edges were de-activated and measurements

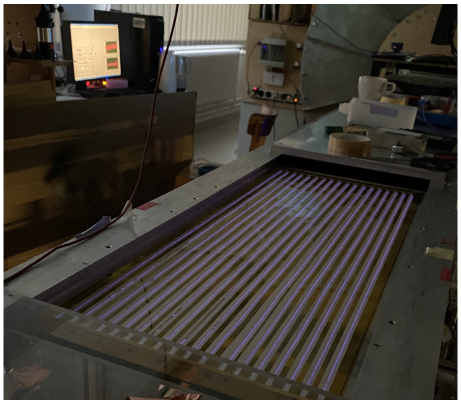

Figure 3: Photography of the operated array of DBD plasma actuators installed on the lower wind tunnel wall.

were performed under these actuation conditions. Small deviations, compared to the full-width actuators measurements, were observed thus making us confident about the validity of the reported data.

Preliminary results showed an increase of the static pressure loss, and equivalently an increase of the flow-exerted drag right at the upstream edge of the actuator for all the tested cases when the actuators were operated. This can be seen in table 1, where for both the tested Reynolds numbers and for all the supplied voltages, the drag modification ($DM = (D_0 - D_a)/D_0$, where $D_0$ is the reference un-actuated value and $D_a$ is the actuated value) attains to negative values at the streamwise station 1 right downstream of the actuators' upstream edge. The same happens also at the second streamwise station which is at about the middle of the streamwise extent of the actuators. On the other side, right downstream of the actuators, namely at station 3, the actuated flows feature lower values of exerted drag. We cannot prove what the cause of this behaviour is but we can elaborate about it. Besides, being the reference study of [7] based on numerical simulations exploiting the periodicity of the streamwise boundary conditions, we cannot compare these results with the literature. What we propose that is happening here is a mix of drag-increasing effects both related to the downwash motions caused by the continuity of mass and related to the approximately-wall-tangential acceleration induced by the actuators. These motions bring closer to the wall larger streamwise-momentum particles which might increase the local viscous drag. Nonetheless, this happens throughout the streamwise extent of the actuators. On the other side, it is believed that, due to these downwash motions, the fluid particles suddenly, while flowing over the actuated walls, face a blockage effect reducing the static pressure. More downstream, instead, it is believed that the beneficial effects of the performed actuation on the turbulent flow and its exerted drag start occurring and building up. Downstream of the actuator, where these beneficial effects might still be there but the downwash motions are not, large values of drag reduction are measured for all the tested conditions. Yet, these beneficial effects soon decay while going even more downstream (not reported). The reported values allow also to see that these trends are increased for the higher value of the supplied voltage, and thus of the actuation strength, with this being valid for both the measured flows. On the other side, for a given operating voltage, it appears that the actuation for higher-$Re_\tau$ flows leads to beneficial effects: milder values of increased drag at the upstream and middle stations and higher values of drag reduction at the downstream station. This is also an interesting aspect which should be further addressed as the actuator spacing was expected to be optimal for $Re_\tau = 315$. Considering the cases with strongest effects, and the spatial resolution of the measurements, a streamwise extent of 900 mm is shown to feature an increase of the flow-exerted drag due to the actuation and a length of 400 mm reports feature drag reduction with the latter being proportional to the supplied voltage, i.e. the actuation intensity.

| $V_{pp}$ [kV]<br>$Re_\tau$ | Station 1<br>360, 405 | Station 2<br>360, 405 | Station 3<br>360, 405 |
|---|---|---|---|
| 7 | -14.65, -13.16 | -15.66, -12.99 | 6.68, 10.90 |
| 8 | -33.27, -22.48 | -31.56, -22.88 | 15.58, 19.18 |
| 9 | ..., -34.84 | ..., -34.58 | ..., 31.22 |

Table 1: Percentage drag modification ($DM$) for different forcing amplitudes and $Re_\tau$ and evaluated at three different streamwise stations. Actuators in parallel configuration.

These preliminary results evidence the deviations occurring between numerical studies based on simplified assumptions and experimental efforts with limited diagnostics and actuation lengths, power and strengths. More in the specific, the streamwise evolution of the operated forcing appears to play a major role and this should spark the demand for further investigations with possibly both methodologies. It appears, in fact, that the initial effect of the operated actuation on the flow has detrimental effects which can overcome or hinder the beneficial ones caused by the conditioning of the wall turbulence mechanisms. This aspect could be here evidenced by manufacturing, installing and operating two large PA arrays covering the whole tunnel width and a streamwise extent of $> 29h$, with $h$ being the channel height of 25 mm (for a total length of the plasma discharge of $\approx 14$ m per actuator). Furthermore, to further inspect this effect, the performed experiments consider also the case where the actuators were mounted one after the other both blowing in the same crossflow direction. Finally, power consumption measurements were also performed allowing to retrieve efficiency evaluations.

## REFERENCES

[1] F. Auteri, A. Baron, M. Belan, G. Campanardi, and M. Quadrio. *Physics of Fluids*, 22(11), 2010.

[2] K.-S. Choi, T. Jukes, and R. Whalley. *Philosophical Transactions of the Royal Society A: Mathematical, Physical and Engineering Sciences*, 369(1940):1443–1458, 2011.

[3] D. Gatti, A. Güttler, B. Frohnapfel, and C. Tropea. *Experiments in Fluids*, 56(5):110, 2015.

[4] D. Gatti and M. Quadrio. *Journal of Fluid Mechanics*, 802:553–582, 2016.

[5] G. E. Karniadakis and K.-S. Choi. *Annual Review of Fluid Mechanics*, 35:45–62, 2003.

[6] J. Kriegseis, B. Simon, and S. Grundmann. *Applied Mechanics Reviews*, 68(2), 2016.

[7] O. Mahfoze and S. Laizet. *International Journal of Heat and Fluid Flow*, 66:83–94, 2017.

[8] P. Ricco and S. Wu. *Experimental Thermal and Fluid Science*, 29(1):41–52, 2004.

**Joint ERCOFTAC/EU-CTFF**
**European Drag Reduction and Flow Control Meeting – EDRFCM 2022**
**September 6$^{\rm th}$–9$^{\rm th}$, 2022, Paris, France**

# WALL COOLING AND HEATING EFFECTS ON THE EXCITATION OF GÖRTLER VORTICES IN COMPRESSIBLE BOUNDARY LAYERS

**D. Xu**
Department of Mechanical Engineering, The University of Sheffield, S1 3JD Sheffield, UK

**P. Ricco**
Department of Mechanical Engineering, The University of Sheffield, S1 3JD Sheffield, UK

## INTRODUCTION

Cooling of turbine engine blades is a widely utilised technique for maintaining the temperature of the surface material within acceptable limits. In this paper, we focus on the wall cooling and heating effects on boundary layers that develop on concave surfaces in the high subsonic regime, as a model for the flow over the pressure side of turbine blades. In particular, we are interested in the control of nonlinear unsteady compressible Görtler vortices excited by free-stream vortical disturbances (FSVD).

El–Hady & Verma (1984) [4] studied the linear Görtler instability of a compressible flow and showed that significant cooling tends to be stabilising the flow. Fu, Hall & Blackaby (1990) [6] examined the compressible Görtler vortices at hypersonic speeds and showed that wall cooling are destabilizing for the mode trapped in the temperature adjustment layer. Bogolepov (1998) [1], Bogolepov (2001) [2] and Elliott & Bassom (2000) [5] investigated the properties of Görtler vortices in the compressible flow and concluded that the wall cooling tends to be destabilising the boundary layers. Recently, by using direct numerical simulations, Sescu *et al.* (2019) [9] studied the wall cooling and heating effects on the Görtler vortices in the boundary layers with Mach number greater than 1.5. They found that wall cooling slightly increases the saturation vortex energy for all Mach numbers.

However, previous works did not take the receptivity of Görtler vortices to FSVD into account. Leib *et al.* (1999) [7] investigated the response of incompressible flat-plate boundary layers to long-wavelength, low-frequency FSVD. Extending their formulation, Viaro & Ricco (2019) [10] studied the linear Görtler vortices excited by FSVD in compressible boundary layers. The work of Viaro & Ricco (2019), restricted to low-intensity turbulent Reynolds numbers, is extended herein to the general case of turbulent Reynolds numbers that are large enough for nonlinearity to play a leading role. A receptivity-instability framework for the study of nonlinear compressible Görtler vortices excited by elevated FSVD is therefore obtained to study the effect of heat transfer on these pre-transitional flows.

## METHODOLOGY

We consider a compressible boundary layer over a concave wall, exposed to free-stream vortical disturbances. The flow is described in an orthogonal curvilinear system $(x, y, z)$, which is normalized by the spanwise integral length of the free-stream turbulence $\Lambda^*$. The dimensionless time variable $t = U^*_\infty t^*/\Lambda^*$ is introduced. The Mach number, Reynolds number, Görtler number and turbulent Reynolds number are defined as

$$\mathcal{M} = U^*_\infty/a^*_\infty = O(1),\ \mathcal{R} = U^*_\infty\Lambda^*/\nu^*_\infty \gg 1,$$
$$\mathcal{G} = \mathcal{R}^{1/2}/(k_1^{3/2} r_0^*) = O(1),\ r_t = \epsilon\mathcal{R} = O(1).$$

where $a^*_\infty$ is the speed of sound in the free stream and $\epsilon \ll 1$ is a measure of the disturbance intensity. FSVD are represented by a pair of vortical modes

$$\boldsymbol{u} - \boldsymbol{i} = \epsilon\hat{\boldsymbol{u}}_i^\infty \mathrm{e}^{\mathrm{i}(\boldsymbol{k}\cdot\boldsymbol{x}-k_1 t)} + \text{c.c.}. \tag{1}$$

where $\boldsymbol{i}$ is the unit vector along the streamwise direction and c.c. indicates the complex conjugate. The wavenumber vector $\boldsymbol{k} = (k_1, k_2, \pm k_3)$ and the amplitude of FSVD $\hat{\boldsymbol{u}}_i^\infty = (\hat{u}^\infty_{i,\pm}, \hat{v}^\infty_{i,\pm}, \hat{w}^\infty_{i,\pm}) = O(1)$ satisfy the solenoidal condition $\boldsymbol{k}\cdot\hat{\boldsymbol{u}}_i^\infty = 0$.

The slow time and spatial variables are introduced as $\bar{t} \equiv k_1 t$ and $\bar{x} \equiv k_1 x$. The flow is decomposed as a sum of the base flow and the perturbation induced by FSVD, namely

$$\boldsymbol{q} = (U(\bar{x},\eta), V(\bar{x},\eta), 0, 1/\gamma\mathcal{M}, T(\bar{x},\eta))$$
$$+r_t(\hat{u}, \sqrt{2\bar{x}k_1/\mathcal{R}}\hat{v}, k_1/k_3\hat{w}, k_1/\mathcal{R}\hat{p}, \hat{\tau})(\bar{x},\eta,z,\bar{t}),$$

where the variable $\eta$ is defined as $\eta = \sqrt{\mathcal{R}/(2x)}\int_0^y \rho(\bar{x},\check{y})\mathrm{d}\check{y}$, and $\rho$ is the density of the flow. The Blasius boundary layer is taken as the unperturbed base flow. The Prandtl number $Pr$ is assumed as a constant $Pr = 0.707$, and the dynamic viscosity $\mu(T) = T^w$ with $w = 0.76$.

In the present nonlinear regime, the disturbance consists of all temporal and spanwise harmonics, and can be expressed as

$$(\hat{u},\hat{v},\hat{w},\hat{p},\hat{\tau}) = \sum_{m,n=-\infty}^{+\infty}\Big(\hat{u}_{m,n}(\bar{x},\eta), \hat{v}_{m,n}(\bar{x},\eta),$$
$$\hat{w}_{m,n}(\bar{x},\eta), \hat{p}_{m,n}(\bar{x},\eta), \hat{\tau}_{m,n}(\bar{x},\eta)\Big)E_{mn}.$$

where $E_{mn} = \exp(\mathrm{i}mk_1t + \mathrm{i}nk_3z)$. The governing equations of excitation and evolution of Görtler vortices are the nonlinear boundary-region equations, (2.23-2.27) in Marensi *et al.* (2017) [8], with additional terms due to the curvature. These Görtler terms appear in the wall-normal momentum equation (2.25): the linear term on the left-hand side,

$$\mathcal{G}(2\bar{x})^{-1/2}\left(2F'\hat{u}_{m,n} - F'^2/T\hat{\tau}_{m,n}\right), \tag{2}$$

and the nonlinear term on the right-hand side,

$$-\mathcal{G}(2\bar{x})^{-1/2}\left(2F'T\widehat{\bar{\rho}\bar{u}} + \widehat{\bar{u}\bar{u}} + r_tT\widehat{\bar{\rho}\bar{u}\bar{u}} - F'^2\widehat{\bar{\rho}\bar{\tau}}\right). \tag{3}$$

The initial and free-stream boundary conditions, which characterize the impact of FSVD on the boundary layer, are the same of Marensi *et al.* [8].

## NUMERICAL RESULTS

Numerical calculations were performed for $\mathcal{M} = 0.69$, $\mathcal{R} = 1124$, $r_t = 7.9$ and $k_1 = 0.0073$. The parameters refer to typical conditions in turbomachinery applications (e.g. Camci & Arts (1990) [3]). Four non-dimensional wall temperatures are adopted as $T_w = 0.5$, 0.75, 1.0 and 1.25. The boundary layer developed over a concave wall with a radius of curvature $r_0^* = 0.1$ m ($\mathcal{G} = 76.1$), while the case with a large radius of curvature $r_0^* = 10$ m ($\mathcal{G} = 0.761$) is shown as a reference. The intensity of the vortices is measured by the root mean square of the fluctuating quantity,

$$q_{rms} \equiv r_t \left[ \sum_{m \neq 0, n} |\hat{q}_{m,n}|^2 \right]^{1/2}, \tag{4}$$

where $q$ is the streamwise velocity or the temperature. The maximum $q_{rms}$ along $\eta$ is $q_{rms,max}(\bar{x}) = \max_\eta q_{rms}(\bar{x}, \eta)$.

Figure 1 and 2 show the streamwise development of $u_{rms,max}$ and $\tau_{rms,max}$ for the cases with Görtler number $\mathcal{G} = 0.761$ and 76.1, respectively. The intensity of the velocity fluctuations of the excited Görtler vortices with respect to the mean value is larger than that of their temperature. The vortices are stabilised by the wall cooling and destabilized by wall heating. Both wall cooling and heating increase the intensity of the temeprature fluctuations. This results does not agree with those of El–Hady & Verma (1984) [4], who reported that cooling has a stabilizing effect on the Görtler vortices. The inconsistency could be due to the fact that El–Hady & Verma did not consider the receptivity of the flow to the external disturbances and restricted their analysis to the linear regime. The effects of wall cooling and heating on the Görtler vortices are intensified by the streamwise curvature.

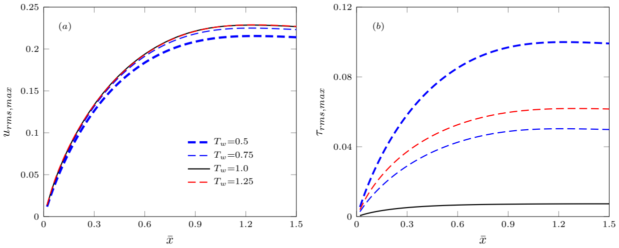

Figure 1: Evolution of the maximum r.m.s. of the streamwise velocity ($a$) and the temperature ($b$) for different wall temperature $T_w$ ($r_t = 7.9$, $\mathcal{M} = 0.69$ and $\mathcal{G}$ =0.761).

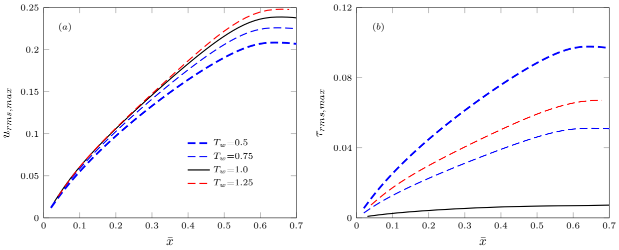

Figure 2: Evolution of the maximum r.m.s. of the streamwise velocity ($a$) and the temperature ($b$) for different wall temperature $T_w$ ($r_t = 7.9$, $\mathcal{M} = 0.69$ and $\mathcal{G}$ =76.1).

## CONCLUSION

In this study, we have investigated the wall cooling and heating effects on the evolution of the compressible Görtler vortices excited by the free-stream vortical disturbances in a boundary layer over concave walls. The free-stream Mach number is assumed to be of $O(1)$ and the FSVD are strong enough for the compressibility and nonlinearity to be both taken into account. The formulation and evolution of Görtler vortices are governed by the compressible boundary-region equations, supplemented by appropriate initial and boundary conditions, which rigorously describe the action of FSVD on the boundary layer. The numerical results showed that the wall cooling decreases the excitation and evolution of the vortical Görtler vortices, while heating has the opposite effect. However, the thermal fluctuations of the Görtler vortices are destabilised by both cooling and heating. It remains to be investigate how the secondary instability of the Görtler vortices is affected by the wall heat transfer.

## ACKNOWLEDGEMENTS

The authors wish to acknowledge the support of EPSRC (Grant No. EP/T01167X/1). PR has also been supported by the US Air Force through the AFOSR grant FA8655-21-1-7005 (International Program Office Dr Douglas Smith).

## REFERENCES

[1] V. V. Bogolepov. Investigation of the spectrum of shortwave Görtler vortices in a gas. *J. Appl. Mech. Tech. Phys.*, 39(5):710–718, 1998.

[2] V. V. Bogolepov. Asymptotic analysis of the structure of long-wave Görtler vortices in a hypersonic boundary layer. *J. Appl. Mech. Tech. Phys.*, 42(5):773–785, 2001.

[3] C. Camci and T. Arts. An experimental convective heat transfer investigation around a film-cooled gas turbine blade. *Trans. ASME J. Turbomach.*, 112(3):497–503, 1990.

[4] N. M. El-Hady and A. K. Verma. Instability of compressible boundary layers along curved walls with suction or cooling. *AIAA J.*, 22(2):206–213, 1984.

[5] J. W. Elliott and A. P. Bassom. The effect of wall cooling on compressible Görtler vortices. *Euro. J. Fluid Mech. B*, 19(1):37–68, 2000.

[6] Y. Fu, P. Hall, and N. D. Blackaby. On the Görtler instability in hypersonic flows: Sutherland law fluids and real gas effects. NASA Rep. 90-85, University of Manchester, 1990.

[7] S. J. Leib, D. W. Wundrow, and M. E. Goldstein. Effect of free-stream turbulence and other vortical disturbances on a laminar boundary layer. *J. Fluid Mech.*, 380:169–203, 1999.

[8] E. Marensi, P. Ricco, and X. Wu. Nonlinear unsteady streaks engendered by the interaction of free-stream vorticity with a compressible boundary layer. *J. Fluid Mech.*, 817:80–121, 2017.

[9] A. Sescu, R. Alaziz, and M. Afsar. Effect of wall transpiration and heat transfer on Görtler vortices in high-speed flows. *AIAA J.*, 57(3):1159–1171, 2019.

[10] S. Viaro and P. Ricco. Compressible unsteady Görtler vortices subject to free-stream vortical disturbances. *J. Fluid Mech.*, 867:250–299, 2019.

**Joint ERCOFTAC/EU-CTFF**
**European Drag Reduction and Flow Control Meeting – EDRFCM 2022**
**September 6th–9th, 2022, Paris, France**

# THE REVERSE LIFT-UP EFFECT IN CROSSFLOW INSTABILITIES OVER SURFACE IRREGULARITIES

**Jordi Casacuberta**[1], **Stefan Hickel**[1], **Marios Kotsonis**[1]
[1]Faculty of Aerospace Engineering, TU Delft, 2629 HS Delft, The Netherlands

## INTRODUCTION

Sharp geometrical imperfections on swept wings of subsonic aircraft may significantly alter the evolution of boundary-layer instabilities and promote laminar-turbulent transition. Considering forward-facing steps, several studies have been conducted to assess the impact of such surface imperfections to a stationary crossflow instability [1, 2, 3]. However, contradictory conclusions were drawn in some cases. We scrutinize the mechanisms of interaction between an imposed stationary crossflow instability mode and forward-facing steps immersed in a three-dimensional incompressible boundary layer.

## ANALYSIS

The swept-wing flow is numerically modelled as flat-plate flow with a prescribed free-stream pressure. Direct Numerical Simulations (DNS) are performed upon computing the steady-state solution that arises from a fully stationary interaction between the steps and a fixed inflow perturbation. The steps are invariant in the wing-span direction, $z$. The chordwise and wall-normal directions are indicated by $x_{\mathrm{st}}$ and $y$, while $u_\infty$ and $\delta_0$ denote characteristic velocity and length scales. The stationary perturbation field from DNS is decomposed in spanwise Fourier modes; the fundamental perturbation Fourier mode is referred to as *primary* and denoted by $(0, 1)$.

Two major flow regimes are identified at the step. *Far* from the wall, the original perturbation lifts off and passes over the step. *Close* to the wall, chordwise-velocity ($u'$) perturbation streaks of alternating sign in $z$ are induced at the step corner (Figure 1). This scenario develops analogously for each Fourier component, implying that a near-wall streak system contained in a particular Fourier mode *has adopted* the spanwise wavelength of the incoming crossflow component that induces it.

A Reynolds-Orr budget analysis applied to each Fourier component independently reveals that, for the primary mode, linear production is the dominant mechanism in both the near- and far-wall regimes. The production term is decomposed into different contributions associated to the action of (primary) perturbation components expressed relative to the *local* base-flow orientation. This decomposition reveals a key role of the so-called lift-up effect: it is responsible for inducing the near-wall streaks as well as for severely distorting the evolution of the incoming crossflow perturbation in the vicinity of the step (Figure 2($c$)), when compared to a no-step case (Figure 2($b$)). The streaky structures in the higher-order Fourier modes are initially induced by an algebraic instability associated to the lift-up effect and destabilized further downstream by a modal inflectional instability supported by the step-distorted flow.

The present stabilisation of a primary stationary crossflow instability by a particular choice of two-dimensional roughness height will be linked to potential swept-wing-flow transition delay in future work.

## FIGURES

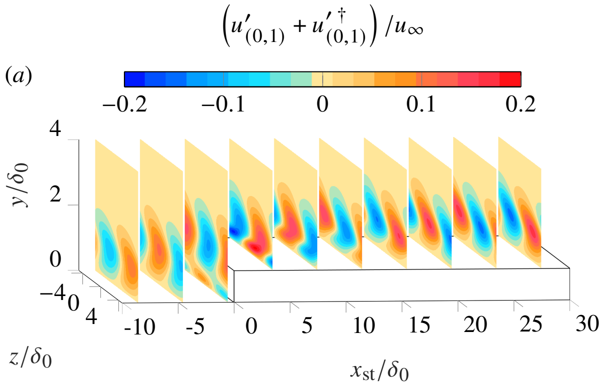

Figure 1: Organization of the primary perturbation Fourier mode.

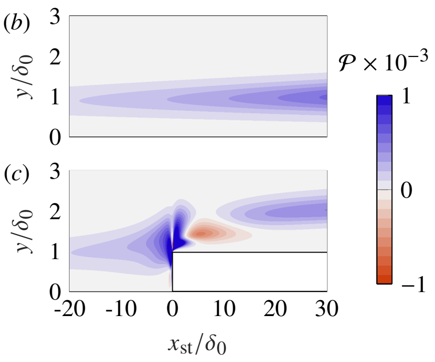

Figure 2: Spatial evolution of the primary Reynolds-Orr production term in the no-step ($b$) and step ($c$) cases.

## REFERENCES

[1] J. Casacuberta, S. Hickel, and M. Kotsonis. Mechanisms of interaction between stationary crossflow instabilities and forward-facing steps. *AIAA Paper 2021-0854*, 2021.

[2] J. L. Eppink. Mechanisms of stationary cross-flow instability growth and breakdown induced by forward-facing steps. *J. Fluid Mech.*, 897:A15, 2020.

[3] A. F. Rius-Vidales and M. Kotsonis. Impact of a forward-facing step on the development of crossflow instability. *J. Fluid Mech.*, 924:A34, 2021.

**Joint ERCOFTAC/EU-CTFF**
**European Drag Reduction and Flow Control Meeting – EDRFCM 2022**
**September 6th–9th, 2022, Paris, France**

# STABILITY ANALYSIS OF MINIATURE VORTEX GENERATORS

**A. Szabó, P.T Nagy**
Department of Hydrodynamic Systems, Budapest University of Technology and Economics, University, H-1521, Budapest, Hungary

**M. Vanierschot, G. de Baets**
Department of Mechanical Engineering, KU Leuven, B-3001 Heverlee, Belgium

**Gy. Paál**
Department of Hydrodynamic Systems, Budapest University of Technology and Economics, University, H-1521, Budapest, Hungary

## INTRODUCTION

For aerodynamic bodies, skin friction is responsible for the main part of the total drag. Therefore, skin friction reduction can potentially lead to significant energy savings. Among the many known skin-friction reduction techniques, delaying laminar-turbulent transition can be considered as one of the most promising ones, especially if the feasibility is also taken into account [2]. In the case of a low external disturbance environment, laminar-turbulent transition is prompted by the two-dimensional Tollmien-Schlichting (TS) waves. The transition procedure can be divided into three phases: (i) the triggering of the disturbances, (ii) the slow growth of the small amplitude instability waves , and (iii) the rapid breakdown to turbulence through nonlinear processes [3]. In general, transition delay approaches target the second phase of the instability growth, as it has the largest spatial extent.

It is well known that introducing a spanwise mean velocity gradient (SVG) can decrease the growth of the TS waves and therefore delay laminar-turbulent transition [1]. A SVG can be generated in several ways; a recently proposed, attractive method is using miniature vortex generators (MVGs). MVGs do not require an external energy source, and are proven both theoretically and experimentally to be able to generate a robust streaky boundary layer with SVG that can dampen the growth of TS waves [1]. The MVGs were proven to attenuate TS waves and oblique disturbances in both the linear and nonlinear regime [8]. Furthermore, the streaks can be reinforced using a second row of MVGs, which allow maintaining SVG in regions with large spatial extent, resulting in continued transition delay [7]. Therefore, MVGs are a promising candidate for saving energy through skin friction reduction.

Although MVGs have received considerable attention in recent studies, further studies are needed before the possibility of industrial application. The most crucial issue is that the optimum MVG parameters are unknown. This is because most of the studies concerned with MVGs were experiments in which examination of many parameter combinations is cumbersome, if not impossible. Numerical studies are more suitable for parametric investigations. However, previous numerical studies [4, 5] modeled MVGs with idealized vortices, and the connection between the MVG geometry and vortex parameters is unclear. In this study, we aim at filling this gap by investigating more MVG parameters than previous studies.

## METHODS AND RESULTS

The examination of the MVGs is carried out by utilizing simplified models, combining the modeling techniques used by Siconolfi et al. [9] and Martín and Paredes [4]. The flow field around the MVG is obtained using three-dimensional CFD calculations. Then, the evolution of the streaky boundary layer is calculated by solving the Boundary Region Equation (BRE). Finally, the stability of the boundary layer is calculated by solving BiGlobal stability equations, and also Parabolized Stability Equations (PSE). For the three-dimensional CFD calculation, commercial CFD codes are utilized. The BRE, BiGlobal stability equations and PSE are solved with the combination of low-order unstructured finite element discretization and distributed sparse linear algebra libraries, which allow a very efficient solution to the problem. In the stability calculation, BiGlobal stability analysis is the main tool, and PSE is used only to check the significance of the non-parallel effects. In the BiGlobal stability calculation, two runs are utilized: one that targets the broadband, high-frequency instabilities in the near-field of the MVGs, and one that aims at tracking the Tollmien-Schlichting instability.

The streak amplitude is measured using the following formula:

$$A(x) = \frac{1}{\hat{U}_0} \int_{-0.5}^{0.5} \int_{0}^{\eta^*} \left| \hat{U}(x, \eta, \zeta) - \hat{U}^z(x, \eta) \right| \mathrm{d}\eta \mathrm{d}\zeta, \qquad (1)$$

where $\hat{\square}$ denotes dimensional variables and regular ones non-dimensional ones. $\hat{x}, \hat{y}$ and $\hat{z}$ denote the streamwise, wall-normal and spanwise coordinates, respectively. $\eta = \hat{y}/\hat{\delta}(\hat{x})$ is the wall-normal coordinate divided by the boundary layer scale $\hat{\delta} = \sqrt{\hat{\nu}\hat{x}/\hat{U}_0}$, $\zeta = \hat{z}/\hat{\Lambda}$, is the spanwise coordinate divided with the periodicity of he configuration. $\hat{U}(\hat{x}, \hat{y}, \hat{z})$ denotes the streamwise velocity, and $\hat{U}_0$ the streamwise velocity in the free stream, and $\hat{U}^z$ is the spanwise average of the streamwise velocity. $\eta^*$ is a sufficiently high location so that the free-stream is undisturbed, i.e., the integrand of Eq. (1) vanishes.

Figure 1 displays the streak amplitude evolution for several rectangular MVG angles, both from the measurement of Sattarzadeh and Fransson [6] and the computational procedure. The streak amplitude from the numerical calculation is in excellent agreement with the experimental data, which verifies our modeling procedure. However, the agreement in other cases (not displayed) is not always that good between simulation and experiments. This may be attributed to the low resolution and the uncertainties in the experiments; e.g., see the variation of the streak amplitude in the case of the MVG with the largest angle. Nevertheless, the modeling approach of the base-flow is verified.

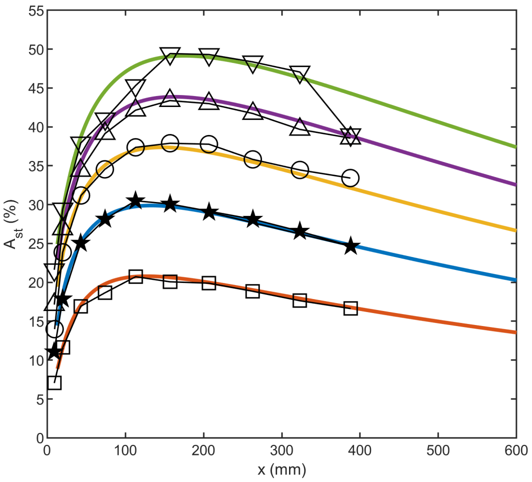

Figure 1: Variation of the streak amplitude as a function of the streamwise distance: comparison between numerical computation and the experiments [6] for multiple MVG angles. Experimental data: □ : $\theta = 6°$; ★ : $\theta = 9°$; ○ : $\theta = 12°$; △: $\theta = 15°$; ▽ : $\theta = 18°$. The continuous curves display the data from the simulation.

Figure 2 displays the maximum growth rate among the multiple instability mechanisms and as a function of the Reynolds number and nondimensional frequency (see caption for the definitions) for the calculation modeling case C02 in the experiments of Sattarzadeh and Fransson [6]. The continuous lines denote the neutral curves of the different instability mechanisms, while the dashed line shows the neutral curve of the undisturbed Blasius boundary layer. In the near-field of the MVG, three different instability modes exist. However, these instabilities are confined to a narrow spatial region, therefore they are unlikely to initiate transition to turbulence. On the other hand, the TS waves are strongly attenuated by the streaky boundary layer generated by the MVGs, so high-frequency external disturbances are unlikely to lead to transition. It must be noted that the that low frequency TS waves, which play a role at higher Reynolds number, are much less affected by the streaks as further downstream the streak amplitude is much lower.

Our calculations display that at high frequency, close to the MVGs, the TS waves are strongly attenuated while the MVG creates multiple unstable modes. However, amplification factors show that a single mode in each case suffers the largest amplification; therefore, this single mode should be considered regarding the MVG leading premature transition. On the other hand, at high $\mathrm{Re}_\delta$, the streak amplitude decays, and the TS waves are only mildly affected by the streaks. Therefore, strongly persistent streaks need to be generated for successful transition delay, or the streaks should be reinforced with a second row of MVGs.

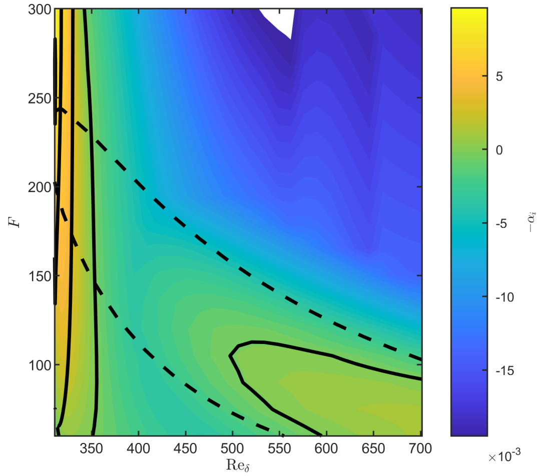

Figure 2: Maximum growth rate among the multiple instability mechanisms as a function of the Reynolds number based on the boundary layer scale and the nondimensional frequency $F = \hat{\omega}\hat{\nu}/\hat{U}_0^2 \cdot 10^6$. The continuous black curves display the neutral curves of the different instability mechanisms. The dashed curves display the neural curve of the TS waves in the undisturbed Blasius boundary layer. The data are shown for the case C02 in the paper of Sattarzadeh and Fransson [6].

## REFERENCES

[1] Jens H M Fransson. Transition to turbulence delay using a passive flow control strategy. *Procedia IUTAM*, 14:385–393, 1 2015.

[2] John Green. Laminar flow control - back to the future? In *38th Fluid Dynamics Conference and Exhibit*, page 3738, 2008.

[3] Y S Kachanov. Physical mechanisms of laminar-boundary-layer transition. *Annual Review of Fluid Mechanics*, 26:411–482, 1994.

[4] Juan A Martín and Pedro Paredes. Three-dimensional instability analysis of boundary layers perturbed by streamwise vortices. *Theoretical and Computational Fluid Dynamics*, 31:505–517, 2017.

[5] Juan A Martín and Pedro Paredes. Transition prediction in incompressible boundary layer with finite-amplitude streaks. *Energies 2021, Vol. 14, Page 2147*, 14:2147, 4 2021.

[6] Sohrab S Sattarzadeh and Jens H M Fransson. On the scaling of streamwise streaks and their efficiency to attenuate tollmien-schlichting waves. *Experiments in Fluids*, 56:58, 3 2015.

[7] Sohrab S. Sattarzadeh, Jens H. M. Fransson, Alessandro Talamelli, and Bengt E. G. Fallenius. Consecutive turbulence transition delay with reinforced passive control. *Physical Review E*, 89:061001, 6 2014.

[8] Shahab Shahinfar, Sohrab S. Sattarzadeh, and Jens H. M. Fransson. Passive boundary layer control of oblique disturbances by finite-amplitude streaks. *Journal of Fluid Mechanics*, 749:1–36, 2014.

[9] L. Siconolfi, S. Camarri, and J. H. M. Fransson. Stability analysis of boundary layers controlled by miniature vortex generators. *Journal of Fluid Mechanics*, 784:596–618, 11 2015.

**Joint ERCOFTAC/EU-CTFF**
**European Drag Reduction and Flow Control Meeting – EDRFCM 2022**
**September 6th–9th, 2022, Paris, France**

# DEVELOPMENT OF AN ALGORITHM FOR CREATING A DEVICE THAT FORMS THE SUBMERGED JET WITH REQUIRED INSTABILITY CHARACTERISTICS

**A. Spasova**
Institute of Mechanics, Lomonosov Moscow State University, 119192, Moscow, Russia

**J. Zayko**
Institute of Mechanics, Lomonosov Moscow State University, 119192, Moscow, Russia

Previously, the linear instability of a submerged jet of circular cross section, formed by a device consisting of a deturbulator and a rapidly expanding diffuser with metal grids at the outlet, was studied in detail (Fig. 1) [2, 6]. Jets with velocity profiles obtained in this way can be absolutely unstable without counterflow [4, 5], in contrast to submerged jets with velocity profiles of another family [3, 1]. By changing the flow velocity at the generalized inflection point, which generates the branch of the most rapidly growing perturbations, and the value of the derivative with respect to the radial coordinate at this point, one can influence the nature of the instability (convective/absolute) and select velocity profiles that will have the required instability characteristics in the linear approximation. The described jet control is of applied interest: long laminar jets are required to create local clean zones, and jets that turbulize as close as possible to their beginning are required to intensify mixing in the combustion chamber nozzles.

In this study, we develop an algorithm for finding the shape of the round diffuser geometry that forms a predetermined jet velocity profile or provides optimal (in the class of jets formed by devices of a specified configuration) instability characteristics of the resulting jet. The search algorithm for the required shape of the diffuser channel wall is realized by a code written in Python (see an example in Fig. 2). The geometry of the diffuser channel is set parametrically as a sixth-degree polynomial. The scheme of the algorithm is as follows: a) we calculate the laminar flow in the forming device by the finite volume method and obtain a jet velocity profile at the diffuser outlet; b) the optimization function is calculated; c) we use the gradient descent method to minimize the functional; d) in accordance with the calculated gradient in the space of the channel wall parameters, we change the geometry and the computational grid used in the calculation of the flow in the forming device. We can choose the characteristics of linear instability or the difference between the velocity profile and the predetermined one, as the function to be minimized.

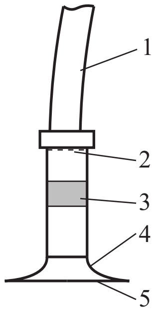

Figure 1: Scheme of the forming device. 1 - air supply line, 2 - grate, 3 - metal meshes that deturbulate the flow, 4 - diffuser, 5 - metal meshes at the outlet of the diffuser.

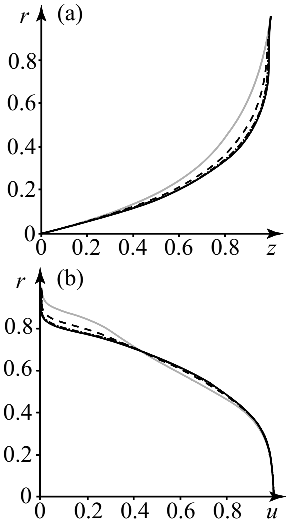

Figure 2: Stages of the optimizer program's work from the initial channel profile and speed (gray curves) to the required, in this example, absolutely unstable, speed profile (solid black curves). The dotted curves correspond to the 12th optimization step, and the dash-dotted curves correspond to the 17th. $z, r$ are dimensionless coordinates along the axis and radius of the jet, respectively, $u$ is the dimensionless longitudinal velocity of the jet. $a$ - diffuser channel profiles; $b$  corresponding velocity profiles.

## REFERENCES

[1] M. Abid, M. Brachet, and P. Huerre. Linear hydrodynamic instability of circular jets with thin shear layers. *Eur. J. Mech. B/Fluids.*, 12(5):683–693, 1993.

[2] L. R. Gareev, J. S. Zayko, A. D. Chicherina, V. V. Trifonov, A. I. Reshmin, and V. V. Vedeneev. Experimental validation of inviscid linear stability theory applied to an axisymmetric jet. *J. Fluid Mech.*, 934, 2022.

[3] P. Huerre and P. A. Monkewitz. Absolute and convective instabilities in free shear layers. *J. Fluid Mech.*, 159:151–168, 1985.

[4] L. Lesshafft and O. Marquet. Optimal velocity and density profiles for the onset of absolute instability in jets. *J. Fluid Mech.*, 662:398–408, 2010.

[5] V. V. Vedeneev and J. S. Zayko. On absolute instability of free jets. *J. Phys: Conf. Series.*, 2018.

[6] J. S. Zayko, L. R. Gareev, A. D. Chicherina, V. V. Trifonov, V. V. Vedeneev, and A. I. Reshmin. Experimental validation of linear-stability theory applied to a submerged jet. *Doklady Physics.*, 66:106–109, 2021.

**Joint ERCOFTAC/EU-CTFF**
**European Drag Reduction and Flow Control Meeting – EDRFCM 2022**
**September 6$^{\text{th}}$–9$^{\text{th}}$, 2022, Paris, France**

# THE DELAY OF NATURAL LAMINAR-TURBULENT TRANSITION USING ELASTIC COATING AND MINIATURE VORTEX GENERATORS

**Péter Tamás Nagy, András Szabó & György Paál**
Department of Hydrodynamic Systems, Faculty of Mechanical Engineering, Budapest University of Technology and Economics, H-1111 Budapest, Hungary

**Maarten Vanierschot & Gilles De Baets**
Department of Mechanical Engineering, Group T Leuven campus, KU Leuven, B-3001 Leuven, Belgium

## INTRODUCTION

One of the most desired aims in fluid dynamics is drag reduction. Among many possibilities, the delay of natural laminar-turbulent transition on a streamlined body is a promising candidate since the turbulent friction can be an order or orders of magnitude larger than that in the case of a laminar state. In this study, two different techniques are investigated to dampen the Tollmien-Schlichting waves and delay the transition at a low disturbance level. The first is an elastic coating consisting of miniature silicone rubber elements [1]. These elements can interact with the disturbances of the fluid with high density, and they can attenuate them. The widely investigated elastic coatings are usually deformable in the wall-normal direction by the pressure. The novelty of the coating is that the elements are moved in the streamwise direction by wall shear stress. The idea is inspired by the results of a controlled wall in the streamwise direction [2]. The other investigated passive technique is the usage of miniature vortex generators (MVGs) [3]. They generate a streaky boundary layer that can delay transition verified by experiments. Here, the linear stability analysis of the near and the far-field of the MVG is carried out by parabolic stability analysis.

## ELASTIC COATING

The elements are assumed to be significantly smaller than the wavelength of critical disturbances. They are modeled as a mechanical impedance that can be prescribed as a boundary condition at the wall. The element consists of two bars representing the elasticity and a rectangular cuboid at the top, representing a mass (Fig. 1). The impedance in the streamwise direction is calculated analytically. The elements are made of silicone rubber, while the fluid is water. The flow over the coating is investigated by spatial stability analysis using the Orr-Sommerfeld equation implemented in Matlab at various frequencies. The spatial growth of the disturbances is integrated in the streamwise direction, and the transition location is estimated by using the well-known $e^N$ method, where $N$ is set to 7. The coating parameters are optimized to maximize the transitional Reynolds number defined by the displacement thickness and the far stream velocity. The spatial growth as the function of the Reynolds number and the non-dimensional frequency can be seen in Fig. 2. The dashed line represents the neutral stability curve in the case of an original rigid wall. It can be seen that the critical Reynolds number was increased slightly. Furthermore, the growth is reduced, and the estimated transitional Reynolds number is 8870, which is roughly 3.5 times larger than in the case of a rigid wall (2570). Since the Reynolds number is defined using the displacement thickness, the usage of the coating can delay the transition by a factor of 10 in the distance from the leading edge over a flat plate. Further analysis of the eigenfunctions shows that the main mechanism of damping is the reduction of energy production, while the increment of dissipation is not a significant factor.

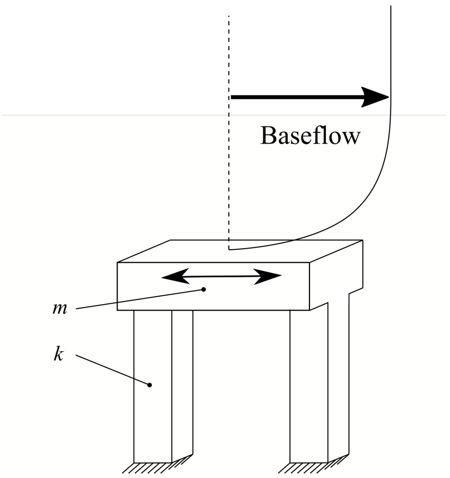

Figure 1: The schematic drawing of the coating

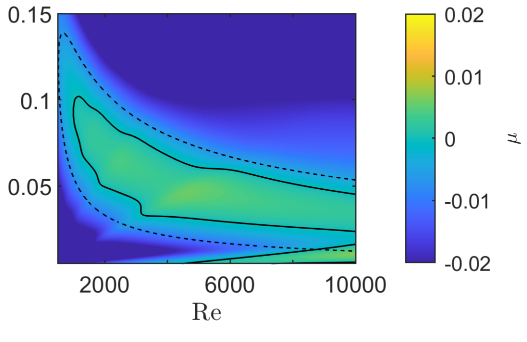

Figure 2: The spatial growth rate as a function of non-dimensional angular frequency and the Reynolds number in the case of the optimized elastic coating.

However, the elastic coatings can only operate in water or other high-density fluids. If the fluid density is small (e.g. air), any solid material acts as a rigid body during the calculation of the wall shear stress and has a negligible effect.

## MINIATURE VORTEX GENERATORS

The efficiency of surface structures and roughness elements on transition delay capability is not influenced by density in contrary to elastic elements. After successfully applying riblets on surfaces in the turbulent regime, their application was a promising way to achieve the transition delay, but after theoretical and experimental investigations, the method was a dead end. At the same time, roughness elements also influence the transition. Usually, they accelerate it, but properly designed elements generate a streaky boundary layer that can delay the transition, which was proven not only theoretically but also experimentally [4]. The effect of triangular MVGs is investigated similarly to the work of [3] in the case studies by Siconolfi et al. [5]. The near field of the vortex generator is solved by using 3D commercial CFD software. The downstream evolution of the flow is calculated by Boundary Region Equations implemented in FreeFem similarly to the stability investigation codes. The evolution of the disturbances is determined by using linear PSE, which accounts for both non-local and non-parallel effects. The initial disturbances are defined using BiGlobal stability equations. In Figs 3(a) and 3(b), the spatial growth rate of the kinetic energy is plotted as a function of the Reynolds number and the frequency parameter. Here, the Reynolds number is defined with the Blasius length scale. In Figure 3(a), the growth rate of the Tollmien-Schlichting instability wave is plotted. The critical Reynolds number is increased from 300 to 545 and the growth is reduced significantly in the unstable regime, which indicates the transition induced by high frequency instabilities is significantly delayed. However, another unstable mode appeared close to the MVG, which has also been reported in [3]. On the contrary, the elastic coating does not support any other linear instability, which can be advantageous in the case of moderate freestream disturbance levels. However, if the transition has not been initiated close to the MVG, it can be delayed significantly.

## CONCLUSION

In this study, two different approaches are investigated to delay the laminar-turbulent transition. Both methods can be optimized to achieve a significant delay in the natural transition and reduced drag. At the same time, previous results and the instability region close to MVG warn us that these methods work only at low external excitation levels where the natural transition occurs. The investigation of the non-linear stability [6] of these configurations will be necessary to develop industrially applicable solutions.

## ACKNOWLEDGMENT

Project no. MEC R 41054 has been implemented with the support provided by the Ministry of Innovation and Technology of Hungary from the National Research, Development and Innovation Fund, financed under the ”Mecenatúra” funding scheme.

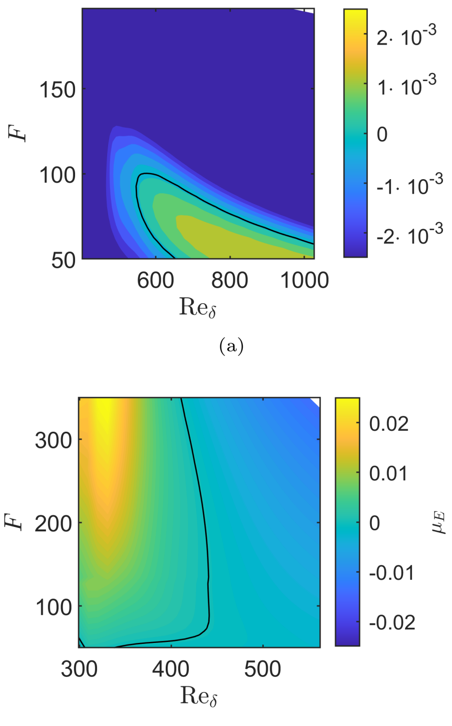

(a)

(b)

Figure 3: The spatial growth rate as a function of Reynolds number and the frequency parameter behind the MVG. (a) Tollmien Schlicting instability wave. (b) Instability mode close to the MVG. The solid black curve represents the neutral stability limit.

## REFERENCES

[1] P. T. Nagy, A. Szabó, M. Kulcsár and G. Paál. The effect of spanwise and streamwise elastic coating on boundary layer transition. *J Fluids Struct*, 110:103521, 2022.

[2] P. T. Nagy and G. Paál. Stabilization of the boundary layer by streamwise control. *Phys. Fluids*, 31:124107, 2022.

[3] J. A. Martín and P. Parades. Three-dimensional instability analysis of boundary layers perturbed by streamwise vortices. *Theor Comput Fluid Dyn*, 31:505–517, 2017.

[4] Shahab Shahinfar, Sohrab S. Sattarzadeh, and Jens H. M. Fransson. Passive boundary layer control of oblique dis- turbances by finite-amplitude streaks. J. *Fluid Mech.*, 749:1–36, 2014.

[5] L. Siconolfi, S. Camarri and J. H. M. Fransson. Stability analysis of boundary layers controlled by miniature vortex generators. J. *Fluid Mech.*, 784, 596-618, 2015.

[6] P. T. Nagy. Enstrophy change of the Reynolds-Orr solution in channel flow. *Phys. Rev. E*, 105:3, 2022.

**Joint ERCOFTAC/EU-CTFF**
**European Drag Reduction and Flow Control Meeting – EDRFCM 2022**
**September $6^{th}$–$9^{th}$, 2022, Paris, France**

# EXPERIMENTAL DETECTION OF NON-MODAL PERTURBATION GROWTH MECHANISM IN A LAMINAR JET

**L. Gareev, D. Ashurov & V. Vedeneev**
Faculty of mechanics and mathematics, Lomonosov Moscow State University, 119234 Moscow, Russia

**O. Ivanov**
Institute of mechanics, Lomonosov Moscow State University, 119192 Moscow, Russia

## INTRODUCTION

Laminar submerged jets, either planar or axisymmetric, are employed in various industrial processes. Creation of laminar jet flows is difficult due to very low critical Reynolds numbers: 4.02 for the planar Bickley jet and 37.6 for axisymmetric jet with "far-downstream" velocity profile. It is important to have a robust theory for predicting evolution of perturbations in jet flows.

It is well known that in near-wall flows with growth of modal instability, non-modal (algebraic) mechanism of perturbation growth plays important role in bypass scenario of transition to turbulence. In unbounded flows, such as submerged jets, theoretical investigations of non-modal growth mechanism has been conducted only in the past decade [1], [3].This mechanism has not been detected yet experimentally and its role in transition to turbulence in such flows remains unclear.

## FORMING DEVICE

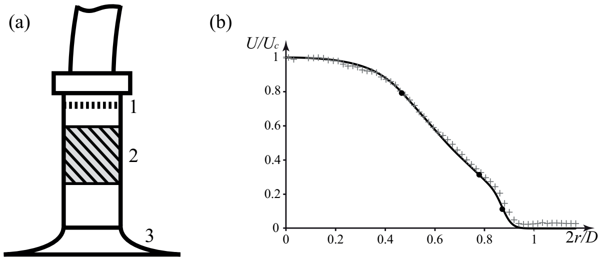

Figure 1: Forming device (a), consists of 1 – perforated plate, 2 – bushing with metal grids, 3 – diffuser. Forming velocity profile considered in this study (b), where pluses denote experimental measurements and solid line denotes calculated profile.

In this study, we considered a laminar axisymmetric jet flow, which is formed by a device of a special type (Fig. 1). It consists of three main parts : a perforated plate – smooths out the stream incoming from the airline, a bushing with two metal grids – reduces the level of turbulence down to 0.1%, a diffuser with a large expansion ratio – the flow expands from 0.04 m to $D = 0.12$ m. The setup is described thoroughly in [4]. Having the jet with long laminar region (no less than $5D$), we could observe the evolution of introduced perturbations at large distances from the orifice.

One regime is selected, in which the air flow has long laminar region with a velocity on the axis $U_{max} = 1.5$ m/s and average velocity $U_{avg} = 0.66$ m/s with $Re = 5400$. The downstream evolution of the unperturbed jet profile is weak and is not taken into account in theoretical analysis and calculations.

## THEORETICAL BASIS

The feature of non-modal spatial instability is that, if the flow is stable, or even if there exist growing modes, a linear combination of modes can give a much stronger growth of the perturbation kinetic energy $E(z)$ than a single mode can provide for a limited range of axial coordinates $z$.

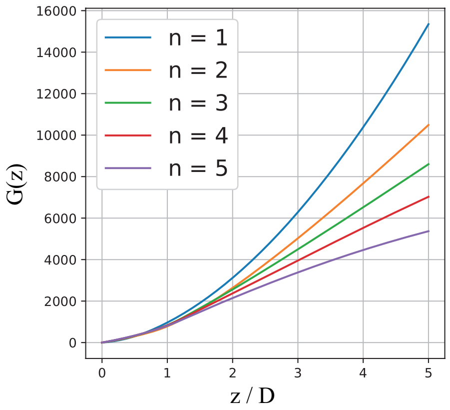

Figure 2: Energy growth of stationary optimal perturbations downstream for various azimuthal numbers $n$.

Boronin etc. [1] showed that for several types of jet flows, stationary perturbations demonstrate the largest non-modal growth. For the profile under consideration, it is also shown that stationary perturbations are the most optimal, i.e. they have the most kinetic energy increase with respect to the highest kinetic energy of a single modal perturbation $E(0)$. Maximum kinetic energy of all perturbations

$$G(z) = \max \frac{E(z)}{E(0)}$$

versus the distance downstream were found for various azimuthal numbers $n = 1, 2, 3, 4, 5$ (Fig. 2). Each curve in Fig. 2 depicts the envelope of the family of curves for the relative kinetic energy of all possible stationary perturbations for a given $n$.

## EXPERIMENTAL RESULTS

To excite non-modal mechanism of perturbation growth, the experiments have been conducted on the facility [4], which was previously used in studies of eigenmodes growth [2]. Special wavy structures (deflectors) are put into the laminar submerged air jet at a short distance from the orifice in order to introduce stationary perturbations (Fig. 3).

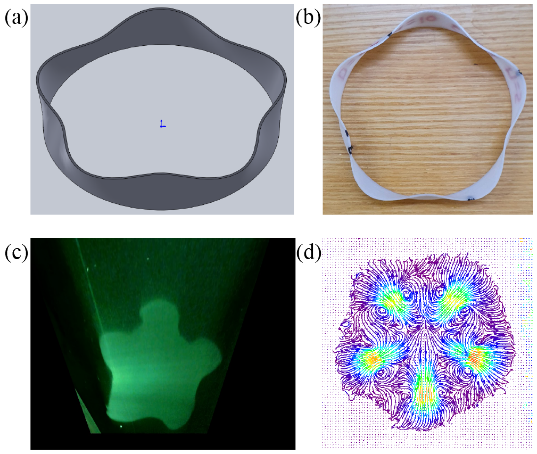

Figure 3: 3D model (a) and printed deflector (b) with azimuthal $n = 5$ and inlet diameter $d_0 = D/2$; visualized deformed cross-section of the jet by deflector (c) and transversal velocity field with streamlines for the disturbance (d) at $z = 1.5D$ for $n = 5$

These perturbations lead to the base flow deformation, gradual "petals" separation and the roller-shaped motion, which corresponds to the lift-up mechanism of perturbations amplification (Fig. 4).

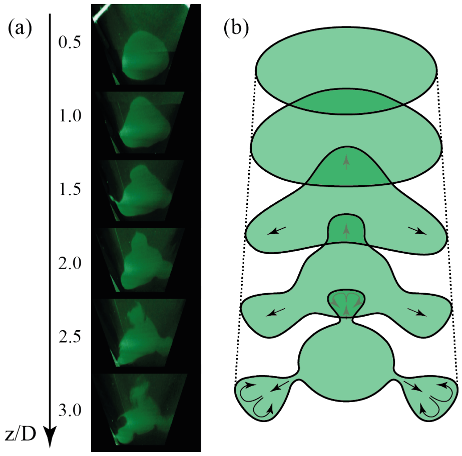

Figure 4: Evolution of stationary perturbations introduced by deflector with $n = 3$ in cross-section photographs (a) and scheme of this evolution (b).

Experimentally obtained parameters via anemometer measurements, laser sheet visualizations and PIV measurements of transverse sections, such as evolution of perturbations, qualitatively corresponds to theoretically calculated parameters of optimal disturbances (those that provide non-modal growth). For example for $n = 3$, at Fig. 5(a), constant increase of "petal" length evidences constant transverse component of velocity perturbations, which was also confirmed by PIV measurements. Also, hot-wire measurements showed axial velocity linear increase inside "petals" (Fig. 5(b)) and axial velocity linear decrease between them (Fig. 5(c)). These experimental results are in accordance with non-modal perturbation properties.

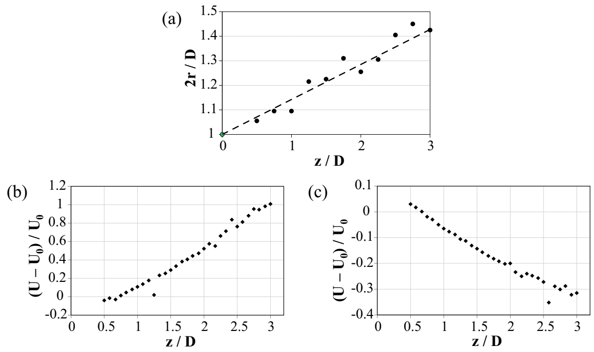

Figure 5: Experimental measurements for deflector with $n = 3$: (a) The "petal" length as a function of $z/D$; axial velocity linear increase (b) inside "petals" and linear decrease (c) between them.

Hence, for the first time a non-modal mechanism for the growth of disturbances in a laminar jet is experimentally detected – an analogue of the "lift-up" mechanism in near-wall flows. The following characteristic features of the "lift-up" growth mechanism have been confirmed:

1. the transverse velocity remains approximately constant downstream;
2. the axial velocity increases downstream approximately linearly;
3. the transverse movement has the form of "roll-like" movements, transferring the outer layers of the liquid inward, and the inner layers outward. This motion causes a local increase in the perturbation of the axial velocity — an analogue of the streaky structure in near-wall flows.

The suppression of the modal growth of Kelvin-Helmholtz waves and the excitation of the non-modal "lift-up" growth mechanism leads to a different scenario of transition to turbulence, not previously observed in jet flows.

## ACKNOWLEDGEMENTS

This work is supported by the Russian Science Foundation under grant 20-19-00404.

## REFERENCES

[1] S. A. Boronin, J. J. Healey, and S. S. Sazhin. Non-modal stabillity of round viscous jets. *J. Fluid Mech.*, 716:96–119, 2013.

[2] L.R. Gareev, J.S. Zayko, A.D. Chicherina, V.V. Trifonov, A.I. Reshmin, and V.V. Vedeneev. Experimental validation of inviscid linear stability theory applied to an axisymmetric jet. *J. Fluid Mech.*, 934:A3, 2022.

[3] J. I. Jimenez-Gonzalez, P. Brancher, and C. Martinez-Bazan. Modal and non-modal evolution of perturbations for parallel round jets. *Phys. Fluids*, 27:044105, 2015.

[4] J. Zayko, S. Teplovodskii, A. Chicherina, V. Vedeneev, and A. Reshmin. Formation of free round jets with long laminar regions at large reynolds numbers. *Phys. Fluids*, 30:043603, 2018.

**Joint ERCOFTAC/EU-CTFF**
**European Drag Reduction and Flow Control Meeting – EDRFCM 2022**
**April 11–14, 2022, Paris, France**

# MODAL ANALYSIS AND FLOW CONTROL ON A REDUCED SCALE SUV

**S. Edwige**
Plastic Omnium, F-01150 Sainte-Julie, France

**Ph. Gilotte**
Plastic Omnium, F-01150 Sainte-Julie, France

**I. Mortazavi**
M2N EA-7340, CNAM, 2 Rue Conté, Paris, France

**C.N. Nayeri**
TU-Berlin, D-10623 Berlin-Charlottenburg

## INTRODUCTION

Sport Utility Vehicles (SUV) represent a large part of the market share. These vehicles have a 47° rear window responsible for massive detachment [3]. Analysis of their wake flow should help to design efficient flow control as shown in [1, 2, 4]. Experimental analysis of a generic reduced scale SUV model, achieved in TU-Berlin wind tunnel, highlights the wake flow features at a Reynolds number of 420 000 (based on 0.2m height) for a far field velocity of 30m/s (Fig.1). The rear pressure sensitivity to active flow control using pulsed blowing jets on the rear bumper is identified. Genetic algorithm enable to find an optimal point leading to a significant Cp reduction on the tailgate. A cross Dynamic Mode Decomposition (DMD) on the unsteady velocity between experimental 2D-PIV and numerical cut-plane is used to understand the mecanism responsible for the pressure loss.

## FLOW TOPOLOGY: EXPERIMENTS AND NUMERICAL SIMULATIONS

The experimental analysis of the wake flow behind the reduce scale SUV model displayed in Fig.1a, has been performed in TU-Berlin wind tunnel. This wind tunnel, sketch in Fig.1b, is characterized by a cross section of 1.6m x 2m with a reference velocity of 30m/s and zero pressure at Pitot tube. The time averaged pressure coefficient in the baseline flow, displayed in Fig.2a, reveals that the main pressure losses are located on the lower part of the tailgate.

The active flow control consists in micro-slots of 1.25x5mm evenly distributed along the lateral and bottom corners of the rear bumper where periodic normal pulsed blowing jets are injected. A genetic algorithm has been used to find the optimal set of parameters in order to reduce the time averaged rear end pressure loss defined as the cost function J=-Cp . The algorithm, detailed in Fig.2a, is based on the machine learning control developed in the work of [5].The optimal set of parameters is achieved evolving 51 individuals (each one corresponding to a set of 10 parameters) during 16 generations by applying evolution processes (mutation, cross-over, copy, elitism). The optimal solution displayed in Fig.2a, led to a pressure increase of 20% on the rear end as shown in Fig.2b.

To deepen the analysis, Large Eddy Simulations are performed using Dynamic Smagorinsky subgrid scale model with a Finite Element Method. The numerical domain has been discretized on a 300 million tetrahedral cell mesh corresponding to 54 million nodes. The time averaged flow features, based on 1.2 seconds converged flow, are in good agreement with experimental measurements as shown in Fig.3.

Based on numerical simulations, an investigation of the wake structures using modal decomposition applied in the flow surrounding the mock-up provides some insights explaining the wake behavior observed in experiments.

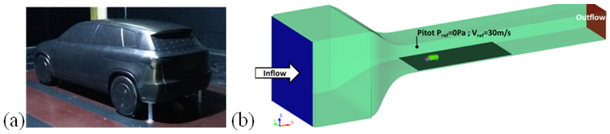

Figure 1: (a) Reduced scale POSUV mockup associated to 0.2m reference height; (b) Sketch of the experimental setup in TU-Berlin wind tunnel.

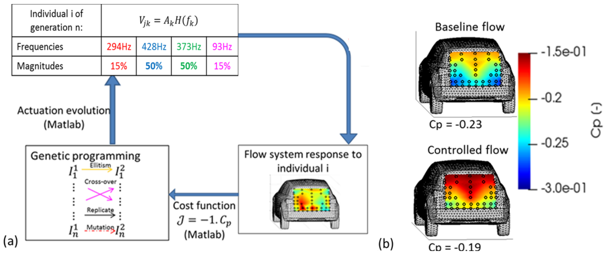

Figure 2: (a) Sketch of the machine learning procedure using genetic algorithm; (b) Time averaged rear Cp in baseline and controlled flow with the best actuation parameters.

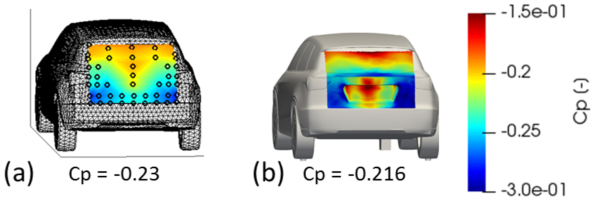

Figure 3: Time averaged pressure coefficient in (a) experiments; (b) CFD.

## CROSS DMD BETWEEN EXPERIMENTS AND SIMULATIONS

Cross-modal analysis method has the advantage to output an estimator of the energy ratio associated to a common dynamical mechanism between experiments and CFD. It is based on the application of the Sparsity Promoting Dynamic Mode Decomposition as proposed by (7; 6), on a concatenation of the time-space databases in experiments and in CFD sampled at the same frequency (Fig. 4). It is applied on the overlapping of the transient databases of velocity in the centered vertical cut plane Y0 and the horizontal cut plane at 140mm from the floor. The numerics provide larger flow dynamics description than in experiments increasing the investigation window size. Experimental data are based on high speed PIV with spatial resolution of 2.5mm. A total of 2001 snapshots, sampled at 2kHz, from both experimental and CFD results were used.

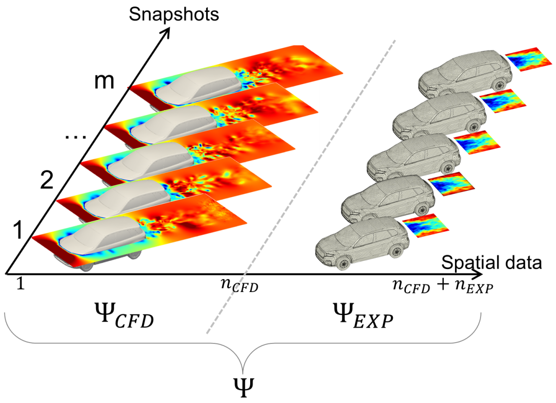

Figure 4: Illustration of the database assembly for cross-DMD between CFD and experiments with $[\Psi_1, \Psi_2, ...\Psi_m]$ the velocity snapshots at different time steps.

We may recall the main steps of the DMD algorithm. First, a SVD decomposition (Singular Value Decomposition) is performed on $\Psi_0$, allowing to compute the DMD matrix $\tilde{A}$. The computation of the complex eigenvalues $\mu$ of $\tilde{A}$ provides the frequencies of the system. The associated complex eigenvectors, projected on the POD matrix $U$, coming from the SVD, provides the spatial DMD modes $\Phi$. Application of this technique on the numerical and experiment databases gives respectively DMD modes $\Phi_{exp}$ and $\Phi_{cfd}$ concatenated in the matrix $\Phi$. This method allows to identify the CFD and experimental energy contributions per DMD components.

The associated modal magnitudes $\alpha$ computed as proposed in (6), are decomposed in an experimental contribution $\alpha_{exp}$ and CFD contribution $\alpha_{cfd}$ by multiplication with $diag(E_{exp})$ and $diag(E_{cfd})$. The experimental/CFD comparison of the spectral energy ratio, presented in Fig. 5a, highlights similar spectral signature even if the energy ratio of the main frequencies at 25Hz and 30Hz are stronger in CFD in the symetric vertical cut-plane Y0 (Fig. 5b).

These peaks correspond to the vortex shedding natural frequency (St=0.2) based either on the square root of the frontal area or on the height of the tailgate. Streamlines in the Y0 cut-section form a S-shape structure controlled by the underbody flow boundary conditions and bounded by the roof spoiler. The aerodynamic losses at this natural frequency can be reduced or suppressed thanks to a periodic flow control localized on the rear bumper. The optimal flow solution obtained with the genetic algorithm is in agreement with this assumption.

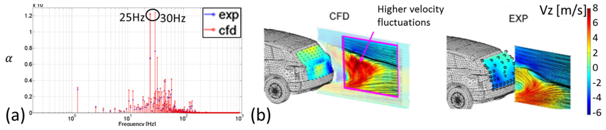

Figure 5: (a) Modal magnitudes from experiments and CFD per DMD mode as a function of the DMD frequency extracted in the overall time-space domain; (b) Reconstructed snapshots of velocity with 25Hz and 30Hz DMD modes with the time average field.

## CONCLUSION

This study highlights the importance of the underbody flow on the wake structure, which can be explained by a non symetric tailgate profil in Y0. Dynamic decomposition enables to extract the main frequencies existing in the wake related to the natural vortex shedding mechanism. Origin of this vortex shedding in the symetric vertical plane seems to be controlled thanks to periodic boundary conditions imposed on the rear bumper. Experiments involving genetic algorithm confirm an operating point leading to a pressure increase on the tailgate.

## REFERENCES

[1] Bideaux, E., Bobillier P., Fournier E., Gilliéron P., El Hajem M., Champagne J.y.,Gilotte P. , Kourta A. Drag reduction by pulsed jets on strongly unstructured wake: towards the square back control . Int. J. of Aerodynamics 1, n°3-4 (2011): 282-98. https://doi.org/10.1504/IJAD.2011.038846.

[2] Edwige S., Eulalie Y., Gilotte P., Mortazavi I.: Wake flow analysis and control on a 47° slant angle Ahmed body. Int. J. of Num. Meth. Heat & Fluid Flow 28, n°5 (2018): 1061-79. https://doi.org/10.1108/HFF-06-2017-0260.

[3] Eulalie Y., Fournier E., Gilotte P., Holst D., Johnson S., Nayeri C.-N., Schütz T., Wieser D.: Active flow control analysis at the rear of an SUV. Int. J. of Num. Meth. Heat & Fluid Flow 28, n°5 (2018):1169-86. https://doi.org/10.1108/HFF-06-2017-0230.

[4] Eulalie Y., Gilotte P., Mortazavi I.: Numerical Study of Flow Control Strategies for a Simplified Square Back Ground Vehicle. Fluid Dynamics Research 49, n°3 (2017): 035502. https://doi.org/10.1088/1873-7005/aa5c54.

[5] Gautier N., Aider J.-L., Duriez T., Noack B. R., Segond M., Abel. M.: Closed-Loop Separation Control Using Machine Learning. Journal of Fluid Mechanics 770 (2015): 442-57. https://doi.org/10.1017/jfm.2015.95.

[6] Jovanović, M. R., Schmid P. J., Nichols J. W.: Sparsity-promoting dynamic mode decomposition. Physics of Fluids 26, n°2 (2014): 024103. https://doi.org/10.1063/1.4863670.

[7] Schmid, Peter J.: Dynamic mode decomposition of numerical and experimental data: Journal of Fluid Mechanics, 656 (2010), pp.5-28. doi:10.1017/S0022112010001217.

**Joint ERCOFTAC/EU-CTFF**
**European Drag Reduction and Flow Control Meeting – EDRFCM 2022**
**September 6$^{\text{th}}$–9$^{\text{th}}$, 2022, Paris, France**

# SUPPRESSING THE PRESSURE DRAG OF A TURBULENT BLUFF BODY WAKE WITH PULSED JET FORCING

**Taihang Zhu**

**Georgios Rigas**

**Jonathan Morrison**
Department of Aeronautics, Imperial College London, SW7 2AZ London, UK

## ABSTRACT

The turbulent axisymmetric bluff body wake is controlled with a high-frequency high-amplitude pulsed jet forcing at $Re_D = 1.88 \times 10^5$. Based on the previous work of Oxlade *et. al* (2015)[1], the actuator is redesigned, which allows us to investigate the high-amplitude forcing conditions. The synchronized particle image velocimetry (PIV) and base pressure measurement are used to analyse the wake dynamics and the flow field. The result shows that at the optimal forcing condition ($f = 700$ Hz or $St_D = 9.17$, $C_\mu = 0.27$), a base pressure recovery of about 88% is achieved, indicating the pressure drag is largely suppressed. The base pressure recovery is associated with a suppression of the turbulent flow separation near the trailing edge and a global reduction in the separation bubble size, accompanied by the shear layer deviation. At the optimal forcing frequency, up to the blowing coefficient $C_\mu = 0.11$, the pulsed jet globally suppresses all the azimuthal modes without any mode selection, while above this threshold, the pulsed jet amplifies the azimuthal modes ($m = 0, \pm1, \pm2$) near the vortex shedding frequency ($St_D = 0.2$).

## EXPERIMENTAL SETUP

Figure 1 presents a schematic of the experimental setup. A bullet-shaped axisymmetric body with a blunt trailing edge is located on the centreline of the wind tunnel. 64 pressure tappings are distributed uniformly on the base to measure the base pressure distribution. 8 Endevco pressure transducers are evenly distributed at $r/D = 0.3$ to measure the base pressure fluctuation at 50 kHz. The inlet velocity is $U_\infty = 15$ m/s and the Reynolds number based on the diameter of the bluff body model ($D = 0.1965$ m) is $Re_D = 1.88 \times 10^5$. An axisymmetric pulsed jet actuator (speaker) is installed to produce a high-amplitude pulsed jet with a maximum blowing/suction coefficient $C_\mu = 0.27$.

The non-dimensional pressure coefficient is given by $C_p = \frac{p - p_\infty}{\frac{1}{2}\rho U_\infty^2}$. The base pressure change is given by $\Delta C_p = \frac{C_p - C_{p0}}{|C_{p0}|}$, where $C_{p0}$ is the unforced base pressure. The area-weighted base pressure coefficient is denoted as $\langle C_p \rangle$. The Strouhal number is given by $St_D = fD/U_\infty$, where $f$ is the dimensional frequency. The pulse jet velocity is expressed as a blowing coefficient which is given by $C_\mu = \frac{u_f^2 A_j}{U_\infty^2 A_b}$, where $u_f$ is the forcing amplitude defined as the amplitude of the Fourier component of the jet centre line velocity, $A_j$ and $A_b$ are the area of the slot and the base, respectively.

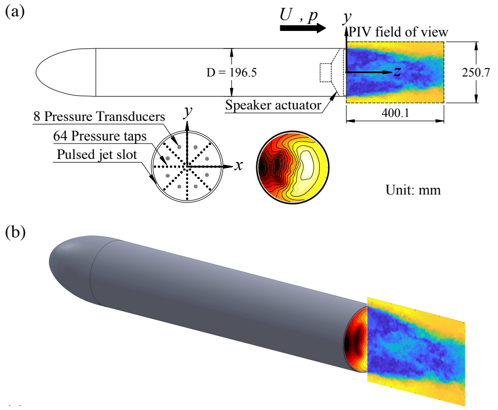

Figure 1: (a) A schematic of the experimental setup. The base pressure taps and the instantaneous base pressure distribution are shown on the lower side. (b) A 3D view of the model with the instantaneous PIV flow field and the synchronized base pressure measurement.

In the unforced wake, a time-resolved two-dimensional two-component PIV is used to measure the near wake velocity fields. As is shown in figure 1(a), the field of view (FOV) covers the near-wake area with a 400 mm x 251 mm rectangular plane passing through the body axis. The vector fields are produced with a sampling frequency of 720 Hz and a resolution of 2.53 mm. The PIV measurement is accompanied by the simultaneously base pressure measurements.

In the forced wake, since the forcing frequency of the pulsed jet is as high as 700 Hz, using a time-resolved PIV to resolve the wake for the whole pulsed jet period is unfeasible. Therefore, phase-locked PIV is used to resolve the near wake velocity fields. A total number of 17,970 vector fields are taken at 40 phases of the forcing period. In the post processing, these vector fields are phase-locked averaged to achieve phase-locked flow fields.

## RESULTS

The response of the area-weighed mean base pressure change $\langle \overline{\Delta C_p} \rangle$ to pulsed jet forcing is shown in figure 2. The upper limit of the forcing amplitude $C_\mu$ is determined by the limit of the actuator (loudspeaker) and the frequency range is bounded by the linear frequency response range of the actuator. The frequency range investigated here is in the high-frequency range of Oxlade *et. al* (2015)[1] and the maximum forcing coefficient is much higher. It shows that base pressure recovery is achieved in the whole map except for some small amplitude area below $C_\mu = 0.01$. At the optimal forcing con-

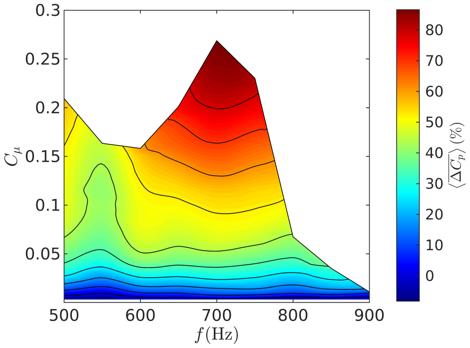

Figure 2: The effect of pulsed jet forcing on area weighted mean base pressure.

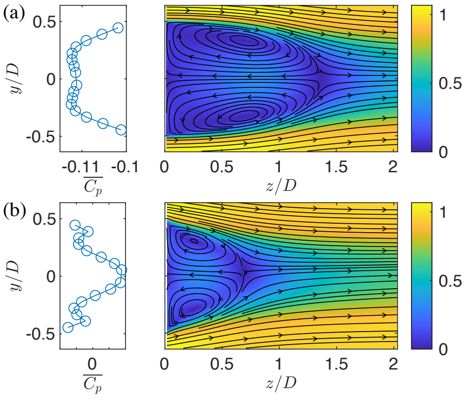

Figure 3: The mean base pressure and PIV velocity field for (a) the unforced wake and (b) the forced wake in the optimal forcing condition (700 Hz or $St_D = 9.17$, $C_\mu = 0.27$).

dition ($f = 700$ Hz or $St_D = 9.17$, $C_\mu = 0.27$), a base pressure recovery of 87.57% is achieved.

The effect of pulsed jet forcing at the optimal condition (700 Hz or $St_D = 9.17$, $C_\mu = 0.27$) is investigated using synchronized PIV and base pressure measurement, with a comparison with the unforced wake (figure 3). The mean flow field shows that the size of the circulation bubble is greatly reduced by the pulsed jet and the wake is narrowed. The stagnation point location is reduced from $z/D = 1.37$ to $z/D = 0.68$ and the shear layer deviates toward the wake centre-line. Near the separation point, the separation streamline has deviated towards the base, forming a concave separation streamline. This result shows that the base pressure recovery in the forced wake is associated with a suppression of the turbulent flow separation near the base edge and a global reduction in the separation bubble size, accompanied by the shear layer deviation and the streamlines becoming concave.

The effect of pulsed jet forcing on the wake dynamics is investigated by analysing the premultiplied pressure spectra of the azimuthal modes (figure 4). A detailed description of the azimuthal decomposition can be found in Oxlade *et. al* (2015)[2] and Rigas *et. al* (2014) [3]. Figure 4 shows how the azimuthal modes change as the forcing amplitude increases at 700 Hz ($St_D = 9.17$). Below $C_\mu = 0.11$, the pulsed jet globally suppresses all the azimuthal modes without mode selection. However, above this threshold, the pulsed jet amplifies the azimuthal modes especially near the vortex shedding frequency ($St_D \sim 0.2$). At $C_\mu = 0.27$, compared with the unforced wake, the $m = 0$ bubble pumping mode is weakened, while another peak appears near the vortex shedding frequency ($St_D \sim 0.2$). The $m = \pm 2$ mode shows a similar trend as the $m = 0$ mode. At the maximum forcing amplitude, the peak near $St_D \sim 0.1$ is weakened and a peak near the vortex shedding frequency ($St_D \sim 0.2$) appears. In the $m = \pm 1$ mode, the symmetry-breaking mode ($St_D \to 0$) and the vortex shedding mode are amplified. These results show that at the optimal forcing condition, the vortex shedding is dramatically amplified with a broadband range of azimuthal wavenumber ($m = 0, \pm 1, \pm 2$).

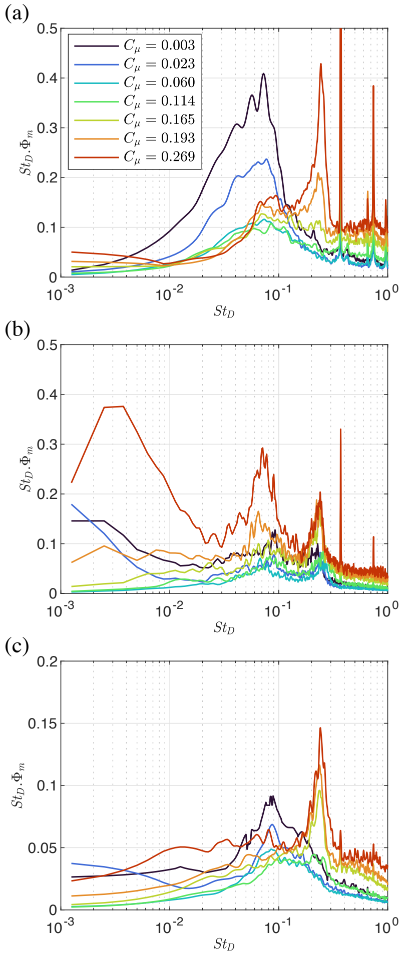

Figure 4: The effect of pulsed jet forcing on the premultiplied pressure spectra of the azimuthal modes for the (a) $m = 0$, (b) $m = \pm 1$, and (c) $m = \pm 2$ modes.

This abstract presents the latest progress in the axisymmetric bluff body drag reduction with pulsed jet forcing. At EDRFCM 2022, we will present further analysis of the forced wake, such as the phase-locked averaged flow fields and proper orthogonal decomposition results.

## REFERENCES

[1] A. R. Oxlade, J. F. Morrison, A. Qubain, and G. Rigas. High-frequency forcing of a turbulent axisymmetric wake. *Journal of Fluid Mechanics*, 770:305–318, 2015.

[2] Anthony Oxlade. *High-frequency Pulsed Jet Forcing of an Axisymmetric Bluff Body Wake.* PhD thesis, Imperial College London, 2013.

[3] Georgios Rigas. *Modelling of turbulent wakes.* PhD thesis, Imperial College London, 2014.

**Joint ERCOFTAC/EU-CTFF**
**European Drag Reduction and Flow Control Meeting – EDRFCM 2022**
**September 6$^{\text{th}}$–9$^{\text{th}}$, 2022, Paris, France**

# AERODYNAMIC DRAG REDUCTION OF A TILT ROTOR AIRCRAFT USING ZERO-NET-MASS-FLUX DEVICES

**H. Truong**
ICUBE, University of Strasbourg, France

**A. Marouf**
ICUBE, University of Strasbourg, France

**J.B. Vos**
CFS Engineering, EPFL Innovation Park, Batiment A, CH-1015 Lausanne, Switzerland

**A. Gehri**
CFS Engineering, EPFL Innovation Park, Batiment A, CH-1015 Lausanne, Switzerland

**Y. Hoarau**
ICUBE, University of Strasbourg, France

## INTRODUCTION

In the frame of the CleanSky2 project AFC4TR (Grant Agreement 886718), detailed studies are made on the use of Active Flow Control (AFC) on the Next Generation Civil Tilt Rotor (NGCTR) aircraft. This is fully in line with the mission of the Clean Aviation Joint Undertaking to develop disruptive new aircraft technologies to support the European Green Deal, and climate neutrality by 2050. The NGCTR is a novel aircraft concept combining the capabilities of vertical take-off and landing of a helicopter with the range and the speed of a fixed wing aircraft. Active Flow Control on the NGCTR is studied using so called Zero Net Mass Flux (ZNMF) devices. The application of these devices have been worldwide intensively investigated due to its effectiveness and simple implementation. These actuators do not require a piping for pressurized air source, yet create non-zero-net momentum flux via periodic suction and ejection of fluid through an orifice. Although the efficiency of ZNMF actuators for relatively simple airfoils in 2D have been pointed out by previous studies, the benefits of integrating ZNMF into a whole aircraft for real and unsteady flight condition is still an open question. More recently, we studied two-dimensional active control using different strategies of steady blowing, transient blowing and blowing-suction method similar as piezo-actuators embedded inside the flap of a high-lift system [1]. The AFC was coupled with a morphing flap [3] using the cambering approach [2]. The coupling could re-attach the boundary layer, enhance the pressure distribution over both the flap and the wing system and decrease the width of the wake. In this study, we expand our previous studies by investigating the benefits of integrating ZNMF into a whole tilt rotor aircraft for real and unsteady flight condition.

## NUMERICAL METHODS

The Navier Stokes Multi Block solver (NSMB) developed in a consortium composed of different universities and industries [4] was used in this study for all the CFD simulations. The solver was using a cell-centered finite volume method with multi block structured grids. It can easily deal with the mesh generation for complex geometries by taking advantages of the patch grid and chimera method. Moreover, a large variety of turbulence models was included in the solver. For unsteady CFD simulations Hybrid RANS-LES models are available as well as the $k-\omega$ Organized Eddy Simulation model which were used for 2D and 3D simulations.

To make sure that the viscous boundary layer is well resolved, we used here O-grid topologies with a geometric cell distribution near the solid walls (wing, aileron, fuselage, nacelle, engine, rotor blades). Figure 1 (a) and (b) show the mesh on the airplane surface as well as the volume mesh around chimera components. Particular attention was also paid to the refinement of the mesh close to the areas where the flow control devices ZNMF devices will be applied later in the study (cf. Figure 1 (c)).

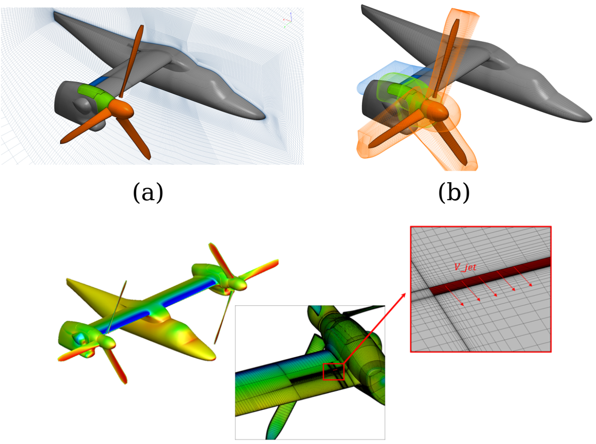

(a) (b)

(c)

Figure 1: Surface mesh (a), volume mesh around chimera components (b) and AFC devices embedded inside the wing (c).

## RESULTS AND DISCUSSION

In order to identify which configurations of the aircraft could benefit from the employment of ZNMF devices, a large number of unsteady simulations of the flow around the Next Generation Civil TiltRotor (NGCTR) aircraft of Leonardo Helicopters were performed. These outcomes in a selected subsonic speed range considering take-off and landing phases, revealed a considerable detachment of the boundary layer and a loss in aerodynamic performances due to an increase of the drag and a decrease in lift. The following three configurations (cf. Figure 2) were chosen for our study:

- Case 1: closed gap, nacelle 0°, aileron deflection 0°;
- Case 2: closed gap, nacelle tilting, aileron deflection 0°;
- Case 3: opened gap, nacelle 0°, aileron deflection downwards.

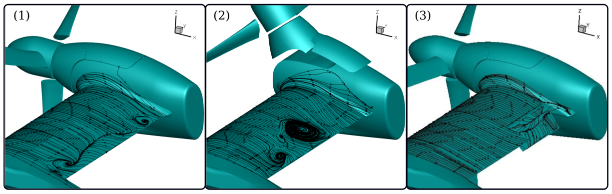

Figure 2: The three studied configurations of the NGCTR aircraft: the fixed-wing plane (1), the nacelle tilting (2) and the aileron deflection (3).

Due to the rotating rotors, the blockage effect induces the formation of a small corner vortex near the wing-nacelle junction. Consequently, six ZNMF devices embedded in different regions near the fuselage-wing junction, the middle of the span and the aileron-nacelle junction in the attempt to reattach the flow. The jets were translated along the chordwise direction in order to investigate the sensitivity of the jet location to the corner vortex as shown in Figure 3. As the jets were moved upstream and far away from the separation line, the effect of these ZNMF becomes less important. However, when they were moved downstream and closer to the trailing edge where the flow is starting to detach, the size of the separation zone was reduced and the vortex at the aileron-nacelle junction almost disappeared.

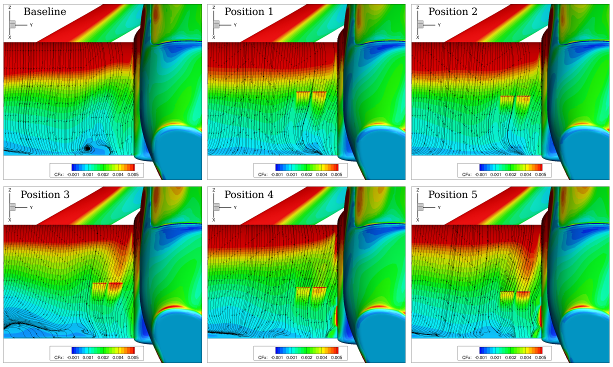

Figure 3: Skin friction $CF_x$ component contours with streamlines of CF $(CF_x, CF_y, CF_z)$ for the baseline (top left) and the controlled cases of configuration 1 with the rotation of blades.

In the case of the configuration 3, the flow remains attached along the span of the wing and is less sensitive to the rotation of the blades. However, the flow around the aileron is fully detached as shown in Figure 2(3). Thus, the interest of using active flow control will be focused on the aileron part where the ZNMF devices will be the most effective. There were in total 6 jets embedded on the aileron and their positions are optimized as in the previous case by moving the jets long the chordwise direction of the aileron. The average value of the drag coefficient $Cx$, the lift coefficient $Cz$ and the lift-to-drag ratio $Cz/Cx$ for all the cases are shown in Table 1. The average value of the drag coefficient $Cx$ seems to be unaffected while the lift coefficient in the controlled cases are improved with respect to the baseline. In addition, the configuration 1 outperforms the other configurations characterized with the highest lift-to-drag ratio.

| Configuration of ZNMF | Cx | Cz | Cz/Cx |
|---|---|---|---|
| Baseline | 0.2759 | 0.6037 | 2.1881 |
| 1 | 0.2688 | 0.6771 | 2.519 |
| 2 | 0.2619 | 0.6569 | 2.5082 |
| 3 | 0.2666 | 0.6654 | 2.4959 |
| 4 | 0.2723 | 0.6671 | 2.4499 |
| 5 | 0.2571 | 0.6301 | 2.4508 |

Table 1: Time-average values of the lift coefficient $Cz$, the drag coefficient $Cx$ and the lift-to-drag ratio $Cz/Cx$ acting on the aileron in the configuration 3 for different cases of the baseline and the one controlled with ZNMF devices. The values are integrated for 1 rotation of the rotor.

In conclusion, we present here the preliminary sesults of CFD simulations using Zero Net Mass Flux (ZNMF) devices for active flow control on the Next Generation Civil Tilt Rotor Technical Demonstrator (NGCTR-TD) aircraft were presented for 2 chosen cases. These devices could potentially reduce flow separations in critical flow regions, as for example the wing-fuselage and wing-nacelle junction. On the aileron the ZNMF devices permitted to increase the aerodynamic efficiency by 15%. Further studies will focus on finding the optimal locations to place the ZNMF devices, and to verify the optimal operating parameters as the ZNMF jet actuation frequency and the jet velocity.

## REFERENCES

[1] A. Marouf, A. Chouippe, J. B. Vos, D. Charbonnier, A. Gehri, M. Braza, and Y. Hoarau. Unsteady CFD simulations for active flow control. American Institute of Aeronautics and Astronautics, 2021.

[2] A. Marouf, N. Simiriotis, Y. Bmegaptche Tekap, J.-B. Tô, M. Braza, and Y. Hoarau. Predictive numerical study of cambered morphing a320 high-lift configuration based on electro-mechanical actuators. In *Fluid-Structure-Sound Interactions and Control*, pages 317–322. Springer Singapore, 2021.

[3] A. Marouf, H. Truong, Y. Hoarau, A. Gehri, D. Charbonnier, J. B. Vos, and M. Braza. *CFD simulations of active flow control devices applied on a cambered flap.* 2022.

[4] J. Vos, A. Rizzi, A. Corjon, E. Chaput, and E. Soinne. Recent advances in aerodynamics inside the NSMB (Navier Stokes Multi Block) consortium. In *36th AIAA Aerospace Sciences Meeting and Exhibit*, 1998.

**Joint ERCOFTAC/EU-CTFF**
**European Drag Reduction and Flow Control Meeting – EDRFCM 2022**
**September 6th–9th, 2022, Paris, France**

# DRAG REDUCTION PERFORMANCE OF SWEEPING JETS ON A SLANTED-BASED CYLINDER

**Xiaodong Chen** **Shan Zhong** **Andrew Weightman**
Department of Mechanical, Aerospace and Civil Engineering, The University of Manchester, M13 9PL, UK

## INTRODUCTION

Today, the operational speed of a commercial high-speed train exceeds 300 km/h, bringing its aerodynamic drag accounts for more than 75% of the total drag. Most of the energy is, therefore, used to overcome air resistance, resulting in a great waste of resources. The pressure drag between train head and tail contributes up to 27% of the aerodynamic drag [5]. This type of drag is mainly due to a significant negative pressure field on the tail surface, which is associated with the presence of a strong afterbody vortex pair [2].

A slanted-base cylinder with a canonical geometry (Fig.1a and b) has been regarded as a generic model for the rear portion of a cargo fuselage or a high-speed train due to its similar afterbody counter-rotating vortex pair. In the past decades, scholars put a lot of effort in reducing drag or controlling the afterbody vortices from the geometry, by using passive flow control methods. Through optimizing passive methods including vortex generators, flaps, spoilers, strakes etc., a series of drag reduction effects of up to 7% were reported [3, 7]. Nevertheless, passive flow control devices could produce parasitic drag of their own and their working adaptability is largely limited for a wide range of freestream conditions. Therefore, an active flow control method with good robustness like a passive control device but with greater adaptability is in great demand.

The sweeping jet actuator so-called fluidic oscillator (Fig.1c) can convert steady air supply to an oscillating jet solely based on its intrinsic flow deflection mechanism without any moving parts [6]. This feature makes the sweeping jet highly robust in a long-term actuating, which has a great advantage in engineering applications. This jet exhibits a temporal fluctuation similar to that of a pulsed jet, while its spatially oscillating behaviour makes it easier in affecting a larger flow field than a normal pulsed jet. In addition, the sweeping jet actuator shares features of dimensional scalability, high frequency and momentum bandwidths, which gives it a better worth in studying its flow control performance.

In this work, an array of sweeping jet actuators with a 2 mm throat was applied to a slanted-base cylinder at Re=200,000. Drag measurements accompanied by stereo particle image velocimetry (stereo PIV) were conducted in wind tunnel experiments to examine the drag reduction performance. This work paves the way for applying sweeping jets to reduce drag on transportation vehicles, such as high-speed trains, in the future.

## EXPERIMENTAL METHODS

A slanted-base cylinder with a 30° slant angle is chosen as the experimental model (Fig. 1). The diameter of the model is 200 mm leading to a solid blockage about 3.8% in a low-speed wind tunnel at The University of Manchester.

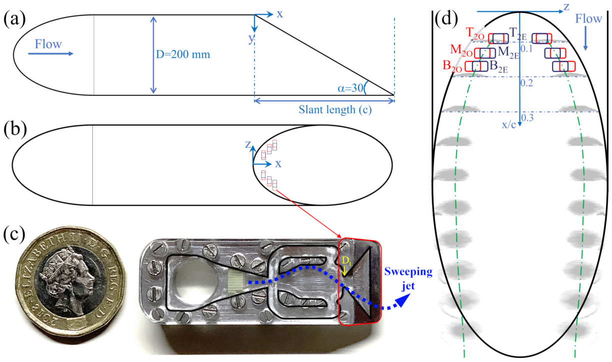

Figure 1: (a) Side view of experimental model; (b) top view; (c) photography of the sweeping jet actuator; (d) enlargement view of endplate showing different actuator placement

Each actuator is with a 2 mm throat ($D_t$ in Fig.1c). The parameters of actuator placement are listed in Table 1.

Table 1 Parameters for the actuator placement

| Case | Streamwise location x/c | Spanwise location z/D |
|---|---|---|
| $T_{2E}$ | 0.07 | ±0.12 |
| $T_{2O}$ | 0.07 | ±0.14 |
| $M_{2E}$ | 0.11 | ±0.18 |
| $M_{2O}$ | 0.11 | ±0.22 |
| $B_{2E}$ | 0.15 | ±0.23 |
| $B_{2O}$ | 0.15 | ±0.27 |

In this work, the drag data of the model were measured by a six-component displacement balance at a sampling frequency of 1 kHz for 30 s with at least three repeat runs. The uncertainty for the drag reduction was estimated to be about 1% based on [4]. The vortices in this work were captured by a stereo PIV technique at 10 Hz with an in-plane vector resolution of 0.8 mm. 500 pairs of PIV images were used to obtain the time-averaged results presented. The uncertainty was estimated to be less than 2% of the local velocity in vortex regions.

## RESULTS

The jet intensity relative to the freestream is quantified by the momentum coefficient $C_\mu$ given in (1)

$$C_\mu = \frac{N\rho_j A_j U_j^2}{0.5\rho_\infty A_m U_\infty^2} = \frac{\dot{m}U_j}{0.5\rho_\infty A_m U_\infty^2}, \tag{1}$$

where N is the number of actuators involved. $A_j$ is the throat area of each actuator; $U_j$ is taken as $U_{bulk}$ at the throat; $A_m$ is the cross-sectional area of the slanted-base model; $\dot{m}$ is the total mass flow rate supplied to the sweeping jet system.

The drag reduction effect is shown in Fig.2. At a small jet strength ranging from $C_\mu = 3.8*10^{-3}$ to $8.5*10^{-3}$, the

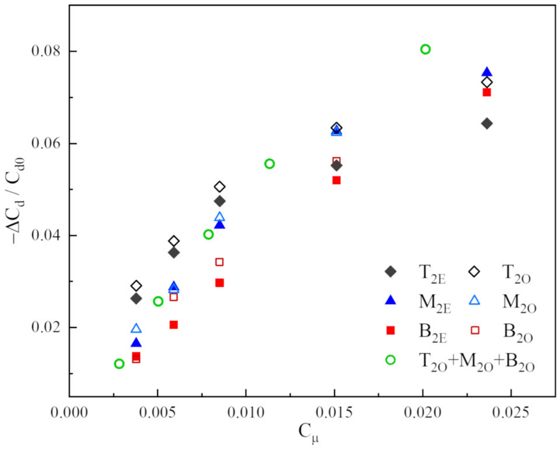

Figure 2: Drag reduction effect in different cases.

streamwise position appears to dominate the drag reduction performance. From cases $T_{2O}$ and $T_{2E}$ at $x/c = 0.07$ to cases $B_{2O}$ and $B_{2E}$ at x/c = 0.15, the drag reduction effect among the cases shows an obvious decreasing trend at each $C_\mu$. A further outboard placement of the actuator appears also helpful to the drag reduction at a small jet strength, which could be due to the sweeping jet is better covered by the vortex region (see Fig.1d). However, the above distribution is changed at a larger jet strength. The drag reduction effects of cases at $x/c = 0.11$ and 0.15 are getting stronger at $C_\mu = 1.5 * 10^{-2}$ and $2.3*10^{-2}$. Case $M_{2O}$ becomes equivalent to case $T_{2O}$ and even exceeds it at the larger $C_\mu$. This difference is related to the change of vortex intensity induced by the sweeping jets at the large strength, which will be explained by PIV data in Fig.4. In addition to the above, the synergy of the three outer pairs of actuators shows a slight winning in drag reduction performance only at a high momentum coefficient.

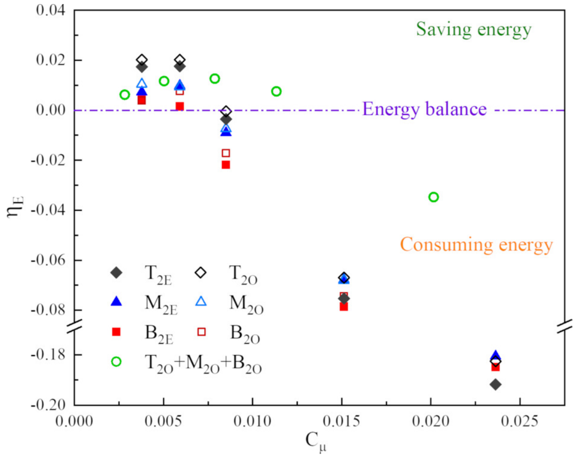

Figure 3: Energy efficiency in different cases.

The power required to drive the sweeping jet actuators can be estimated as $E_{in} \approx \dot{m}P_{in}/\rho$ then the energy efficiency can be estimated using the (2)

$$\eta_E = \frac{\Delta E - E_{in}}{E_0} = \frac{C_{d0} - C_{d1}}{C_{d0}} - \frac{\dot{m}P_{in}}{C_{d0}\frac{1}{2}\rho^2 U_\infty^3 A_m}, \qquad (2)$$

Where $P_{in}$ is the driving pressure of the actuator, $C_{d0}$ and $C_{d1}$ is the baseline and after-control drag coefficient. The energy efficiency is shown in Fig.3. The upstream and outboard actuators obtain a better control efficacy with more than 2% energy saving at $C_\mu$ less than $5.9 * 10^{-3}$. Energy consumption will happen and exacerbate at a larger $C_\mu$ due to a higher driving pressure required for an internal flow separation mechanism of the actuator.

The time-averaged vorticity contour is shown in Fig.4. At a smaller jet strength $C_\mu = 3.8{*}10^{-3}$, the difference in vorticity among different cases is almost indistinguishable. However, at a larger jet strength $C_\mu = 1.5{*}10^{-2}$, the vortex intensity in case $M_{2O}$ is significantly reduced and that of $B_{2O}$ has a detectable effect as well. The vortex intensity in case $T_{2O}$ still remains unchanged. A stronger vortex will impart a lower pressure on the endplate and hence increase the pressure drag [1], therefore the distribution of drag performance among different cases was changed at higher jet strengths in Fig.2.

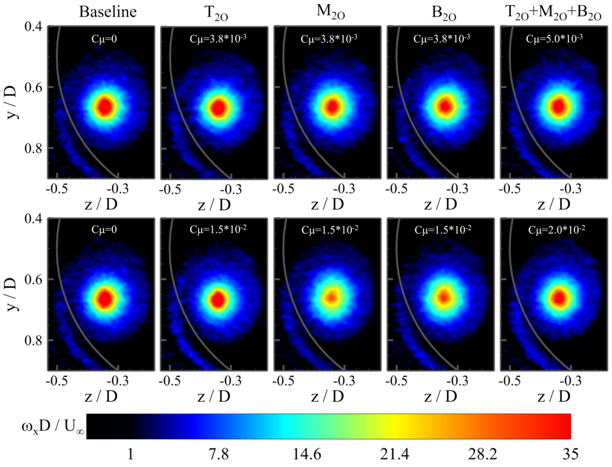

Figure 4: Time-averaged vorticity contour obtained by stereo PIV at x/c=1.0 for different cases.

## CONCLUSIONS

The drag reduction performance by using sweeping jets on a slanted-based cylinder is affected mainly by two factors: actuator position and affected vortex intensity. Actuators located more upstream and outboard facilitate a higher drag reduction efficacy at a low jet strength due to an earlier jet-vortex interaction and the negligible change in the afterbody vortex intensity. At a larger jet strength, the reduced vortex intensity by actuating the sweeping jets increases the drag reduction effect, indicating the affected vortex intensity becomes equivalently important with the actuator position in terms of decreasing the pressure drag.

## REFERENCES

[1] G. Batchelor. *J. Fluid Mech.*, 20(4):645–658, 1964.

[2] J. R. Bell. *J. Fluids Struct.*, 61:168–183, 2016.

[3] D. S. Bulathsinghala, Z. Wang, and I. Gursul. *J. Aircr.*, 55(6):2380–2391, 2018.

[4] R. J. Moffat. *Exp. Therm. Fluid Sci.*, 1(1):3–17, 1988.

[5] A. Orellano and S. Sperling. Springer Berlin, 2009.

[6] F. Ostermann, R.Woszidlo, C. N. Nayeri, and C. O. Paschereit. *J. Fluid Mech.*, 857:216–238, 2018.

[7] A. Wortman. *J. Aircr.*, 36(3):501–506, 1999.

**Joint ERCOFTAC/EU-CTFF**
**European Drag Reduction and Flow Control Meeting – EDRFCM 2022**
**September $6^{\text{th}}$–$9^{\text{th}}$, 2022, Paris, France**

# ON-OFF PUMPING FOR DRAG REDUCTION IN A TURBULENT CHANNEL FLOW

**G. Foggi Rota**
Complex Fluids and Flows Unit, OIST, Okinawa, Japan
Dep. Aerospace Sciences and Technologies, Politecnico di Milano, Italy

**A. Monti**
Complex Fluids and Flows Unit, OIST, Okinawa, Japan

**M. E. Rosti**
Complex Fluids and Flows Unit, OIST, Okinawa, Japan

**M. Quadrio**
Dep. Aerospace Sciences and Technologies, Politecnico di Milano, Italy

## INTRODUCTION

A set of demanding Direct Numerical Simulations is employed to assess whether a pulsating pressure gradient with a simple on/off waveform can yield energetic advantages with respect to its steady counterpart.

The steady injection of power into a pumping system is only one of the possibilities available to force a fluid flow into a duct, and not necessarily the most convenient. Since periodically driven currents are frequently found in nature, we are lead to wonder if those may provide some energetic advantage. The assessment of such an advantage — that we call drag reduction for short — requires care, as the very concept of drag reduction becomes elusive in this context: a clear reference flow to compare to is lacking. Inspired by the work of Frohnapfel, Hasegawa and Quadrio [1], we therefore introduce a proper metric to quantify the savings derived from the use of an unsteady on/off forcing.

A family of step-wise wave-forms, generated varying the amplitude, the duty-cycle of the pump and the period of the on/off cycle, is explored. Few similar studies exist, and it has been recently proven [4] that the parameters above are crucial for the effectiveness of the control. In general such wave forms are described by three parameters, but we reduce their number to two by linking the duty cycle $\xi$ and the amplitude of the "on" stage, which is set at $1/\xi$. Even within this limitations, we unequivocally demonstrate that a net gain is possible: significant energy savings may be achieved by driving the flow through intense but brief surges of pumping power, followed by much longer periods of deceleration in which the pump is turned off. The flow alternately visits the turbulent and the laminar regimes, and this is the key reason for the energetic advantage.

A preliminary understanding of the turbulent structures governing the unsteady dynamics of the cyclic transition process is fundamental for the success of the control, which would otherwise remain at an empirical level. Similar structures have already been analysed [2]: after a quasi-step-wise increase of the flow rate, the usual low-speed streaks undergo a significant stretching, followed by the appearance of new turbulence in concentrated spots. However, to the best of our knowledge, no one has ever considered an acceleration that ends before the appearance of such spots. This is the scenario that we are set to investigate.

## METHODS

Our numerical experiments simulate the flow of an incompressible Newtonian fluid among the walls of a planar channel. Such flow is described by the classic Navier–Stokes equations, here made dimensionless with the flow variables of a turbulent uncontrolled reference channel flow at $Re_\tau = 180$.

The external forcing is an homogeneous, time-dependent streamwise pressure gradient $\Pi(t)$. Its waveform (represented in figure 1) is a simple on/off step-wise pulsation. That is completely determined by three parameters, namely the period, $T$, the duty-cycle, $\xi$, and the amplitude, which becomes $\frac{1}{\xi}$ under the additional constraint that the integral of the pressure gradient over one period equals that of the steady reference case.

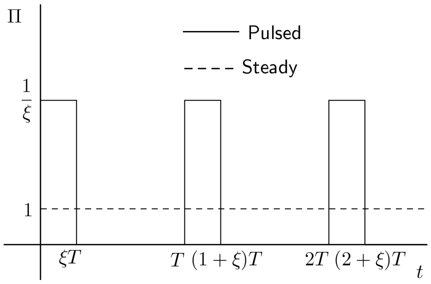

Figure 1: Pictorial representation of the forcing employed

The equations of motion are solved with an efficient in-house code (named Fujin), capable of second-order accuracy thanks to central finite-differences in space and Adams-Bashfort's method in time. Key results of this code are validated by re–running the relevant cases with a different DNS code [5], which uses mixed discretization, employs Fourier modes in the homogeneous directions and integrates in time with different schemes.

Having defined the forcing and its parameters, a proper metric is now needed to evaluate its performance. In order to carry out a meaningful analysis, a single controlled case needs to be compared not only to the steady-state reference one, but also to all the turbulent uncontrolled cases possible. Such idea lays at the base of the approach suggested in [1]. There, the authors represent in the so-called money-time plane the pumping energy $E$ required to drive a certain amount of flow through a straight duct versus the quantity $1/U_b$, which represents the time for a fluid particle to travel a unit length, referring the first variable as "money" and the (inverse of ) the second as "time" or "convenience". A natural turbulent flow is described by a point on this curve, which moves depending on the Reynolds number. The curve can be drawn by e.g. choosing the Blasius' correlation to relate the friction coefficient $C_f$ with the Reynolds number, so that $C_f \propto U_b$ and $E \propto U_b^{7/4}$. By adding the laminar line, for which $C_f \propto 1/U_b$ and $E \propto U_b$, the plane is partitioned in three regions (as in figure 2). Theoretical arguments ensure that it is impossible (even with active flow control, if control power is accounted for) to reach below the laminar line, and the goal of flow control becomes achieving a flow represented by a point that sits below the turbulent line.

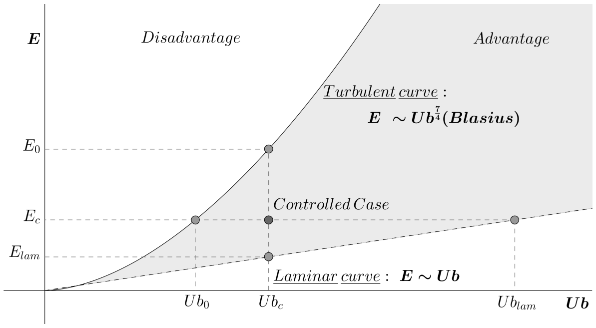

Figure 2: The money-time plane. Adapted from [1].

## RESULTS

Our parametric study covers three values for the period and six values for the duty cycle, hence a total of 18 parameter pairs. Inspired by the work of Iwamoto et al.[3], we have set them to $T^+ = 3600, 10800, 14400$ and $\xi = 0.005, 0.0125, 0.025, 0.0375, 0.05, 0.1$.

Results computed on the largest domain, which provide the most interesting performance and have all been checked for spurious discretization effects, are first plotted as circles in figure 3. There, a non-dimensional version of the money-time plane is employed: energy, represented by $C_f Re_b^2$, is plotted against $Re_b$. Squares, instead, refer to the results obtained in [3] and [4]. The results correspond to a configuration where 512 points are employed in the homogeneous directions and 160 in the wall-normal one, distributed in a domain of size $6\pi \times 3\pi \times 2$. All the simulations at $T^+ = 14400$ with $\xi \geq 1.25\%$ denote savings both in terms of energy and time.

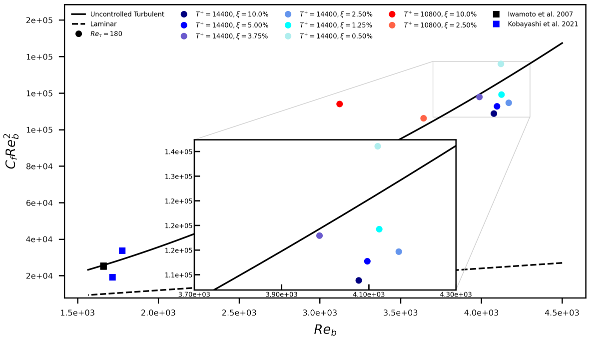

Figure 3: Results plotted in the money-time plane.

The success of our control descends from the repeated transition among a quasi-laminar and a fully turbulent state. The random breakdown to turbulence is marked by a sharp change in the decrease rate of the instantaneous $U_b$ during the "off" period of the forcing, where no pressure gradient is driving the flow (point B in figure 4). A partial re-laminarization is attained at the end of the acceleration phase (point A in figure 4). Between A and B, the flow dynamics is dominated by intense anomalous streaks, whose instability and sudden breakup leads to turbulence. The ability to control their lifetime and intensity is essential to achieve successful control.

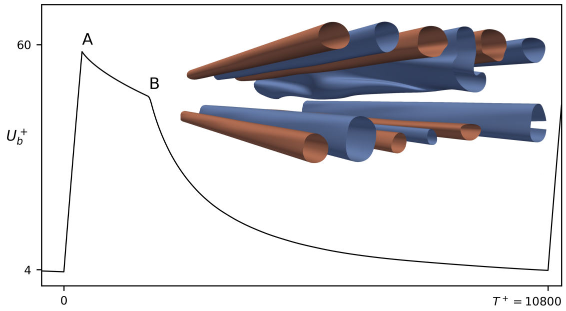

Figure 4: Bulk velocity during one forcing period. Inset: positive (red) and negative (blue) contours of the streamwise velocity fluctuations in the early decay (between A and B).

Our results are relevant as a proof of concept, to unequivocally demonstrate that it is possible to do better than injecting pumping power steadily into the system. So many possible choices exist for the control parameters, that it is currently difficult to comment on the true potential of the technique. At the Meeting, we will describe our results in full and elaborate on their scaling. We will also provide details on the flow structures that appear in the re-transition process and grow through a peculiar instability mechanism, in the hope that their understanding will be essential to drive further research in this subject.

## REFERENCES

[1] B. Frohnapfel, Y. Hasegawa, and M. Quadrio. Money versus time: Evaluation of flow control in terms of energy consumption and convenience. *J. Fluid Mech.*, 700:406–418, 2012.

[2] S. He and M. Seddighi. Turbulence in transient channel flow. *J . Fluid Mech.*, 715:60–102, 2013.

[3] K. Iwamoto, N. Sasou, and H. Kawamura. Direct numerical simulation of pulsating turbulent channel flow for drag reduction. In *Advances in Turbulence XI*, pages 709–711. Springer, 2007.

[4] W. Kobayashi, T. Shimura, A. Mitsuishi, K. Iwamoto, and A. Murata. Prediction of the drag reduction effect of pulsating pipe flow based on machine learning. *International Journal of Heat and Fluid Flow*, 88:108783, April 2021.

[5] P. Luchini and M. Quadrio. A low-cost parallel implementation of direct numerical simulation of wall turbulence. *J. Comp. Phys.*, 211(2):551–571, 2006.

**Joint ERCOFTAC/EU-CTFF**
**European Drag Reduction and Flow Control Meeting – EDRFCM 2022**
**September 6th–9th, 2022, Paris, France**

# GLOBAL MOMENTUM BUDGET FOR TURBULENT FLOW CONTROL VIA MICROBLOWING

**Georg Fahland, Alexander Stroh, Bettina Frohnapfel & Gatti**
Institute of Fluid Mechanics (ISTM), Karlsruhe Institute of Technology, 76131 Karlsruhe, Germany

**Marco Atzori**
Department of Particulate Flow Modelling, Johannes Kepler University, 4040 Linz, Austria

## INTRODUCTION

The technique of uniform blowing (or microblowing) has been present in the flow control research throughout several decades. Many studies have proven its effectiveness which consolidates in significant local skin friction drag reduction of up to 80% [6, 8] and also promising trends for higher Mach numbers [4] or Reynolds numbers [3]. This is especially interesting for applications in aerospace industry since drag reduction directly correlates with reduced fuel consumption and carbon dioxide emissions. However, a comprehensive assessment of the effort required to enable this particular turbulent flow control concept similar to existing assessments for laminar flow control is still missing [7]. In the present work we focus on the main contribution to the actuation cost, which is the origin of the fluid expelled by the control and how it affects the global momentum budget. The assessment is tested on a sample set of numerical simulations with low (RANS) and high (LES) fidelity.

## METHODOLOGY

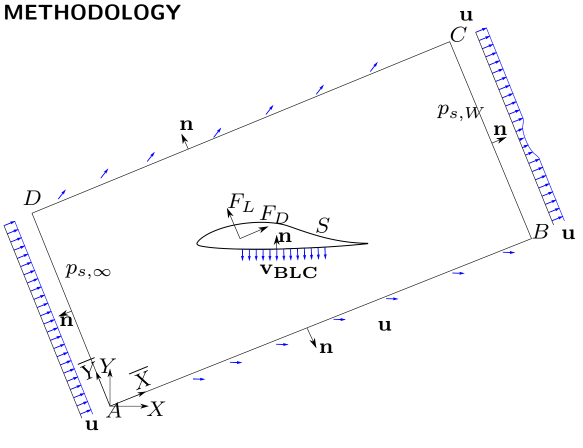

Figure 1: Control Volume (CV) for the airfoil momentum budget in which $\mathbf{n}$ is the normal vector pointing out of the CV).

The objective of the present study is to clarify the relation of different drag assessment methods commonly used in numerical and experimental studies. The first method is the integral force measurement of the body. We term this the *body drag* which we present as the dimensionless drag coefficient $c_{d,B}$. It represents the drag force $F_D$, acting in the free stream direction $\overline{\mathbf{X}}$ (see figure 1), normalized by the free-stream total pressure $q_\infty = \rho/2U_\infty^2$ and a reference area $S_{ref} = s \cdot c$ with span $s$ and chord $c$. The *body drag* can be measured with a balance in experiments or by integrating the surface pressure $p$ and skin friction $\tau$ over the whole surface $S$ of the body:

$$c_{d,B} = \frac{2F_D}{\rho U_\infty^2 S_{ref}} = \frac{2}{\rho U_\infty^2 S_{ref}} \left( \iint_S p\mathbf{n} + \tau\mathbf{t} \quad dS \right) \cdot \overline{\mathbf{X}}. \tag{1}$$

where $\mathbf{n}$ and $\mathbf{t}$ correspond to normal and tangential unit vectors in respect to the surface.

The second option of drag estimation is to measure the momentum deficit downstream of the body (see figure 1, line $\overline{BC}$) in order to assess the drag which we term the *wake survey drag* $c_{d,W}$. Multiple wake survey methods are reported for application in practice, e.g. by [5] and [2], however, these methods commonly result in a formulation linked to the momentum thickness of a boundary layer if the pressure behind the body has recovered to the free-stream static pressure:

$$c_{d,W} = \frac{2}{c}\int_B^C \frac{u}{U_\infty}\Big(1 - \frac{u}{U_\infty}\Big) d\overline{Y} + \frac{2}{c}\int_W -\frac{\overline{u'^2}}{U_\infty^2} d\overline{Y}. \tag{2}$$

For the *wake survey drag* it is assumed that the flux leaving the control volume over the top ($\overline{CD}$) and bottom ($\overline{AB}$) edges has the free-stream velocity $U_\infty$. Since this is not entirely true for a finite CV, this leads to minor deviations in the drag assessment compared to integrating over the whole CV surface or the body surface. However, in the case of an airfoil with additional mass flux through its surface like uniform blowing a correction term $c_{d,S}$ has to be introduced covering for the inflow-momentum introduced by the uniform blowing with the intensity $v_{\mathrm{BLC}}$ over the control region length $l_{\mathrm{BLC}}$:

$$c_{d,B} = c_{d,W} - 2\frac{v_{\mathrm{BLC}}}{U_\infty}\frac{l_{\mathrm{BLC}}}{c} = c_{d,W} + c_{d,S}. \tag{3}$$

For the realization of blowing technique in a real world application the fluid expelled at the surface of the body has to be taken from somewhere else. If this source of fluid is ultimately the free-stream which the body is experiencing, then the momentum-loss drag $c_{d,ML}$ linked to the utilization of this fluid will be inevitably equal to the same term as the source thrust $c_{t,S}$ but with an opposite sign. This can be shown by applying the momentum budget to an isolated air-intake where the control fluid is drawn from the free-stream. Consequently we introduce the *inclusive drag* $c_{d,\mathrm{inc}}$ which accounts for this drag portion:

$$\underbrace{c_{d,\mathrm{inc}}}_{\text{inclusive drag}} = \underbrace{c_{d,B}}_{\text{body drag}} + \underbrace{c_{d,ML}}_{\text{momentum loss drag}} = \underbrace{c_{d,W}}_{\text{wake survey drag}} \tag{4}$$

The *inclusive drag* includes the sink drag of taking in fluid from the free-stream and is equal to the *wake survey drag*. In the case of an alternative source of fluid the *body drag* resembles the actual drag that has to be overcome which is less then the *wake survey drag*.

In order to analyze the contributions to eq. 4 we employ Reynolds-Averaged Navies-Stokes (RANS) simulations of 2D airfoil flow for $Re_C = [10^3, 10^7]$ and direct numerical simulations (DNS) at very low-Re numbers. RANS simulations are carried out using the OpenFOAM toolbox with different turbulence models to also assess how well they cover the Reynolds stress term in the wake survey. We also reassess the results of Large Eddy Simulations (LES) at $Re_C = 4 \cdot 10^5$ [1] carried out with the spectral code Nek5000. For the turbulence control we apply a uniform blowing boundary condition on the airfoil surface in the region of $x = [0.25, 0.86]c$ either on the suction side (SS) or the pressure side (PS) of the airfoil.

## RESULTS

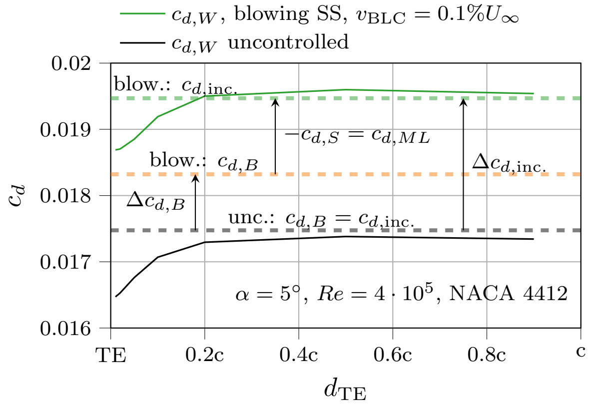

Figure 2: Relation of *wake survey* (solid lines) drag to *body drag* and derived *inclusive drag* (dashed lines) for different distance of the wake plane downstream of the trailing edge based on LES data.

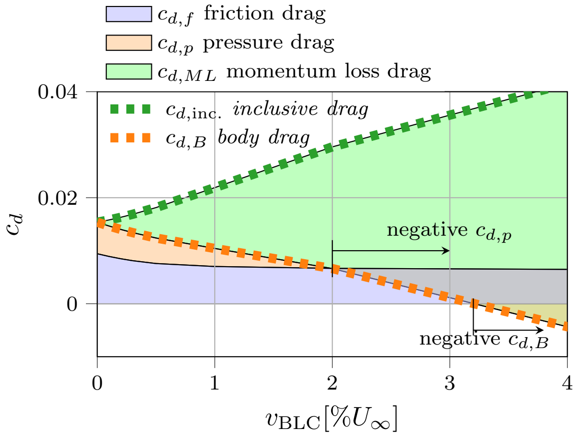

Figure 3: Drag portion development for increasing uniform blowing on PS intensity for NACA 4412, $Re = 4 \cdot 10^5$, $\alpha = 5°$ based on RANS data.

The comparison between *wake survey drag* estimation at different distances downstream of the trailing edge, $d_{TE}$, and *body drag* for the LES data is presented in figure 2. Despite the aforementioned uncertainties resulting from the assumptions made in the derivation of the *wake survey drag*, the agreement with the evaluated *body drag* is confirmed to be good. The poor agreement very close to the trailing edge can be explained by the presence of viscous stresses which are neglected based on the assumption that the Reynolds stresses are dominant. Obviously, this not true in the shear layer in close proximity to the body. Moreover, it becomes clear that the difference of the *inclusive drag* to the *body drag* is significant despite the small blowing velocity of $v_{\mathrm{BLC}} = 0.001 U_\infty$ in this example. Also, figure 2 clearly shows, that the change in *wake survey drag* closely resembles the change in *inclusive drag*. This is an important finding since experimental drag measurements using a wake survey are usually more accurate than a balance measurement.

When applying blowing on the PS of an airfoil (figure 3) even a pressure drag reduction is possible enabling a significant *body drag* reduction which is not present for blowing on the SS (figure 2). Yet the *inclusive drag* is still increasing for this particular example which leaves two future research questions for successful practical application open:

- Is it possible to find a uniform blowing configuration where also the *inclusive drag* is reduced?
- Is it possible to find a different source of fluid than the free-stream, *e.g.* generated through suction flow control scheme, so the *body drag* becomes the relevant figure of merit for drag reduction?

## CONCLUSIONS

We present a new interpretation of drag estimates originating from integral methods on a body and its wake flow. We show that the drag on the body is always smaller than the wake survey momentum deficit suggests when applying a flow control scheme which adds mass flux to the flow. However, the drag on the body corresponds to the total drag only if the fluid used for the boundary layer control is not taken from the free-stream. If this cannot be avoided than the *inclusive drag* is relevant for performance estimates which is equal to the classical *wake survey drag*.

## REFERENCES

[1] M. Atzori, R. Vinuesa, G. Fahland, A. Stroh, D. Gatti, B. Frohnapfel, and P. Schlatter. Aerodynamic Effects of Uniform Blowing and Suction on a NACA4412 Airfoil. *Flow Turbul. Combust.*, 105:735–759, April 2020.

[2] A. Betz. Ein Verfahren zur direkten Ermittlung des Profilwiderstandes. *ZFM*, 16:42–44, 1925.

[3] G. Fahland, A. Stroh, B. Frohnapfel, M. Atzori, R. Vinuesa, P. Schlatter, and D. Gatti. Investigation of Blowing and Suction for Turbulent Flow Control on Airfoils. *AIAA J.*, 59(11):4422–4436, July 2021.

[4] D. Hwang. Review of research into the concept of the microblowing technique for turbulent skin friction reduction. *Prog. Aerosp. Sci.*, 40(8):559–575, November 2004.

[5] B. M. Jones. The measurement of profile drag by the pitot traverse method. Technical Report of the Aeronautical Research Committee for the Year 1935-1936, no. 1688, Cambridge, 1937.

[6] Y. Kametani and K. Fukagata. Direct numerical simulation of spatially developing turbulent boundary layers with uniform blowing or suction. *J. Fluid Mech.*, 681:154–172, August 2011.

[7] J.-L. Rioual, P. A. Nelson, P. Hackenberg, and O. R. Tutty. Optimum drag balance for boundary-layer suction. *J. Aircr.*, 33(2):435–438, March 1996.

[8] A. Stroh. *Reactive Control of Turbulent Wall-Bounded Flows for Skin Friction Drag Reduction.* Dissertation, Karlsruhe Institute of Technology, Karlsruhe, 2016.

**Joint ERCOFTAC/EU-CTFF**
**European Drag Reduction and Flow Control Meeting – EDRFCM 2022**
**September 6th–9th, 2022, Paris, France**

# EFFECT OF THE REAR LINKING TUNNELS AND BLOWING ACTIVE FLOW CONTROL ON AERODYNAMIC PERFORMANCE OF BLUFF BODY

**B. Mohammadikalakoo**
Aerodynamics Group, Faculty of Aerospace Engineering, Delft University of Technology, Delft, The Netherlands

**P. Schito**
Mechanical Engineering Department, Politecnico di Milano, Via La Masa 1, Milano, Italy

**K. Shariloo**
Aerospace Engineering Department, Amirkabir University of Technology, Tehran, Iran

**M. Mani**
Aerospace Engineering Department, Amirkabir University of Technology, Tehran, Iran

## INTRODUCTION

According to the International Energy Agency, oil consumption in transportation has doubled in the first 30 years of the 21st century, and greenhouse gases have doubled [1]. For this reason, studies about flow behavior around the ground vehicles attracted huge attention, especially in the field of drag reduction, due to its significant impact on reducing vehicle energy consumption, and air pollution.

There are plenty of ways to reduce bluff body drag force and improve their aerodynamic performance since most of the objects in the world are not streamlined shape including vehicles for which the pressure drag is larger than friction drag [13]. Two forms of flow control methods including passive and active can be used with various mechanisms like separation delay to control the flow and reduce the wake zone size. Passive flow control can be of different types, like: adding vortex generators [3], flaps and plates [5], shape modifications [7], etc. In the second method, called active flow control, external energy plays the main role. Some of the actuators that have been used on the Ahmed body are: microjets [4], blowing jets [8], synthetic jets [11], and plasma actuators [10]. The combination of active and passive flow control methods on the Ahmed model was numerically studied by Bruneau et al. for the first time, which used the blowing jet and porous layer to reduce drag by 30% [6]. In another numerical study, the effect of simultaneous use of plasma actuators and Rear Linking Tunnels (RLTs) on the Ahmed body with curved slant was studied with interesting results [9]. The purpose of this work is to study, experimentally and numerically, the flow around a simplified car model called Ahmed body [2] and try to improve its aerodynamic performance in terms of drag reduction. Implementing an innovative passive flow control technique introduced previously by the author of this paper [12] and attempting to combine it with steady and periodic blowing jets is the main aim of this ongoing work. The frequency range of blowing active flow control is between 20 Hz and 120 Hz. The simultaneous effect of RLTs and blowing jets at different arrangements has been investigated experimentally and numerically. The numerical simulation is an ongoing research work, and therefore only some results of the experimental section discussed in this paper.

## EXPERIMENTAL SETUP

The experimental model used in the present study is a full-scale Ahmed body with a slant angle of 25° and the modified model same as the previous study by B. Mohammadikalakoo et al. [12]. All experimental tests have been performed in the wind tunnel of the Amirkabir University of Technology which is an open circuit wind tunnel with a square cross-section of $1\,m \times 1\,m$ and its test section length is 1.8 m. The maximum free-stream velocity is 60 m/s and the turbulence intensity is less than 0.1%. The tests were performed at speeds of 10 to 20 m/s, with Reynolds number ranging based on the length of the model from $0.7 \times 10^6$ to $1.4 \times 10^6$. The drag force is measured by a single point load cell (L6D-C3 ZEMIC). The measurement range and error of the load cell were ±10 kg and ±0.02%FS, respectively. Pressure measurements were obtained from 66 pressure transducers (Honeywell HSC Series +0.25 FSS BFSL) which were located on the slant surface, rear vertical surface, and the top surface of the model. The jet frequency is generated by a device called High Frequency Blowing System (HFBS) which is designed in this experiment mainly consists of a micro-controller that can control several solenoid valves. This system is capable of generating frequencies from 1 to 120 Hz. The pressure supplied by the air compressor enters the HFBS, which it was located inside the model, and 10 branches of it can blow the periodic pressure. The schematic of the experimental setup is shown in figure 1.

## JET CONFIGURATIONS

13 different configurations have been considered in the experimental test divided into three categories. In the first category, the effect of blowing jet inside RLTs has been studied to improve their performance in terms of drag reduction. The second category aims to identify the best jet injection location. Thus, the injection position of the jets on the top, slant and vertical surfaces was displaced and their effect in the presence of RLTs has been studied. Comparison of steady and unsteady blowing jets without RLTs as well as the importance of blowing frequency on instability vortices in the wake region have been studied in the third category. The second category is presented in figure 2. Third category is the same as the second category, but in the third category, there are no RLTs. The missing numbers in figure 2 belong to the third category

which are not presented for the sake of brevity.

## EXPERIMENTAL RESULTS

The results related to the combined effect of active and passive flow control are presented in Table 1 for only one configuration out of total 13 configurations, to just present the significant effect of this new method of flow control technique in which almost 16% drag reduction can be achieved. The obtained results for the third category confirm the dependence of drag reduction on the blowing jet frequency. According to the experimental results, at the frequencies of 20 and 100 Hz, the maximum drag reduction is observed, which could be related to the neutralization of the vortices in the wake region by these blowing jet frequencies and their possible harmonics which needs more frequency analysis. It is quite interesting that the least effect is related to the injection of steady blowing jet. The comparison of drag reduction for three rows of vertical surface is shown in figure 3. The results obtained from the first category show a greater drag reduction in combined mode than in the case with only passive flow control. After injecting the jet inside the RLTs, the drag reduction rate increases from 3.69% (only RTLs) to 9.16% (RTLs + blowing jets) corresponding to 1.5 times efficiency enhancement.

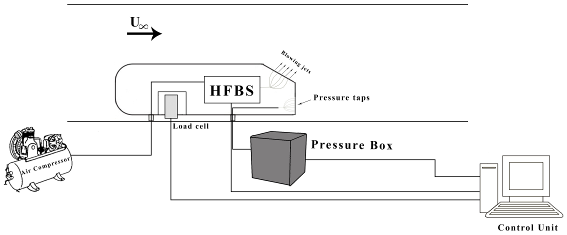

Figure 1: Schematic diagram of the experimental setup

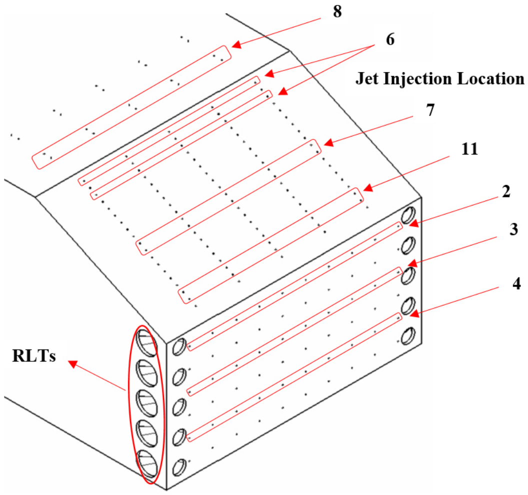

Figure 2: Combined passive and active flow control configurations

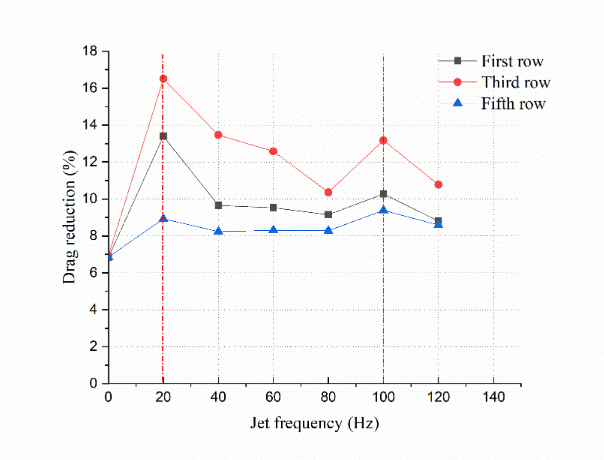

Figure 3: Drag reduction performance of flow control

Table 1: Experimental results of jet injection into the third row of rear vertical surface in presence of RLTs (Config.3)

| Velocity (m/s) | Jet Frequency (Hz) | Drag reduction(%) |
|---|---|---|
| 20 | Steady | 6.94 |
| 20 | 20 | 16.51 |
| 20 | 40 | 13.46 |
| 20 | 60 | 12.58 |
| 20 | 80 | 10.36 |
| 20 | 100 | 13.17 |
| 20 | 120 | 10.77 |

## REFERENCES

[1] Interntational energy agency.

[2] Syed R Ahmed, G Ramm, and Gunter Faltin. *SAE Transactions*, pages 473–503, 1984.

[3] Jean-Luc Aider, Jean-François Beaudoin, and José Eduardo Wesfreid. *Experiments in fluids*, 48(5):771–789, 2010.

[4] Sandrine Aubrun, Jonathan McNally, Farrukh Alvi, and Azeddine Kourta. *Experiments in fluids*, 51(5):1177–1187, 2011.

[5] Jean-François Beaudoin and Jean-Luc Aider. *Experiments in fluids*, 44(4):491–501, 2008.

[6] Charles-Henri Bruneau, Emmanuel Creusé, Delphine Depeyras, Patrick Gilliéron, and Iraj Mortazavi. *Computers & Fluids*, 39(10):1875–1892, 2010.

[7] Charles-Henri Bruneau and Iraj Mortazavi. *Computers & Fluids*, 37(5):488–498, 2008.

[8] Pierric Joseph, Xavier Amandolese, and Jean-Luc Aider. *Experiments in fluids*, 52(5):1169–1185, 2012.

[9] S Karimi, B Mohammadikalakoo, and P Schito. *Journal of Wind Engineering and Industrial Aerodynamics*, 209:104488, 2021.

[10] Saber Karimi, Arash Zargar, Mahmoud Mani, and Arman Hemmati. *Fluids*, 5(4):244, 2020.

[11] Azeddine Kourta and Cédric Leclerc. *Sensors and Actuators A: Physical*, 192:13–26, 2013.

[12] Babak Mohammadikalakoo, Paolo Schito, and Mahmoud Mani. *Journal of Wind Engineering and Industrial Aerodynamics*, 205:104330, 2020.

[13] Cornelis P Van Dam. *Progress in Aerospace Sciences*, 35(8):751–798, 1999.

**Joint ERCOFTAC/EU-CTFF**
**European Drag Reduction and Flow Control Meeting – EDRFCM 2022**
**September 6th–9th, 2022, Paris, France**

# ON THE DEVELOPMENT OF A BAYESIAN OPTIMISATION FRAMEWORK FOR TURBULENT DRAG REDUCTION

**M. Diessner** and **Y. Guan**
School of Computing, Newcastle University, NE1 7RU Newcastle upon Tyne, UK

**J. O'Connor**, **S. Laizet** and **A. Wynn**
Faculty of Engineering, Imperial College London, SW7 2AZ London, UK

**K. Wilson**
School of Mathematics, Statistics and Physics, Newcastle University, NE1 7RU Newcastle upon Tyne, UK

**R. D. Whalley**
School of Engineering, Newcastle University, NE1 7RU Newcastle upon Tyne, UK

## INTRODUCTION

Discovering control strategies for turbulent fluid flows that simultaneously maximise the drag reduction while achieving net energy savings remains a challenging problem. Predominantly, this challenge arises from the expensive nature of the underlying experiments. Physical experiments require costly equipment and tools, such as a calibrated wind tunnel, energy-efficient blowing actuators and advanced sensors. Computational experiments present as an equally expensive option since evaluating one control strategy means simulating a full flow profile requiring specialised software and solvers, such as Xcompact3d [4], as well as a large budget for computing costs. Furthermore, both forms of experiments require a high level of expert knowledge and training to operate these tools and perform the experiments. Therefore, a cost-effective optimisation algorithm that only requires a limited amount of evaluations is instrumental to the success of finding effective control strategies. Bayesian optimisation presents as such an approach as it is a derivative-free optimisation algorithm that aims to find the global optimum of an objective function in a minimum number of function evaluations [1]. There already exists a limited number of studies suggesting that Bayesian optimisation is an effective optimisation strategy for skin-friction drag reduction problems. For example, Talnikar et al. [2] achieve a drag reduction of 60% when optimising a travelling wave and Nabae et al. [5] achieve a similar drag reduction of 60.5% with an optimised travelling wave-like wall deformation. However, to our knowledge, Mahfoze et al. [3] is the only study implementing Bayesian optimisation to optimise for turbulent skin-friction drag reduction with energy savings. They find a strategy with a global skin-friction drag reduction of 36.5% and 5% energy savings after as little as eleven function evaluations in one of their simulation campaigns.

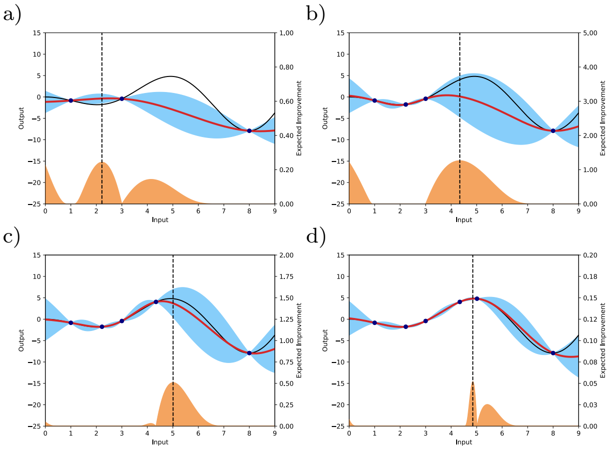

Figure 1: Four iterations of the Bayesian optimisation algorithm. True objective function (solid black line), observations (navy points), posterior mean of the Gaussian process (solid red line), uncertainty of Gaussian process (blue area), Expected Improvement acquisition function (orange area), next candidate point (dashed black line).

## BAYESIAN OPTIMISATION

Given an objective function $f$, points $\mathbf{X}$ can be evaluated resulting in observations $f(\mathbf{X}) = \mathbf{y}$ (e.g. the level of skin-friction drag reduction as a function of blowing control). Bayesian optimisation represents the belief of this objective function using a surrogate model, usually a Gaussian process. A Gaussian process is a non-parametric model that is defined by a mean vector resulting from a mean function $\mathbf{m}_i = \mu_0(\mathbf{x}_i)$ and a covariance matrix computed from a positive-definite covariance function or kernel $\mathbf{K}_{\mathbf{x}_i,\mathbf{x}_j} = k(\mathbf{x}_i, \mathbf{x}_j)$. All parameters of a Gaussian process can be estimated from the data making it a convenient model to use. Once fitted to the training data, the prior of the Gaussian process represents any finite set of points as a multivariate Normal distribution $f \mid \mathbf{X} \sim \mathcal{N}(\mathbf{m}, \mathbf{K})$. It can then be used to compute the posterior predictive distribution of a new point, also called a candidate point $\mathbf{x}$ conditional on some observations $\mathcal{D}_n = \{(\mathbf{x}_i, y_i)\}_{i=1}^n$:

$$Y \mid \mathcal{D}_n \sim \mathcal{N}(\mu_n(\mathbf{x}), \sigma_n^2(\mathbf{x})) \tag{1}$$

with posterior mean and variance:

$$\mu_n(\mathbf{x}) = \mu_0(\mathbf{x}) + \mathbf{k}(\mathbf{x})^T(\mathbf{K} + \sigma^2\mathbf{I})^{-1}(\mathbf{y} - \mathbf{m}) \tag{2}$$

$$\sigma_n^2(\mathbf{x}) = k(\mathbf{x}, \mathbf{x}) - \mathbf{k}(\mathbf{x})^T(\mathbf{K} + \sigma^2\mathbf{I})^{-1}\mathbf{k}(\mathbf{x}) \tag{3}$$

where $\mathbf{K} = k(\mathbf{x}_{1:n}, \mathbf{x}_{1:n})$ and $\mathbf{k} = k(\mathbf{x}, \mathbf{x}_{1:n})$ [1]. This predictive distribution reflects the belief about the response value of the new candidate point based on the previously evaluated training data.

This posterior distribution is used by an acquisition function, essentially a heuristic, that suggests the next candidate point to sample from the objective function when optimised. The literature proposes a wide range of acquisition functions that can be roughly divided into four groups: (i) improvement-based acquisition functions compute the candidate point that improves upon the previous best point with the highest probability, (ii) optimistic acquisition functions suggest the best-case candidate point, assuming that the computed uncertainty of the Gaussian process is true, (iii) information-based acquisition functions use information about the location of the global optimiser $\mathbf{x}^*$ and (iv) portfolios that use combinations of the previous approaches and select the most promising at each optimisation step [1]. One of the main characteristics of acquisition functions is the exploration-exploitation trade-off. This trade-off suggests that there needs to be a balance between sampling candidate points from areas where no points, or only a small number of them, have been evaluated and sampling from areas where points with promising response values have already been evaluated. Favouring exploration increases the risk of never finding the global optimum (i.e. control parameters to obtain highest level of skin-friction drag reduction), while favouring exploitation increases the likelihood of getting stuck in a local minimum (i.e. finding only a sub-optimal control strategy). Some acquisition functions balance this trade-off inherently (Expected Improvement) while others include a hyper-parameter that needs to be specified (Upper Confidence Bound). The choice of acquisition function depends on the characteristics of the underlying problem, for example the number of input parameters.

After the point suggested by the acquisition function is sampled from the objective function, the new point and its response value are added to the training data and the Bayesian optimisation algorithm starts over by fitting a new Gaussian process and computing the acquisition function anew. Figure 1 shows four iterations of the algorithm on a simple one-dimensional objective function. While the Gaussian process does not resemble the true objective function in plot a), it gets closer with each iteration until it represents the objective function well in plot d), and a candidate point close to the true optimum is found.

## APPLICATION

As an exemplary application of Bayesian optimisation to a drag reduction and flow control scenario, consider the following computational fluid dynamics problem. Using the flow solver Xcompact3D [4], the wall-turbulence over a flat plate, which can be manipulated by a region of low-amplitude wall-normal blowing, is simulated. The resulting effect on the global drag reduction (covering the blowing area and the downstream computational domain) can be measured and should be maximised as the objective of this simulation. The profile of the low-amplitude blowing is restricted to a wave that is specified by four parameters as depicted in Figure 2. The wave is defined by an amplitude in the range of 0.01 to 1.00% of the overall free-stream velocity and a wavelength between 0.00 and 0.02 (inner scaling). The angular frequency, restricted to values between -0.25 and 0.25 (inner scaling), allows the sine wave to travel up- and downstream. Lastly, a shift parameter displaces the wave vertically up and down. This parameter is restricted to values between -1.00 and 1.00% of the free-stream velocity. The blowing turns into suction for cases where the blowing profile is negative.

For this four-dimensional problem, the Bayesian optimisation algorithm was used to maximise the global drag reduction.

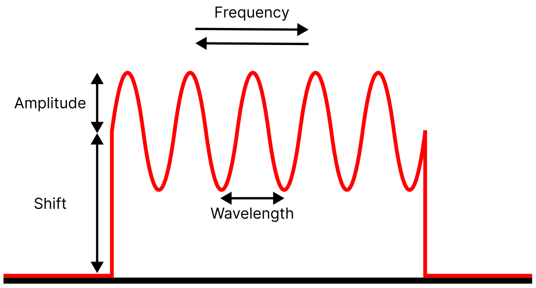

Figure 2: Travelling wave blowing profile specified by an amplitude, a wavelength, a travelling frequency and a shift parameter.

Within the algorithm, a Gaussian process with a zero mean function and a Matern kernel with $\nu = 5/2$ was defined and its hyperparameters were estimated from 16 initial training data points using maximum likelihood estimation. The Upper Confidence Bound with $\beta = 1$, an optimistic policy that allows the computation of multiple candidate points at each iteration of the Bayesian optimisation algorithm, was chosen for the acquisition function as it has been shown to perform well on a variety of problems. Computing batches of candidate points can save time in simulated problems because all candidate points, i.e. all control strategies, can be evaluated simultaneously, using concurrent simulations [3].

The Bayesian optimisation algorithm was able to find a control strategy that reduced the global drag reduction of this problem by up to 22% (and up to 80% locally in the blowing area). Finding this strategy required only eight evaluations, showing that Bayesian optimisation is an effective method for optimising drag reduction and flow control experiments.

## ACKNOWLEDGMENTS

The work has been supported by the Engineering and Physical Sciences Research Council (EPSRC) under grant numbers EP/T020946/1, EP/T021144/1 and the EPSRC Centre for Doctoral Training in Cloud Computing for Big Data under grant number EP/L015358/1.

## REFERENCES

[1] B. Shahriari et al. Taking the human out of the loop: A review of bayesian optimization. *Proceedings of the IEEE*, 104:148–175, 1 2016. In-depth summary of BO.

[2] C. Talnikar et al. Parallel optimization for large eddy simulations. *arXiv preprint arXiv:1410.8859*, 10 2014.

[3] O. A. Mahfoze et al. Reducing the skin-friction drag of a turbulent boundary-layer flow with low-amplitude wall-normal blowing within a bayesian optimization framework. *Physical Review Fluids*, 4, 2019.

[4] P. Bartholomew et al. Xcompact3d: An open-source framework for solving turbulence problems on a cartesian mesh. *SoftwareX*, 12, 2020.

[5] Y. Nabae et al. Bayesian optimization of traveling wave-like wall deformation for friction drag reduction in turbulent channel flow. *Journal of Fluid Science and Technology*, 16, 2021.

**Joint ERCOFTAC/EU-CTFF**
**European Drag Reduction and Flow Control Meeting – EDRFCM 2022**
**September 6th–9th, 2022, Paris, France**

# FLOW PHYSICS OF A TURBULENT BOUNDARY LAYER ACTUATED VIA WALL-NORMAL BLOWING IN DIFFERENT CONFIGURATIONS

**J. O'Connor**, **S. Laizet** and **A. Wynn**
Department of Aeronautics, Imperial College London, London, UK

**M. Diessner** and **Y. Guan**
School of Computing, Newcastle University, Newcastle upon Tyne, UK

**K. Wilson**
School of Mathematics, Statistics and Physics, Newcastle University, Newcastle upon Tyne, UK

**R. D. Whalley**
School of Engineering, Newcastle University, Newcastle upon Tyne, UK

## INTRODUCTION

Skin friction drag is a major engineering concern, with implications across many industries and applications. In the aviation industry, for example, skin friction drag is estimated to account for roughly half of total drag [1]. Clearly, strategies aimed at reducing skin friction have the potential to offer substantial improvements in aerodynamic efficiency, reduce operating costs, and help meet emission targets. Active flow control strategies, such as surface jets, require a power supply to drive the actuation and are among the most promising approaches to tackle skin friction drag due to their increased performance, robustness, and flexibility. However, designing effective active control policies is a difficult task owing to the nonlinear, high-dimensional, and chaotic dynamics of wall turbulence. Furthermore, any performance benefits must be weighed against the power required to drive the actuation.

The challenges associated with designing active flow control policies have led to a trend towards adopting optimisation techniques. Bayesian optimisation is one such technique that is well suited to problems with a moderate number of input dimensions and where the objective function is expensive to evaluate, such as with high-fidelity computational fluid dynamics (CFD) simulations. This approach has recently shown to be successful in fluid dynamics applications [4, 5], with optimal control strategies demonstrating up to 20% global drag reduction and up to 5% net energy savings, when accounting for the required power input, for a canonical turbulent boundary layer flow [4]. However, real-world adoption of such control strategies necessitates a thorough understanding of their performance, including the resulting drag reduction mechanisms and flow physics. This work will build on a recent set of Bayesian optimisation campaigns for a canonical turbulent boundary layer flow controlled by low-amplitude wall-normal blowing in various configurations. To provide a better understanding of the drag reduction mechanisms in turbulent flows over aerodynamic surfaces, a subset of high-performing configurations is chosen for a more detailed analysis.

## NUMERICAL METHODS

The incompressible Navier-Stokes equations are solved using the high-order compact finite differences-based solver Xcompact3d [2, 3]. The present work makes use of a sixth-order spatial discretisation scheme combined with a semi-implicit third-order Adams-Bashforth scheme for time integration. The pressure Poisson equation is solved up to machine precision using a highly efficient spectral solver that relies on fast Fourier transforms. In the present work, an implicit large eddy simulation (LES) approach is adopted, where the sixth-order compact stencils are modified to add numerical dissipation to model the non-resolved scales without any additional cost.

This work adopts a Bayesian optimisation framework (see the submission from Diessner et al. "On the development of a Bayesian optimisation framework for turbulent drag reduction") to find effective open-loop active flow control strategies. Bayesian optimisation is a derivative-free, non-intrusive approach that is well suited to non-convex objective functions that are expensive to evaluate (e.g. LES simulations) and have a moderate number of dimensions. The basic idea behind Bayesian optimisation is to build a surrogate model of the objective function, typically via Gaussian processes, that is updated and improved as more samples are collected. Subsequent samples are selected by optimising the acquisition function, which is typically chosen to balance exploration and exploitation of the parameter space and relies on efficient estimation of the objective function via the underlying surrogate model.

## SIMULATION SETUP

Figure 1 shows a schematic of the simulation setup, which consists of a turbulent boundary layer with dimensions of $L_x \times L_y \times L_z = 750\delta_0 \times 80\delta_0 \times 30\delta_0$, where $x$, $y$, and $z$ denote the streamwise, wall-normal, and spanwise directions, respectively, and $\delta_0$ denotes the boundary layer height at the inlet (which is prescribed as a laminar Blasius solution). The Reynolds number at the inlet is $Re_\theta = 170$, based on the momentum thickness. A convective boundary condition is prescribed at the outlet, a homogenous Neumann condition in the far-field, and periodic conditions in the spanwise direction. The mesh resolution is $n_x \times n_y \times n_z = 1536 \times 128 \times 64$, resulting in a resolution of $\Delta x^+ = 29.0$, $0.5 \leq \Delta y^+ \leq 6.7$, and $\Delta z^+ = 13.9$, where the wall units are with respect to the friction velocity at the start of the blowing region. To accelerate the transition to turbulence, a random volume forcing

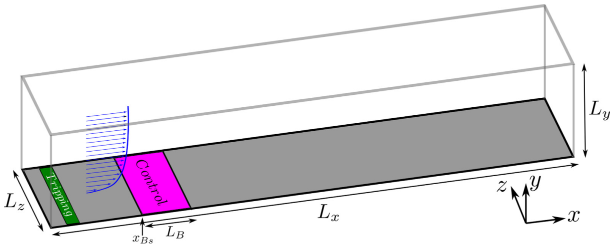

Figure 1: Schematic of the simulation setup. Reproduced from [4].

approach [6], located at $x = 3.5\delta_0$, is used to trip the boundary layer. Wall-normal blowing is implemented as a velocity boundary condition, which starts at $x = 68\delta_0$ and extends to $x = 145\delta_0$, corresponding to $470 \leq Re_\theta \leq 700$, and covers the entire spanwise extent of the domain. The flow is initialised to a laminar Blasius solution through the entire domain and allowed to develop until $t = 4250$ (inner scaling) before the statistics begin recording. The spanwise-averaged skin friction profile along the domain of interest is monitored at each time step, and the mean squared difference between successive time steps is used as a stopping criteria for each simulation.

## PRELIMINARY RESULTS

Three different blowing configurations are investigated, each with a separate parameterisation and optimisation campaign. These are: 1) a standing wave of alternating wall-normal blowing/suction strips; 2) streamwise-travelling waves of wall-normal blowing; and 3) static streamwise-varying profiles of wall-normal blowing (via cubic splines). The Bayesian optimisation framework seeks to maximise either global drag reduction or net energy saving for each configuration. Following the optimisation campaign, a set of high-performing samples is chosen for further analysis to gain a deeper understanding of the drag reduction mechanisms and flow physics.

Figure 2 shows the instantaneous streamwise velocity at $y^+ = 10$ for the canonical turbulent boundary layer and the same case with uniform wall-normal blowing at 0.5% of the free-stream velocity. Clearly, the streamwise velocity in the blowing region is decreased significantly. While this is recovered somewhat after the blowing region, the effect of the blowing persists far downstream, with a reduction in the size of high-velocity streaks until approximately $80\delta_0$ downstream of the blowing region. This delay in the recovery of the streamwise velocity, which is directly related to the skin friction drag, has a significant effect on the global drag reduction and, ultimately, the net energy saving, since the effect of the blowing extends far beyond just the blowing region [4]. This work will build on these results by investigating, in more detail, the difference between different actuation strategies and the resulting flow physics, via modal decomposition (e.g. dynamic mode decomposition) and the FIK identity.

## ACKNOWLEDGMENTS

The work was supported by the Engineering and Physical Sciences Research Council (EPSRC) under grant numbers EP/T020946/1, EP/T021144/1 and the EPSRC Centre for Doctoral Training in Cloud Computing for Big Data under grant number EP/L015358/1. The authors would also like to acknowledge the support provided by the UK Turbulence Consortium (EP/R029326/1) for the use of the ARCHER2 UK National Supercomputing Service.

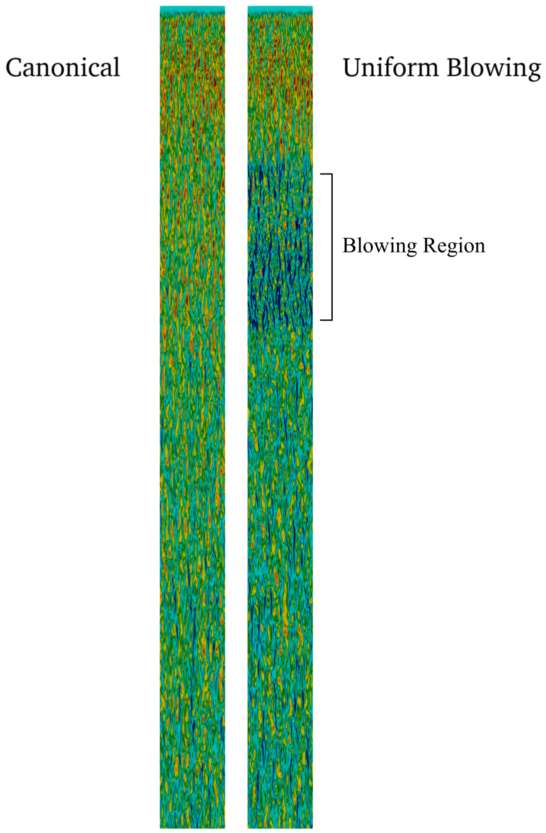

Figure 2: Visualisation of the instantaneous streamwise velocity at $y^+ = 10$. For display purposes the domain is clipped at $x = 375\delta_0$.

## REFERENCES

[1] A. Abbas, G. Bugeda, E. Ferrer, S. Fu, J. Periaux, J. Pons-Prats, E. Valero, and Y. Zheng. Drag reduction via turbulent boundary layer flow control, 2017.

[2] P. Bartholomew, G. Deskos, R.A.S. Frantz, F.N. Schuch, E. Lamballais, and S. Laizet. Xcompact3D: An open-source framework for solving turbulence problems on a Cartesian mesh. *SoftwareX*, 12:100550, 2020.

[3] S. Laizet and N. Li. Incompact3d: A powerful tool to tackle turbulence problems with up to O(105) computational cores. *Int. J. Numer. Methods Fluids*, 67(11):1735–1757, 2011.

[4] O.A. Mahfoze, A. Moody, A. Wynn, R.D. Whalley, and S. Laizet. Reducing the skin-friction drag of a turbulent boundary-layer flow with low-amplitude wall-normal blowing within a Bayesian optimization framework. *Phys. Rev. Fluids*, 4(9):094601, 2019.

[5] Y. Morita, S. Rezaeiravesh, N. Tabatabaei, R. Vinuesa, K. Fukagata, and P. Schlatter. Applying Bayesian optimization with Gaussian process regression to computational fluid dynamics problems. *J. Comput. Phys.*, 449:110788, 2022.

[6] P. Schlatter and R. Örlü. Assessment of direct numerical simulation data of turbulent boundary layers. *J. Fluid Mech.*, 659:116–126, 2010.

**Joint ERCOFTAC/EU-CTFF**
**European Drag Reduction and Flow Control Meeting – EDRFCM 2022**
**September 6th–9th, 2022, Paris, France**

# NUMERICAL INVESTIGATION OF HOMOGENEOUS BLOWING AND SUCTION ON AN AIRFOIL IN COMPRESSIBLE FLOW

**A. Frede, A. Stroh, G. Fahland, D. Gatti**
Institute of Fluid Mechanics, Karlsruhe Institute of Technology, 76131 Karlsruhe, Germany

## INTRODUCTION

Commercial air traffic is responsible for about 2.6 % of the global carbon dioxide emissions, with an annual increase of 5.3 % in the passenger-kilometers, the contribution of $CO_2$ emissions from air traffic to the global emission will rise in the next years [2]. Among the means to reduce $CO_2$ emissions by improving the efficiency of an aircraft, the reduction of friction drag in turbulent boundary layers is promising despite the technological challenges and is considered here. Passive drag reduction strategies, like riblets, do not require additional energy and lead to a decrease in drag of about 6 % [5]. Active control strategies do require additional energy during the operation process, but promise to achieve larger viscous drag reduction margins.

Many studies show the effectiveness of uniform blowing and suction, an active control strategy (see, for instance, [3, 4, 1]). Considering canonical geometries, Kametani et al. [3] showed that uniform blowing reduced the skin friction drag and uniform suction increased it, while Stroh et al. [4] investigated a drag-reduction control scheme by inducing a constant mass flux in wall-normal direction, with a positive effect on the drag. Fahland et al. [1] conducted a large parametric study about homogeneous wall-normal blowing and suction on airfoils. Incompressible RANS simulations were conducted with a NACA4412 profile. The most promising configuration was found to be blowing on the pressure side, where the effect of drag reduction increases with increasing Reynolds number ($Re$). A positive effect on the aerodynamic efficiency was also found with suction on the suction side. Blowing on the suction side does not show a global benefit, a reduction in the friction drag can be observed, accompanied by a large increase in the pressure drag, so overall a decrease in the aerodynamic efficiency.

However, for commercial aviation bodies with a complex geometry as well as compressible flows are relevant. In this study the effect of compressibility, i.e. of the Mach number $Ma$, on the performance of wall-normal blowing and suction is investigated.

## METHODOLOGY

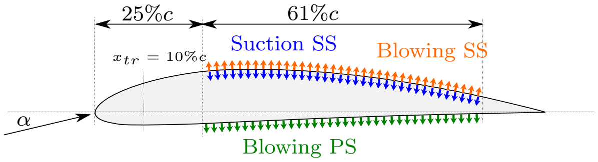

Figure 1: Sketch NACA4412 with the three different control regimes [1].

The compressible flow around different airfoils of chord length $c$ is investigated with RANS simulations, which are conducted with the steady-state solver included in the open-source CFD code $SU^2$. The $k$-$\omega$-SST model was used as the turbulence model. The transition was fixed at $x/c = 0.1$.

The applied control strategy is homogeneous wall-normal blowing and suction. The control region on the airfoil is fixed between $x/c = 0.25\,\%$ and $x/c = 0.86\,\%$. Three control configuration were investigated: blowing on the suction side, suction on the suction side and blowing on the pressure side. For the parametric study different parameters such as the Reynolds number, the Mach number, the airfoil shape, angle of attack (AoA) and control intensity were varied. Figure 1 shows a sketch of a NACA4412 with the different control regions.

## RESULTS FOR NACA4412

The drag polar for a variation of the AoA between $\alpha = -2°$ and $8°$ for a NACA4412 is shown in Figure 2. The chord Reynolds number was fixed at $Re = cu_\infty/\nu = 1 \cdot 10^6$, where $u_\infty$ is the freestream velocity. The freestream Mach number is $Ma = u_\infty/a_\infty = 0.4$, where $a_\infty$ is speed of sound at freestream, and the control intensity was $v_{blc} = 0.1\,\%\,u_\infty$ and $0.2\,\%\,u_\infty$.

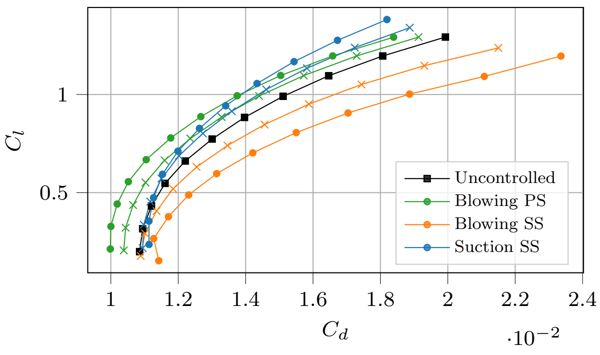

Figure 2: Polar plot of an example case for $Re = 1 \cdot 10^6$, $Ma = 0.4$ and $v_{blc} = 0.1\,\%\,u_\infty$ (× symbols) and $v_{blc} = 0.2\,\%\,u_\infty$ (● symbols).

For blowing on the suction side an overall increase in the drag coefficient $C_d = \frac{2D'}{\varrho_\infty u_\infty^2 c}$ ($D'$ is the drag per unit depth and $\varrho_\infty$ the freestream density) can be observed, which is accompanied by a decrease in the lift coefficient, $C_l = \frac{2L'}{\varrho_\infty u_\infty^2 c}$ ($L'$ is the lift force per unit depth). The effect is smaller at lower AoA, but significant at higher AoA. The boundary layer thickness is increased, which is accompanied by a decrease in the friction coefficient $C_f = \frac{2\tau_w}{\varrho_\infty u_\infty^2}$ ($\tau_w$ is the wall shear stress), but also a large increase in the pressure drag $C_p = \frac{2(p-p_\infty)}{\varrho_\infty u_\infty^2}$ ($p$ and $p_\infty$ are the local and freestream pressure). The increase in the pressure coefficient can be observed in Figure 3. The separation of the boundary layer is moved upstream, which can be observed in the wall shear stress curve (Figure 3) crossing zero at lower x-values compared to the uncontrolled case.

Opposite effects can be observed for suction on the suction side. The lift increases compared to the uncontrolled case, which is particularly significant for high AoA. A reduction of the drag can be observed for higher AoA. Suction leads to an increase in the wall shear stress, which can be observed in Figure 3, but also to a reduction of the pressure drag. This is accompanied by a reduction of the pressure coefficient for almost the whole suction side (Figure 3). For $\alpha = 5°$ the lift increases by about 6.6 % and the drag decreases by about 5.1 % for $v_{blc} = 0.2\,\%\,u_\infty$.

The pressure gradient on the pressure side is mild compared to the pressure gradient on the suction side (Figure 3). Blowing on this side reduces the friction drag, but the boundary layer does not increase significantly. So an overall decrease in the drag can be observed, as of about 9 % for $v_{blc} = 0.2\,\%\,u_\infty$. The lift is not affected by blowing on the pressure side.

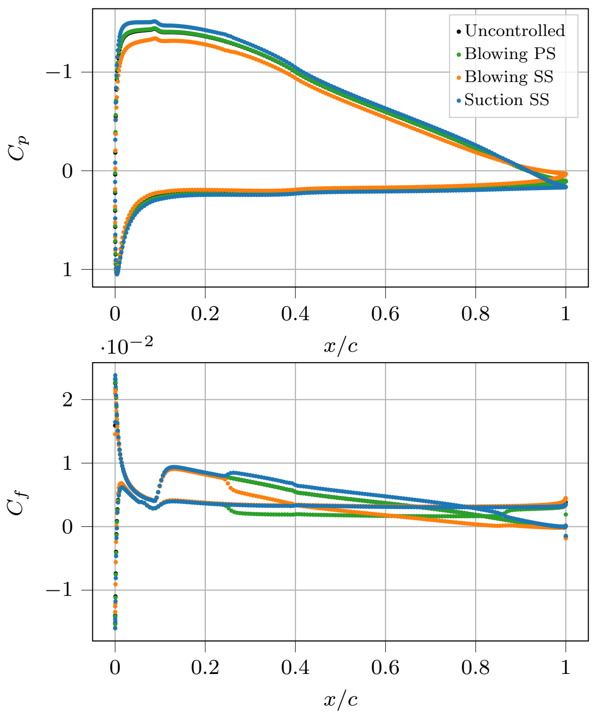

Figure 3: Pressure coefficient $C_p$ and skin friction coefficient $C_f$ for $Re = 1 \cdot 10^6$, $Ma = 0.4$, NACA4412, $\alpha = 5°$ and $v_{blc} = 0.2\,\%\,u_\infty$.

## RESULTS FOR RAE2822

For the transonic flow the RAE2822 airfoil was investigated. As an example case the results for $Re = 1 \cdot 10^6$, $Ma = 0.8$, $AoA = 1°$ and $v_{blc} = 0.2\,\%\,u_\infty$ are shown in Figures 4.

In this configuration the effect of the homogeneous wall-normal blowing and suction on the position of the shock is investigated. As already observed for the NACA4412 airfoil suction on the suction side leads to an increase in the skin friction coefficient on the suction side and blowing leads to a reduction of the skin friction coefficient on the respective side. Suction on the suction side leads to a shift of the shock position further downstream on the airfoil's surface, respectively blowing on the suction side shifts the shock further upstream. The same can be observed for the pressure side, where blowing also leads to a shift of the shock position further upstream. Further simulations with lower Mach numbers will be conducted, to investigate the effect of the active control strategy on the shock position at the suction side.

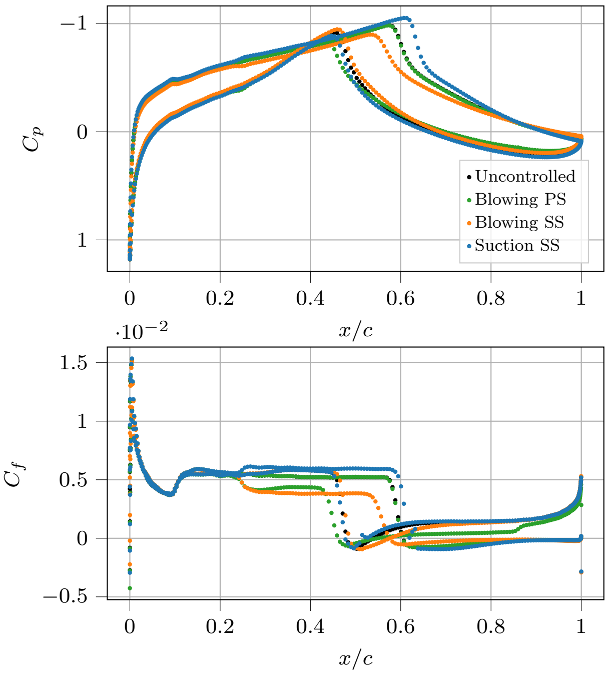

Figure 4: Pressure coefficient $C_p$ and skin friction coefficient $C_f$ for $Re = 1 \cdot 10^6$, $Ma = 0.8$, RAE2822, $\alpha = 1°$ and $v_{blc} = 0.2\,\%\,u_\infty$.

## CONCLUSION

The first results of the parametric study show promising results, that homogeneous wall-normal blowing and suction has a positive effect on the aerodynamic efficiency. The two most promising control configurations in the compressible flow for a NACA4412 airfoil are blowing on the pressure side and suction on the suction side, which agrees with previous studies in the incompressible regime. In the transonic regime the control strategy also influences the position of the shock. In future studies this effect should be investigated in more detail, by a detailed variation of the position and the size of the control regime as well as different control intensities to see the effect on the shock position.

## REFERENCES

[1] G. Fahland, A. Stroh, B. Frohnapfel, M. Atzori, R. Vinuesa, P. Schlatter, and D. Gatti. *AIAA Journal*, 59(11):4422–4436, 2021.

[2] International Energy Agency (IEA). Energy technology perspectives 2016, 2016.

[3] Y. Kametani and K. Fukagata. *J. Fluid Mech.*, 681:154–172, August 2011.

[4] A. Stroh, Y. Hasegawa, P. Schlatter, and B. Frohnapfel. *J. Fluid Mech.*, 805:303–321, October 2016.

[5] M. J. Walsh, W. L. Sellers, and C. B. McGinley. *Journal of Aircraft*, 26(6):570–575, 1989.

European Drag Reduction and Flow Control Meeting -FDRFCM 2022
September 6~9, 2022, Paris, France

# Drag Reduction of Aqueous Suspensions of Fine Solid Matter in Pipe Flows

**K. Watanabe[1] and S. Ogata[2]**

1. NPO Research Society for the Effective Utilization of Fluid Energy, Kawasaki, Japan
2. Tokyo Metropolitan University Department of Mechanical Systems Engineering, Tokyo, Japan

## INTRODUCTION

It is well known that drag reduction properties of polymer solutions in pipe flows are classified into two categories, based on the relationship between the friction factor and the Reynolds number. The degree of drag reduction either increases with an increase in the Reynolds number or is independent of the Reynolds number. In the latter case, the drag reduction behavior is referred to as Type-B behavior. The experimental results for the drag reducing fine-solid-particle suspensions demonstrated that the behavior of the friction factor corresponded with the Type-B behavior of the drag reduction. In this study, the velocity profile of turbulent pipe flows that it is predictable from the friction factor data, was calculated by paying the attention to the result.

## RESULTS AND DISCUSSIONS

Fig. 1 shows the friction factor of graphene oxide suspensions (1) in pipe flows. As our results indicated that the drag reduction behavior of the tested suspensions corresponded to that of Type-B polymer solutions, we replotted the experimental data for the friction factor according to the following equation (2):

$$\mathrm{S'} = \frac{1}{\sqrt{f}} - \frac{1}{\sqrt{f_n}} \tag{1}$$

where $f$ and $f_{\mathrm{n}}$ are the friction factors of the suspensions and Newtonian fluids, respectively. The second term on the right-hand side of Eq. (1) represents the Prandtl-Kármán formula which is given as follows,

$$\frac{1}{\sqrt{f_{\ n}}} = 4.0 \log_{10} Re\sqrt{f_{\ n}} - 0.4$$

where, Re is Reynolds number. Because the Prandtl-Kármán formula is derived from the logarithmic velocity profile for fully developed turbulent flow in a pipe, the experimental results for the friction factor assist with the prediction of the velocity profile of these suspensions (3). In other words, we can predict the mean velocity profile of the suspensions in in the range of turbulent flow by using Eq. (1).

The mean velocity profile for fully-development turbulent flow through a smooth pipe, is given by the following equation:

$$u^{+} = \frac{1}{\kappa} \ln \mathrm{y}^{+} + C \tag{2}$$

where, $u^{+} = \frac{\bar{\mathrm{u}}}{u_*}$ and $\mathrm{y}^{+} = \frac{u_*}{\nu}\mathrm{y}$. Here, ū is the mean velocity over time and $u_*$ is the friction velocity ($u_* = \sqrt{\tau_w/\varrho}$ ;, where $\tau_{\mathrm{w}}$ and ρ are the shear stress and the density, respectively). The parameter y is the distance measured from the wall, y=(ɑ− r ), where ɑ is the pipe radius). The quantity κ is a universal constant. In our study, $\kappa = 0.4$ and $C = 5.5$. It is seen that these profiles provide a reasonably good approximation of a fully turbulent velocity profile all the pipe centerline.

Using example from the experimental results for the friction factor of aqueous suspensions of fine solid matter in regions of turbulent flow, we assume the velocity profile as given by Eq. (1).

As a result, the fiction factor is calculated as

$$\frac{1}{\sqrt{f}} = \frac{1}{\kappa\sqrt{2}}\ln Re\sqrt{f} - \frac{1}{\kappa\sqrt{2}}\ln 2\sqrt{2} + \frac{1}{\sqrt{2}}\left(C - \frac{3}{2\kappa}\right) \qquad (3)$$

Substituting Eq. (2), in Eq. (1), and modifying the constant vale to fit that of Newtonian fluids when S'=0, we obtain the following equation.

$$C = 5.5 + \frac{3}{\sqrt{2}}\boldsymbol{S'} \qquad (4)$$

## SUMARRY

Thus, we can predict the velocity profile of a pipe flow without measuring the velocity profile if the pressure loss data are obtained experimentally using Eq. (4). For example, the velocity profiles of Graphene oxide suspensions and Xanthan gum solutions were obtained as follows,

For the 5000 ppm Graphene oxide suspensions: $u^+ = 2.5\ln y^+ + 8.9$;
For the 100 ppm Xanthan gum solutions: $u^+ = 2.5\ln y^+ + 20.4$.

Fig. 2 shows these results. The results suggest that the region where viscous sublayers are observed is extended across a pipe wall when drag reduction occurs.

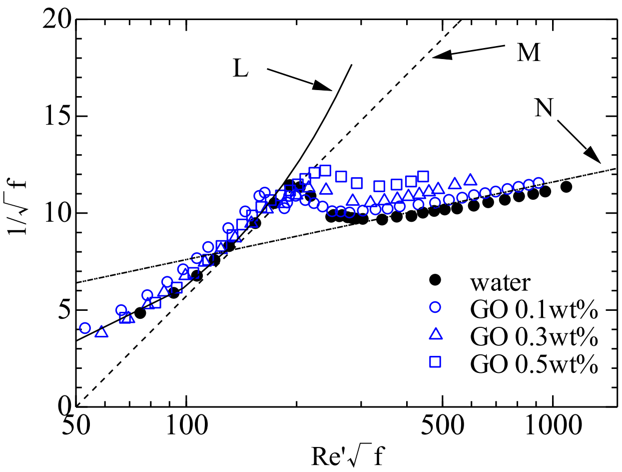

Fig. 1 Friction factor of graphene oxide suspensions

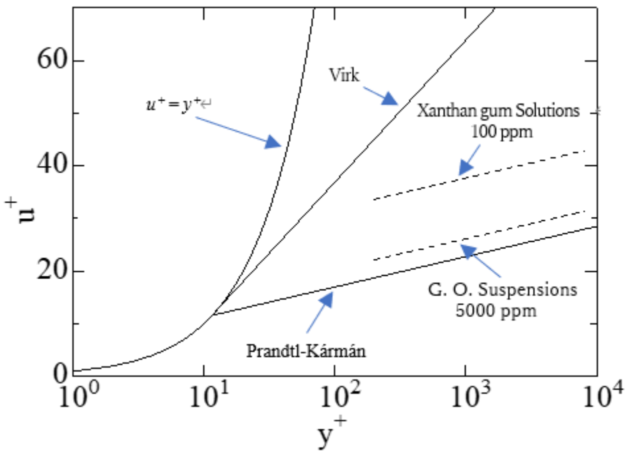

Fig. 2 Predicted velocity profiles

1. Ogata S, Nishina Y, Tochigi H, Watanabe K. Tans. of JSME. 2020; 86(885), DOI:10. 1299/ transjsme.20-00047:1-11(in Japanese).
2. Virk PS, Chen RH. Proc. of the 2nd Inter. Sym. on Seawater Drag Reduction, 2005:545-558.
3. Watanabe K, Ogata S, AICh E Journal 2021; e17241: 1-7.

European Drag Reduction and Flow Control Meeting -FDRFCM 2022
September 6~9, 2022, Paris, France

# Heat Transfer Improvement and Drag Reduction of Graphene Oxide Suspensions

**S. Ogata[1], Y. Nishina[2], H. Tochigi[3], and K. Watanabe[4]**

1. Tokyo Metropolitan University, Department of Mechanical Systems Engineering, Tokyo, Japan
2. Research Core for Interdisciplinary Sciences, Okayama University, Okayama, Japan
3. Cosmo Oil Lubricants Co., LTD., Saitama 340-0193, Japan
4. Tokyo Metropolitan University, Faculty of Systems Design, Tokyo, Japan

## INTRODUCTION

Methods for flow drag reduction have become very important from an energy-saving viewpoint in recent years (1). However, when a drag-reducing agent is used in equipment such as a heat exchanger that generates heat and flow, the drag decreases. Simultaneously, the heat-transfer performance deteriorates, hindering the performance enhancement of the heat exchangers (2). Thus, it is important to mitigate the effects of the drag-reducing agent on reduction of the heat-transfer performance. To this end, we focus on graphene oxide (GO) nanosheets having excellent thermal conductivity and water dispersibility as additives to achieve a trade-off between heat-transfer performance and drag reduction (3). GO is obtained via the oxidation of graphene, a single-phase carbon sheet that produces a 2D sheet-like substance with a thickness of about one carbon atom. Thus, because this material has a thin plate shape with a high aspect ratio, it is expected to behave like fiber suspensions. Additionally, GO nanosheets are likely to have excellent thermal conductivity derived from the graphene skeleton. However, our current understanding is that the thermal-flow characteristics of GO nanosheet suspensions have not been sufficiently clarified. The purpose of this study is to experimentally clarify not only the heat-transfer characteristics but also the pressure-drop characteristics of GO nanosheet suspensions flowing within a circular pipe.

## RESULTS AND DISCUSSIONS

Figure 1 presents a diagram of the experimental apparatus used for the heat-transfer measurement. The equipment consists of a water tank, a chiller, a double-tube heat exchanger, a hot air blower, a pressure loss measurement pipe, a differential pressure gauge, and a flow meter, and the temperature inside the water tank is adjusted within 0.1 ° C. The double-tube heat exchanger is made of stainless steel and has a length of 1000 mm, the central circular tube has an inner diameter of 10 mm, and the outer circular tube has an inner diameter of 16 mm. Thermocouples were inserted into the inlet and outlet of the outer and inner circular tubes to measure the fluid temperature at the inlet and outlet. The pressure drop measuring tube is made of stainless steel and has two pressure measuring holes. The inner diameter is 10 mm and the pressure measurement section is 400 mm. Pressure drop is measured by a pressure transducer. The experiment was carried out by using a hot air blower to flow high-temperature air through the inner pipe of the double pipe and flowing the test low-temperature liquid through the outer pipe of the double pipe so as to be a countercurrent. Test suspensions with three different concentrations (0.03, 0.05, and 0.1 wt%) were prepared using distilled water.

Figure 2 shows the heat-transfer coefficient, $h$, in terms of the relationship between the Nusselt number, $Nu=hd_i/k$, and the modified Reynolds number, $Re'$. Here, $k$ is the thermal conductivity of the test suspension, which was calculated using the Hamilton and Crosser correlation. The solid line shown shows the convective heat transfer trend for a fully developed turbulent flow inside a circular pipe. As observed in Fig. 2, for all concentrations, the GO nanosheet suspensions exhibited superior heat-transfer characteristics compared with water. Moreover, the heat-transfer coefficient increased slightly with increasing concentrations of the suspensions. The experiments show that the Nusselt number of GO nanosheet suspensions increase by 90% under turbulent flow.

Figure 3 shows the relationship between the friction factor, $\lambda$, and the modified Reynolds number, $Re'$. Line $L$ represents the exact solution for laminar flow in the circular pipe, whereas line $N$ shows the Blasius formula. As observed in Fig. 3, in the turbulent-flow regime, the friction factor for the GO nanosheet suspensions was reduced more than that of distilled water. Additionally, this reduction increased with the increasing concentration of the suspension. The experiments show that the friction factor of GO nanosheet suspensions decrease by up to 40% compared with that of distilled water in the Reynolds number range where heat-transfer performance enhancement occurs.

It can be inferred that GO nanosheet suspensions, in addition to suppressing flow turbulence, improve the effective thermal conductivity, owing to the high thermal conductivity of graphene. In combination with the thermal motion of particles, they enhance thermal conductivity. The results, therefore, demonstrate that GO nanosheet suspensions possess both characteristics of drag reduction and heat-transfer enhancement, which have hitherto been considered difficult to achieve simultaneously.

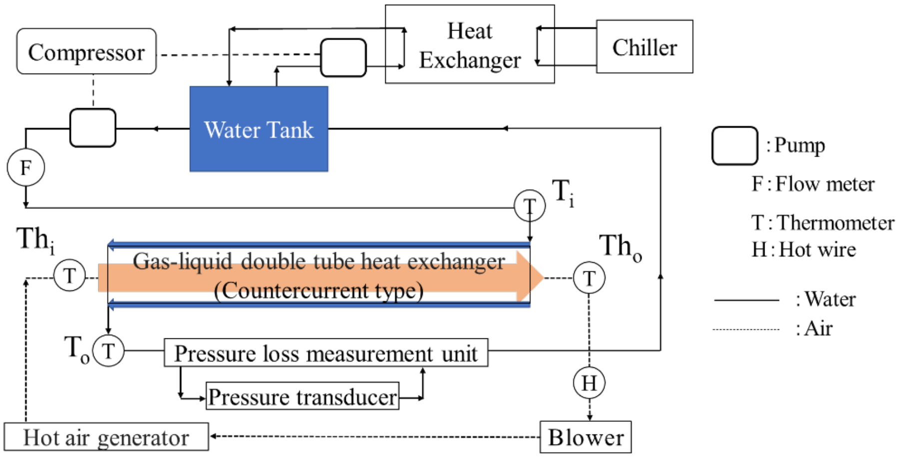

Fig. 1 Experimental apparatus

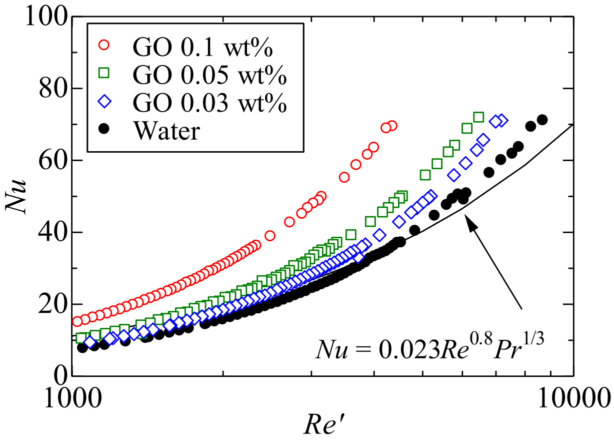

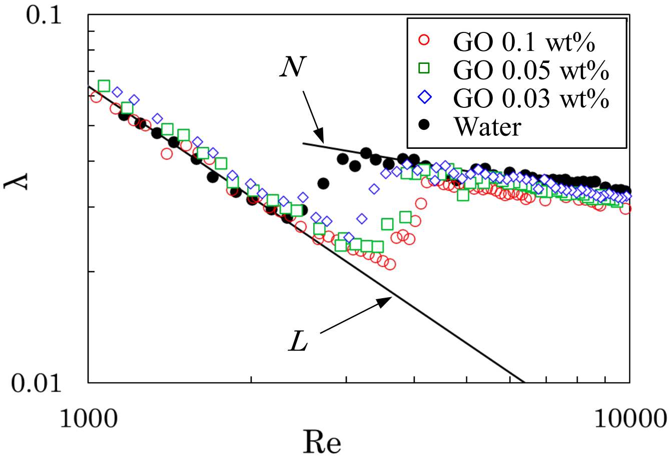

Fig. 2 Relationship between $Re'$ and $Nu$ Fig. 3 Relationship between $Re'$ and $\lambda$

## REFERENCES

1. H. Shi, W. Ge, H. Oh, S.M. Pattison, J.T. Huggins, Y. Talmon, D.J. Hart, S.R. Raghavan, J.L. Zakin, Photoreversible micellar solution as a smart drag-reducing fluid for use in district heating/cooling systems, Langmuir 29(1) (2013) 102-109.
2. F.-C. Li, B. Yu, J.J. Wei, Y. Kawaguchi, Turbulent Drag Reduction by Surfactant Additives, Wiley & Sons, 2012, ISBN-13: 978-1118181072.
3. H. Kinoshita, Y. Nishina, A.A. Alias, M. Fujii, Tribological properties of monolayer graphene oxide sheets as water-based lubricant additives, Carbon 66 (2014) 720-723.

**Joint ERCOFTAC/EU-CTFF**
**European Drag Reduction and Flow Control Meeting – EDRFCM 2022**
**September 6th–9th, 2022, Paris, France**

# CAPTURING THE EFFECT OF SLIP/NO-SLIP SUPERHYDROPHOBIC TEXTURES IN TEXTURE-LESS SIMULATIONS

**W. Xie and R. García-Mayoral**
Department of Engineering, University of Cambridge, CB2 1PZ Cambridge, UK

## INTRODUCTION

The present work focuses on the effect on the overlying turbulence of idealised superhydrophobic surfaces consisting in slip/no-slip patterns on an otherwise smooth surface, a popular model for these surfaces [9]. In the limit of vanishingly small texture size, $L^+ \ll 1$, the overlying turbulence does not perceive the detail of each individual texture element and the surface is adequately represented by slip conditions [8, 2]. The streamwise and spanwise slip lengths are equivalent to the streamwise and spanwise protrusion heights for riblets [7, 6]. [10] investigated the limits of slip-length models for slip/no-slip textures, and showed that for texture sizes $L^+ \gtrsim 10$ the instantaneous correlation between velocity and shear at the surface was lost, which would appear to set the upper limit for the applicability of a slip-length model. [4, 3] later investigated the correlation between surface velocity and shear discriminating between flow lengthscales, and found that even scales much larger than the texture size displayed an apparent loss of correlation, arguing that this was caused by the presence of a texture-coherent flow. They used the flow decomposition of [1] to show that, if the texture-coherent flow is filtered out, the resulting signal – the background turbulence – exhibits a linear correlation between velocity and shear, at least up to textures of size $L^+ \gtrsim 50$. However, when replacing the texture by the corresponding slip-length conditions, results differed for $L^+ \gtrsim 25$. Under homogeneous slip conditions, the flow remains smooth-wall-like for any amount of slip [5], and the same is observed for flows over textures up to $L^+ \approx 25$. For larger textures, the flow is no longer smooth-wall-like, even though the effective slip conditions remain valid. [3] argued that the discrepancy in $\Delta U^+$ between texture-resolving and homogeneous-slip simulations must arise from the texture-coherent flow altering the Reynolds shear stress of the background turbulence, an effect that mainly occurs in a region of the flow not in the immediate vicinity of the surface, $5 \lesssim y^+ \lesssim 25$. In the present work, we investigate how these extra Reynolds stresses arise from the non-linear interaction between the texture-coherent flow and the texture-incoherent, background turbulence. We do so by conducting direct simulations where the presence of the texture is replaced by the corresponding slip conditions plus the above mentioned non-linear interaction, introduced as additional forcing on Navier-Stokes equations.

## METHODOLOGY

We conduct direct simulations (DNSs) of channels using a spectral discretisation in the streamwise and spanwise directions, and finite differences in the wall-normal direction. Time integration uses a fractional-step, Runge-Kutta scheme. Simulations are run at friction Reynolds number, $Re_\tau \approx 180$, at a constant mean pressure gradient, in channels of size $2\pi \times \pi \times 2$ in the streamwise ($x$), spanwise ($z$) and wall-normal ($y$) directions, respectively. In the texture-resolving simulations, alternating free-slip/no-slip boundary conditions are applied to both walls, using a multi-block grid with standard DNS resolution in a central block and 24 points in $x$ and $z$ per texture period in the near-wall blocks, taking the form of additional Fourier modes compared to the channel centre. In the simulations with homogeneous slip boundary conditions, additional advective terms are included in the momentum equations as derived from conventional triple decomposition or from the amplitude-modulated decomposition of [1, 3]. The surface textures considered are square posts with a solid fraction of 1/9 and $L^+ \approx 18$, 24, 35, 47, 71 and 94.

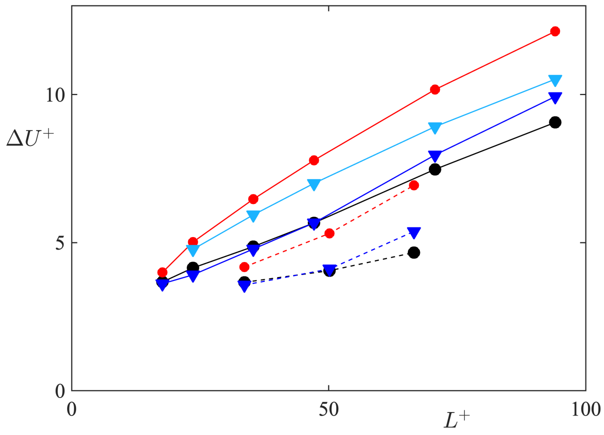

Figure 1: Drag-reducing $\Delta U^+$ vs texture size $L^+$. ●, texture-resolved simulations; ●, homogeneous slip simulations; ▼, simulations with forcing using triple decomposition; ▼, simulations with forcing using the decomposition of [1]. Solid lines are for collocated textures, and dashed lines for staggered ones.

## RESULTS

Figure 1 illustrates how the homogeneous-slip results deviate from the texture-resolved data for $L^+ \gtrsim 25$, as the velocity offset $\Delta U^+$, which causes the decrease in drag, is overpredicted by the slip simulations. Including the additional advective terms derived from conventional triple decomposition corrects some of this, but including those from amplitude-modulated decomposition yields $\Delta U^+$ values very close to those of texture-resolving simulations, at least up to $L^+ \approx 70$. The method not only captures the effect of the texture on drag, but also its detailed effect on the rms fluctuations and their spectral distribution, as shown in figures 2 and 3, while using conventional triple decomposition cannot reproduce all the length scales present in the fully resolved flow, nor their contribution to the rms fluctuations.

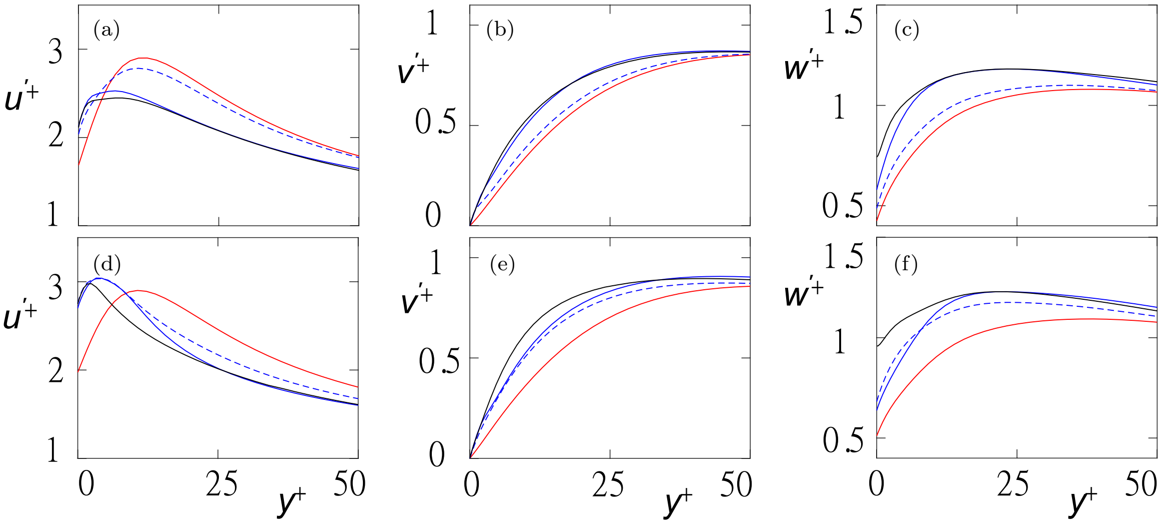

Figure 2: Rms fluctuations for collocated textures. (a-c), $L^+ \approx 35$; (d-f), $L^+ \approx 70$. ——, texture-resolving simulations; ——, slip simulations; - - -, simulations with forcing from triple decomposition; ——, with forcing from amplitude-modulated decomposition.

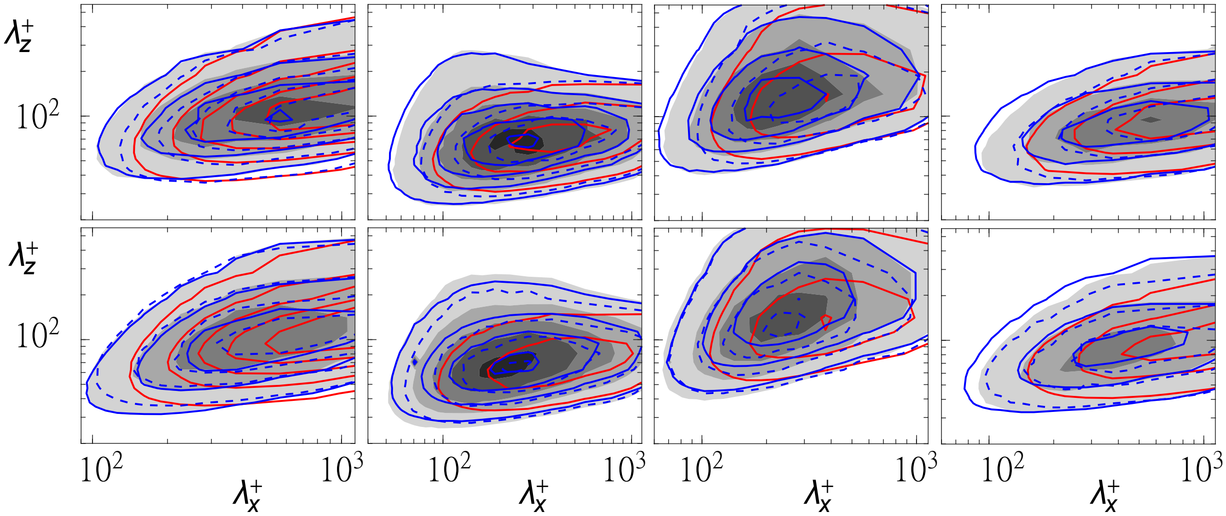

Figure 3: Spectral energy densities of velocity fluctuations and Reynolds stress at $y^+ \approx 15$ for collocated texture arrangement. Filled contours, texture-resolving simulations; ——, slip simulations; - - -, simulations with forcing from triple decomposition; ——, with forcing from amplitude-modulated decomposition.

## REFERENCES

[1] N. Abderrahaman-Elena, C. T. Fairhall, and R. García-Mayoral. Modulation of near-wall turbulence in the transitionally rough regime. *J. Fluid. Mech.*, 865:1042–1071, 2019.

[2] A. Busse and N. D. Sandham. Influence of an anisotropic slip-length boundary condition on turbulent channel flow. *Phys. Fluids*, 24:055111, 2012.

[3] C. T. Fairhall, N. Abderrahaman-Elena, and R. García-Mayoral. The effect of slip and surface texture on turbulence over superhydrophobic surfaces. *J. Fluid Mech.*, 861:88–118, 2019.

[4] C. T. Fairhall and R. García-Mayoral. Spectral Analysis of the Slip-Length Model for Turbulence over Textured Superhydrophobic Surfaces. *Flow Turbul. Combust.*, 100:961–978, 2018.

[5] J. I. Ibrahim, G. Gómez-de-Segura, D. Chung, and R. García-Mayoral. The smooth-wall-like behaviour of turbulence over drag-altering surfaces: a unifying virtual-origin framework. *J. Fluid Mech.*, 915, 2021.

[6] P. Luchini. The relevance of longitudinal and transverse protrusion heights for drag reduction by a superhydrophobic surface. In *EDRFCM 2015*, pages 81–82, 2015.

[7] P. Luchini, F. Manzo, and A. Pozzi. Resistance of a grooved surface to parallel flow and cross-flow. *J. Fluid Mech.*, 228:87–109, 1991.

[8] T. Min and J. Kim. Effects of hydrophobic surface on skin-friction drag. *Phys. Fluids*, 16:L55–L58, 2004.

[9] J. P. Rothstein. Slip on superhydrophobic surfaces. *Annu. Rev. Fluid Mech.*, 42:89–109, 2010.

[10] J. Seo and A. Mani. On the scaling of the slip velocity in turbulent flows over superhydrophobic surfaces. *Phys. Fluids*, 28:025110, 2016.

**Joint ERCOFTAC/EU-CTFF**
**European Drag Reduction and Flow Control Meeting – EDRFCM 2022**
**September 6$^{\text{th}}$–9$^{\text{th}}$, 2022, Paris, France**

# DEVELOPMENT OF AN APPARATUS FOR FLAT PLATE DRAG MEASUREMENTS AND ITS APPLICATION FOR COMPLIANT COATINGS IN TURBULENT BOUNDARY LAYERS

**M. van Nesselrooij**
Aerodynamics, Wind Energy, Flight Performance and Propulsion Department, Delft University of Technology,
2629 HS Delft, The Netherlands

## ABSTRACT

Accurately measuring small changes in aerodynamic drag over a flat surface stands at the core of the development of technologies capable of reducing turbulent friction drag. A wind tunnel drag measurement system was developed which improves significantly on the state of the art (Molton et al. [2015]). Experimental tests demonstrated that a root mean square repeatability of better than 0.2% of $C_D$ is achieved already at drag values below 1 N. This was replicated in two different wind tunnels. A match with literature on riblet performance within 1% of $C_D$ was obtained as a validation of the system. A crucial aspect of the design is the implementation of a correction for the pressure forces on the streamwise-facing surfaces of the test plate assembly. The flexible architecture of the system in the present realisation makes it suitable for most wind tunnels having a test section width of 400 mm or larger, demonstrated schematically in Figure 1. This allows for accelerated development of turbulent drag reduction concepts from moderate-size low-cost facilities towards flow conditions relevant to the intended industrial application. The applicability of the system is demonstrated with a drag characterisation of single-layer compliant surfaces.

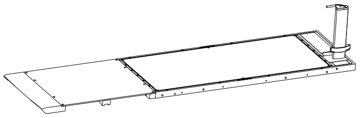

(a) Elliptical leading edge, with floor opening (expels tunnel boundary layer through floor)

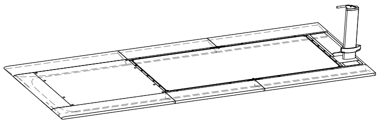

(b) Elliptical leading edge, without floor opening (guides the tunnel boundary layer below the setup)

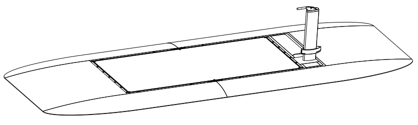

(c) Hill-like configuration (guides the tunnel boundary layer over the test surface)

Figure 1: Examples of alternative system configurations for compatibility with a wide range of wind tunnels

## CORRESPONDING PAPER

M. van Nesselrooij, O. W. G. van Campenhout, B. W. van Oudheusden, F. J. J. Schrijer, and L. L. M. Veldhuis. Development of an experimental apparatus for flat plate drag measurements and considerations for such measurements. *Measurement Science and Technology*, 33(5):055303, 2022

## REFERENCES

P. Molton, D. Hue, and R. Bur. Drag induced by flat-plate imperfections in compressible turbulent flow regimes. *Journal of Aircraft*, 52(2):667–679, 2015.

**Joint ERCOFTAC/EU-CTFF**
**European Drag Reduction and Flow Control Meeting – EDRFCM 2022**
**September 6$^{\text{th}}$–9$^{\text{th}}$, 2022, Paris, France**

# ON THE DETECTION AND CHARACTERISATION OF HIBERNATING TURBULENCE IN BOUNDARY-LAYER FLOWS

**T. Liu[1], A. Moody[1], M. Wilkes[1], D.C. Swailes[2], R.D. Whalley[1]**
[1]School of Engineering, Newcastle University, Newcastle NE1 7RU, United Kingdom
[2]School of Mathematics, Statistics and Physics , Newcastle University, Newcastle NE1 7RU, United Kingdom

## INTRODUCTION

Turbulent skin-friction drag reduction in liquid flows can be achieved by dissolving long-chain polymers in the working fluid, which become stretched by the wall-turbulence flow structures leading to a suppression in turbulent skin friction [1, 2]. Once a sufficient concentration of polymer is dissolved in the working fluid, the mean streamwise velocity profile falls onto the so-called maximum drag reduction (MDR) asymptote [1]. Recent numerical [2] and experimental [3, 4] investigations of an intrinsic low-drag state called "hibernating turbulence" revealed time intervals where the instantaneous streamwise velocity profiles approached the MDR asymptote, even in Newtonian fluid flows. To date, investigations on the hibernating phenomena have been limited to low-Reynolds number transitional channel flow investigations. Here we present the detection and characterisation of the hibernating turbulence phenomena in turbulent boundary-layer flows in a series of wind tunnel and water flume experiments.

## EXPERIMENTAL SET-UP

The experiments are carried out in an open return wind tunnel with a cross-section of 350 × 490 mm and a water flume with a cross-section of 325 × 200 mm (width×height). In each facility, the boundary-layer flow is tripped into a turbulent regime over a 3 m long flat plate. The intervals of hibernating turbulence are detected from the instantaneous wall-shear stress measurements made by a flush-mounted hot-film probe. As the instantaneous wall-shear stress measurements from the hot-film are damped in air flow [5], we calibrate the hot-film probe for wall-shear stress measurements using a Non-Linear Regression (NLR) technique [6], which has hitherto been used to calibrate hot-film probes in liquid flows. The wall-shear stress data from the hot-film probe is compared to the simultaneously acquired wall-shear stress data from LDV in Figure 1, which shows excellent agreement. During the experiments, the instantaneous wall-shear stress is measured with the hot-film probe, whilst simultaneously, the streamwise velocity is measured at various wall-normal locations with LDV, for several hours. During post-processing, the streamwise velocity is conditionally sampled during the low-drag intervals of hibernating turbulence. The experiments are conducted at $Re_\tau = 700$ in wind tunnel and $Re_\tau = 940$ in the water flume, respectively.

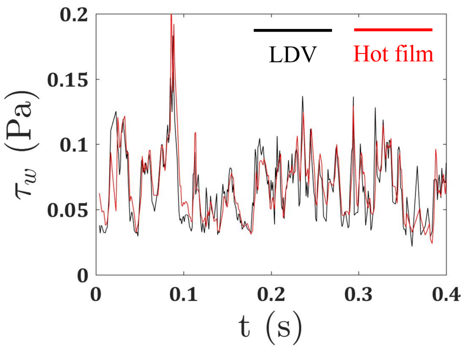

Figure 1: Comparison of the wall-shear stress $\tau_w$ obtained simultaneously from the NLR calibrated hot-film and with LDV using the near-wall velocity gradient technique.

## RESULTS

The hibernating turbulence intervals are detected when the instantaneous wall-shear stress $\tau_w$ drops 0.9 below the mean

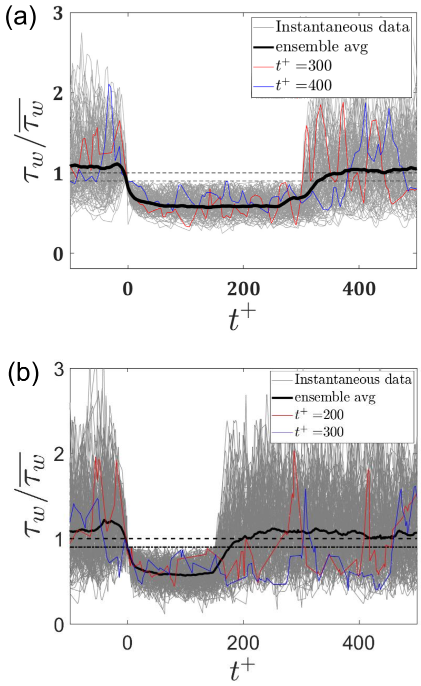

Figure 2: (*a*) Low drag hibernating turbulence events in a wind tunnel by hot-film; (*b*) low drag hibernating events in water flume by LDV. Grey solid lines: instantaneous wall-shear stress; black solid line: ensemble-averaged wall-shear stress of all the hibernating turbulence events; red and blue solid line: examples of hibernating turbulence event with duration: $t^+ = 300$ for red line and $t^+ = 400$ for blue line in (*a*); $t^+ = 200$ for red line and $t^+ = 300$ for blue line in (*b*).

wall-shear stress $\overline{\tau_w}$ and lasts for a duration of $\Delta t^+ = 300$ for the wind tunnel investigation ($\Delta t^+ = 150$ for the water flume data), where $t^+$ is the inner time scale defined as $t^+ = t u_\tau^2/\nu$ ($\nu$ is the kinematic viscosity of the fluids). The instantaneous hibernating turbulence events are plotted in grey solid lines in Figure 2: (*a*) for wind tunnel; (*b*) for water flume.

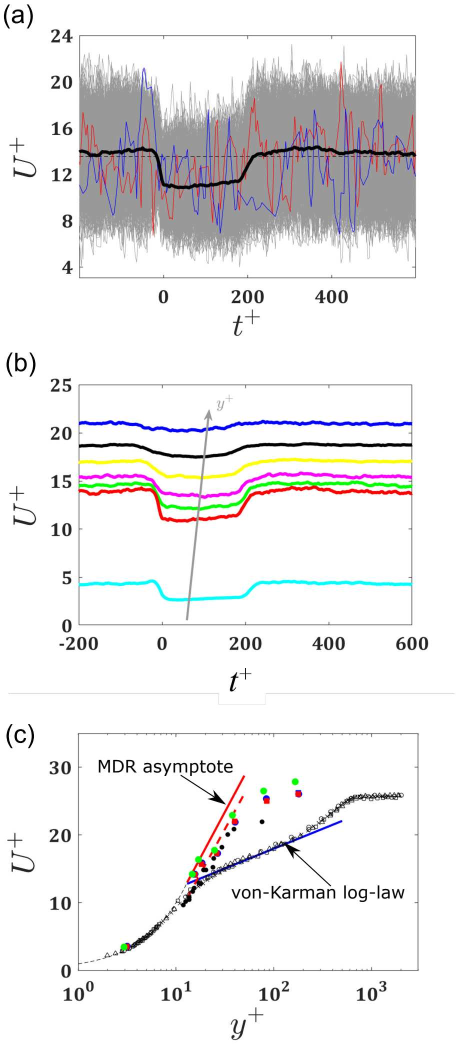

Figure 3: (*a*) Conditionally sampled streamwise velocity $U^+$ scaled by the ensemble-averaged wall-shear stress measured at wall distance $y^+ = 20$ in wind tunnel; grey solid lines: instantaneous wall-shear stress; black solid line: ensemble-averaged wall-shear stress of all the hibernating events; red and blue solid line: examples of hibernating event; (*b*) ensemble-averaged streamwise velocity during hibernating events at different wall distances; (*c*) turbulent boundary layer profile in wind tunnel at $Re_\tau = 700$: black hollow symbols are time-averaged profile; color closed symbols represents the time-averaged velocity during the low drags events with different detection criterion; black closed symbols: channel flow data during low drag events at $Re_\tau = 70-100$ [3, 4]; blue solid line is the von-Karman log-law and red solid line is the MDR asymptote; read dashed line is the 95% confidence interval to the MDR asymptote.

The black solid lines in Figure 2 show the ensemble-averaged wall shear stress of the hibernating turbulence events. The ensemble-averaged curve rises above the $\overline{\tau_w}$ before dropping to a low-drag plateau. We can see that the hibernating turbulence intervals can be detected in air or water turbulent boundary-layer flows. The instantaneous conditionally sampled streamwise velocity $U^+$ scaled with the ensemble averaged wall-shear stress at $y^+ = 20$ in the wind tunnel during the low drag events is illustrated in Figure 3 (*a*) in grey solid lines. The ensemble-averaged $U^+$ is also lower than the mean $U^+$ when the flow is in the low-drag state. The ensemble-averaged $U^+$ at different wall-normal distances $y^+$ is shown in Figure 3 (*b*). The lower $U^+$ during the low-drag plateau becomes less distinct as $y^+$ away from the wall, almost as though communication is lost with the wall part way through the logarithmic region. The time-averaged streamwise velocity profile during the low-drag intervals is plotted in Figure 3 (*c*) in closed color symbols, which appears to approach the MDR asymptote (red solid line) in the buffer and log-law regions.

## CONCLUSIONS AND FUTURE WORK

The hibernating turbulence has been detected in turbulent boundary-layer flows. Striking resemblance to previous transitional channel flow data is also found. During intervals of hibernating turbulence, the conditionally sampled streamwise velocity approaches the MDR asymptote, which is only routinely associated with polymer drag reduced flows.

In a set of future experiments, we plan to carry out two-component LDV measurements in the water flume to study the changes of Reynolds stress during these low drag states. In addition, stereo-PIV measurements will be conducted to investigate the vortical flow structures during hibernating turbulence in the turbulent boundary-layer flows.

## ACKNOWLEDGMENTS

The work has been supported by the Air Force Office of Scientific Research under grant number FA9550-17-1-0231.

## REFERENCES

[1] P. S. Virk. Drag reduction fundamentals. *AIChE Journal*, 21(4):625–656, 1975.

[2] Li Xi and M.D. Graham. Active and hibernating turbulence in minimal channel flow of newtonian and polymeric fluids. *Phys. Rev. Lett.*, 104:218301, May 2010.

[3] R.D. Whalley, J.S. Park, A. Kushwaha, D.J.C. Dennis, M.D. Graham, and R.J. Poole. Low-drag events in transitional wall-bounded turbulence. *Phys. Rev. Fluids*, 2:034602, Mar 2017.

[4] R.D. Whalley and D.J.C. Dennis. An experimental investigation into spatiotemporal intermittencies in turbulent channel flow close to transition. *Experiments in Fluids*, 60, May 2019.

[5] P.H. Alfredsson, A.V. Johansson, J.H. Haritonidis, and H. Eckelmann. The fluctuating wall-shear stress and the velocity field in the viscous sublayer. *The Physics of Fluids*, 31(5):1026–1033, 1988.

[6] R. Agrawal, R.D. Whalley, H.C.-H. Ng, D.J.C. Dennis, and R.J. Poole. Minimizing recalibration using a nonlinear regression technique for thermal anemometry. *Experiments in Fluids*, 60, July 2019.

**Joint ERCOFTAC/EU-CTFF**
**European Drag Reduction and Flow Control Meeting – EDRFCM 2022**
**September 6$^{\text{th}}$–9$^{\text{th}}$, 2022, Paris, France**

# THE CHARACTERIZATION OF DRAG REDUCING AGENTS FOR APPLICATION IN LOW-ENTHALPY GEOTHERMAL WELLS AND DISTRICT HEATING SYSTEMS

**A.T. van Nimwegen**
Heat Transfer and Fluid Dynamics, TNO, 2628 CA Delft, The Netherlands

**S.A. Jones**
Faculty of Civil Engineering and Geosciences, Delft University of Technology, 2628 CN Delft, The Netherlands

**H.R. Fischer**
Material Solutions, TNO, 5656 AE Eindhoven, The Netherlands

**P.L.J. Zitha**
Faculty of Civil Engineering and Geosciences, Delft University of Technology, 2628 CN Delft, The Netherlands

**P.S. Shoeibi Omrani**
Heat Transfer and Fluid Dynamics, TNO, 2628 CA Delft, The Netherlands

## INTRODUCTION

In both low-enthalpy geothermal wells and district heating systems the pumping power required to overcome the frictional losses in the wells and pipelines decrease the efficiency. Using drag reducing agents (DRAs) to reduce the pressure losses in turbulent flow would allow saving on energy cost in current systems and on the construction of future systems where a smaller pipe diameter would suffice.

The difficulty to apply DRAs in these systems are the operating conditions. Older district heating systems have temperatures of up to 120°C with a return temperature 60°C lower (modern district heating systems operate at lower temperatures, with a maximum temperature of 50-80°C). In low enthalpy geothermal wells, such as those found in the Netherlands, the maximum temperature is limited to about 90 °C. In these wells the salt concentration is typically in the range of 100,000 to 300,000 ppm.

The overarching goal of the DRAGLOW project is to estimate both the physical and economic impact of introducing DRAs in low-enthalpy geothermal wells and district heating networks. In this first part of the project, 12 DRAs are characterised to determine which are suitable to investigate further in the project.

In this first part of the research, potential DRAs are characterized for their potential use in the considered applications. Both polymers and surfactants are considered. Surfactants will be most suitable for district heating systems in which the DRA solution is circulated through a pump. Pumps typically degrade polymers [1], while recirculating systems exist in which the surfactants have been used for months [2]. For low-enthalpy geothermal systems, where the DRAs move through the system only once, both polymers and surfactants can be applied.

## CHARACTERIZATION METHODS

Three different characterization tests are used to determine whether a DRA is suitable for continued research:

- Oven tests. The DRAs are stored in the oven at high temperatures (90-100 degrees) with the correct water composition. The compatibility of the DRA with the temperature and the water chemistry is determined by visual inspection and through measurement of the NMR spectrum before and after storing the samples in an oven.
- Beaker/vortex tests. DRA solutions in a beaker are stirred using a magnetic stirrer. For the pure solvent, a vortex is formed. If the DRAs are working well, the vortex should be significantly reduced when the solvent with the DRA is stirred at the same rate.
- Rheological tests. The DRA solutions are placed in an Anton Paar MCR302, where the rheology is measured for temperatures between 20 and 90°C. The focus of these experiments is on the higher shear rates as encountered in turbulent flow.

## OVEN TESTS

Two examples of oven tests are presented in figure 1. The top DRA solution was stable for the entire period. This DRA might be suitable for operation under the conditions (brine and temperature) considered in the oven test. The bottom DRA solution did degrade over time, such that it should not be applied at the considered conditions.

The difference between a stable and an unstable DRA solution in the oven can also be seen from the NMR spectra. From the example shown in figure 2 it can be observed that the NMR spectrum changes for the top DRA sample: the change in the NMR spectrum corresponds to the solution becoming opaque, such that it is clear that this DRA sample is unsuitable for application at the considered conditions.

## BEAKER TEST

A common test to screen a DRA is to determine whether a vortex can be suppressed by the addition of the agent to

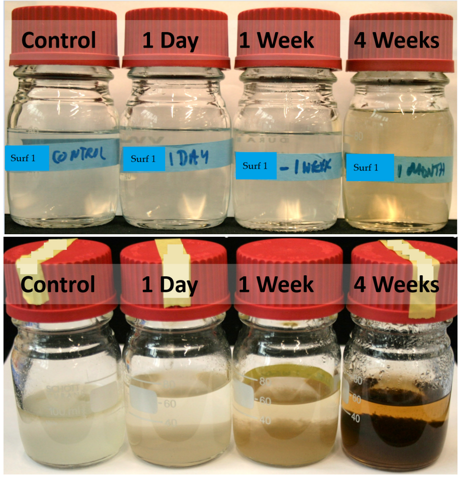

Figure 1: Example of a successful oven test (top) and an unsuccesfull oven test (bottom).

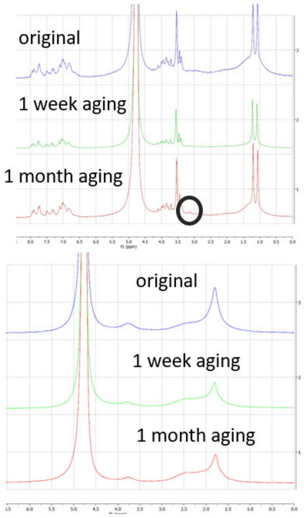

Figure 2: NMR spectra of two DRA solutions before and after storage in an oven.

the solvent [3]. This simple experiment was performed here to make sure that a DRA is working. Only if it is, the subsequent rheological experiments are performed. An example of a beaker test is presented in figure 3.

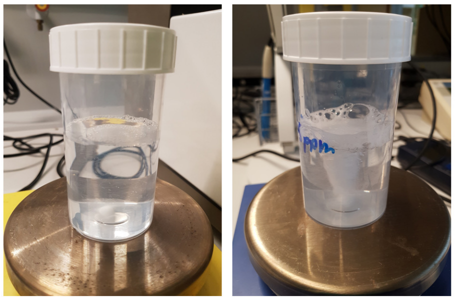

Figure 3: Example of a beaker test for examining DRAs. The vortex created using the magnetic stirrer at very low concentration (right) is no longer present at high concentration (left).

## RHEOLOGICAL MEASUREMENTS

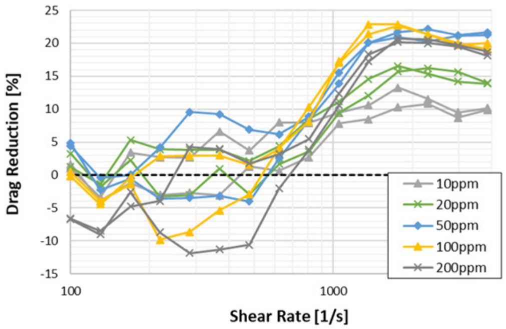

Figure 4: Example showing the results of rheological measurements for one of the considered DRAs.

In figure 4 the results of rheological measurements are presented for one of the DRAs in a brine with 300,000 ppm of salts. The results are always compared to a measurement of only the solvent as follows:

$$DR = \frac{M_{\text{solvent}} - M_{\text{solvent+DRA}}}{M_{\text{solvent}}} \times 100\% \qquad (1)$$

In which $M$ indicates the torque measured by the rheometer. At low shear rates the viscosity of the solutions is higher as the flow in rheometer is laminar. Only at shear rate the flow becomes turbulent the torque is decreased. In a later stage of the research, these rheological measurements will be related to measurements of drag reduction in pipelines.

## CONCLUSIONS

Among the 12 DRA which have been tested, several molecules showed thermal and solution stability with an acceptable drag reduction (up to 30% in the rheometer) for different ranges of temperature and salinities, representative for different type of district heating-cooling systems and low-enthalpy geothermal wells. The results of this characterization will be used in next steps within the DRAGLOW project. The DRAs that showed the best performance will be used for further testing in turbulent pipe flows and core-flood experiments to quantify the drag reduction which can be achieved in turbulent pipe flows and understand the DRA-geothermal reservoir interaction

## ACKNOWLEDGEMENTS

This work is performed using a subsidy from RVO under the MOOI program, with project partners TNO, Delft University of Technology, Well Engineering Partners, ECW, Nouryon, Enertrans, the city of Amsterdam, the city of Rotterdam, Nijkamp, Wayland Energy and Roemex.

## REFERENCES

[1] J.M.J den Toonder. Drag reduction by polymer additives in a turbulent pipe flow: Laboratory and numerical experiments, 1996.

[2] F Hammer. Demonstration of smooth water in the district heating system of herning, denmark, 1991.

[3] Vladimir Jovancicevic, Sunder Ramachandran, Young Soo Ahn, and BA Alink. Corrosion inhibition and drag reduction in multiphase flow. In *CORROSION 2001*. OnePetro, 2001.

**Joint ERCOFTAC/EU-CTFF**
**European Drag Reduction and Flow Control Meeting – EDRFCM 2022**
**September 6$^{\text{th}}$–9$^{\text{th}}$, 2022, Paris, France**

# CONTROL OF UNSTEADY WAKE FLOWS BY MACHINE LEARNING

**T. Guégan**[1], **O. Semeraro**[2], **M. A. Bucci**[3], **L. Mathelin**[2] and **L. Cordier**[1]

1: Institut Pprime, CNRS, Université de Poitiers, ISAE-ENSMA, Poitiers, France
2: LISN, CNRS, Université de Paris-Saclay, Orsay, France
3: LISN, INRIA, Université de Paris-Saclay, Orsay, France

In this work, we develop a specific *closed-loop control strategy* so that the control can adapt, if possible in real time, to changes in the flow. In general, the action is determined via an expert or a mathematical model, previously developed. This dynamical model must predict the behavior of the system under the effect of the control. However, for many physical systems, and in particular for turbulent flows, there are no sufficiently efficient physical models. Indeed, the physics may be poorly known, or the resolution of the equations too slow, compared to the dynamics involved. Although reduced order models can be useful, they can lose accuracy under control, resulting in poor performance. An alternative strategy is to develop a fully *data-driven approach*. Here, we consider **Deep Reinforcement Learning**, a method coming from machine learning. This method combines reinforcement learning with deep neural networks used to represent the control objective and the policy (actions). In this framework, an agent seeks to learn an optimal policy by interacting with the environment to be controlled via actions as inputs and observations and rewards as outputs. We carry out applications to the control of the so-called *fluidic pinball* configuration (see Fig. 1), governed by the Navier-Stokes equations. The efficiency of reinforcement learning is demonstrated for this dynamical system, either for the quality of the obtained control law (see Fig. 2), for the speed of convergence or for the robustness of the learning (see Fig. 3).

**Keywords**: deep reinforcement learning, flow control, artificial intelligence, fluid mechanics, mechanical engineering

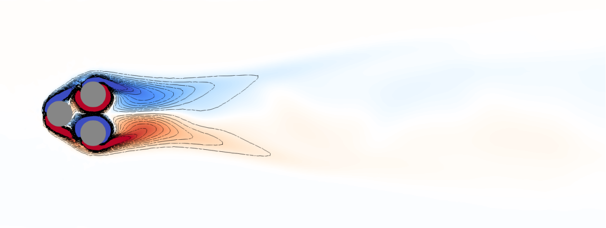

(a) Mean flow under control.

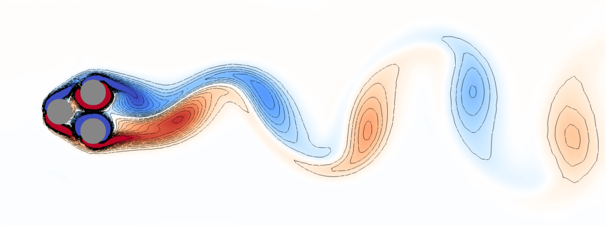

(b) Unsteady dynamics under control.

Figure 1: Numerical simulation of the fluidic pinball at Re $=100$ with the control law learned from Proximal Policy Optimization (PPO) for 3 wake pressure probes. Control parameters determined with an embedding of the dynamics, introduction of noise on observations and control, and no control penalty in the reward. Representation of the vorticity $\omega_z \in [-2, 2]$.

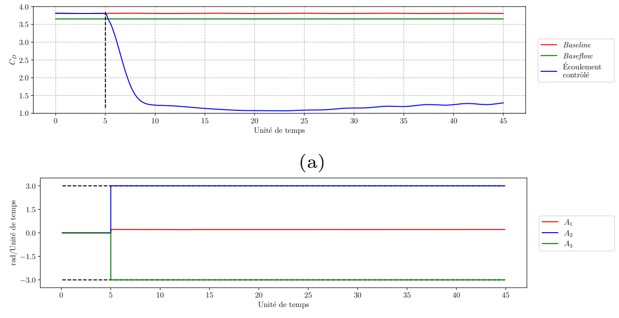

(a)

(b)

Figure 2: Results of PPO learning for 3 pressure sensors in the wake. (a) Time evolution of the drag coefficient at Re = 100 for the controlled, baseline and baseflow flows. A reduction of 70 % of the drag is obtained. (b) Control laws determined by learning. The control is activated at $t = 5$. The horizontal dashed lines shown in figure (b) represent the admissible control limits. Control parameters determined with an embedding of the dynamics, introduction of noise on observations and control, and no control penalty in the reward.

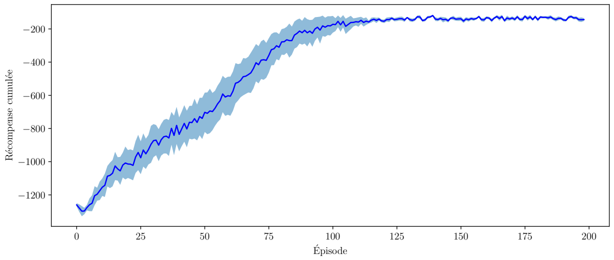

Figure 3: Robustness of the PPO learning process for 3 pressure sensors in the wake. Cumulative rewards for 20 independent learnings performed with the same set of hyperparameters but different random seeds. The average over all learnings is shown using the solid line. The colored band represents ± the variance. Control parameters determined with an embedding of the dynamics, introduction of noise on observations and control, and no control penalty in the reward.

**Joint ERCOFTAC/EU-CTFF**
**European Drag Reduction and Flow Control Meeting – EDRFCM 2022**
**September 6$^{\text{th}}$–9$^{\text{th}}$, 2022, Paris, France**

# BAYESIAN OPTIMIZATION OF ACTIVE FLOW CONTROL IN THE TURBULENT BOUNDARY LAYER ON A NACA4412 PROFILE

**N. Charisoudis, G. Semprini Cesari,**
**F. Mallor, T. Mukha, S. Rezaeiravesh and P. Schlatter**
SimEx/FLOW, Engineering Mechanics,
KTH Royal Institute of Technology, 100 44 Stockholm, Sweden

## INTRODUCTION

In recent years, the increasing need for efficient transportation and industrial processes has resulted in an extensive study of flow control methods in wall-bounded turbulent flows aimed at minimizing skin friction. To this day, most fundamental studies are conducted in either turbulent channel flows or canonical zero-pressure gradient (ZPG) turbulent boundary layer (TBL) flows; most notable are the works of Choi *et al.* [4], Quadrio *et al.* [11] and Kametani *et al.* [5] and Stroh *et al.* [13] in order to assess the effectiveness of several active control methods. However, due to the increased complexity, few data are available on adverse-pressure gradient boundary layer [3]. A detailed database of uniform suction and blowing has been recently created by means of high-fidelity large-eddy simulations (LES) on a NACA4412 airfoil at moderate Reynolds number [1], and a similar study is being conducted now based on the OpenFOAM open source software to establish a low-cost reproducible framework for enabling control studies in aeronautical flows. Since novel flow control methods are continuously improved, our future task will be to optimise parameters for such methods, in particular non-uniform blowing and suction. This topic was recently investigated in the framework of a ZPG turbulent boundary layer by Mahfoze *et al.* [6] using direct numerical simulations.

The present work extends the work by Atzori *et al.* [2], by carrying out a Bayesian optimization (BO) [8] of the blowing/suction control scheme on the suction side of a NACA 4412 wing profile. Therefore, the design parameters are the parameters defining the profile shown in Figure 2 (bottom). Reynolds Averaged Navier-Stokes (RANS) simulations are used in the optimization process. The choice of BO based on Gaussian processes [8] has the advantage of requiring only a limited number of RANS simulations for obtaining the global optimum for a small to moderate number of design parameters. The cost-efficiency of the BO-GP compared to other black-box optimization relies on the fact that the algorithm is fully data-driven for adaptive sampling from the space of design parameters. In another part of our study, the effect of the control strategy on the TBL in the uncontrolled, baseline (uniform blowing and suction) and most optimal cases, are investigated in detail by means of wall-resolved LES, and eventually also high-order DNS and LES as documented by Atzori *et al.* [3].

## METHODOLOGY AND VALIDATION

During the optimization process, the incompressible flow around the airfoil is simulated by means of RANS with the open-source computational fluid dynamics toolbox OpenFOAM [14] at a chord-based Reynolds number of $Re = 4 \cdot 10^5$ and angle of attack of $\alpha = 5°$. In particular, the steady state, incompressible solver `simpleFoam` is employed with the $k$-$\omega$-$SST$ turbulence model [7]; second order finite volume schemes are being utilised.

A numerical grid of hexahedral cells in a 2D C-shaped block with C-radius of $r_C = 5$ and a trailing edge to outlet distance of $r_C = 10$ has been created. In order to apply the turbulence model without wall function being applied, the requirement of $y^+_{wall} \leq 1$ has been enforced in the turbulent region of the airfoil, starting at $x/c = 0.1$.

To correctly simulate the flow, a trip is enforced as a semi-implicit scalar source [10] in the turbulent kinetic energy budget equation, defined in the OpenFOAM dictionaty `fvOptions` by only accounting for the explicit part of this source. The trip location, both on the suction and pressure side of the airfoil, starts at $x/c = 0.1$ and spans 1% of the chord in the streamwise direction and $\delta_{99}/2$ in the wall normal direction.

Preliminary validation results are shown in Fig. 1, which show good agreement with reference data for control on airfoils, compared to our OpenFOAM implementations, both for LES and RANS.

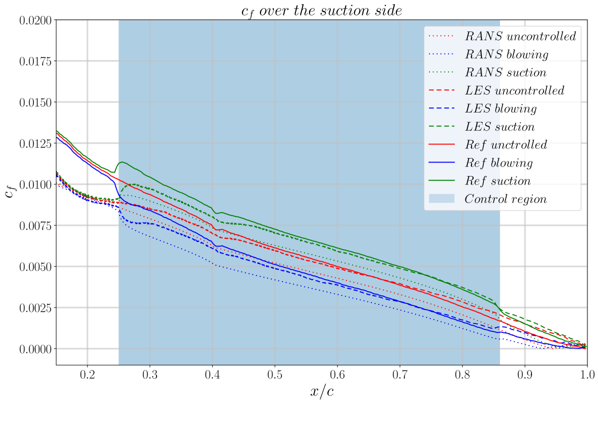

Figure 1: Local skin friction coefficient for the suction side of the airfoil obtained using our OpenFOAM implementation based on both RANS and LES. The reference data is taken from the high-order simulations by Atzori *et al.* [2].

## OUTLOOK

The boundary layer control is applied on the suction side of the airfoil from $x/c = 0.25$ to $x/c = 0.86$, according to the precedent works carried out by the group [2]. Uniform suction and blowing schemes are then modified to define a streamwise dependent blowing/suction boundary condition through the parameterization of the blowing/suction intensity by means of a number of collocation parameters along the wing surface.

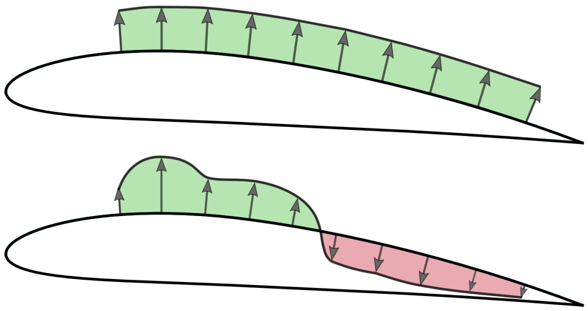

Figure 2: Sketch of the NACA 4412 wing profile with uniform blowing (top) and mixed blowing and suction (bottom) flow-control schemes. The arrows stem from the collocation points in which the control strategy is optimized (*i.e.* its parameterization), and green and red areas indicate blowing and suction, respectively. Zero-mass flux may be maintained to ensure practical feasibility of the control strategy.

In particular, these parameters are designed in such a way to define a spline spanning on the whole control region; given the values of these, linearly related weights are then superimposed to a uniform blowing/suction condition to enforce a non-uniform one, as showed in Figure 2. A Bayesian optimization method based on Gaussian process regression [9] is consequently applied to define the best parameters configuration in order to achieve (for instance) the greatest lift-to-drag ratio, or other relevant objective functions. In order to assure feasibility of the control in practical applications, several constraints are being imposed related to maintaining zero mass flux for the control actuation; both on suction and pressure sides of the profile.

Eventually, wall-resolved LES of the uncontrolled, baseline and most optimal cases are run to provide an estimation of the RANS simulations' accuracy; also these simulations are performed within our OpenFOAM framework.

As an extension of this work, using wall-modelled LES to perform the simulations will be considered. It is anticipated that the control will modify the velocity profiles in such a way that canonical log-law wall models will not be directly applicable. Suitable modifications will have to be developed. As a result, a hierarchy of modelling approaches of increasing fidelity will be established, which can be levered together using a suitable multi-fidelity approach [12].

The final conference contribution will contain a detailed description of our OpenFOAM setup together with the various control schemes stemming from the optimization procedure. The case will eventually be provided online for other groups in an effort to establish an accessible baseline for low-order simulations of control.

## REFERENCES

[1] M. Atzori. *Coherent structures and control in wall-bounded turbulent flows.* KTH Royal Institute of Technology, 2021.

[2] M. Atzori, R. Vinuesa, G. Fahland, A. Stroh, D.e Gatti, B. Frohnapfel, and P. Schlatter. Aerodynamic Effects of Uniform Blowing and Suction on a NACA4412 Airfoil. *Flow, Turbulence and Combustion*, 105:735–759, 2020.

[3] M. Atzori, R. Vinuesa, A. Stroh, D. Gatti, B. Frohnapfel, and P. Schlatter. Uniform blowing and suction applied to nonuniform adverse-pressure-gradient wing boundary layers. *Physical Review Fluids*, 6(11):113904, 2021.

[4] H. Choi, P. Moin, and J. Kim. Active turbulence control for drag reduction in wall-bounded flows. *Journal of Fluid Mechanics*, 262:75–110, 1994.

[5] Y. Kametani, K. Fukagata, R. Örlü, and P. Schlatter. Effect of uniform blowing/suction in a turbulent boundary layer at moderate Reynolds number. *International Journal of Heat and Fluid Flow*, 55:132–142, 2015.

[6] O. A. Mahfoze, A. Moody, A. Wynn, R. D. Whalley, and S. Laizet. Reducing the skin-friction drag of a turbulent boundary-layer flow with low-amplitude wall-normal blowing within a bayesian optimization framework. *Phys. Rev. Fluids*, 4:094601, 2019.

[7] F. R. Menter, M. Kuntz, and R. Langtry. Ten years of industrial experience with the sst turbulence model. *Heat and Mass Transfer*, 4:625–632, 2003.

[8] Y. Morita, S. Rezaeiravesh, N. Tabatabaei, R. Vinuesa, K. Fukagata, and P. Schlatter. Applying bayesian optimization with gaussian process regression to computational fluid dynamics problems. *Journal of Computational Physics*, 449:110788, 2022.

[9] Y. Morita, S. Rezaeiravesh, N. Tabatabaei, R. Vinuesa, K. Fukagata, and P. Schlatter. Applying Bayesian optimization with Gaussian process regression to computational fluid dynamics problems. *Journal of Computational Physics*, 449:110788, 2022.

[10] S. V. Patankar. *Numerical Heat Transfer and Fluid Flow (1st ed.).* CRC Press, 1980.

[11] M. Quadrio, P. Ricco, and C. Viotti. Streamwise-travelling waves of spanwise wall velocity for turbulent drag reduction. *Journal of Fluid Mechanics*, page 161–178, 2009.

[12] S. Rezaeiravesh, R. Vinuesa, and P. Schlatter. Towards multifidelity models with calibration for turbulent flows. In *14th WCCM-ECCOMAS Congress*. CIMNE, 2021.

[13] A. Stroh, B. Frohnapfel, P. Schlatter, and Y. Hasegawa. A comparison of opposition control in turbulent boundary layer and turbulent channel flow. *Physics of Fluids*, 27(7):075101, 2015.

[14] H. G. Weller, G. Tabor, H. Jasak, and C. Fureby. A tensorial approach to computational continuum mechanics using object-oriented techniques. *Computers in Physics*, 12(6):620–631, 1998.

**Joint ERCOFTAC/EU-CTFF**
**European Drag Reduction and Flow Control Meeting – EDRFCM 2022**
**September 6$^{\text{th}}$–9$^{\text{th}}$, 2022, Paris, France**

# MEASURING THE UNSTEADY DRAG OF SUPERHYDROPHOBIC SURFACE TREATMENT USING NEURAL NETWORKS AND EXPERIMENTAL DISPLACEMENT TIME SERIES

**S. Davey, C. Atkinson and J. Soria**
Laboratory for Turbulence Research in Aerospace and Combustion, Department of Aerospace and Mechanical Engineering, Monash University, 3800 Melbourne, Australia

## INTRODUCTION

The vertical acceleration $a_z$ of a sphere of mass $m_s$ and diameter $d$, settling under the influence of gravity $g$ in a fluid of density $\rho_f$ and viscosity $\mu$ at rest, assuming negligible history force, is given as [6]

$$\left(m_s + \frac{1}{2}m_f\right)a_z(t) = \left(m_s - m_f\right)g - D(t), \tag{1}$$

where $m_f$ is the fluid mass displaced by the sphere [4, 2, 8] and $D(t)$ is the drag force acting on the sphere. For a sphere starting at rest, $D(t)$ increases as the sphere accelerates until is is equal to $(m_s - m_f)g$ and the sphere reaches its terminal velocity $w_\infty$. At terminal velocity, the Reynolds number and drag coefficient [6] of the sphere can be calculated from the fluid and sphere properties, and the measured terminal velocity using

$$Re_\infty = \frac{\rho_f w_\infty d}{\mu}, \tag{2}$$

and

$$C_{D,\infty} = \frac{4dg\left(\zeta - 1\right)}{3w_\infty^2}, \tag{3}$$

where $\zeta$ is the sphere-to-fluid density ratio, respectively. This method has been used to measure the relative drag of surface treatments by calculating the terminal drag coefficient and Reynolds number for spheres with and without surface treatment [5, 1, 3]. This can be repeated with spheres of varying diameter to determine empirically the relationship of $C_{D,\infty}$ to $Re_\infty$ for a given surface treatment.

While this method allows for the relatively simple measurement of relative drag for surface treatments, it is limited to the region of terminal velocity. In order to obtain the transient drag of the sphere using (1), the acceleration must be determined over the full motion of the sphere. In the case where the displacement of the sphere is measured, this requires differentiation of the experimental data, which results in significant noise.

## EXPERIMENTAL METHOD

The displacement over time is measured for sphere of diameter 10, 15 and 20 mm, with and without superhydrophobic surface treatment using the 1m vertical tank filled with water at rest, shown in figure 1. The spheres are released remotely using a solenoid, and the motion of the sphere is captured at 1000 Hz using two high-speed cameras arranged vertically. The position of the sphere in each image is determined relative to the first image using cross-correlation digital particle image velocity [7] for each camera, and the displacement data from each camera is concatenated to form the full displacement time series of the sphere.

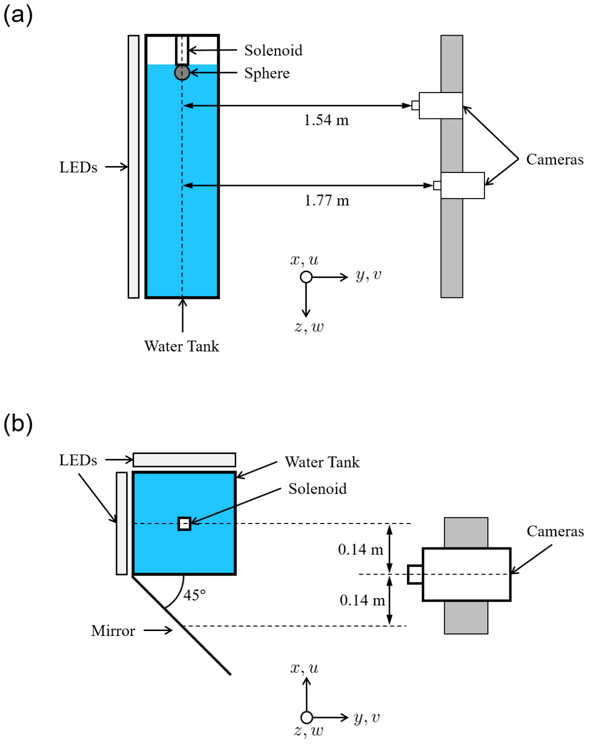

Figure 1: (a) Top and (b) side view of the experimental setup, showing the cameras LEDs and mirror for capturing the 3D motion of the sphere.

## NEURAL NETWORK APPLICATION

Defining the non-dimensional variables

$$t^\star = \frac{t}{\sqrt{d/a_z(0)}}, \tag{4}$$

$$z^\star = \frac{z}{d}, \tag{5}$$

$$w^\star = \frac{w}{\sqrt{da_z(0)}}, \tag{6}$$

$$a_z^\star = \frac{a_z}{a_z(0)}, \tag{7}$$

and

$$D^\star = \frac{D}{\left(m_s - m_f\right)g}, \tag{8}$$

where $a_z(0) = \frac{\zeta - 1}{\zeta + \frac{1}{2}} g$ is the initial acceleration of the sphere, collapses the measured displacement time series $z^\star(t^\star)$ and the derived velocity time series $w^\star(t^\star)$ onto a single curve for each of the surfaces, as shown in figure 2.

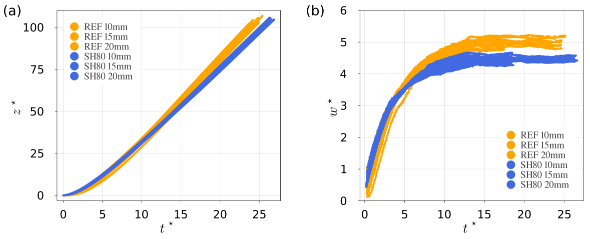

Figure 2: Non-dimensional (a) displacement and (b) velocity time series for the untreated (REF) and superhydrophobic (SH80) spheres of diameters 10, 15 and 20 mm.

However, the unsteady drag difference between the spheres with and without surface treatment becomes difficult to distinguish in the derived acceleration $a_z^\star(t^\star)$ and drag force $D^\star(t^\star)$ time series due to increased noise, as shown in figure 3.

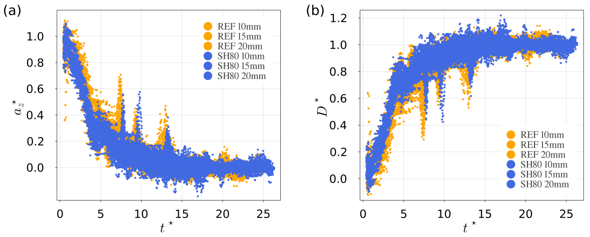

Figure 3: Non-dimensional (a) acceleration and (b) drag force time series for the untreated (REF) and superhydrophobic (SH80) spheres of diameters 10, 15 and 20 mm.

The non-dimensional form of (1) can shown to become

$$a_z^\star(t^\star) = 1 - D^\star(t^\star). \tag{9}$$

For a known $D^\star$, the vertical displacement $z^\star$ and velocity $w^\star$ of the sphere over time can be determined by solving the ordinary differential equation

$$\frac{d}{dt^\star}\begin{bmatrix} z^\star \\ w^\star \end{bmatrix} = \begin{bmatrix} w^\star \\ 1 - D^\star \end{bmatrix}. \tag{10}$$

We investigate the use of a neural network in place of the unknown $D^\star$ to solve (10) using the non-dimensional displacement time series from the 10 mm spheres and the initial dimensionless acceleration $a_z^\star(0) = 1$. The trained neural networks are then used to predict the displacement of the 15 and 20 mm spheres to determine how well the neural network captures the dimensionless dynamics of spheres with and without surface treatment. This is compared to the results of the non-dimensional form of the exponential fit proposed in [6]. The solutions to (10) for each surface treatment are used to assess the difference in unsteady drag between the superhydrophobic and untreated spheres.

## REFERENCES

[1] K M T Ahmmed, C Patience, and A-M Kietzig. Internal and external flow over laser-textured superhydrophobic polytetrafluoroethylene (ptfe). *ACS applied materials & interfaces*, 8(40):27411–27419, 2016.

[2] TR Auton, JCR Hunt, and M Prud'Homme. The force exerted on a body in inviscid unsteady non-uniform rotational flow. *Journal of Fluid Mechanics*, 197:241–257, 1988.

[3] M Castagna, M P Eisfelder, H Taylor, N Mazellier, A Kourta, and J Soria. Effects of super-hydrophobic coatings on free falling spheres. In *21st Australasian Fluid Mechanics Conference*, 2018.

[4] M R Maxey and J J Riley. Equation of motion for a small rigid sphere in a nonuniform flow. *The Physics of Fluids*, 26(4):883–889, 1983.

[5] Glen McHale, NJ Shirtcliffe, CR Evans, and MI Newton. Terminal velocity and drag reduction measurements on superhydrophobic spheres. *Applied Physics Letters*, 94(6):064104, 2009.

[6] N Mordant and J-F Pinton. Velocity measurement of a settling sphere. *The European Physical Journal B-Condensed Matter and Complex Systems*, 18(2):343–352, 2000.

[7] M Raffel, C Willert, S Wereley, and J Kompenhans. Particle image velocimetry. experimental fluid mechanics. *Springer, Berlin. doi*, 10(1007):978–3, 2007.

[8] M Rivero, J Magnaudet, J Fabre, et al. Quelques résultats nouveaux concernant les forces exercées sur une inclusion sphérique par un écoulement accéléré. *CR Acad. Sci. Paris*, 312:1499–1506, 1991.

**Joint ERCOFTAC/EU-CTFF**
**European Drag Reduction and Flow Control Meeting – EDRFCM 2022**
**September 6$^{\text{th}}$–9$^{\text{th}}$, 2022, Paris, France**

# EXPLORATION STRATEGIES FOR CONTROL OF CHAOTIC DYNAMICAL SYSTEMS USING REINFORCEMENT LEARNING

**Rémy Hosseinkhan Boucher**
LISN, CNRS, University Paris-Saclay, 91400 Orsay, France

**Amine Saibi**
JR-D'Alembert, UPMC–Sorbonne Université, 75005 Paris, France
LISN, CNRS, University Paris-Saclay, 91400 Orsay, France

**Michele Alessandro Bucci**
TAU–Team, INRIA Saclay, LISN, Université Paris-Saclay, 91400 Orsay, France

**Onofrio Semeraro**
LISN, CNRS, University Paris-Saclay, 91400 Orsay, France

**Lionel Mathelin**
LISN, CNRS, University Paris-Saclay, 91400 Orsay, France

Numerous research efforts have been devoted to the application of control theory to fluid flows in the last decades. Common approaches consist of reduced order models of the original system, often within the linear limit, for enabling the control design based on standard control theory. However, these approximated representations are often the main limitation of standard applications, as these control techniques usually exhibit poor performance when applied in off-control design conditions; an example is provided by the impact that non-linearities have on the dynamics of the closed-loop when neglected [9].

## REINFORCEMENT LEARNING

An alternative is represented by fully data-driven methods where a physical model is not employed; Reinforcement Learning (RL) algorithms allow such a strategy while preserving optimality of the control solutions. Indeed, some RL algorithms can be regarded as a fully data-driven counterpart of the discrete-in-time optimal control strategies based on the Bellman equation, where the policy – i.e., the control action – is directly learnt from interactions of the system with the environment without relying on an a-priori physical model [10]. The relevance of a control action when the system is in a given state is measured by a reward and the expected cumulative rewards (or Value function) is the objective to be maximized. When neural networks are employed as an approximation format, the framework is referred to as deep RL (DRL). Recent works show the feasibility of the approach for the control of instabilities classically found in fluid mechanics systems [7, 2, 6].

## IMPROVING LEARNING BY IMPROVING THE EXPLORATION

The methods we consider here are fully data-driven, without prior knowledge of a model. This implies that the modelling step is now replaced by the so-called *exploration.* Since the dimension of the phase space of the system under consideration is very large with respect to traditional tasks in Reinforcement Learning, the data efficiency of state-of-the-art methods such as Proximal Policy Optimization [8] and Deep Deterministic Policy Gradient [5] must be improved.

As an illustration in this work, we will consider the system governed by the Kuramoto-Sivashinsky (KS) equations. This system is described by a partial differential equation with initial value and spatial periodicity conditions:

$$\frac{\partial u}{\partial t}(t,x) = -u(t,x)\frac{\partial u}{\partial x}(t,x) - \frac{\partial^2 u}{\partial x^2}(t,x) - \frac{\partial^4 u}{\partial x^4}(t,x), \qquad (1)$$

with an initial condition $u(0,x)$, and periodicity in space $u(t,x+M) = u(t,x)$ given a length of the domain $M \in \mathbb{R}_+$. This 1-D dynamical system exhibits a chaotic behavior for a range of values of $M$ and is often used as a convenient proxy of turbulent flow regimes. As such, it has recently been used as a practical tool to evaluate the robustness of machine learning methods. Properties of the KS system as discussed in detail in [4]. As an illustration, a controllable trajectory in the chaotic regime is depicted in Fig. 1. In a previous work [3], we have shown that using the Deep Deterministic Policy Gradient (DDPG) algorithm allows to stabilize these chaotic trajectories; Fig. 2 shows an illustration of the method. More precisely, the controller task is to drive the trajectory of the chosen dynamical system to transit from one system equilibrium to an other one by accumulating statistical knowledge of the solution space (environment). The resulting policies were however far from being the optimal ones discussed in [1]. In this contribution, we hence intend to understand and identify the multiple factors and their influence on the policy identification, with a quantitative scope, but without relying on physics constraints or prior knowledge. In particular, we develop consistent exploration strategies which allow to carefully sample new observations, based on the previous ones, in order to achieve the knowledge of the system to be controlled. As a result, better control policies – in principle, the optimal ones – could be obtained with a lower amount of interactions with the system. From this perspective, we rely on *information theory* and *optimal design of experiments* to quantify the knowledge the controller gathers during the process.

We will compare the control policies achieved with the different strategies, and contrast them with the standard linear solutions. More generally, the final goal is to improve the use of data-driven and statistical learning for computational fluid dynamics, and specifically reinforcement learning. This approach, at the crossing between machine learning and dynamical systems, can also be of help to the streaming learning community to gather insights for explaining and understanding behaviour of data-based modelling.

## REFERENCES

[1] A. Armaou and P. D. Christofides. Feedback control of the kuramoto–sivashinsky equation. *Physica D: Nonlinear Phenomena*, 137(1-2):49–61, 2000.

[2] G. Beintema, A. Corbetta, L. Biferale, and F. Toschi. Controlling rayleigh–bénard convection via reinforcement learning. *Journal of Turbulence*, 21(9-10):585–605, 2020.

[3] M. A. Bucci, O. Semeraro, A. Allauzen, G. Wisniewski, L. Cordier, and L. Mathelin. Control of chaotic systems by deep reinforcement learning. *Proceedings of the Royal Society A: Mathematical, Physical and Engineering Sciences*, pages 278–285, 2019.

[4] P. Cvitanović, R. L. Davidchack, and E. Siminos. On the state space geometry of the kuramoto–sivashinsky flow in a periodic domain. *SIAM Journal on Applied Dynamical Systems*, 9:1–33, 2010.

[5] T. P. Lillicrap, J. J. Hunt, A. Pritzel, N. Heess, T. Erez, Y. Tassa, D. Silver, and D. Wierstra. Continuous control with deep reinforcement learning. 2015.

[6] R. Paris, S. Beneddine, and J. Dandois. Robust flow control and optimal sensor placement using deep reinforcement learning. *Journal of Fluid Mechanics*, 913, 2021.

[7] J. Rabault, M. Kuchta, A. Jensen, U. Réglade, and N. Cerardi. Artificial neural networks trained through deep reinforcement learning discover control strategies for active flow control. *Journal of Fluid Mechanics*, 865:281–302, 2019.

[8] J. Schulman, F. Wolski, P. Dhariwal, A. Radford, and O. Klimov. Proximal policy optimization algorithms. 2017.

[9] D. Sipp and P. J. Schmid. Linear Closed-Loop Control of Fluid Instabilities and Noise-Induced Perturbations: A Review of Approaches and Tools. *Applied Mechanics Reviews*, 68, 2016.

[10] R. S. Sutton and A. G. Barto. *Reinforcement Learning: An Introduction*. The MIT Press, 2018.

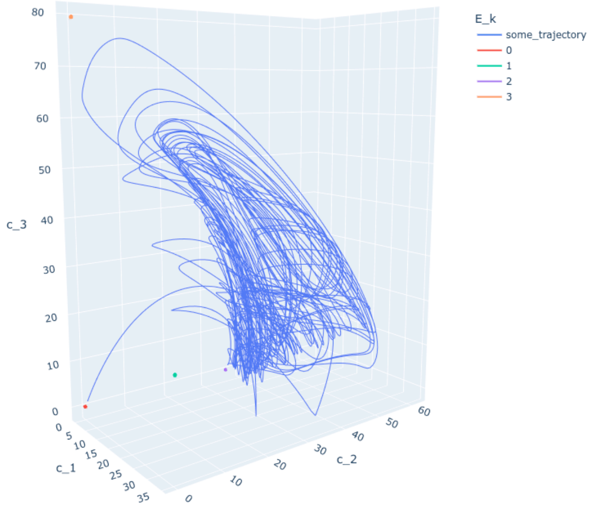

Figure 1: A sampled chaotic trajectory emanating from the neighbourhood of the equilibrium $u = 0$ of the Kuramoto-Sivashinsky equation under chaotic regime ($M = 22$); the visualization is obtained by projecting on the first 3 Fourier modes. The 3 non-trivial equilibria (stationary solutions) are also shown.

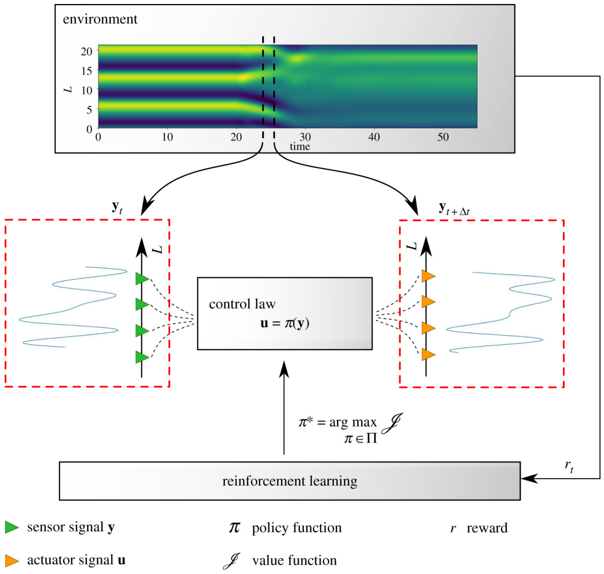

Figure 2: Reinforcement Learning scheme: from an initial state, the control law applies a forcing to the state of the dynamical system. Given this forcing action (or control) and the new state, a reward is obtained. An optimal reinforcement learning policy is a set of control decisions which maximises the asymptotical sum of rewards. In this case, a reward or cost could be the energy of the system. Taken from [3].

**Joint ERCOFTAC/EU-CTFF**
**European Drag Reduction and Flow Control Meeting – EDRFCM 2022**
**September 6$^{th}$–9$^{th}$, 2022, Paris, France**

# FLOW CONTROL FOR BLUFF BODY DRAG REDUCTION USING REINFORCEMENT LEARNING WITH PARTIAL MEASUREMENTS

**Chengwei Xia*   Georgios Rigas†   Eric C. Kerrigan‡**

**This work focuses on a practical active flow control (AFC) problem using reinforcement learning (RL) with partial measurements (PM). The control objective is to minimize the mean drag of the flow past a 2D rectangular cylinder. For PM, sensors are placed on the rear surface of the cylinder. Performance degradation of 39.61% (with respect to the maximum drag reduction) is observed in the PM configuration compared to the case with full measurements (FM), where sensors are placed in the wake. A recurrent neural network (RNN) is then used, which improves the drag reduction by 9.34%, compared to the feedforward neural network (FNN). The performance is further improved by symmetry reduction and the drag can be reduced by 57.53% in PM case, but there is still a gap between PM and FM performance.**

## INTRODUCTION

Data-driven control by reinforcement learning (RL) has been successfully employed for drag reduction by attenuating the vortex shedding in the wake of bluff bodies [4, 3]. In most of the past studies, the RL agent (controller) utilises information from the entire flowfield (full state). However, in practical applications, measurements are typically restricted to the surface of the bluff body, which leads to considerable performance degradation. This work contributes to improving the performance of the RL controller in PM environments.

When only partial state measurements are available, the RL framework can be described as Partially Observable Markov Decision Process (POMDP), instead of a general Markov Decision Process (MDP). It has been shown that RNN outperforms FNN in many POMDP problems, such as [1]. The underlying mechanism is that recurrence implicitly improves the state estimation, on the basis of Takens' embedding theorem [7]. Therefore, RNN is applied to RL in the flow control problem. Moreover, a symmetry reduction [8] that takes into account the symmetry properties of the vortex shedding is employed, resulting to further drag reduction in PM environments.

## METHODOLOGY

The RL framework used in this study consists of two parts: a flow simulation environment and an RL agent where the learning process and the controller are embedded. The flow environment for the RL agent to collect experience is provided by the flow solver FEniCS and the Dolfin library, using the implementation in [4, 5]. The sketch of the environment and instantaneous snapshots of the uncontrolled and controlled flow are shown in figure 1. Pressure sensors are placed on the base of the body in the PM configuration. Two jets with blowing and suction are used as actuators. The Reynolds number is $Re = 100$, based on the width of the body and the freestream velocity.

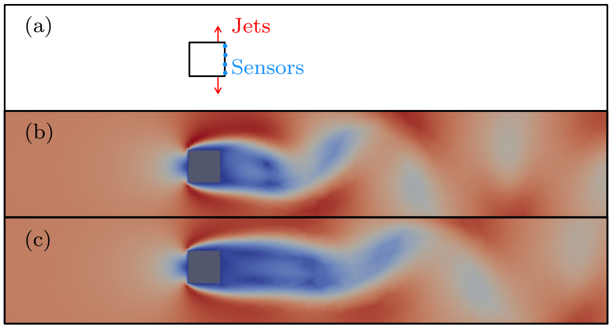

Figure 1: (a) The sketch of flow environment. 4 pressure sensors are visualized at the base of the cylinder. (b) Flowfield without control. (c) Flowfield with control in PM case.

In RL, the actions $a_t$ are the mass flow rates of the two jets, and observations $o_t$ are the pressure measurements. The reward $r_t$ is defined as

$$r_t = -\langle C_D \rangle_T - 0.2 \left| \langle C_L \rangle_T \right| , \tag{1}$$

where $C_D$ is drag coefficient and $C_L$ is lift coefficient. $\langle\ \rangle_T$ denotes time average. The RL agent is implemented in TensorForce [2], and the proximal policy optimization algorithm (PPO) [6] is used for the agent. Gated recurrent units (GRU) are used in the RL agent as RNN.

## RESULTS

The measurement $o(t)$ at time $t$ of the plain PM cases is defined as

$$o(t) = \{p_i(t)\} , \tag{2}$$

where $i = 1, 2, ..., N$ and $p_i(t)$ is the pressure measurement from the $i^{th}$ sensor, and $N$ is the total number of the sensors. In this study, $N = 64$ is used. The location of the $i^{th}$ sensor is defined as

$$loc_i = \left\{ x_{base}, y_{top} - \frac{iB}{(N+1)} \right\} , \tag{3}$$

where $x_{base}$ is the $x$ coordinate of cylinder base and $y_{top}$ is the $y$ coordinate of the cylinder top surface. $B$ is the width of the cylinder orthogonal to the flow direction.

For symmetry reduction, the inputs to the RL agent correspond to the antisymmetric pressure component of the base

---

[*] Department of Aeronautics, Imperial College London, SW7 2AZ London, UK

[†] Department of Aeronautics, Imperial College London, SW7 2AZ London, UK

[‡] Department of Electrical and Electronic Engineering, Imperial College London, SW7 2AZ London, UK

defined as the difference between measurements at symmetric sensor locations. Notice that any signal can be decomposed into symmetric and antisymmetric components, with the latter serving as a proxy of the antisymmetric vortex shedding in the wake. The measurement $o_{sr}(t)$ at time $t$ of the symmetry reduction PM cases is defined as (5)

$$o_{sr}(t) = \{(p_i(t) - p_{N+1-i}(t))\}\,, \tag{4}$$

where $i = 1, 2, ..., \frac{N}{2}$. Therefore, the number of inputs is reduced to half compared to the plain PM case.

The lift force measurement, $o_l(t)$, is also investigated as a single observation signal. Also, a time-delay embedding is introduced to leverage past lift observations:

$$o_l(t) = \{C_L(t - j\tau)\}\,, \tag{5}$$

where $j = 0, 1, ..., n$ and $\tau$ is time step. $n = 8$ is used as the number of past measurements included in the inputs.

The learning curve of the return is presented in figure 2. The return is a weighted summation of rewards and the purpose of RL is to maximize the return. A large performance drop can be noticed from FM case to PM case using FNN. The use of RNN in the PM case leads to higher return. In the symmetry reduction case, less fluctuations can be observed from the curve, which indicates that learning is assisted. In the lift measurement case, the growth of the return is faster and convergence is achieved within fewer training episodes.

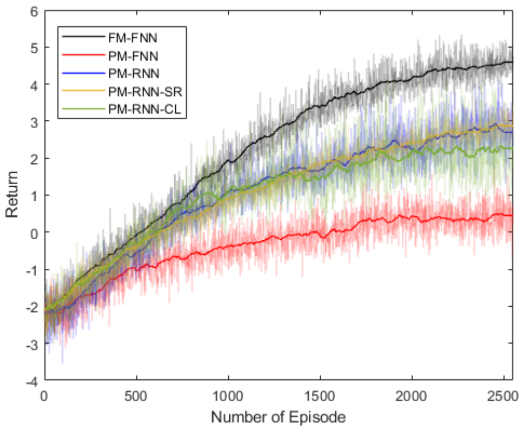

Figure 2: Learning curve of return in both FM and PM cases. In the legends, “SR” denotes “Symmetry Reduction” and “CL” denotes lift measurements. The solid line is the rolling average of return.

After the convergence of the learning stage, the controller (actor) is applied to the same environment to test its performance. The control results of $C_D$ are shown in figure 3. The control performance of drag reduction is quantified as

$$R_{C_D} = \frac{\left\langle C_{D_U} \right\rangle_T - \left\langle C_{D_C} \right\rangle_T}{\left\langle C_{D_U} \right\rangle_T - \left\langle C_{D_B} \right\rangle_T}, \tag{6}$$

where $C_{D_U}$ , $C_{D_C}$ and $C_{D_B}$ are the drag coefficients of the uncontrolled flow, controlled flow and base flow without vortex shedding, respectively. The time average values are obtained from the last 50 non-dimensional time in the steady stage of the control implementations. The $R_{C_D}$ values are given in table 1.

Table 1: Drag reduction ratio $R_{C_D}$ for different PM cases.

| Case | FNN | RNN | RNN-SR | RNN-CL |
|---|---|---|---|---|
| $R_{C_D}(\%)$ | 43.09 | 52.43 | 57.53 | 51.94 |

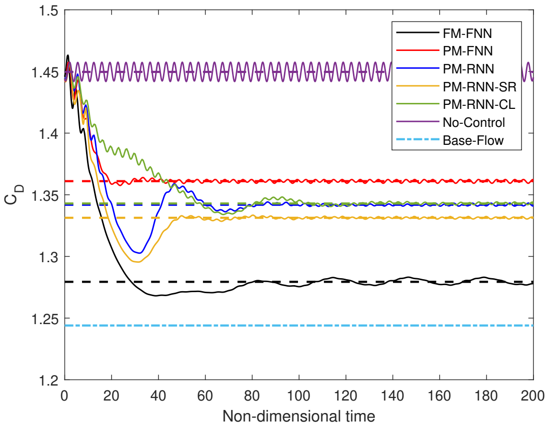

Figure 3: Control results of drag coefficient $C_D$ in both FM and PM cases. Dashed line represents the average $C_D$ in the last 50 time units.

## CONCLUSIONS AND FUTURE WORKS

In this work, we have proposed two strategies to improve the performance of RL control for bluff body drag reduction in partial measurement environments. First, RNN outperforms FNN in PM environments. Second, further performance improvement is achieved by taking into account the antisymmetry of the instability (vortex shedding) through symmetry reduction techniques. Although the final results in PM cases are still sub-optimal compared to FM, a considerable drag reduction of 57.53% is achieved. The underlying mechanism and performance degradation in PM environments need further investigation.

## REFERENCES

[1] M. Hausknecht and P. Stone. In *AAAI 2015 fall symposium series*, 2015.

[2] A. Kuhnle, M. Schaarschmidt, and K. Fricke. Web page, 2017.

[3] R. Paris, S. Beneddine, and J. Dandois. *Journal of Fluid Mechanics*, 913, 2021.

[4] J. Rabault, M. Kuchta, A. Jensen, U. Reglade, and N. Cerardi. *Journal of Fluid Mechanics*, 865:281–302, 2019.

[5] J. Rabault and A. Kuhnle. *Physics of Fluids*, 31(9):094105 (9 pp.), 2019.

[6] J. Schulman, F. Wolski, P. Dhariwal, A. Radford, and O. Klimov. *arXiv:1707.06347 [cs]*, 2017.

[7] F. Takens. In *Dynamical systems and turbulence*, pages 366–381. Springer, 1981.

[8] K. Zeng and M. D. Graham. *Physical Review E*, 104(1):014210, 2021.

**Joint ERCOFTAC/EU-CTFF**
**European Drag Reduction and Flow Control Meeting – EDRFCM 2022**
**September 6th–9th, 2022, Paris, France**

# LARGE-SCALE OPPOSITION FLOW CONTROL OF THE LOGARITHMIC LAYER

**A. Guseva**
Department of Applied Mathematics, University of Leeds, LS2 9JT Leeds, UK

**J. Jiménez**
The School of Aeronautical and Space Engineering, Universidad Politécnica de Madrid, 28040 Madrid, Spain

## INTRODUCTION

Control of turbulence in wall-bounded fluid flows is an important challenge in fluid dynamics; industrial devices where such flows appear can benefit from resulting drag reduction or increase in mixing. One of the most successful control strategies is to interfere with the near-wall turbulent cycle, suppressing the formation of streamwise vortices close to the wall. This strategy can be implemented by modifying the wall shape with riblets [3], by applying spanwise oscillations to channel walls [5], or via opposition flow control [1]. The opposition flow control is an active control strategy that modifies the wall-bounded flow by blowing and suction at the wall. Its conventional setup consists of measuring wall-normal velocity in the buffer layer of the near-wall turbulence ($y^+ \sim 10$) and opposing it at the wall, with a feedback between detection and actuation. Physically, this control method inhibits the vertical transport of streamwise momentum and weakens the linear coupling between wall-normal velocity and vorticity near the wall, resulting in up to 20% of friction drag reduction.

However, implementing opposition flow control of [1] in a real experimental setup is difficult, and so far, has been implemented in the form of a single pairs of sensors and actuators [6]. The main challenge here is that the lifetimes of the eddies in the buffer layer in real-world applications are of order of milliseconds, and therefore too fast compared to the resolution restrictions of sensors and actuators. Instead of targeting the buffer layer, it is more practically achievable to modify the flow structures in the logarithmic layer where the time scales of the most energetic eddies are slower ($\sim s$). However, since the flow sensors are likely to be located at the wall in this control method, only limited information about the flow velocity in the logarithmic layer will be available. Only large attached structures creating a footprint on the wall can be reliably reconstructed from the wall measurements, and their size increases with the distance from the wall [2]. In this work, we study the influence of opposition flow control on these large-scale eddies in the logarithmic layer.

## NUMERICAL MODEL

We set the detection plane for opposition flow control further away from the wall, in the logarithmic layer ($y^+ \sim 100$), where control could be feasible experimentally. We apply the control on a fully turbulent, numerically modelled channel flow at $Re_\tau = 932$, and only on the eddies with relatively large wave lengths ($\lambda/h > 0.1$) in both streamwise and spanwise directions. Detection and actuation is performed on wall-normal velocity, and implemented in Fourier space on the modes with wave numbers $k_{x,z}$ corresponding to these length scales. The control is introduced as a relation between their Fourier coefficients at the wall and the detection plane, $\hat{v}_w = -A\hat{v}_d$. The complex control coefficient $A$ has two parameters: the control gain $|A|$ and the control phase $\varphi \in [-\pi, \pi]$. The latter can be interpreted as a streamwise shift between detection and acturation, $\varphi = -k_x x_0$. When $\varphi > 0$, the control actuation is shifted upstream and is lagging with respect to detection; when $\varphi < 0$, the actuation is shifted downstream, and is advancing detection. To explain our findings from the direct numerical simulations (DNS), we also develop a linear model of the controlled turbulent channel flow which is linearized about the turbulent mean profile. We considered both inviscid linear model and the model including turbulent viscosity. More details about our numerical setup can be found in [4].

## RESULTS

The DNS results indicate that large-scale opposition control creates a minimum in the intensity of the wall-normal velocity between the detection plane and the wall, so an imperfect "virtual-wall" effect is established. Nevertheless the momentum transfer is never fully inhibited. The control induces a large response in the streamwise velocity in the buffer layer (see figure 2), compared to the normal streaky structure of the uncontrolled turbulent flow at this location (figure 1). It is also accompanied by the enhancement of Reynolds stresses near the wall, with a substantial friction drag increase. If the actuation is shifted downstream with respect to the detection, the drag increases moderately, and is up to 50% larger compared to the uncontrolled flow. If the actuation is shifted upstream, however, this increase can be up to 4 times larger than in the uncontrolled case. In both cases, the structure of the near-wall turbulence is significantly modified. Oblique waves are observed in the flow controlled with downstream shifts, and spanwise-homogeneous rollers in the case of upstream shifts. Our linearized model of the turbulent channel flow can predict these flow structures and relate to them increase in friction [4]. We found that the turbulent mean flow profile is linearly unstable when $\phi > 0$ in the inviscid controlled channel flow, and all wave lengths are affected by this instability, albeit at different $|A|$. Its growth rates increase as the phase of control approaches $\pi$, i.e. perfect reinforcement instead of opposition, and we interpret this instability as an unstable feedback loop. When turbulent viscosity is introduced into analysis, the growth rates of the most unstable wave numbers correlate well with the drag increase in the DNS. As the result of the linear instability, the altered steady-state flow features prominent spanwise rollers near the wall while remaining turbulent. When the control is shifted downstream, $\phi < 0$, the linear instability is inactive; yet the wall-normal shape of the velocity spectra is captured reasonably well by the most amplified resolvent responses of the linearized Navier-Stokes operator. Periodicity of $A$ with respect to $\varphi$ and $x_0$ implies that the regions of stability and instability are repeated periodically for each streamwise wave mode $k_x$ as the control is moved further upstream or downstream. Our results suggest executing caution in applying large-scale opposition control for drag reduction, especially with a lagging delay between sensors and actuators, equivalent to shifting control upstream. However, the linearity, governing the controlled flow, opens a possibility to affect its large scales in a controlled manner when enhanced turbulence intensity is desired.

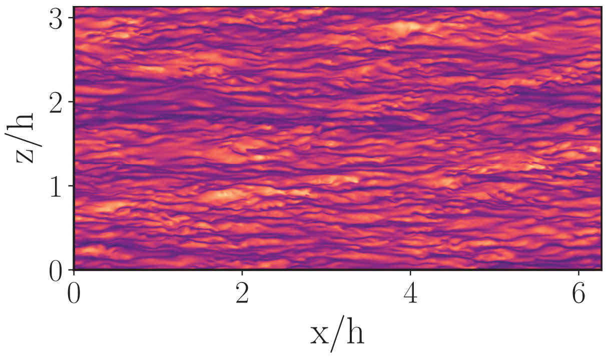

Figure 1: Near-wall turbulent structures in the uncontrolled flow. An instantateous snapshot of streamwise velocity fluctuations in the buffer layer of the channel flow, $y^+ = 10$.

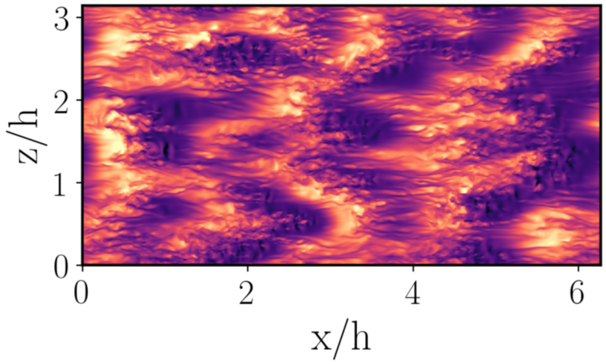

Figure 2: The effect of the large-scale opposition flow control on the streamwise velocity fluctuations in the buffer layer, $y^+ = 10$.

## REFERENCES

[1] H. Choi, P. Moin, and J. Kim. Active turbulence control for drag reduction in wall-bounded flows. *Journal of Fluid Mechanics*, 262:75–110, 1994.

[2] M. P Encinar and J. Jiménez. Logarithmic-layer turbulence: A view from the wall. *Physical Review Fluids*, 4(11):114603, 2019.

[3] R. Garcia-Mayoral and J. Jiménez. Drag reduction by riblets. *Philosophical transactions of the Royal society A: Mathematical, physical and engineering Sciences*, 369(1940):1412–1427, 2011.

[4] A. Guseva and J. Jiménez. Linear instability and resonance effects in large-scale opposition flow control. *Journal of Fluid Mechanics*, 935, 2022.

[5] I. Marusic, D. Chandran, A. Rouhi, M. K Fu, D. Wine, B. Holloway, D. Chung, and A. J Smits. An energy-efficient pathway to turbulent drag reduction. *Nature communications*, 12(1):1–8, 2021.

[6] H. Rebbeck and K. Choi. A wind-tunnel experiment on real-time opposition control of turbulence. *Physics of Fluids*, 18(3):035103, 2006.

**Joint ERCOFTAC/EU-CTFF**
**European Drag Reduction and Flow Control Meeting – EDRFCM 2022**
**September 6th–9th, 2022, Paris, France**

# DEEP REINFORCEMENT LEARNING FOR BLUFF BODY WAKE CONTROL

**E. Amico**,**G. Cafiero**,**G. Iuso**
Dipartimento di Ingegneria Meccanica ed Aerospaziale, Politecnico di Torino, 10129, Torino

## INTRODUCTION

DRL (Deep Reinforcement Learning) framework is used to control the wake of a model (scale 1:10) of a square back vehicle in order to reduce the aerodynamic drag. Control is achieved by jets of compressed air placed at the edges of the rear of the model. The aim of this work is to extend the excellent results obtained on this topic [1, 2, 3] paving the way towards implementations for greater potential application in the automotive field. The results obtained demonstrate the agent's ability to discover efficient forcing conditions that reduce the aerodynamic drag of the vehicle by values as large as 10%.

## EXPERIMENTAL SETUP

The experiments are carried out in the open-circuit wind tunnel at Politecnico di Torino. A diagram of the experimental setup is shown in figure 1. The model is instrumented to measure static pressure using multi-input pressure transducers (for measuring static pressure) and microphone capsules for measuring pressure fluctuation. The drag measurement is performed using a one-axis load cell Dacell UU-K002 with a full scale of $2Kgf$ and an accuracy of 0.002% of the full scale. The sampling parameters are summarised in the table 1.

| | Frequency [Hz] | Time [s] |
|---|---|---|
| Load Cell | 2000 | 20 |
| Microphones | 2000 | 20 |
| Static Pressure | 50 | 20 |

Table 1: Acquisition parameters.

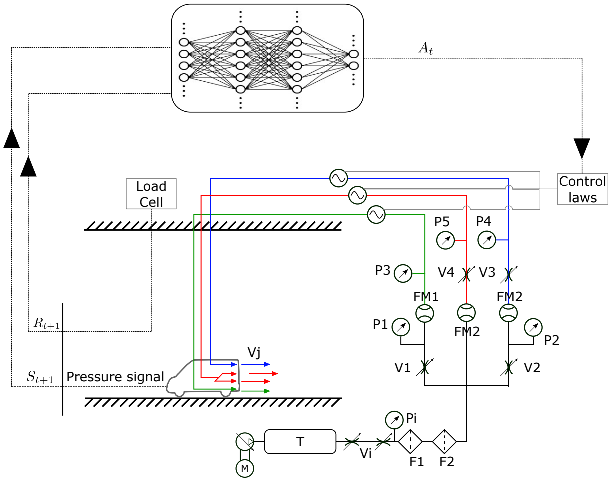

Figure 1: Implementation scheme of the DRL algorithm.

## DEEP REINFORCEMENT LEARNING ENVIRONMENT

Deep Reinforcement Learning belongs to the family of machine learning algorithms. An agent, typically modeled with an artificial neural network (ANN), by interacting (exchanging information) with an environment is able to learn the optimal control law. A schematic representation of the interaction existing between the environment and the algorithm is reported in figure 1.
The agent can acts through actions $a$ on the environment, which can be described by the state or observation $s$. These cause a change in the environment and, through the reward $r$, it is possible to assess the performance of the agent.

The Tensorforce library [4] was used to implement the algorithm and the Tensorforce agent was selected.

For the state, the 29 static pressure signals that populate the base of the model and normalised according to equation 1 were used.

$$Cp = \frac{\overline{p} - \overline{p}_\infty}{0.5 \cdot \rho \cdot V_\infty^2} \tag{1}$$

The reward was defined as $r = Cd_0 - Cd$, where $Cd_0$ indicates the drag coefficient as measured without forcing and $Cd$ the drag coefficient under the generic action $a$.

Actions are the means used by the agent to modify the environment, so the state. In this case, actions are the parameters of the control law that need to be optimised. A sinusoidal control law was chosen, yielding three amplitudes and three frequencies as the output of the DRL.

## RESULTS

All tests are conducted at $Re = \frac{U_\infty \cdot L_{ref}}{\nu} \sim 10^5$, with $L_{ref} = 0.1850m$ being the average of the cross-section dimensions of the model base.

A maximum number of timesteps is set to 15 and the number of episodes is equal to 50.

Figure 2 shows the path followed by the reward as a function of the episodes. In particular, the maximum, mean and minimum value of the reward obtained at each episodes (i.e. across the 15 events) is reported. It is clear how the agent learns a strategy to minimize the aerodynamic drag within about 40 episodes, corresponding to an experimental time of about 8 hours.

The corresponding value of the percentage drag reduction is reported in figure 3. The agent, during the training phase, is capable of attaining values of the drag reduction as large as 10%.

The evaluation of the performance of the agent is generally carried out on an independent test. During the evaluation the network is not updated and the ability to explore is deleted. In figure 4 the first timestep corresponds to the natural condition, from the second onward the agent controls the wake. A reduction of $Cd$ of about 10% is observed also in the evaluation.

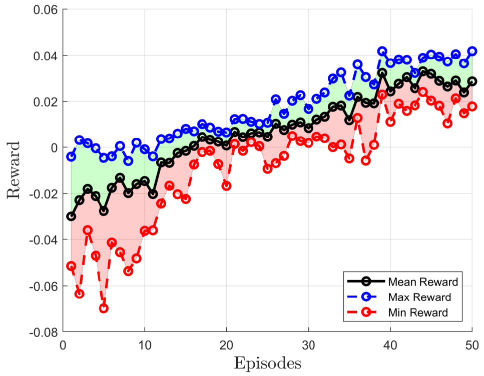

Figure 2: Agent reward as a function of the episodes.

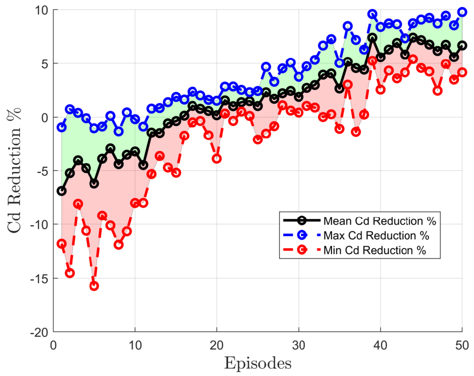

Figure 3: Percentage drag reduction as a function of the episodes.

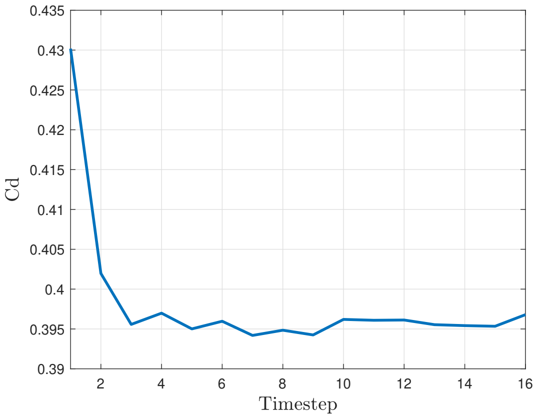

Figure 4: Evaluation trained agent.

In order to assess the effect of the action of the agent on the structure of the wake, the comparison of the $Cp$ distribution between the natural and the forced condition is reported in figure 5. It is shown that the controlled case attains a symmetric state of the wake as an effect of the forcing, in good agreement with previous investigations [5, 6].

It can be observed how the control acts in a way to minimize the pressure deficit in the wake, attaining an average value of the $\overline{Cp} = -0.063$, as opposed to the natural case, where the $\overline{Cp} = -0.145$. This suggests that the drag reduction can be primarily ascribed to the pressure recovery occurring in the model's near wake.

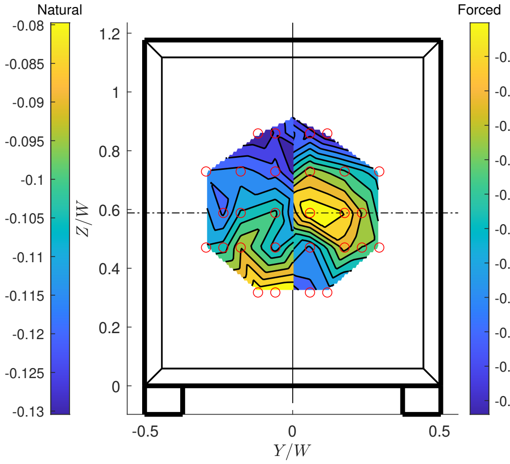

Figure 5: Cp distribution at the base of the model. On the left the natural condition, on the right the forced condition.

## REFERENCES

[1] Jean Rabault, Miroslav Kuchta, Atle Jensen, Ulysse Reglade, and Nicolas Cerardi. Artificial neural networks trained through deep reinforcement learning discover control strategies for active flow control. *Journal of Fluid Mechanics*, 865, 2019.

[2] Fabio Pino, Lorenzo Schena, Jean Rabault, Alexander Kuhnle, and Miguel A. Mendez. Comparative analysis of machine learning methods for active flow control, 2022.

[3] R. Castellanos, G. Y. Cornejo Maceda, I. de la Fuente, B. R. Noack, A. Ianiro, and S. Discetti. Machine-learning flow control with few sensor feedback and measurement noise. *Physics of Fluids*, 34(4):047118, 2022.

[4] Alexander Kuhnle, Michael Schaarschmidt, and Kai Fricke. Tensorforce: a tensorflow library for applied reinforcement learning. Web page, 2017.

[5] J.J. Cerutti, C. Sardu, G. Cafiero, and G. Iuso. Active flow control on a square-back road vehicle. *Fluids*, 5(2), 2020.

[6] L. Dalla Longa, Aimee S. Morgans, and Jeremy A. Dahan. Reducing the pressure drag of a d-shaped bluff body using linear feedback control. *Theoretical and Computational Fluid Dynamics*, 31:567–577, 2017.

**Joint ERCOFTAC/EU-CTFF**
**European Drag Reduction and Flow Control Meeting – EDRFCM 2022**
**September 6th–9th, 2022, Paris, France**

# MACHINE LEARNING CONTROL OF 2D FALLING LIQUID FILM

**F. Pino**
Dep. Environmental and Applied Fluid Dynamics, von Kármán Institute for Fluid Dynamics, Sint-Genesius-Rode, Belgium

**B. Scheid**
Transfers, Interfaces and Processes (TIPs) laboratory, Université libre de Bruxelles, Belgium

**M.A. Mendez**
Dep. Environmental and Applied Fluid Dynamics, von Kármán Institute for Fluid Dynamics, Sint-Genesius-Rode, Belgium

The ability to control disturbances in fluid systems is of great importance in many industrial processes. In a coating process called hot-dip galvanizing, the stabilization of a 2D falling liquid film instabilities would enable higher production rates and a wider range of operating conditions.

Common approaches to control these flows consists in combining linear stability analysis [7] or adjoint based optimization [2] with reduced order models (ROM) of the liquid film flow. Although very efficient, these approaches suffer model uncertainties and are limited by intrinsic assumptions and simplifications of the model used to derive the control law. Despite efforts in going beyond ROMs, bridging modelling with experiments [3], a reliable workflow circumventing model limitations is still missing.

Among different new approaches, machine learning methods emerged as a viable alternative, capable of efficiently treating the control problem as a black box (model-free) optimization problem. These approaches solely rely on input-output relations, based on action-reward-new state tuples. Machine learning based techniques have given proof of being a reliable solution in controlling representative flow control system of increasing complexity [5]. In addition, the heuristic nature of the algorithm ensures robust control actions for different system's dynamics [6]. However, in the domain of liquid film control, the application of these methods is limited to the stabilization of a simple 2D falling liquid film model [1].

In this work, we extend the use of these techniques applying various machine learning based control methods to the stabilization of 2D and 3D waves in a liquid film dragged by a moving substrate. The analysis includes Reinforcement Learning (RL), Genetic programming (GP) and Bayesian Optimization (BO) to control various sets of pneumatic actuators. The liquid film flow is modelled via a reduced order model that extends the Kapitza-Skhadov model [4], and the control performances are measured in terms of wave attenuation.

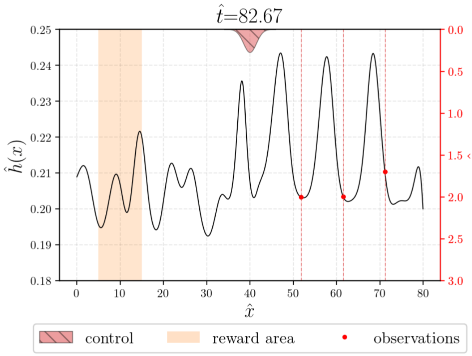

Figure 1: Perturbation evolution in a 1D ROM of a liquid film over a moving substrate (from right to left), attenuated by a controller (red Gaussian) which selects actions based on three observations (red dots) to have a flat liquid film in the reward area (orange shadowed area).

## REFERENCES

[1] Vincent Belus, Jean Rabault, Jonathan Viquerat, Zhizhao Che, Elie Hachem, and Ulysse Reglade. Exploiting locality and translational invariance to design effective deep reinforcement learning control of the 1-dimensional unstable falling liquid film. *AIP Advances*, 9(12):125014, 2019.

[2] E Boujo and M Sellier. Pancake making and surface coating: optimal control of a gravity-driven liquid film. *Physical Review Fluids*, 4(6):064802, 2019.

[3] Radu Cimpeanu, Susana N Gomes, and Demetrios T Papageorgiou. Active control of liquid film flows: beyond reduced-order models. *Nonlinear Dynamics*, 104(1):267–287, 2021.

[4] MA Mendez, Anne Gosset, Benoît Scheid, Mikhael Balabane, and J-M Buchlin. Dynamics of the jet wiping process via integral models. *Journal of Fluid Mechanics*, 911, 2021.

[5] Fabio Pino, Lorenzo Schena, Jean Rabault, Alexander Kuhnle, Miguel Mendez, et al. Comparative analysis of machine learning methods for active flow control. *arXiv preprint arXiv:2202.11664*, 2022.

[6] Hongwei Tang, Jean Rabault, Alexander Kuhnle, Yan Wang, and Tongguang Wang. Robust active flow control over a range of reynolds numbers using an artificial neural network trained through deep reinforcement learning. *Physics of Fluids*, 32(5):053605, 2020.

[7] Alice B Thompson, Susana N Gomes, Grigorios A Pavliotis, and Demetrios T Papageorgiou. Stabilising falling liquid film flows using feedback control. *Physics of Fluids*, 28(1):012107, 2016.

**Joint ERCOFTAC/EU-CTFF**
**European Drag Reduction and Flow Control Meeting – EDRFCM 2022**
**September 6th–9th, 2022, Paris, France**

# DESIGN EXPLORATION OF LOW DRAG NLF AND HLFC WINGS

**Anand Sudhi**
Institute of Fluid Mechanics, TU Braunschweig, 38108 Braunschweig, Germany

**Rolf Radespiel**
Institute of Fluid Mechanics,, TU Braunschweig, 38108 Braunschweig, Germany

**Camli Badrya**
Institute of Fluid Mechanics,, TU Braunschweig, 38108 Braunschweig, Germany

## INTRODUCTION

Rising fuel costs and adverse effects of $CO_2$, $NO_x$, and relevant emissions on climate change are driving the momentum towards sustainable climate-friendly aviation. The development of low drag and energy-efficient aircraft can pave the way to a zero-emission future using cleaner energy sources such as hydrogen and electric batteries. Presently, fuel costs constitute up to 33% of an airline's total operating cost (4). Crucial drag reduction can be achieved by reducing the skin friction drag. Almost all the operating mid and long-range airlines have a turbulent boundary layer which is responsible for 40%-50% of the total drag. Recent work by Beck et al. (1) concluded that an overall fuel burn reduction of 47% can be attained for a mid-range aircraft like Airbus A320 by drag reduction technologies such as Hybrid Laminar Flow Control (HLFC) which extend the laminar flow regions.

Flow transition to turbulent flow is dominated by Tollmien–Schlichting Instabilities (TSI) for wings with lower Sweeps. Natural Laminar Flow (NLF) can be maximized by delaying the onset on the adverse pressure gradient region while satisfying the design criteria (8). Further reduction of the profile drag can be achieved by extending the laminar flow using Boundary Layer Suction (BLS) in the adverse pressure gradient region (8), where BLS removes a small amount of low momentum flow near the wall to dampen the propagating instabilities and stabilize the boundary layer. However, at transonic speeds, designing a laminar wing at higher Reynolds numbers is challenging due to the premature flow transition from the prominent Cross Flow Instabilities (CFI) generated by the higher wing sweeps. Hence, Natural Laminar Flow (NLF) wings is limited to lower sweep angles. As CFI instabilites are dominant in an accelerating flow like the leading edge, transition can be mitigated by damping CFI using boundary layer suction near the leading edge and use airfoil shaping to further control the growth of TSI and CFI to maximize the laminar flow.

Coupled optimization of a 3D wing geometry with BLS using RANS based gradient based optimization is challenging due to the discontinuous nature of the objective function which requires a good start geometry to begin the optimization to evade local minima. Hence, 3D RANS optimization is not a good candidate for exploring the design space. In this context, the present work uses genetic algorithm, which is a gradient free method, to optimize the airfoil sections along the span using a fast 2D aerodynamic Euler solver. The method uses a diverse set of 200 initial airfoils from the UIUC airfoil database in order to effectively search the design space. In addition, the geometrical bounds on the optimization are relaxed to generate new airfoils that minimizes the objective function. The optimization toolchain that simultaneously optimizes the airfoil shape and leading edge suction distribution for maximum laminar flow is developed for a tapered swept wing by 2.75D conical flow assumption. The airfoil sections are optimized for various spanwise locations based on the spanwise lift distribution from conceptual design. The optimized wing is then analyzed using 3D RANS simulation to account for the 3D flow effects from the wing-fuselage section and wing tip and verify the extend of spanwise laminar flow predicted by the 2.75D approach.

## METHODOLOGY

A Fast and Elitist Multi-objective Genetic Algorithm based on evolutionary principles developed by Deb et al. (2) called "Non-dominated Sorting Genetic Algorithm" (NSGA II) was chosen as the optimizer for airfoil design. Constraints are applied using a penalty method to generate feasible airfoil shapes. Genetic algorithms tend to converge near the global minima, especially when the initial airfoils used to start the optimization has a good spread over the design space. In this study, 200 randomly chosen airfoils from the UIUC airfoil library with a good mix of transonic and subsonic airfoils are chosen for the initial population. Diversity in the initial population explores the design space effectively as new airfoils are generated from these airfoils via cross-over. A better convergence to a minima is observed when the competing drag components were used as objectives. The optimal solutions lie on the Pareto front from which the airfoil with minimum total drag is selected as the optimal design. Sample results of the optimization can be found in (9). Competing objectives help preserve diverse airfoil shapes in each generation and help evade local minima. The objectives are the following,

- **Objective 1:** Maximize the laminar region ($X_{\mathrm{LAM}}/c$)
- **Objective 2:** Minimize ($C_{dp} + C_{ds}$)

where $X_{\mathrm{LAM}}/c$ is the sum of the laminar flow length on the upper and lower surfaces and $C_{dp}$ is the pressure drag. The optimal airfoil with minimum total drag is extracted from the Pareto-optimal front solutions. Note that each objective represents a component of the total drag with $X_{\mathrm{LAM}}/c$ representing the friction drag. Hence, the competing components reliably explore the design space while maintaining diversity in each generation. The coefficient of ideal suction power, $C_{ds}$,

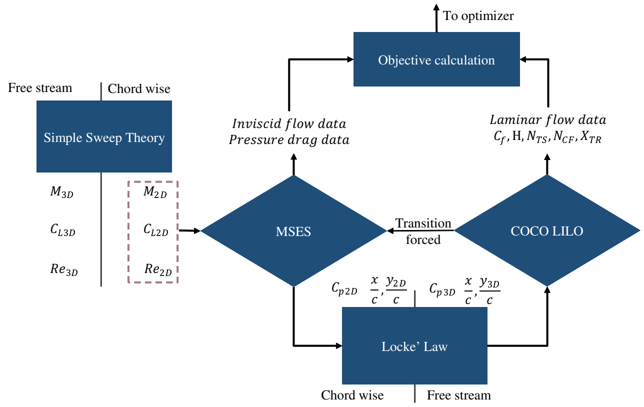

Figure 1: Coupling between MSES and COCO-LILO

is considered as a pressure drag (8). Since the effects of suction also affect the $X_{\mathrm{LAM}}/c$ as previously shown in a previous study (8), both objectives are coupled.

Flow calculations are performed using a fast 2D compressible Euler solver called MSES (3) and transition is predicted using higher fidelity Linear Stability Theory (LST). MSES is coupled with BL solver (COCO) (6), which solves the conical compressible boundary layer equations and local linear stability solver (LILO) (7), as shown in Fig. 1. Sweep-taper theory and Locke's equivalence law (5) are employed to transform between leading edge normal reference frame used in MSES and freestream reference frame using COCO using conical flow assumption (2.75D approach) . The freestream flow represented by a subscript 3D ($M_{3D}$, $Re_{3D}$, $C_{L3D}$) are transformed to a leading edge normal reference frame in the chord-wise direction denoted by subscript 2D ($M_{2D}$, $Re_{2D}$, $C_{L2D}$) as shown in Fig. 2. The calculated pressure distribution from MSES and the airfoil geometry is transformed back to the freestream reference frame by Locke's equivalence Law (5) and fed in to COCO-LILO. The transition predicted by LST is forced in MSES and the calculation is repeated until the pressure distribution and transition locations converge. Further details on the methodology can be found in (9) where airfoils sections were optimized for infinitely swept wings.

## PRELIMINARY RESULTS AND OBJECTIVES

A preliminary design study was conducted on a wing with 25m span with a leading edge sweep angle of 17° and taper ration of 0.25. Figure 2 shows the optimized span-wise airfoil sections adhering to the local lift distributions at their respective Reynolds number. A multi point optimization was performed to ensure off design performance(+/- 0.1) around the design $C_l$ as a single point optimization from the toolchain is often too well optimized for one design point. Suction was applied to span length of 15m after which an NLF airfoil is optimized. Figure 3 shows the sectional drag breakdown and the transition line along the span. Laminar flow is maintained till approximately 70% of the local chord on the upper surface when suction is active. Laminar flow on the lower surface improves from around 30% of the local chord near the root to 50% of the local chord as the local Reynolds number decreases, since CFI are stronger at higher Reynolds numbers. Corresponding reduced skin friction drag coefficient ( $2.5 \cdot 10^{-3}$) is also observed in Fig.3 along the span.

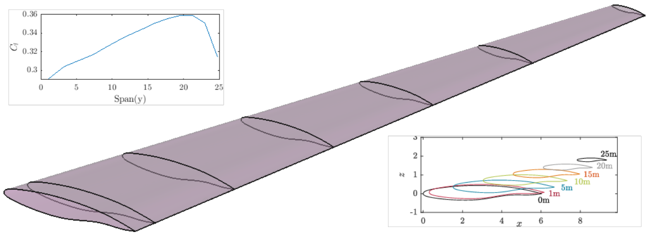

Figure 2: Wing geometry and airfoil sections

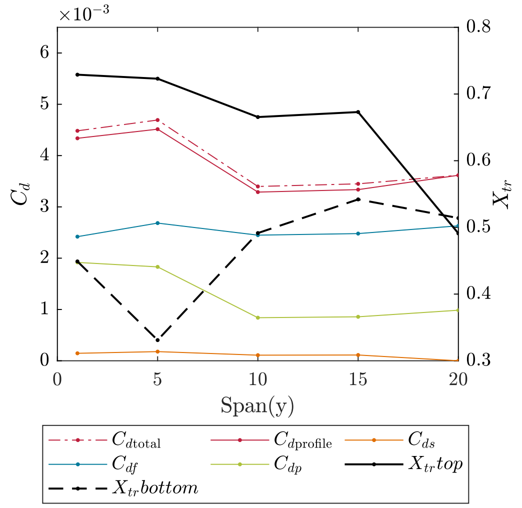

Figure 3: Drag breakdown of spanwise airfoils sections

### Proposed study objectives

1. Design optimal HLFC airfoil over ranges of Reynolds number, Mach number and design $C_l$.
2. Design a forward swept and backward swept HLFC wing using the 2.7dD sectional airfoil design approach
3. Verify the solutions using RANS computation using DLR TAU.

## REFERENCES

[1] Nils Beck, Tim Landa, Arne Seitz, Loek Boermans, Yaolong Liu, and Rolf Radespiel. *Energies*, 11(1), 2018.

[2] Kalyanmoy Deb, Amrit Pratap, Sameer Agarwal, TAMT Meyarivan, and A Fast. *IEEE transactions on evolutionary computation*, 6(2):182–197, 2002.

[3] Mark Drela. In *Aerospace Design Conference*, page 969, 1993.

[4] IATA. Products and Services Release: The Airline Industry Story for 2012, 2013.

[5] RC Lock. NPL, 1962.

[6] G Schrauf. *ZARM Technik report*, 1998.

[7] G Schrauf. *Bremen, Germany, GSSC Technical Report*, 6, 2006.

[8] Anand Sudhi, Ali Elham, and Camli Badrya. *AIAA Journal*, 59(12):5158–5173, 2021.

[9] Anand Sudhi, Rolf Radespiel, and Camli Badrya. In *AIAA AVIATION 2021 FORUM*, page 2606, 2021.

**Joint ERCOFTAC/EU-CTFF**
**European Drag Reduction and Flow Control Meeting – EDRFCM 2022**
**September 6th–9th, 2022, Paris, France**

# ON THE EFFECTS OF FILAMENTS INCLINATION ON CANOPY FLOWS

**S. Nicholas**
Department of Mechanical and Aeronautical Engineering, City, University of London, EC1V 0HB London, UK

**A. Monti**
Okinawa Institute of Science and Technology OIST, Okinawa 904-0495, Japan

**M. E. Rosti**
Okinawa Institute of Science and Technology OIST, Okinawa 904-0495, Japan

**M. Omidyeganeh**
Department of Mechanical and Aeronautical Engineering, City, University of London, EC1V 0HB London, UK

**A. Pinelli**
Department of Mechanical and Aeronautical Engineering, City, University of London, EC1V 0HB London, UK

## ABSTRACT

We have undertaken a series of numerical investigations to study the effect of the filaments inclination on a turbulent shear flows developing above a canopy. The latter is composed of rigid, cylindrical filaments, flush mounted onto the impermeable bottom wall of an open channel. The inclination angle of the canopy has been varied whilst maintaining a constant in-plane solid fraction $\Delta S/H = \pi/48$ and filament length ($h/H = 0.1$). In all the resulting configurations, it is indeed the inclination angle that dictates the solidity ($\lambda$) of the canopy, leading to the establishment of different flow regimes. The results unravel the behaviour of the different regimes induced by the interplay between the external flow structures, the intra-canopy flow and the inclined filaments.

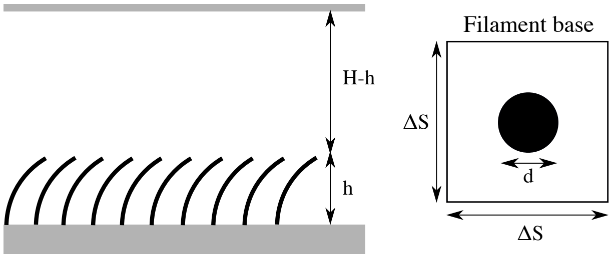

Figure 1: Geometrical parameters characterising an idealised canopy composed of cylindrical filaments [3], with $\Delta S$, $h_\perp$, $d$ and $H$ representing the mean filament spacing, height, diameter and open channel depth, respectively

## INTRODUCTION

Canopy flows are commonly found in our surroundings, from natural environments to man-made urban areas. Vegetative canopies in rivers present an interesting case, due to their significant role in complex processes including nutrient and light uptake, turbulent mixing and sediment transport [3]. Some animal species use ciliated or textured surfaces to reduce the skin and form drag when moving in water or air. Independently of the considered setting, the interactions of the filamentous layers with an external turbulent shear flow are generally classified into three regimes [3] depending on the value of the canopy solidity, i.e. the geometrical ratio between the frontal projected area and the bed area defined as $\lambda = ah$ where $a = d/\Delta S^2$ (see Figure 1). $\lambda$ is the parameter commonly used to discriminate between the appearance of the sparse ($\lambda < 0.1$) and dense ($\lambda > 0.1$) regimes. In between these two limiting regimes, there exists a transitional condition ($\lambda \simeq 0.15$) where both type of drags are important [2]. The elements embedded in the majority of the naturally occurring aquatic canopies or in swimming animals often assumes a streamlined posture that is oriented along the dominant flow direction (see Figure 1). The filaments configuration plays a key role in modulating the drag experienced by the outer flow by inducing a mutual sheltering between the inner canopy flow and the external one. In this condition, simple models used to describe the transitional regime [2] in straight canopies (i.e. when the filaments are perpendicular to the wall), may not applicable since the inclination may lead to a localised modulation of the wall normal permeability at the edge of the canopy layer.

| Case | $\theta$ | $h_\perp/H$ | $\lambda$ | $\Delta S/h_\perp$ | Symbol |
|---|---|---|---|---|---|
| NI | 0 | 0.1 | 0.56 | 0.66 | ▽ |
| WI | 33.5 | 0.085 | 0.48 | 0.77 | □ |
| MI | 48.25 | 0.07 | 0.39 | 0.94 | △ |
| RSI | 60 | 0.06 | 0.31 | 1.19 | + |
| SI | 77.5 | 0.03 | 0.17 | 2.18 | o |
| VSI | 90 | 0.02 | 0.08 | 6.55 | ⋆ |

Table 1: Considered configurations: NI - Negligible Inc., WI - Weak Inc., MI - Mild Inc., RSI - Relatively Strong Inc., SI - Strong Inc., VSI - Very Strong Inc.

## NUMERICAL TECHNIQUE

The numerical investigations are based on the solution of the incompressible Navier-Stokes equations, discretised in space with a second order, cell centred finite volume method and advanced in time by a semi-implicit, second order pressure correction scheme [2]. All canopy filaments are modelled as rigid solid cylinders, mounted on an impermeable wall and resolved with an immersed boundary method IBM. The canopy bed is uniformly partitioned into non overlapping square tiles with area $\Delta S^2$. Each individual tile hosts a single filament with its local position assigned by a random uniform distribution. More information of the IBM implementation and its extensive validation in the framework of canopy flows can be found in [2].

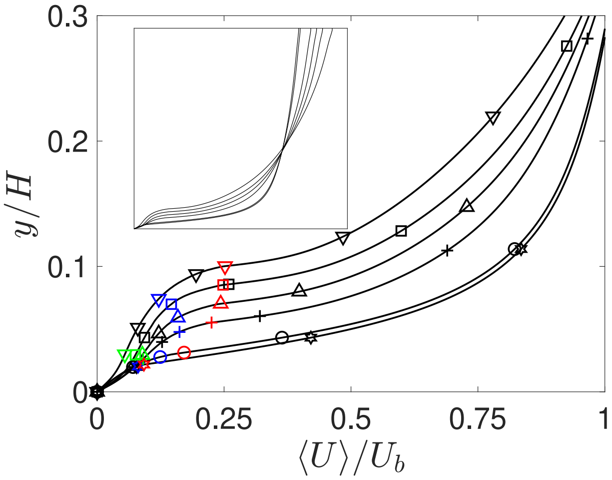

Figure 2: Mean velocity profile as a function of the wall normal distance. The red, blue and green symbols represent the mean locations of the external inflection point, outer flow virtual origin and the internal inflection point

## RESULTS

The distributions of the mean velocity profiles scaled in outer units (depth $H$ and bulk velocity $U_b$) at $Re_b = HU_b/\nu = 6000$ for all the cases detailed in table 1 are presented in Figure 2. The profiles exhibit a behaviour which strongly depend on the respective solidities, especially, in the intra canopy region. In particular, the velocity distributions present a concave shape which curvature appears to be controlled by $\theta$. In Figure 2, three important points of the mean velocity can be identified: i.e. the virtual origin of the outer flow and two inflection points (IP). The former can be interpreted as the virtual location ($y_{vo}$) of the wall seen by the outer turbulent boundary layer developing above the canopy and its location is computed enforcing the canonical shifted logarithmic boundary formulation on the outer layer mean velocity profile [2]. The outermost IP is induced by the discontinuity of the drag at the canopy tip, whilst the internal is a result of the merging of the mean flow developing by the wall with the velocity distribution underneath the canopy tip [2]. These particular points in the mean velocity profile allow to distinguish two layers in the intra-canopy flow: an inner layer, developing between the canopy bed and the inner inflection point; an outer layer spanning the region from the canopy-tip to the position of the virtual origin. While the origin for the internal layer corresponds to the canopy bed yielding the inner friction velocity based on the wall shear stress, the external layer is associated with the virtual origin, enabling the computation of an outer friction velocity based on the total stress at $y_{vo}$. The mean velocity distributions scaled with the two friction velocities are represented in Figure 2. The same figure also incorporates the profile obtained for a smooth wall open- channel turbulent flow considering the same nominal bulk Reynolds number. In the internal region, all the configurations reveals a good collapse with the smooth wall profile suggesting that the region in proximity of the canopy bed is dominated by the wall frictional drag, and does not depend on the canopy morphology. When moving away from the bottom impermeable wall, the effect of filament inclination is limited to the shift in the mean velocity distribution in the logarithmic region. This shift $\Delta U^+$ termed as the *drag change*, is a wall offset added to the the logarithmic law to characterise the momentum deficit/surplus induced by the wall texture. It can be seen that the $\Delta U^+$ value decreases monotonically as the inclination is increased. Thus, we can identify two regimes: drag reducing (SI and VSI configurations) and drag increasing (NI,WI, MI and RSI inclinations), i.e. when the drag offered by the canopy is either lower or higher than the skin frictional drag on a smooth wall. In the drag reducing regime, the velocity profiles (subplot of Figure 2) appear to be similar to the ones typical of a transitionally rough surface. It is noticed that $\theta = 90^o$ maximises the drag reducing property of the filamentous layer.

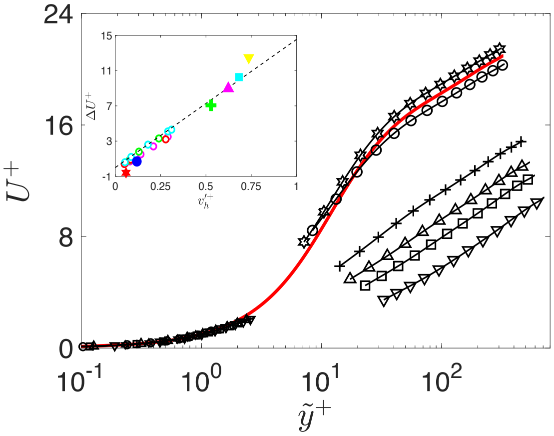

Figure 3: Mean velocity profile normalised with two friction velocities. Solid red line represents the smooth wall open turbulent channel flow. The subplot presents the drag change as a function of the transpiration intensity at the canopy edge. The *o* symbols are data from Abderrahaman *et al.* [1]

## CONCLUSIONS

We have carried out highly resolved simulations of turbulent flows over rigid filamentous canopies. The statistical characterisation of the flows reveals that the value of the inclination $\theta$ determines the inception of different flow regimes. These regimes are characterised by the locations of the inflectional points and the virtual origins of the mean velocity profile within the filamentous layer. While the low and the mildly inclined scenarios share certain features with the flows over canopies composed of perpendicular filaments, the SI and VSI configurations, obtained by an extreme inclination, feature a radically different behaviour. In particular, the SI and VSI configurations present a drag reducing property (as compared to a smooth wall) showing a behaviour similar to the one found for turbulent shear flows above transitionally rough surfaces and on certain anisotropic porous walls [4].

## REFERENCES

[1] N Abderrahaman-Elena, C T Fairhall, and R García-Mayoral. *Journal of Fluid Mechanics*, 865:1042–1071, 2019.

[2] A Monti, M Omidyeganeh, B Eckhardt, and A Pinelli. *Journal of Fluid Mechanics*, 891, 2020.

[3] Heidi M Nepf. *Annual review of fluid mechanics*, 44:123–142, 2012.

[4] M E Rosti, L Brandt, and A Pinelli. *Journal of Fluid Mechanics*, 842:381–394, 2018.

**Joint ERCOFTAC/EU-CTFF**
**European Drag Reduction and Flow Control Meeting – EDRFCM 2022**
**September 6th–9th, 2022, Paris, France**

# TURBULENCE OVER ANISOTROPIC POROUS SUBSTRATES: A HOMOGENIZATION-BASED STUDY

**E. N. Ahmed**
DICCA, Università degli Studi di Genova, 16145 Genova, Italy

**S. B. Naqvi**
DIME, Università degli Studi di Genova, 16145 Genova, Italy

**A. Bottaro**
DICCA, Università degli Studi di Genova, 16145 Genova, Italy

## INTRODUCTION

It has been reported by several researchers that adequately engineered permeable substrates can reduce drag in wall-bounded turbulent flows [1, 2] by interrupting the dynamically effective near-wall cycle involving the interaction of turbulent vortices and streaks [3]. In this work, a homogenization-based approach is employed to study turbulent channel flows with different porous substrates on one boundary, i.e. transverse or longitudinal cylindrical inclusions, to alleviate the computational requirements of feature-resolving direct numerical simulations; relevant applications are described in [4, 5].

## MODEL FORMULATION AND VALIDATION

The microscale problem within the porous media was first analyzed via asymptotic expansion of the microscopic variables in terms of a small parameter ($\epsilon$) representing the ratio between the length of a porous unit cell and half the channel height; effective boundary conditions are sought up to second-order accuracy at the virtual interface $Y = 0$ (see figure 1). The mathematical work proceeds along the lines of Naqvi and Bottaro [5]. The formal expressions of the dimensionless effective boundary conditions are

$$U(X,0,Z,t) = \epsilon\lambda_x S_{12} + \epsilon^2 \mathcal{K}_{12}^{itf} \frac{\partial S_{22}}{\partial X} + \mathcal{O}(\epsilon^3), \tag{1}$$

$$V(X,0,Z,t) = -\epsilon^2 (\mathcal{K}_{12}^{itf} \frac{\partial S_{12}}{\partial X} + \mathcal{K}_{32}^{itf} \frac{\partial S_{32}}{\partial Z}) + \epsilon^2 \mathcal{K}_{22} \frac{\partial S_{22}}{\partial Y} + \mathcal{O}(\epsilon^3), \tag{2}$$

$$W(X,0,Z,t) = \epsilon\lambda_z S_{32} + \epsilon^2 \mathcal{K}_{32}^{itf} \frac{\partial S_{22}}{\partial Z} + \mathcal{O}(\epsilon^3), \tag{3}$$

with $S_{12}$, $S_{22}$ and $S_{32}$ the normalized macroscopic components of the stress in streamwise, wall-normal and spanwise directions. The classical Navier-slip conditions for the streamwise ($U$) and spanwise ($W$) components of the velocity vector are modified at second order by corresponding gradients of the normal stress $S_{22}$. A normal (transpiration) velocity component ($V$) appears only at second order in $\epsilon$, reflecting the effect of surface permeability on near-wall turbulence. The homogenized coefficients of the model ($\lambda_x$, $\lambda_z$, $\mathcal{K}_{12}^{itf}$, $\mathcal{K}_{32}^{itf}$, $\mathcal{K}_{22}$) are dependent on geometry of the porous substrates and porosity ($\theta$), to be calculated via numerical solution of *ad hoc* auxiliary systems arising through analysis of the microscale problem.

To assess the accuracy of the effective conditions proposed in [5], the turbulent channel flow over a porous substrates composed by spanwise ($Z$-aligned) cylindrical elements with $\epsilon = 0.2$ and porosity $\theta = 0.5$ is studied at a friction velocity Reynolds number $Re_\tau = 193$. A feature-resolving simulation has also been carried out to provide reference results for validation (figure 1). The model coefficients were first calculated based on the given porosity; the following values were obtained: $\lambda_x = 0.0451$, $\lambda_z = 0.0688$, $\mathcal{K}_{12}^{itf} = 0.0024$, $\mathcal{K}_{32}^{itf} = 0.0056$, $\mathcal{K}_{22} = 0.0018$.

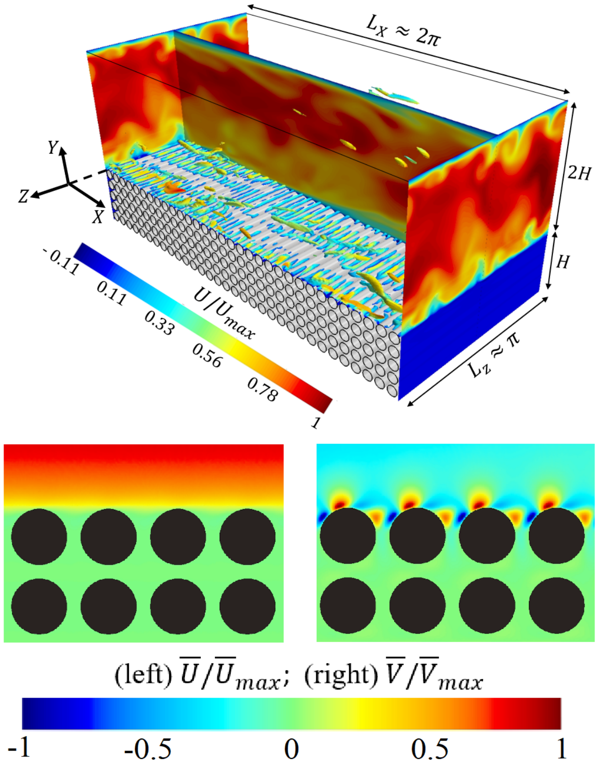

Figure 1: Feature-resolving simulation of turbulent channel flow over a porous bed of spanwise cylinders; the relative dimensions of the computational domain are indicated in the figure, together with the near-interface patterns of mean streamwise and normal velocities.

It has been found that the total shear stress at the substrate/channel interface ($\tau_w^\ell$) is considerably larger than that at the upper smooth surface of the channel ($\tau_w^u$), which implies a significant role of the transpiration/slip velocity in the turbulence cycle near the permeable wall. Typical values of corresponding shear velocities ($u_\tau^\ell$, $u_\tau^u$) are given in table (1) together with other parameters of interest, evaluated for the purpose of validating the macroscopic model. It is important to mention that the shear velocity Reynolds number ($Re_\tau$) and the drag coefficient ($C_f$) are calculated in this study using a bulk stress ($\tau_w^{\Delta p}$) based on the pressure gradient along $X$-direction as $\tau_w^{\Delta p} = \dfrac{\Delta P}{L_x} H$. The corresponding shear velocity ($u_\tau^{\Delta p} = \sqrt{\tau_w^{\Delta p}/\rho}$) is used to normalize rms velocity fluctuations (table 1) and the velocity profile in wall coordinates (figure 2). Generally, a drag increase of more than 22% (relative to the smooth channel case) is found, corresponding to a volumetric flow rate ($Q$) decrease of about 10% (the results given here are preliminary).

Table 1: Predictions of main parameters based on feature-resolving and model simulations with second-order effective conditions. Solution of the wall bounded smooth channel case is also shown for comparison.

| Case | Smooth | Porous (full) | Porous (model) |
|---|---|---|---|
| Total mesh | $2 \times 10^6$ | $26 \times 10^6$ | $2 \times 10^6$ |
| $U^+$, $max$ | 18.164 | 16.646 | 16.314 |
| $V_{rms}$, $max$ | 0.829 | 0.957 | 0.938 |
| $W_{rms}$, $max$ | 1.069 | 1.357 | 1.322 |
| $u_\tau^\ell/u_\tau^{\Delta p}$ | 1 | 1.091 | 1.102 |
| $u_\tau^u/u_\tau^{\Delta p}$ | 1 | 0.900 | 0.886 |
| $\Delta C_f$ % | 0 | 22.35% | 23.92% |
| $\Delta Q$ % | 0 | -9.60% | -10.17% |

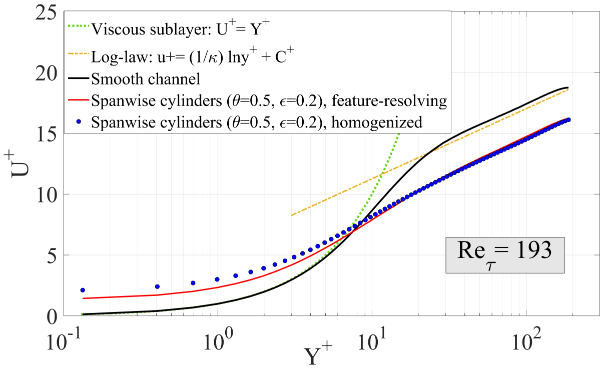

Figure 2: $U^+$ versus $Y^+$ in the range $Y = 0$ to $H$.

## DRAG REDUCTION BY LONGITUDINAL INCLUSIONS

The validated macroscopic model is further employed to study turbulence over porous substrates formed by in-line longitudinal inclusions (with $\theta = 0.5$) at different values of $\epsilon$. This is of much interest since porous substrates of preferential permeability in the streamwise direction can, under specific conditions, lead to drag reduction [1, 2]. The inclusions considered here are longitudinal cylindrical elements modified with four longitudinal protrusions in the shape of parallelepipeds, equally-spaced along the circumference; the typical dimensions are shown on a $1 \times 1$ unit cell in figure 3. The model coefficients are first calculated: $\lambda_x = 0.1130$, $\lambda_z = 0.0590$, $\mathcal{K}_{12}^{itf} = 0.0121$, $\mathcal{K}_{32}^{itf} = 0.0041$, $\mathcal{K}_{22} = 0.00012$. Figure 3 depicts the effect of the periodicity ($\epsilon$) on the velocity profile in terms of slip velocity and the behavior in the inertial region. It is clear that drag reduction can be attained with adequate arrangements of longitudinal elements, while the same types of grains may lead to drag increase at large values of $\epsilon$; this finding is corroborated by figure 4. Typically, maximum drag reduction of about 5% can be realized at $S^+ = \epsilon \, Re_\tau \approx 15 - 20$.

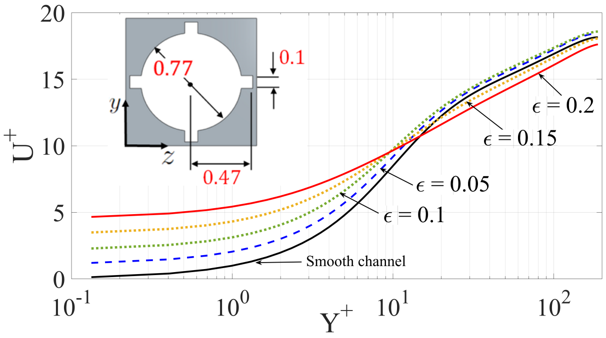

Figure 3: $U^+$ vs. $Y^+$ at different values of the periodicity ($\epsilon$).

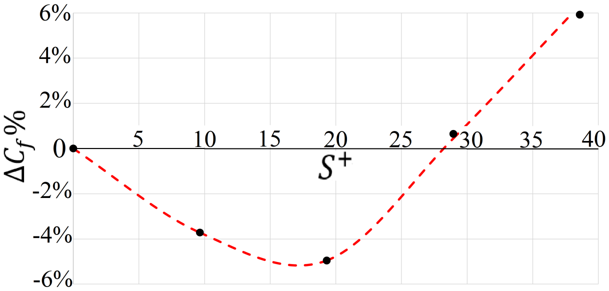

Figure 4: Percentage change in $C_f$, for longitudinal inclusions at different values of $S^+$.

It is shown in figure 5 that longitudinal inclusions with $\epsilon = 0.1$ ($S^+ \approx 20$) can mitigate turbulence in the buffer layer, resulting in a more uniform flow field as compared to the case of $\epsilon = 0.2$ ($S^+ \approx 40$); this observation helps to explain the drag reduction caused by the former arrangement.

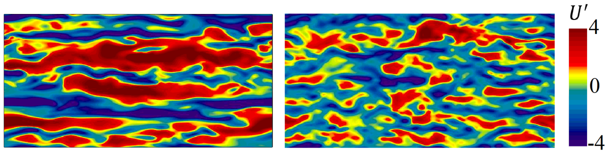

Figure 5: Streamwise velocity fluctuations at the plane $Y^+ \approx 20$: (left) $\epsilon = 0.1$; (right) $\epsilon = 0.2$.

## REFERENCES

[1] E. N. Ahmed, S. B. Naqvi, L. Buda, and A. Bottaro. *Fluids*, 7(5), 2022.

[2] G. Gómez-de Segura and R. García-Mayoral. *Journal of Fluid Mechanics*, 875:124–172, 2019.

[3] J. Jiménez and A. Pinelli. *Journal of Fluid Mechanics*, 389:335–359, 1999.

[4] U. Lācis, Y. Sudhakar, S. Pasche, and S. Bagheri. *Journal of Fluid Mechanics*, 884:A21, 2020.

[5] S. B. Naqvi and A. Bottaro. *International Journal of Multiphase Flow*, 141:103585, 2021.

**Joint ERCOFTAC/EU-CTFF**
**European Drag Reduction and Flow Control Meeting – EDRFCM 2022**
**September 6$^{\text{th}}$–9$^{\text{th}}$, 2022, Paris, France**

# TURBULENT BOUNDARY LAYERS OVER SURFACES WITH STREAMWISE-PREFERENTIAL PERMEABILITY

**F.H. Hartog**
Aerodynamics, Wind Energy, Flight Performance and Propulsion Department, Delft University of Technology,
2629 HS Delft, The Netherlands

## ABSTRACT

Recent numerical studies have suggested the ability of surfaces with streamwise-preferential permeability to reduce turbulent friction, and a theoretical framework behind the working mechanism has been proposed by Gómez-de Segura and García-Mayoral [2019]. This work is the first experimental study on this concept in air and in which the permeability requirements for predicted drag reductions are met. A 3D-printed structure with streamwise-preferential permeability was investigated through wind tunnel experiments using direct force measurements and planar (2D-2C) particle image velocimetry (PIV). Results show an increase in drag ($0\% < \Delta C_D < 8\%$) and turbulent intensity. No significant flow modulation in terms of turbulent events or change in coherent structures is observed. The measurements and results are a first of its kind and none of the theoretical framework predictions on drag reduction or flow modulation are found. This is visualised for the predicted slip length in Figure 1. Based on analytical derivations relating characteristic length scales to permeability, the validity of the theoretical framework and its assumptions under actual experimental conditions is questioned. It is thought that there is an inherent mismatch between the pore size assumption and the virtual origin approach taken in the framework. In conclusion, it is deemed unlikely that turbulent drag reduction by means of streamwise-preferential permeable surfaces is feasible in experimental settings. Nevertheless, given the relatively small increase in drag, streamwise-preferential permeable surfaces might be interesting for other (flow control) purposes involving turbulent boundary layers.

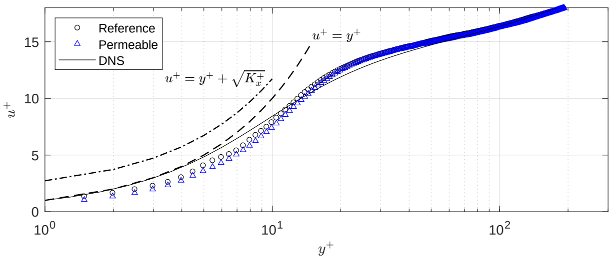

Figure 1: Mean velocity boundary layer profiles for smooth wall and permeable surface, inner layer at $U_\infty = 10$ m/s. $Re_\tau = 720$, $\sqrt{K_x^+} = 2.7$. Predicted slip: $u^+ = y^+ + \sqrt{K_x^+}$. DNS data for $Re_\tau = 670$ from Schlatter and Örlü [2010].

## CORRESPONDING PAPER

F. H. Hartog, M. van Nesselrooij, O. W. G. van Campenhout, B. W. van Oudheusden, F. F. J. Schrijer, and K. Masania. Turbulent boundary layers over surfaces with streamwise-preferential permeability. Physics of Fluids, 2022. Manuscript in preparation.

## REFERENCES

G. Gómez-de Segura and R. García-Mayoral. Turbulent drag reduction by anisotropic permeable substrates – analysis and direct numerical simulations. *Journal of Fluid Mechanics*, 875:124–172, 2019.

P. Schlatter and R. Örlü. Assessment of direct numerical simulation data of turbulent boundary layers. *Journal of Fluid Mechanics*, 659:116–126, 2010.

**Joint ERCOFTAC/EU-CTFF**
**European Drag Reduction and Flow Control Meeting – EDRFCM 2022**
**September $6^{\text{th}}$–$9^{\text{th}}$, 2022, Paris, France**

# DISCUSSION ON THE POSSIBILITY OF TURBULENT DRAG REDUCTION BY A STREAMWISE PREFERENTIAL POROUS MEDIUM

**M. Morimoto**, **Y.Kuwata & K.Suga**
Department of Mechanical Engineering, Osaka Metropolitan University, Sakai, 599-8531, Japan

## INTRODUCTION

It is well known that turbulent drag increases if flows are bounded by porous media. Indeed, many studies have been conducted to clarify such flow characteristics. Recently, Rosti et al.[3] and Gómez-de-Segura and García-Mayoral [2], however, reported direct numerical simulation (DNS) studies which indicated that more than 20% turbulent drag reduction (DR) could be achieved if the porous characteristics were anisotropic with dominant streamwise permeability. Since these direct simulations treated the porous effects using the volume-averaged theory with some assumptions, the exact porous-structural effects were not considered. This indicates that the DR effect by such porous media is still unproven. Therefore, to confirm whether turbulent drag reduces with such porous media, we have performed particle image velocimetry (PIV) experiments of turbulent flows over a porous medium whose properties are within the DR conditions proposed by the DNS [2]. The measured flows are in a square duct over the porous substrate at the bulk Reynolds numbers of 5,000-15,000. We have designed the structure of the porous medium using fine mesh sheets to satisfy the proposed DR conditions. From the obtained experimental data, we have discussed whether the porous medium has the DR ability.

## EXPERIMENTAL APPARATUS

Figure 1(a) illustrates the cross-section of the present square duct, whose height is $H$=50mm. Its bottom wall is covered by a $h$=10mm thick porous substrate consisting of stainless-steel woven-wire-mesh-sheets whose mesh spacing and wire diameter are $G$=0.15mm and $d$=0.1mm, respectively, as shown in Figure 1(b). As seen in Figure 1(a), the mesh sheets are piled to form a cardboard-like structured porous medium. The characteristics of the porous medium are listed in Table 1. The porosity $\varphi$ is obtained from the measured density. The diagonal component of the permeability tensor, $K_{\alpha\alpha}$, is measured from the relation between the pressure drops and the flow rates through the porous medium stuffed into the duct flow facility. The permeability ratio parameter is defined as $\psi_{\alpha\beta}=\sqrt{K_{\alpha\alpha}/K_{\beta\beta}}$. The measured bulk Reynolds numbers are $Re_b(=U_bH/\nu)$=5,000-15,000, where $U_b$ is the bulk mean velocity and $\nu$ is the kinematic viscosity of water as the working fluid.

## RESULTS AND DISCUSSION

Gómez-de-Segura and García-Mayoral [2] suggested that when $\psi_{xy}$ >3.6, $\sqrt{K_{yy}}^+ \leq 0.48$ and $h/\sqrt{K_{xx}}$ >2, significant drag reduction took place. Here, the permeability Reynolds number is defined as $\sqrt{K_{\alpha\alpha}}^+ = u_\tau\sqrt{K_{\alpha\alpha}}/\nu$. For the cases with $\psi_{xy} \simeq 11.4$, 5.5 and 3.6, they reported that the drag reduction effect was maximum around $\sqrt{K_{yy}}^+$=0.3, while for $\sqrt{K_{yy}}^+$ >0.6 no drag reduction effect was observed.

Table 1: Characteristics of the porous medium.

| $\varphi$ | $K_{xx}$[mm$^2$] | $K_{yy}$[mm$^2$] | $K_{zz}$[mm$^2$] | $\psi_{xy}$ | $\psi_{zy}$ |
|---|---|---|---|---|---|
| 0.9 | 0.0269 | 0.00145 | 0.00416 | 4.3 | 1.7 |

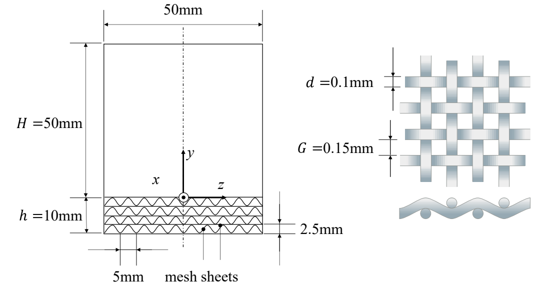

($a$) Cross-sectional view. ($b$) Mesh geometry.

Figure 1: Geometries of the test section and the porous medium.

The permeability Reynolds numbers calculated from the present flow conditions are listed in Table 2. Since it is difficult to directly measure the friction velocity $u_\tau$ for the present experimental facility, we estimate it by using the correlation proposed by Gavrilakis [1]. The correlation function gives the Darcy-Weisbach friction factor $f = 8u_\tau^2/U_b^2$ as $f = 0.281Re_b^{-1/4.13}$. As seen in Tables 1 and 2, the present flow conditions at $Re_b \leq 10,000$ satisfy the DR conditions for $\psi_{xy}$ and $\sqrt{K_{yy}}^+$. For the porous substrate thickness, the present case is $h/\sqrt{K_{xx}} = 61$ and it is thick enough.

To discuss the effects of the porous substrate, we first compare the mean velocity profiles at the symmetry plane in the semi-logarithmic chart as in Figure 2. At $Re_b$=15,000, the profile of the porous wall side is clearly below that of the solid wall side. Note that the downward shift of the mean velocity which is usually called the roughness function corresponding to the increase of the wall friction. It suggests that the friction increases on the porous substrate at $Re_b$=15,000 and this is consistent with the results of the DNS study [2]. Although the turbulent friction over the porous substrate was expected to reduce at $Re_b$ ≤10,000, the velocity profiles over the porous substrate do not imply such a trend since the profiles are almost the same as those over the solid smooth top wall side. This means that the roughness function $\Delta U^+ = 0$ for the present cases at $Re_b$ <10,000. Gómez-de-Segura and García-Mayoral [2] however suggested that the negative roughness function $-\Delta U^+$ was approximately $\sqrt{K_{xx}}^+ - \sqrt{K_{zz}}^+$ at $\sqrt{K_{yy}}^+ \leq 0.38$ and the present data of $\sqrt{K_{xx}}^+ - \sqrt{K_{zz}}^+$ at

Table 2: Permeability Reynolds numbers.

| $Re_b$ | 5,000 | 7,500 | 10,000 | 15,000 |
|---|---|---|---|---|
| $\sqrt{K_{yy}}^+$ | 0.26 | 0.36 | 0.48 | 0.69 |
| $\sqrt{K_{xx}}^+ - \sqrt{K_{zz}}^+$ | 0.68 | 0.95 | 1.24 | 1.80 |

$Re_b \leq 7,500$ are always positive which means drag reduction.

To discuss why the inconsistency between the DNS and the present cases emerges, we next focus on the bursting events, which contribute to turbulence generation through the Reynolds shear stress, by performing the quadrant analysis method. The quadrant $Q_m$ is defined as $Q_m = \overline{(u'v')}_m = \Sigma\frac{(u'v')_m}{\overline{u'v'}}$, where the subscript $m$(=1-4) corresponds to each quadrant. In the present paper, we discuss $Q_2$: ejections and $Q_4$: sweeps which directly contribute to the generation of the Reynolds shear stress. In Figure 3, we can see that although the $Q_4$ profiles near the porous wall are larger than those near the solid wall at $Re_b$=10,000 and 15,000, they are almost the same at $Re_b$=5,000. As for the $Q_2$ profiles, those near the porous side always exceed those on the solid wall side irrespective of the Reynolds number. From these profiles, it is considered that generally sweeps and ejections are enhanced by the porosity of the wall since the porous wall weakens the wall blocking effects. Such enhancement contributes to the increase of the Reynolds shear stress and then the wall friction. At $Re_b$=5,000, however, the mean streamwise velocity indicates no drag increase as shown in Figure 2.

To understand why the aforementioned trends take place, Figure 4 shows the mean wall-normal velocities at the symmetry plane. We can see clearly that the profiles near the porous wall are always larger than those near the solid wall. In the region near the wall, turbulence driven secondary flows, which are typically observed near corner boundaries, are enhanced by the flows coming out from the porous substrate at the symmetry plane. It is considered that these enhanced upward flows lead to enhanced ejections, as seen in Figure 3a. This implies that if such enhancement of the ejections is suppressed, the Reynolds shear stress is also suppressed resulting in lagging the drag increase. Particularly at $Re_b = 5,000$, reduction of the $Q_2$ events would lead to drag reduction. Accordingly, we should reassess the performance of the present substrate in flows which are free from the secondary flow effects.

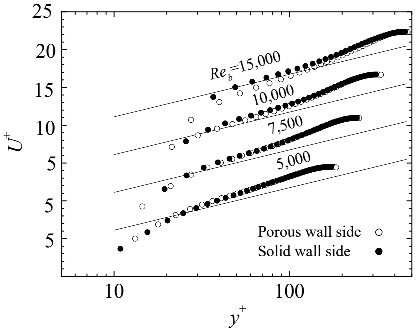

Figure 2: Mean streamwise velocities at the symmetry plane. The solid lines denote $U^+ = \kappa^{-1} \ln y^+ + 5.5$ with $\kappa = 0.41$.

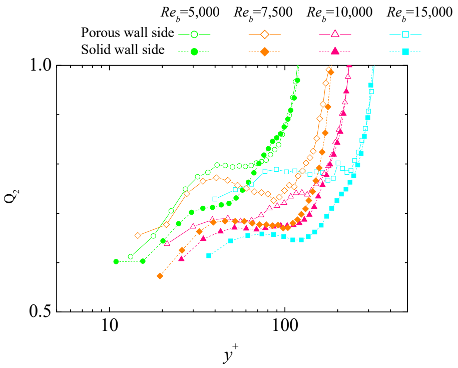

(a) $Q_2$: ejections.

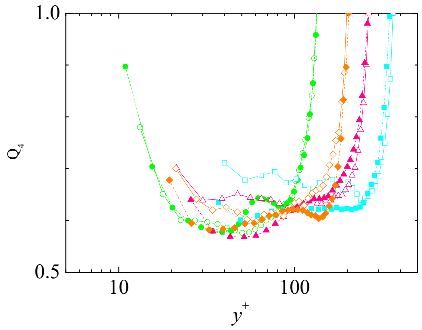

(b) $Q_4$: sweeps.

Figure 3: Distribution profiles of ejections($Q_2$) and sweeps ($Q_4$) at the symmetry plane.

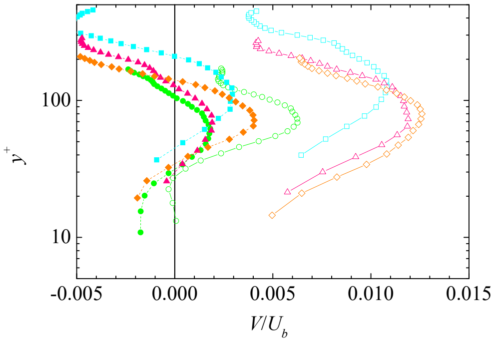

Figure 4: Mean wall-normal velocities at the symmetry plane. See Figure 3 for the legend of the symbols.

## CONCLUSION

To assess the DR probability by the streamwise-preferential porous media which are discussed by the DNS study [2], PIV measurements have been carried out for turbulent square duct flows over a porous substrate. Although the present flow conditions satisfy the DR conditions of the DNS at $Re_b \leq$10,000, DR effects are not observed. At $Re_b$=5,000, the mean streamwise velocity profiles suggest that the wall friction on the present porous substrate is almost the same as the smooth wall friction while ejections are rather enhanced by the secondary flows coming up from the porous region. This suggests that if flows are free from such turbulence-driven secondary flows, the present porous substrate may achieve turbulent drag reduction as predicted by Gómez-de-Segura and García-Mayoral [2]. It is, therefore, necessary to reassess the performance of the present substrate in flows free from the secondary flow effects like in 2D channel and boundary layer flows. Such a project is now under preparation and will be presented shortly soon.

## REFERENCES

[1] S. Gavrilakis. Post-transitional periodic flow in a straight square duct. *Journal of Fluid Mechanics*, 859:731–753, 2019.

[2] G. Gómez-de Segura and R. García-Mayoral. Turbulent drag reduction by anisotropic permeable substrates – analysis and direct numerical simulations. *Journal of Fluid Mechanics*, 875:124–172, 2019.

[3] M. Rosti, L. Brandt, and A. Pinelli. Turbulent channel flow over an anisotropic porous wall - drag increase and reduction. *Journal of Fluid Mechanics*, 842:381–394, 2018.

**Joint ERCOFTAC/EU-CTFF**
**European Drag Reduction and Flow Control Meeting – EDRFCM 2022**
**September 6th–9th, 2022, Paris, France**

# SUPERSONIC PRE-TRANSITIONAL STREAKS OVER POROUS SURFACES

**L. Fossà, P. Ricco**
Department of Mechanical Engineering, University of Sheffield, S1 3JD, UK

Free-stream disturbances play a key role in the dynamics of boundary layers. They may penetrate the boundary layer to generate low-frequency pre-transitional disturbances (streaky Klebanoff modes), excite instability modes through a receptivity mechanism, and, when their amplitude is sufficiently intense, bypass transition may play a major role to the flow breakdown to turbulence. It is therefore crucial to control boundary layers exposed to free-stream disturbances to achieve a delay of transition and enhance the flow system performance. Porous walls have been shown to effectively reduce the growth of the compressible second mode of instability [1], but their effects on the Klebanoff modes and the base-flow receptivity for the excitation of Tollmien-Schlichting (TS) waves are unknown [2].

Motivated by the lack of knowledge in this area, we investigate supersonic laminar boundary layers flowing over flat porous plates with a regular microstructure. We utilize theoretical analysis based on asymptotic theory and numerical simulations. The impact of the porous wall on the boundary-layer response to small-amplitude free-stream vortical disturbances is evaluated by computing the growth of low-frequency, streamwise-elongated streaky structures known as Klebanoff modes. The effect of porosity on the excitation and growth of Tollmien-Schlichting waves further downstream is studied as well, and the numerical results are compared with triple-deck asymptotic results.

The perturbations of the laminar base flow are assumed to be small enough for nonlinear interactions to be considered negligible. A single free-stream disturbance component of the convected-gust type [3],

$$\underline{\boldsymbol{u}} - \widehat{\boldsymbol{i}} = \varepsilon \widehat{\underline{\boldsymbol{u}}}_{\infty} e^{\mathrm{i}(k_z z - k_x t)} + \text{c.c.}, \qquad (1)$$

is considered, where $\varepsilon \ll 1$, $\widehat{\underline{\boldsymbol{u}}}_{\infty} = \mathcal{O}(1)$, $k_z$ and $k_x$ are the non-dimensional spanwise and streamwise wavenumbers, respectively, and c.c. denotes the complex conjugate. The laminar streaks are elongated in the streamwise direction ($k_x \ll 1$) and have a characteristic spanwise wavelength $\lambda_z^*$, which is used as reference length scale.

The downstream evolution of the velocity, pressure and temperature perturbations is described by the compressible linearized unsteady boundary region (CLUBR) equations [3], valid at a distance $\overline{x} = k_x x = \mathcal{O}(1)$ from the leading edge. The spanwise diffusion plays a leading role at these locations as the boundary layer thickness has increased to a magnitude comparable with that of $\lambda_z^*$.

The adopted regular-microstructure porous coating model, proposed by [4, 5], is shown in figure 1. Regularly spaced cylindrical microcavities of radius $r$ and depth $h$ are carved out of an otherwise solid flat plate. The pressure and the wall-normal velocity fluctuations are coupled at the porous wall boundary via an admittance

$$A = \frac{v}{p} = -\frac{\phi}{Z_0}\tanh\left(mh\right), \qquad (2)$$

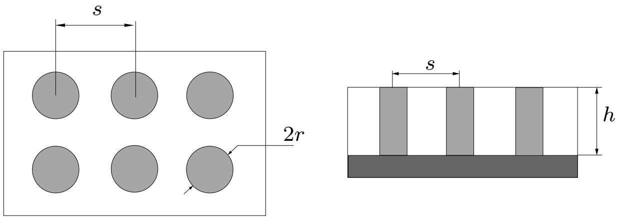

Figure 1: Porous layer microstructure (adapted from [4]).

where $\phi$ is the porosity, and $Z_0$ and $m$ are the characteristic impedance and the constant of propagation of the velocity and pressure disturbances in a cylindrical cavity, respectively.

The response of the boundary layer has been evaluated for $\mathrm{Ma}_\infty = U_\infty^*/c_\infty^* = 6$ and $\mathrm{Re}_{\lambda_z} = U_\infty^* \lambda_z^*/(2\pi\nu_\infty^*) = 1.2 \cdot 10^7$, where $U_\infty^*$, $\nu_\infty^*$, $c_\infty^*$ denote the free-stream velocity, kinematic viscosity and sound speed, respectively.

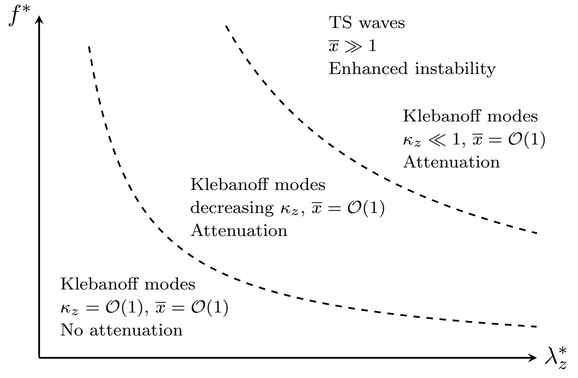

Figure 2: Schematic of the influence of a porous layer on the downstream growth of Klebanoff modes and TS waves.

The impact of the wall permeability on the algebraic growth of the Klebanoff modes and the TS waves is highly dependent on the characteristic frequency and spanwise wavelength of the disturbances, as summarized in figure 2. The influence of the frequency $f^*$ and the spanwise wavelength $\lambda_z^*$ is expressed through the asymptotic parameter $\kappa_z = k_z/\sqrt{k_x \mathrm{Re}_{\lambda_z}} = \lambda_z^{*-1}\sqrt{2\pi\nu^*/f^*}$, which represents the relevance of the spanwise viscous diffusion when $\overline{x} = k_x x = \mathcal{O}(1)$.

The streaks are not attenuated when $\kappa_z = \mathcal{O}(1)$. Their intensity is instead damped as $\kappa_z$ decreases, which occurs for increasing $f^*$ and/or $\lambda_z^*$. Figure 3 depicts a case for which the intensity of the Klebanoff modes is stabilized. The streamwise velocity and the temperature fluctuations are attenuated by the presence of the porous layer in similar fashion, whereas the transverse velocity components are only mildly stabilized. The pressure fluctuations are also attenuated. When $\kappa_z \ll 1$, the algebraic growth of the Klebanoff modes is followed further downstream by the exponential growth of oblique TS waves ($\overline{x} \gg 1$, see figure 3), as found by [3]. Figure 4 shows the

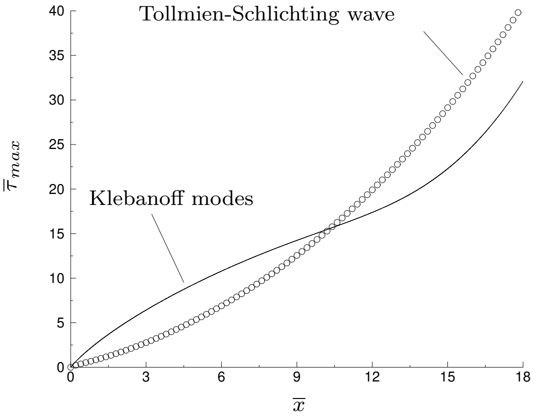

Figure 3: Downstream evolution of maximum temperature for $f^* = 30000$Hz and $\lambda_z^* = 10$mm. The presence of the porous layer (dots) effectively damps the Klebanoff modes, and yet enhances the growth of the TS waves with respect to the solid plate case (solid curve).

interactive physical mechanism. Quasi three-dimensional decaying Lam-Rott eigensolutions [6] are excited by the external low-frequency disturbances. At downstream locations where $\overline{x} = \mathcal{O}(\kappa_z^{-1})$, an interactive triple-deck structure unfolds. The boundary layer splits in three regions: a lower deck located at $\eta = \mathcal{O}(\kappa_z^{1/2})$, a main deck at $\eta = \mathcal{O}(1)$ deck, and an upper deck at $\eta = \mathcal{O}(\kappa_z^{-1/2})$. The wall-normal velocity component of the Lam-Rott disturbances is brought to zero in the upper deck via a pressure disturbance. The latter is transmitted to the lower deck, where it interacts with the spanwise and wall-normal velocity components, creating an interactive triple-deck regime. This regime is responsible for the growth of the unstable TS waves. In the lower-deck, the wall-normal velocity solution at the wall is coupled with the pressure at the wall via (2) when the wall is porous, thus influencing the fluctuating velocity components and altering the instability.

While the admittance $A$ must be at least of order $\mathcal{O}(\mathrm{Re}_{\lambda_z}/k_x)$ to affect the velocity disturbance of the laminar streaks ($\kappa_z = \mathcal{O}(1)$ and $\overline{x} = \mathcal{O}(1)$), a much smaller admittance $A = \mathcal{O}(k_x^{-1/2}\mathrm{Re}_{\lambda_z}^{-3/2})$ can effectively interact with the near-wall oblique TS waves ($\kappa_z \ll 1$ and $\overline{x} \gg 1$).

The wavelength and the growth rate of the unstable TS modes are computed via a dispersion relation $\Delta = 0$, where

$$\begin{aligned}\Delta = \int_{\eta_0}^{\infty} \mathrm{Ai}\,\mathrm{d}\breve{\eta} - \\ \left(\frac{\mu_w}{T_w}\right)^{1/3} \frac{\mathrm{i}F''\left(0\right)\left(2\mathrm{i}F''\left(0\right)\alpha_1\kappa_z\overline{x}\right)^{2/3}\mathrm{Ai}'\left(\eta_0\right)}{2\alpha_1\kappa_z\overline{x}\left(\mathrm{i}\alpha_1 F''\left(0\right) - \left(2\kappa_z\overline{x}\right)^{1/2}T_w^2\right)},\end{aligned} \tag{3}$$

where $F$ is the Blasius function (refer to [3] for details). The imaginary part of $\alpha_1$ computed via the numerical solution of the CLUBR equations is plotted in figure 5 along with the solution of the dispersion relation (3) at $\mathrm{Ma}_\infty = 3$. The CLUBR results are in quantitative agreement with those obtained via the triple-deck theory. Whereas the wall porosity reduces the growth of the Klebanoff modes, it moves the location of the instability upstream and enhances the growth rate of the oblique TS waves. These results prove that the wall porosity has a stabilizing effect on the algebraically growing streaks and a destabilizing effect on the boundary-layer instability.

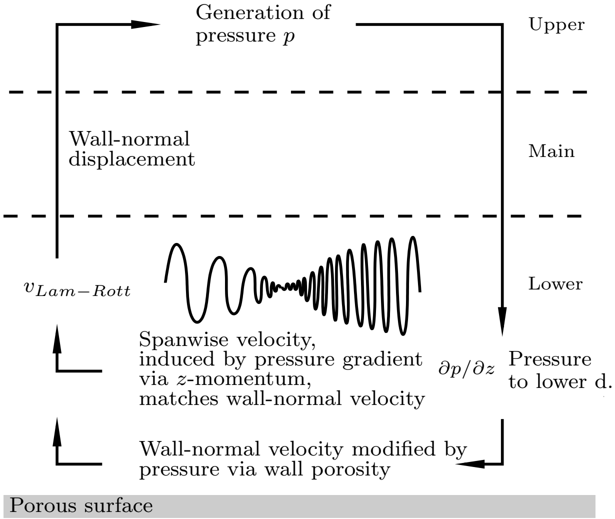

Figure 4: Schematic of triple-deck interactive regime in the presence of a porous surface.

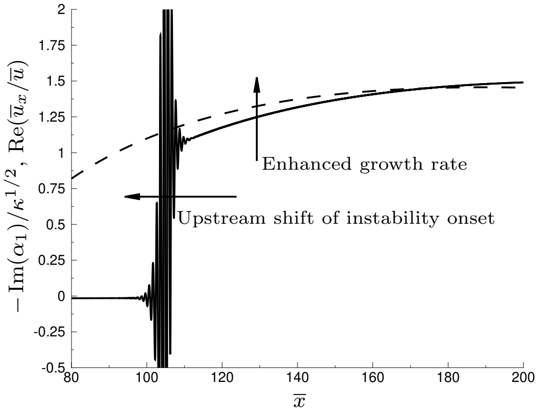

Figure 5: Growth rate of the growing disturbance for $M = 3$ and $\kappa = 0.0005$ for a porous wall ($\widetilde{A} = A\sqrt{k_x/\mathrm{Re}_{\lambda_z}}/\kappa^2$=-2+0.5i). The solid curve indicates the CLUBR solution and the dashed one denotes the triple-deck solution.

## ACKNOWLEDGEMENTS

The authors wish to acknowledge the support of the US Air Force through the AFOSR grant FA8655-21-1-7005 (International Program Office - Dr Douglas Smith). PR has also been supported by EPSRC (Grant No. EP/T01167X/1).

## REFERENCES

[1] I. V. Egorov, A. V. Fedorov, V. G. Soudakov, *J. Fluid Mech.* **601**, 165–187 (2008).

[2] A. V. Fedorov, *Ann. Rev. Fluid Mech.* **43**(1), 79 (2011).

[3] P. Ricco and X. Wu, *J. Fluid Mech.* **587**, 97–138 (2007).

[4] A. V. Fedorov, N. D. Malmuth, A. Rasheed, H. G. Hornung, *AIAA Journal* **39**(4), 605 (2001).

[5] A. A. Maslov, A. N. Shiplyuk, A. A. Sidorenko, D. Arnal, *J. Fluid Mech.* **426**, 73–94 (2001).

[6] M. E. Goldstein, *J. Fluid Mech.* **127**, 59 (1983).